Electron spin dynamics of erbium ions in scheelite crystals, probed with superconducting resonators at millikelvin temperatures

Marianne Le Dantec

université PARIS-SACLAY

Electron spin dynamics of erbium ions in scheelite crystals, probed with superconducting resonators at millikelvin temperatures

Dynamique des spins électroniques d'ions erbium dans des cristaux de scheelite, sondés avec des résonateurs supraconducteurs à des températures de l'ordre du millikelvin

Thèse de doctorat de l'université Paris-Saclay

École doctorale n° 564, physique en Ile-de-France (PIF)
Spécialité de doctorat : physique
Graduate School : physique, Référent : faculté des sciences d'Orsay

Thèse préparée dans l'unité de recherche SPEC (Université Paris-Saclay, CEA, CNRS, SPEC, 91191, Gif-sur-Yvette, France), sous la direction de Patrice BERTET

Thèse soutenue à Paris-Saclay, le 24 janvier 2022, par

Marianne LE DANTEC

Composition du jury

Olivier Krebs Directeur de recherche, Université Paris-Saclay	Président
Wolfgang Tittel Professeur, TU Delft	Rapporteur & Examinateur
Jörg Wrachtrup Professeur, Université de Stuttgart	Rapporteur & Examinateur
Signe Seidelin Maître de conférences, Université Grenoble Alpes	Examinatrice
Diana Serrano Chargée de recherche, CNRS	Examinatrice
Patrice Bertet Directeur de recherche, CEA Saclay	Directeur de thèse

THESE DE DOCTORAT
NNT : 2022UPASP009

Remerciements

Ces trois années passées au sein du groupe Quantronique furent très riches en apprentissages et en rencontres. Je voudrais remercier toutes les personnes ayant contribué à me faire progresser et sans lesquelles le travail présenté ici aurait été bien différent.

D'abord, je remercie mon directeur de thèse, Patrice Bertet, pour m'avoir acceptée dans son équipe et confié les débuts du projet sur l'erbium. Merci Patrice de m'avoir guidée avec bienveillance, rigueur et sagacité tout au long de mon parcours et d'avoir été très présent pour discuter du résultat des manips ou de toute question scientifique. Pour réaliser les expériences, j'ai eu la chance de travailler avec Miloš Rančić, qui n'a jamais peur de rien sachant tout réparer lui-même. Merci Miloš, les heures passées ensemble en salle de manip à fermer un frigo à dilution, souder des fils supraconducteurs, démonter un ordinateur ou bien réparer mes chaussures furent des moments à la fois ludiques et très instructifs.

Bien sûr, je remercie l'ensemble du groupe Quantronique pour la bonne entente qui règne au labo. En particulier, merci Denis de te rendre autant disponible pour faire avancer chaque projet et partager très pédagogiquement ton savoir et ton bon sens. Merci Daniel d'avoir été toujours si curieux de connaître mes petites avancées et pour le temps passé ensemble à défricher la théorie de la diffusion spectrale. Merci Emmanuel, partager un bureau pendant ces trois ans fut fort sympathique. Merci Pascal, pour m'avoir montré dix fois comment utiliser les machines de l'atelier. Merci à tous les autres membres permanents, Cristian, Hélène, Hugues, Marcelo et Philippe, pour vos conseils et encouragements. Je souhaiterais remercier également les doctorants et post-doctorants avec lesquels j'ai partagé de bons moments pendant ma thèse : Anil, Bartolo, Boris, Cyril, Dan, Emanuele, Eric, Fernanda, Leandro, Léo, Louis, Manas, Maria, Moonjoo, Nicolas, Vishal, Yutian, Zhiren, ainsi que tous ceux qui m'ont précédée et qui ont contribué à faire de la manip ce qu'elle était lorsque j'ai commencé ma thèse.

Je voudrais maintenant remercier les équipes du SPEC qui nous soutiennent quotidiennement. Merci à l'équipe de nanofab, Pief et Sébastien, pour votre expertise et vos bons conseils. Merci à l'équipe de cryogénie, Aurélia, Mathieu, Patrick et Philippe, et à l'atelier de mécanique, Dominique, Jean-Claude et Vincent. Enfin, merci à la direction du SPEC, en particulier pour nous avoir permis de travailler correctement malgré la crise sanitaire et les confinements successifs qu'aura traversés cette thèse. Je remercie également François Ladieu du SPEC et Véronique Terras de l'école doctorale, leur aide au moment d'affronter toutes les démarches administratives du doctorant est très précieuse.

En dehors du SPEC, je tiens à remercier tous les collègues participant à ce projet sur l'erbium : Philippe Goldner, Diana Serrano et Alban Ferrier de ChimieParisTech, qui ont fabriqué certains de nos échantillons, Thierry Chanelière de l'institut Néel, qui nous a notamment donné un bon coup de pouce pour traiter nos données d'ESEEM, et Sylvain Bertaina de l'IM2NP, qui m'a accueillie quelques jours dans son labo à Marseille. Discuter et échanger avec vous fut une grande source d'inspiration. Côté théorie, certaines simulations furent réalisées par Sen Lin et Ren Bao Liu, de l'université de Hong Kong, et je les remercie pour cette fructueuse collaboration.

Je suis très reconnaissante à mon jury de thèse, Olivier Krebs, Signe Seidelin, Diana Serrano, Wolfgang Tittel et Jörg Wrachtrup, d'avoir accepté d'évaluer ce travail.

Ces quelques mots ne sauraient se conclure sans remercier mes proches. Merci à ma famille pour son soutien sans faille depuis le début de cette aventure. Merci à mes amis d'école, aux copains de la pizza du mardi et à ceux des orchestres du plateau de Saclay. Enfin, merci Daniel de m'apporter joie et bonne humeur au quotidien.

Contents

Useful physical constants

Constants in SI units [1] :

- vacuum magnetic permeability, $\mu_0 = 4\pi \times 10^{-7}$ H/m
- Planck constant, $h = 6.63 \times 10^{-34}$ Js
- reduced Planck constant, $\hbar = h/2\pi = 1.05 \times 10^{-34}$ Js
- Bohr magneton, $\mu_B = 9.274 \times 10^{-24}$ J/T, $\mu_B/h = 13.996$ GHz/T
- nuclear magneton, $\mu_N = 5.051 \times 10^{-27}$ J/T, $\mu_N/h = 7.622$ MHz/T
- Boltzmann constant, $k_B = 1.38 \times 10^{-23}$ J/K

[1] Values from NIST (https://physics.nist.gov/cuu/Constants/index.html)

List of abbreviations

- CCE: cluster-correlation expansion
- EPR: electron paramagnetic resonance
- ESEEM: electron spin-echo envelope modulation
- ESR: electron spin resonance
- FID: free induction decay
- FWHM: full-width-at-half-maximum
- HEMT: high electron mobility transitor
- HWHM: half-width-at-half-maximum
- ID: instantaneous diffusion
- JTWPA: Josephson traveling-wave parametric amplifier
- LO: local oscillator
- PCB: printed circuit board
- ppb: part per billion
- ppm: part per million
- REI: rare-earth ion
- RF: radio frequency
- rms: root-mean-square
- SD: spectral diffusion
- SNR: signal to noise ratio
- VNA: vector network analyzer
- ZEFOZ: zero-first-order-Zeeman

Résumé détaillé

Les ordinateurs d'aujourd'hui sont basés sur des transistors qui traitent de l'information classique, codée par deux états 0 et 1. Leur puissance de calcul est directement liée au nombre de transistors par processeur. Depuis 50 ans, les ordinateurs sont devenus de plus en plus puissants, suivant la loi de Moore, qui prédit en 1965 un doublement du nombre de transistors par puce chaque année [Moo06]. Cela fut rendu possible par le retrécissement de la taille des transistors, atteignant actuellement l'échelle nanométrique. Cependant, à cette échelle, les effets quantiques, comme le passage d'un électron à travers une barrière de potentiel, doivent être pris en compte et la poursuite de la loi de Moore nécessite de nouvelles architectures.

En parallèle, la réalisation d'un nouveau type d'ordinateur, basé sur la mécanique quantique, a suscité un intérêt mondial pour sa capacité à résoudre certains types de problèmes bien plus efficacement qu'un ordinateur classique. Dans les ordinateurs quantiques, l'information est codée sur les états de base $|0\rangle$ et $|1\rangle$ d'un système quantique à deux niveaux. Un état quelconque du qubit (ou bit quantique) s'écrit $|\psi\rangle = \alpha\,|0\rangle + \beta\,|1\rangle$, où α et β sont des nombres complexes tels que $|\alpha|^2 + |\beta|^2 = 1$. Appliqué à un grand registre de qubits, ce principe de superposition des états de base peut conduire à une parallélisation extrême des calculs. L'algorithme quantique le plus connu a été inventé par Shor en 1994. Son algorithme factorise un grand nombre entier en ses facteurs premiers dans un temps polynomial par rapport à la taille du nombre entier [Sho94], alors que le temps requis par les algorithmes classiques augmente exponentiellement. La difficulté à factoriser un nombre en ses facteurs premiers est au coeur des systèmes actuels de chiffrement, utilisés constamment pour sécuriser nos informations. Les ordinateurs quantiques seraient donc capables de casser la cryptographie actuelle et de nouveaux systèmes de chiffrement devraient alors être implémentés. Suite à l'algorithme de Shor, bien d'autres algorithmes ont été proposés, promettant une accélération quantique dans de nombreux domaines, comme les calculs de chimie quantique ou les problèmes d'optimisation. Tout cela motive un effort de recherche mondial pour construire une telle machine.

Les ordinateurs quantiques n'existent pas encore car l'information quantique est très fragile. En effet, les interactions des qubits avec leur environement nuisent à la cohérence quantique. Les protéger de la décohérence nécessite des codes correcteurs d'erreur complexes, ce qui met des contraintes fortes sur la qualité des qubits physiques à réaliser.

La recherche autour des processeurs quantiques a fait émerger plusieurs types de qubits potentiels. En matière condensée, deux candidats particulièrement prometteurs sont les qubits supraconducteurs, où l'information quantique est codée dans l'état quantique d'un circuit électrique, et les qubits de spin, où l'information quantique est codée dans l'état de spin d'un défaut cristallin. Chacun de ces systèmes a des avantages et des inconvénients.

Les circuits supraconducteurs sont faciles à contrôler et à fabriquer en grand nombre, ils interagissent aussi facilement entre eux. Google et IBM ont déjà démontré des processeurs quantiques comprenant environ une centaine de qubits [Aru+19]. Malgré les progès récents, le temps de cohérence relativement faible de ces qubits reste le facteur limitant des processeurs quantiques supraconducteurs (le plus long temps de cohérence mesuré est 1 ms

[Som+21]).

De l'autre côté, les défauts cristallins ont des transitions de spins électronique et nucléaire avec des temps de cohérence record : les centres azote-lacune (NV) dans le diamant, les donneurs dans le silicium et les ions de terres rares dans les solides sont tous des systèmes pour lesquels des temps de cohérence approchant ou dépassant une seconde ont été mesurés [Bar+13 ; Tyr+12 ; Ran+18]. Mais, contrairement aux circuits supraconducteurs, les qubits de spin sont difficiles à contrôler et à intriquer. La plate-forme la plus avancée de qubits de spin est faite de donneurs individuels de phosphore dans le silicium et le contrôle d'un spin unique a été démontré il y a presque une décennie, alors que l'intrication des qubits entre eux reste un défi majeur [Pla+12 ; Tos+17] (notez que nous ne discuterons pas dans cette thèse les qubits de spin basés sur des électrons piégés dans des puits quantiques définis lithographiquement).

En raison des inconvénients propres à chaque qubit, les systèmes quantiques hybrides, combinant différents types de qubits pour profiter de tous leurs avantages, ont été envisagés comme une architecture prometteuse pour traiter l'information quantique [Xia+13]. Par exemple, les qubits supraconducteurs peuvent être couplés à des ensembles de spins, les premiers formant l'unité de calcul et les seconds la mémoire. Pour cela, l'ensemble de spins doit posséder une transition cohérente à des fréquences de l'ordre du gigahertz, correspondant aux fréquences typiques des circuits supraconducteurs, et il doit également être capable de se coupler fortement à des résonateurs supraconducteurs afin d'échanger efficacement des photons micro-ondes. Les qubits supraconducteurs et les ensembles de spins peuvent être couplés par un bus quantique, fourni par un résonateur supraconducteur, reliant les deux systèmes.

De nombreux défauts cristallins ont été étudiés dans cette optique. Une preuve de concept, couplant un qubit supraconducteur à un ensemble de spins via un bus quantique, a été réalisée avec des centres NV dans le diamant [Kub+11], tandis que les donneurs de bismuth dans le silicium ont permis de stocker des champs micro-ondes quantiques jusqu'à 100 ms [Ran+20b]. D'autres candidats pour de telles applications sont les ions erbium dans des cristaux En effet, les ions erbium ont un spin électronique effectif $1/2$ qui peut se coupler magnétiquement à des résonateurs supraconducteurs. De plus, les ions erbium ont l'avantage supplémentaire de posséder une transition optique à 1.5 μm qui est optimale pour transmettre des photons à faible perte dans les fibres optiques [Sag+15]. Les cristaux dopés à l'erbium sont donc particulièrement attractifs dans la perspective d'un futur internet quantique, où l'information quantique devra voyager entre des processeurs supraconducteurs distants. Pour ces deux raisons, les ions erbium ont été proposés dans plusieurs architectures hybrides, comme les mémoires quantiques micro-ondes [Afz+13 ; Pro+15] et la transduction d'un photon micro-onde en un photon optique [WCL14 ; Fer+15], où l'ensemble de spins d'erbium est couplé à un résonateur supraconducteur. Un avantage spécifique de l'erbium est également son fort moment magnétique qui permet un couplage efficace à d'autres systèmes quantiques. La détection d'ions erbium uniques couplés à des cavités nanophotoniques a été démontrée très récemment en optique [Che+20].

Ces propositions de systèmes quantiques hybrides basés sur l'erbium reposent sur un long temps de cohérence de la transition de spin électronique de l'erbium et, jusqu'à maintenant, cette propriété manquait. En effet, les mesures précédentes sur des cristaux dopés à l'erbium ont rapporté des temps de cohérence du spin électronique inférieurs à 50 μs [Pro+15 ; Ber+07], à l'exception des transitions d'horloge où un temps de cohérence de 1.5 ms a été mesuré [Rak+20].

Dans cette thèse, nous étudions la dynamique des spins électroniques d'ions erbium dans des cristaux de scheelite ($CaWO_4$) pour comprendre les mécanismes conduisant à

la décohérence du spin électronique. Les expériences sont réalisées à des températures inférieures au Kelvin et utilisent des micro-résonateurs supraconducteurs fabriqués sur la surface de l'échantillon pour détecter les spins. Trois échantillons avec des concentrations d'erbium très différentes sont étudiés (deux autour de 1 ppb -partie par milliard- et un à 20 ppm -partie par million-). L'un des résultats principaux de cette thèse est l'amélioration considérable du temps de cohérence du spin électronique de l'erbium obtenue en refroidissant les échantillons à des températures de l'ordre de la dizaine de millikelvin. Le temps de cohérence y atteint 1 ms pour l'échantillon fortement concentré et 30 ms pour les échantillons faiblement concentrés. Cela s'explique par la suppression de la diffusion spectrale due aux impuretés paramagnétiques, car baisser la température augmente progressivement leur polarisation dans leur état fondamental. Cette dernière valeur de 30 ms représente une amélioration de presque trois ordres de grandeur pour les ions erbium dans $CaWO_4$ [Ber+07] et d'un ordre de grandeur pour toutes les transitions de spin électronique dans des matériaux à abondance naturelle, sur une transition sensible au champ magnétique [Li+20]. De plus, dans l'échantillon le moins concentré, une raie inhomogène de l'erbium étroite de 1 MHz est rapportée, ce qui est particulièrement intéressant pour la transduction de photons micro-ondes en photons optiques [Fer+15]. Enfin, nous démontrons que les ions erbium peuvent atteindre le régime Purcell, où la relaxation de spin est dominée par l'émission spontanée de photons micro-ondes, plutôt que de phonons.

Cette thèse se décompose en trois parties. La première fournit le bagage nécessaire à la compréhension des expériences. La deuxième présente les résultats obtenus avec les échantillons faiblement dopés et la troisième avec l'échantillon fortement dopé. Le contenu de chaque chapitre est décrit avec plus de détails ci-dessous.

Contexte

L'erbium appartient à une classe d'atomes appelés terres rares, qui ont des propriétés très similaires. En particulier, la moitié d'entre eux, y compris l'erbium, sont des ions de Kramers, avec un état fondamental formant un doublet qui se comporte comme un spin électronique effectif $1/2$. Les propriétés spectroscopiques des ions de terres rares sont introduites au chapitre 2, en mettant l'accent sur les propriétés des ions erbium dans $CaWO_4$.

Le doublet de l'état fondamental des ions de Kramers peut être séparé en appliquant un champ magnétique. La transition de spin électronique effectif atteint une fréquence typique de 5 GHz avec un champ magnétique modéré de 100 mT, ce qui est compatible avec les circuits supraconducteurs. Nous utilisons des circuits supraconducteurs pour la détection de spins, ce qui permet une sensibilité record [Bie+16b ; Ran+20a]. Le chapitre 3 décrit le couplage des spins électroniques au résonateur supraconducteur utilisé pour détecter dans le régime quantique.

Le principe de l'expérience est expliqué dans la figure 1. La figure 1a montre la maille élémentaire du $CaWO_4$ avec un ion erbium remplaçant un atome de calcium. En raison de la symétrie tétragonale de la matrice de scheelite, le spin électronique de l'erbium a un tenseur $\mathbf{g}$ anisotrope, avec $g_c = g_\parallel = 1.247$ et $g_{a/b} = g_\perp = 8.38$. Pour détecter le spin électronique de l'erbium par résonance magnétique, un résonateur en niobium, comprenant un condensateur interdigité en parallèle avec un fil d'inductance étroit, d'une largeur typique de quelques micromètres, est fabriqué directement sur l'échantillon de $CaWO_4$ (voir figure 1b). Le spin électronique est couplé au résonateur par le champ magnétique $\boldsymbol{B_1}$ généré autour du fil d'inductance, qui oscille à la fréquence du résonateur ω_0. Ce couplage magnétique induit des oscillations de Rabi du spin à la fréquence $\Omega_R = \sqrt{\Delta^2 + (2g_0\alpha)^2}$, où Δ est le désaccord fréquentiel entre le spin et le résonateur, α le champ dans le résonateur

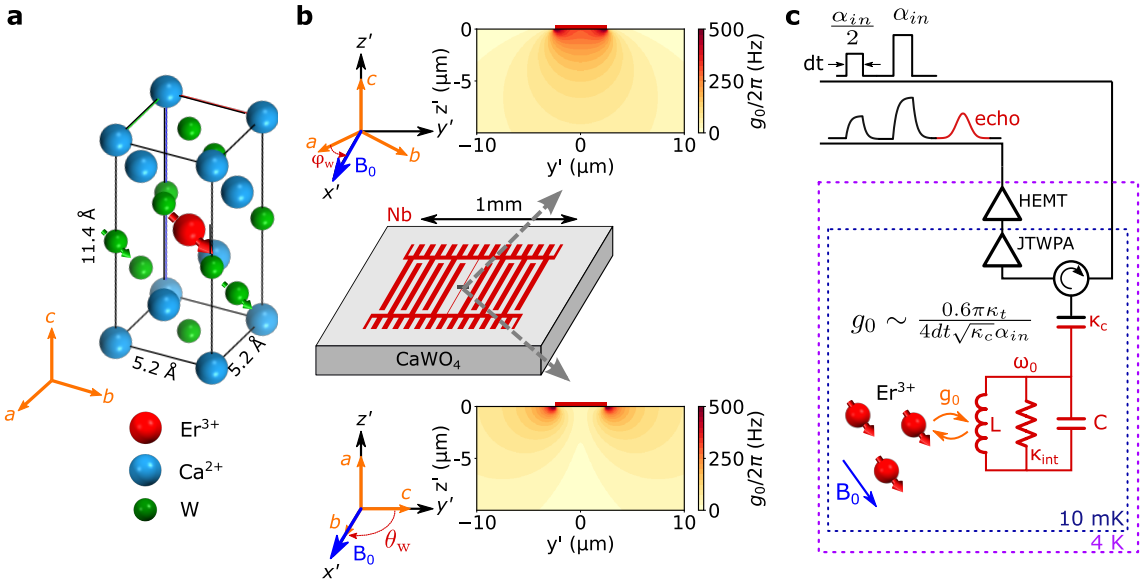

FIGURE 1 – **Dispositif de résonance paramagnétique électronique pour étudier les ions erbium à 10 mK. a.** Maille élémentaire du $CaWO_4$ avec un ion erbium central remplaçant un atome de calcium. Les atomes d'oxygène sont cachés pour une meilleure visibilité. Les ions erbium ont un spin électronique effectif 1/2, tandis qu'une fraction des atomes de tungstène (14%) a un spin nucléaire 1/2. **b.** Dessin typique d'un résonateur supraconducteur en niobium, fabriqué sur un échantillon de $CaWO_4$. Le spin électronique de l'erbium est couplé magnétiquement au résonateur via la constante de couplage g_0. Cette constante de couplage est représentée sur une coupe transversale sous le fil d'inductance du résonateur, avec le champ magnétique appliqué le long du fil. Elle est montrée ici pour deux orientations cristallines différentes, soit avec l'axe c pointant hors du plan (en haut), soit avec c dans le plan et perpendiculaire au fil (en bas). Ces deux configurations seront rencontrées dans la thèse. **c.** Schéma de l'expérience. Des micro-ondes sont envoyées au résonateur qui se trouve à l'étage à 10 mK d'un réfrigérateur à dilution. La séquence d'impulsions la plus courante est la séquence d'écho de Hahn, consistant en deux impulsions de durée dt et d'amplitudes $\alpha_{in}/2$ et α_{in}. Ces impulsions déclenchent un écho de spin qui sonde principalement les spins dont la constante de couplage est $g_0 \sim 0.6\pi\kappa_t/(4dt\sqrt{\kappa_c}\alpha_{in})$. Le signal d'écho est d'abord amplifié par un amplificateur paramétrique à ondes progressives Josephson (JTWPA) à 10 mK, puis par un transistor à haute mobilité électronique (HEMT) à 4 K, et enfin par un amplificateur additionnel à température ambiante (non représenté sur ce schéma).

et g_0 la constante de couplage spin-résonateur. Cependant, comme $\boldsymbol{B_1}$ varie typiquement en r^{-1}, où r est la distance du spin au fil d'inductance, la constante de couplage g_0 est très anisotrope, de même que la fréquence de Rabi Ω_R. La carte 2D de la constante de couplage est représentée dans la figure 1b pour deux orientations cristallines, soit avec c hors du plan, soit avec c dans le plan et perpendiculaire au fil d'inductance. Dans ce dernier cas, les spins sous le résonateur sont moins couplés en raison de leur faible valeur du tenseur $\mathbf{g}$ dans la direction de $\boldsymbol{B_1}$, alors que c'est l'inverse dans le premier cas.

Le dispositif expérimental est schématisé dans la figure 1c. L'échantillon avec son résonateur de niobium est placé dans un réfrigérateur à dilution qui peut descendre à 10 mK. Des champs micro-ondes continus ou pulsés peuvent être envoyés au résonateur. Le signal de sortie est amplifié à différents étages, incluant un amplificateur paramétrique à bas-bruit à 10 mK. La séquence d'impulsions principale utilisée dans ce travail est la séquence d'écho de Hahn, où deux impulsions micro-ondes d'amplitudes $\alpha_{in}/2$ et α_{in}

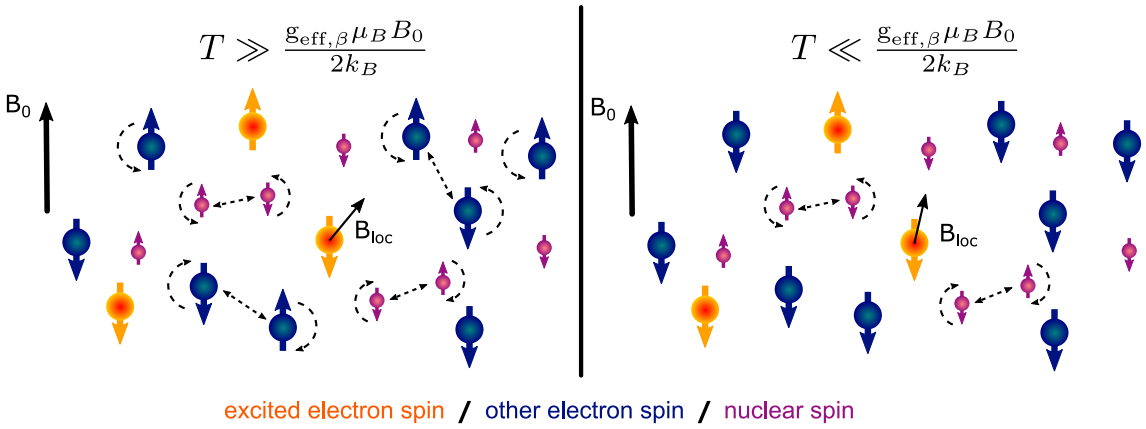

FIGURE 2 – **Diffusion spectrale.** Un spin électronique central (spins orange) est excité par les micro-ondes d'entrée. A cause des autres spins électroniques et nucléaires dans son environnement (spins bleus et violets respectivement), chaque spin sondé voit un champ magnétique local qui fluctue lorsque ces spins changent d'état. Cependant, la température peut être abaissée suffisamment pour que le bain de spins électroniques (de facteur g, $g_{eff,\beta}$) soit entièrement polarisé, tandis que les spins nucléaires restent non polarisés en raison de leur différence d'énergie bien plus faible.

sont envoyées au système. On peut montrer que le signal d'écho généré par les spins est dominé par la contribution de ceux qui tournent d'environ $0.6\pi/2$ et 0.6π [Ran+20c]. Cela correspond aux spins dont la constante de couplage est $g_0 \sim 0.6\pi\kappa_t/(4dt\sqrt{\kappa_c}\alpha_{in})$. Cette relation implique que les amplitudes d'impulsion fortes sondent des spins peu couplés, situés dans le cœur du cristal, alors que les amplitudes d'impulsion faibles sondent des spins fortement couplés, qui sont proches du résonateur. La plupart des mesures de cette thèse sont faites à forte puissance et sondent donc des spins au cœur du cristal.

Avec ce dispositif, nous nous intéressons au temps de cohérence des spins électroniques d'erbium dans la scheelite, mesuré en faisant varier le temps entre les impulsions τ d'une séquence d'écho de Hahn. La décohérence de spins électroniques dilués dans des cristaux vient principalement de leurs interactions dipolaires avec un bain de spins. Le chapitre 4 passe en revue les divers procédés conduisant à la décohérence du spin électronique. Trois d'entre eux sont pertinents dans cette thèse (voir figure 2) :

- Un spin mesuré interagit avec d'autres spins à la même fréquence (les autres spins orange de la figure 2). Ceux-ci sont également renversés par l'impulsion de refocalisation de la séquence d'écho de Hahn, ce qui entraîne la décohérence du spin mesuré. Ce procédé s'appelle la diffusion instantanée (ID).

- Les impuretés paramagnétiques à d'autres fréquences (spins bleus dans la figure 2) conduisent également à la décohérence du spin mesuré car leur état évolue dans le temps, soit par des échanges de spin avec leurs voisins ("flip-flop"), soit par retournement de leur spin dû à la relaxation. C'est la diffusion specrale (SD) par le bain d'impuretés paramagnétiques.

- Enfin, les spins nucléaires (violets dans la figure 2) conduisent à la décohérence du spin mesuré car leur état évolue dans le temps par flip-flop avec d'autres spins nucléaires du bain. C'est la diffusion spectrale par le bain de spins nucléaires.

La diffusion spectrale peut être réduite par deux moyens, le premier étant la réduction de la concentration d'impuretés paramagnétiques et de spins nucléaires. Cela motive le

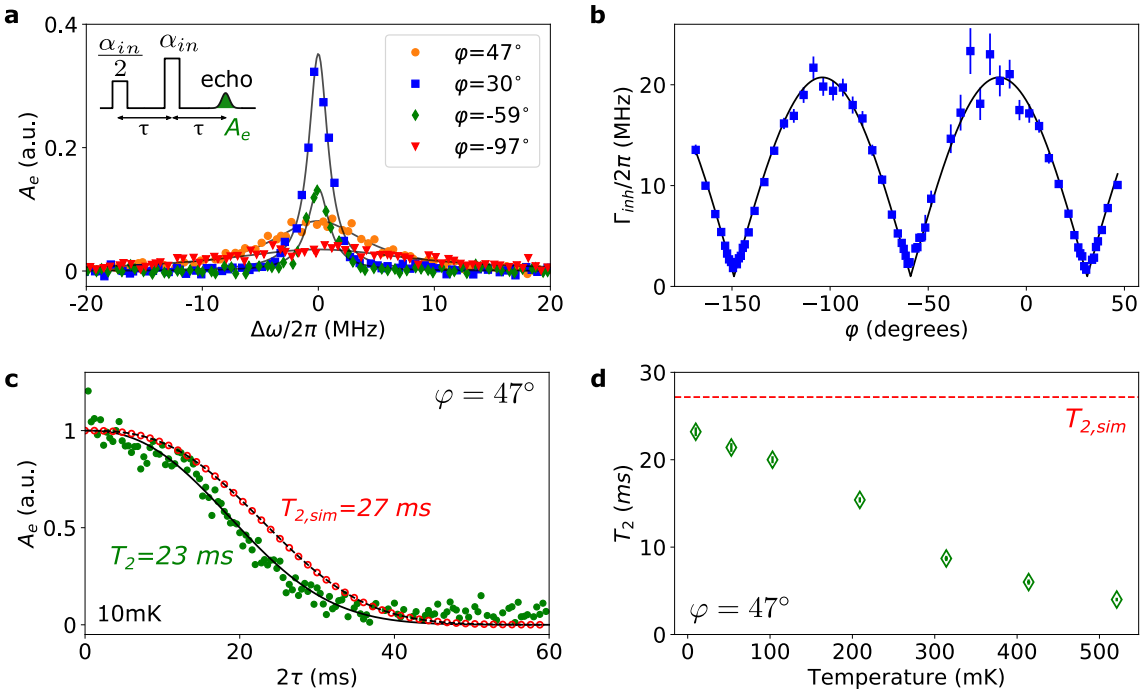

FIGURE 3 – **Spectroscopie et temps de cohérence des ions erbium dans le $CaWO_4$ pur.** L'échantillon étudié ici a l'axe c hors du plan et le champ magnétique peut être appliqué avec une direction arbitraire dans le plan (a, b) du cristal. **a.** Spectroscopie autour de la transition de spin électronique de l'erbium, où l'amplitude de l'écho de Hahn, A_e, est mesurée en fonction de l'amplitude du champ magnétique B_0. L'axe x est redimensionné en un désaccord fréquentiel $\Delta\omega$. Le champ magnétique est appliqué avec différents angles φ par rapport à l'axe cristallin a. Les données (symboles colorés) sont ajustées avec une distribution lorentzienne (ligne grise continue). **b.** Largeur à mi-hauteur de la raie d'erbium Γ_{inh} en fonction de l'angle du champ magnétique φ. Les données sont ajustées avec un modèle prenant en compte des gradients de champs électriques le long de l'axe c de typiquement 32 kV/cm. **c.** Mesure du temps de cohérence à 10 mK (température du cryostat) et $\varphi = 47°$. Les données (cercles verts) sont l'amplitude de l'écho de Hahn en fonction de l'intervalle de temps 2τ. L'ajustement de la décroissance de l'écho avec le modèle donne un temps de cohérence $T_2 = 23$ ms. Les données sont comparées avec une simulation de "cluster-correlation expansion" (CCE), prédisant un temps de cohérence de $T_{2,\text{sim}} = 27$ ms. **d.** Dépendence en température du temps de cohérence (diamants verts) à $\varphi = 47°$. La valeur simulée par CCE, $T_{2,\text{sim}}$, qui est constante dans notre intervalle de température, est indiquée avec une ligne pointillée rouge.

choix du $CaWO_4$ pur comme cristal. Ensuite, la diffusion spectrale paramagnétique peut être supprimée en grande partie par polarisation des impuretés paramagnétiques dans leur état fondamental à température suffisamment basse. Notez que la diffusion spectrale des spins nucléaires ne peut quant à elle pas être supprimée, car la température à atteindre devrait être bien plus basse que celle d'un cryostat à dilution.

Expérience 1 : dynamique de spins d'ions erbium dans des cristaux de $CaWO_4$ pur

La deuxième partie est consacrée à l'étude d'échantillons de scheelite pure, où sont présents des traces d'ions de terres rares, incluant l'erbium, avec des concentrations de l'ordre du ppb. Le chapitre 5 décrit les deux échantillons de scheelite nominalement non dopés

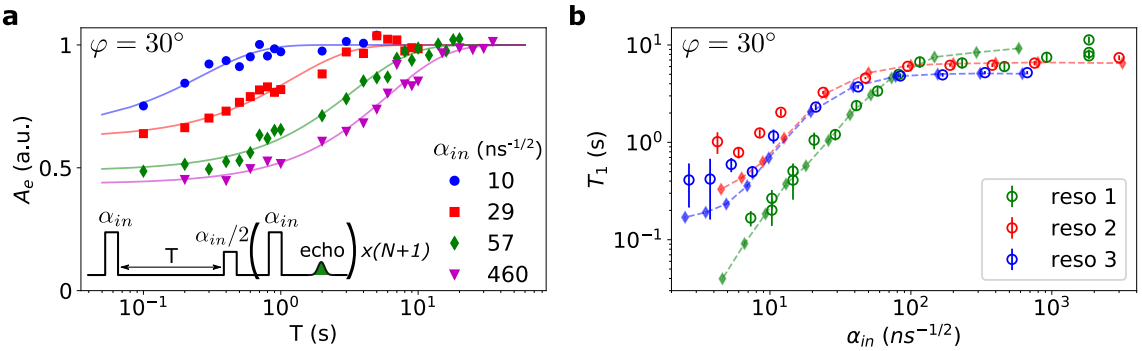

FIGURE 4 – **Temps de relaxation d'ions erbium dans le $CaWO_4$ pur et effet Purcell. a.** Amplitude de l'écho A_e généré par une séquence de récupération par inversion, comprenant une impulsion d'inversion d'amplitude α_{in}, suivi après un délai T par une séquence d'écho de Hahn de même amplitude. La dernière impulsion est répétée pour moyenner le signal obtenu et augmenter ainsi le rapport signal sur bruit. L'amplitude de l'écho est représentée en fonction du délai T pour plusieurs amplitudes d'impulsion α_{in} (symboles colorés) et les données sont ajustées avec des courbes exponentielles (lignes continues). Ces mesures sont faites à $\varphi = 30°$. **b.** Temps de rexalation en fonction de l'amplitude des impulsions α_{in}, mesurés pour les trois résonateurs fabriqués sur l'échantillon (cercles colorés). Les diamants colorés résultent de simulations où les seuls paramètres ajustables sont le temps de relaxation par les phonons et l'atténuation de la ligne d'entrée.

utilisés dans l'expérience, la conception du résonateur supraconducteur et le dispositif expérimental.

La figure 3 et la figure 4 montrent les résultats principaux de cette expérience. L'échantillon utilisé pour prendre ces données est orienté de telle sorte que le champ magnétique peut être tourné dans le plan (a, b). D'abord, nous mesurons la largeur inhomogène de l'erbium en fonction de φ, l'angle du champ magnétique par rapport à l'axe cristallin a (voir figure 3a). La largeur à mi-hauteur varie d'un facteur 20 dans le plan (a, b) (voir figure 3b). Cela s'explique par la dépendence angulaire de la sensibilité du rapport gyromagnétique à des champs électriques inhomogènes présents dans le cristal. Celle-ci s'annule à $\varphi = 31°$, où la largeur de raie atteint 1 MHz. Il s'agit, à notre connaissance, de la largeur inhomogène la plus étroite observée pour le spin électronique de l'erbium, ce qui est intéressant dans l'optique de réaliser des expériences de transduction de photons micro-ondes en photons optiques [WCL14]. Ces mesures spectroscopiques sont détaillées au chapitre 6.

Le temps de cohérence du spin électronique de l'erbium est étudié au chapitre 7. L'amplitude de l'écho est mesurée en fonction de l'intervalle 2τ et decroît avec une constante de temps $T_2 = 23$ ms à 10 mK. De plus, des calculs de la décroissance de l'écho due à la diffusion spectrale par les spins nucléaires prévoient une constante de temps de 27 ms (voir figure 3c). La similarité des deux décroissances mesurée et simulée indique que le temps de cohérence à basse température est principalement limité par la diffusion spectrale due aux spins nucléaires. De plus, le temps de cohérence decroît rapidement lorsque la température augmente (voir figure 3d). Cela s'explique par la diffusion spectrale paramagnétique, qui domine aux températures plus élevées. En mesurant un second échantillon avec l'axe c dans le plan, nous atteignons un temps de cohérence de 30 ms à 10 mK, en appliquant le champ magnétique selon l'axe cristallin c.

Le chapitre 8 se concentre sur les mesures de relaxation de spin, utilisant une séquence de récupération par inversion. Les résultats principaux sont montrés dans la figure 4a, pour différentes amplitudes d'entrée α_{in}. T_1 varie fortement en fonction de α_{in} pour tous les résonateurs supraconducteurs fabriqués sur l'échantillon (voir figure 4b). A faible puissance d'entrée, T_1 devient plus court avec une dépendence quadratique en α_{in}. C'est une signature

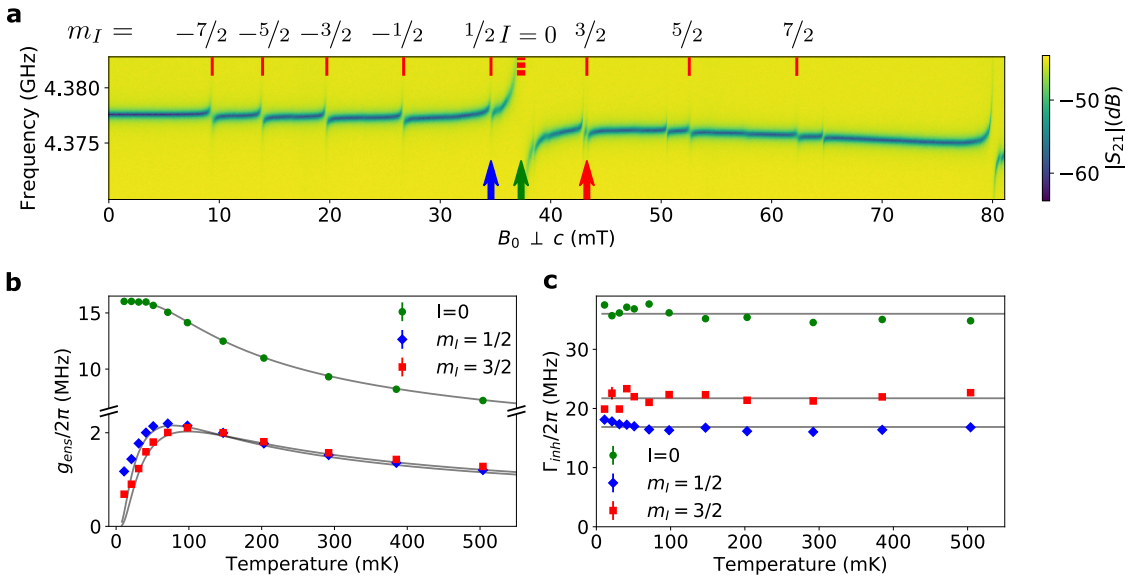

FIGURE 5 – **Spectroscopie des ions erbium avec une concentration de 20 ppm dans $CaWO_4$. a.** Spectroscopie à ondes continues à 100 mK. Le coefficient de transmission du résonateur S_{21} est mesuré en fonction de l'amplitude du champ magnétique B_0, qui est appliqué le long de l'axe cristallin a. La plupart des croisements évités sont attribués aux transitions de spin électronique de l'erbium, identifiées par leur état de spin nucléaire. D'autres signaux visibles proviennent de l'ytterbium. **b & c.** Valeurs ajustées du couplage d'ensemble g_{ens} et de la largeur inhomogène Γ_{inh} en fonction de la température du cryostat pour les trois transitions de l'erbium indiquées par une flèche colorée dans la figure a.

de l'effet Purcell, pour lequel, à résonance, $T_1 = \kappa_t/(4g_0^2)$ et, dans notre système, g_0 est à peu près inversement proportionnel à α_{in}. A forte puissance d'entrée, la relaxation est dominée par les phonons. En diminuant la puissance, nous observons donc un passage entre une relaxation dominée par les phonons ou par l'effet Purcell. La relaxation Purcell de spins électroniques dans les solides a été observée pour la première fois avec des donneurs de bismuth dans le silicium [Bie+16a] et nous rapportons ici la première observation pour les ions de terres rares dans des cristaux.

Expérience 2 : dynamique de spins d'ions erbium dans un cristal de $CaWO_4$ fortement dopé

La troisième partie présente des mesures faites avec un échantillon bien plus dopé (20 ppm d'erbium, 10 ppm d'ytterbium). Le chapitre 9 présente l'échantillon, le résonateur et le montage. Le dispositif expérimental est très similaire à celui de l'expérience précédente.

Des mesures de spectroscopie à ondes continues sont présentées dans le chapitre 10. La figure 5a montre la mesure du coefficient de transmission du résonateur S_{21} lorsque le champ magnétique est balayé le long de l'axe a. En raison de la concentration élevée, le système résonateur-ensemble de spins est dans le régime de forte coopérativité, ce qui se manifeste par l'appartition de croisements de niveaux évités. Le croisement évité le plus fort vient des isotopes d'erbium avec un spin nucléaire nul (qui ont une abondance naturelle de 77%), tandis que huit croisements plus faibles correspondent aux transitions hyperfines de l'isotope ^{167}Er. Par ailleurs, d'autres croisements évités sont visibles et sont dus à une concentration similaire d'ions ytterbium dans le cristal. En ajustant les spectres avec un modèle présenté dans le chapitre 10, nous extrayons le couplage d'ensemble et la largeur inhomogène de plusieurs transitions de l'erbium. La figure 5b et c montre leur dépendence

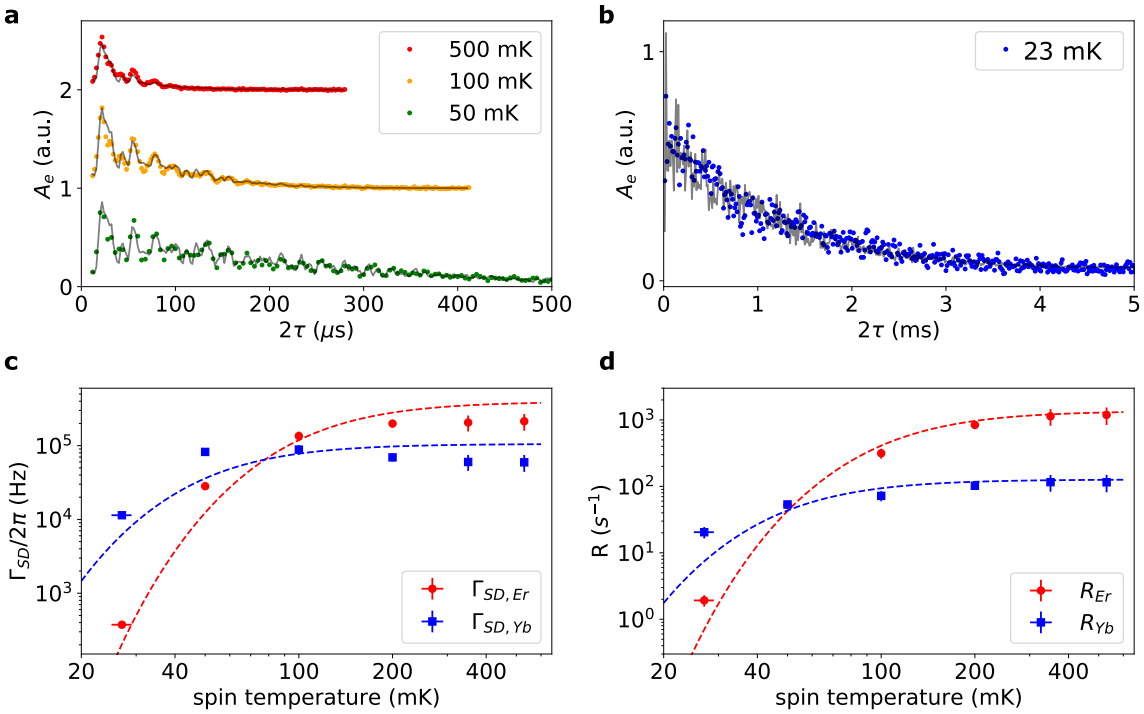

FIGURE 6 – **Temps de cohérence et étude de la diffusion spectrale sur la transition hyperfine de l'erbium $m_I = 3/2$. a. & b.** Mesure du temps de cohérence du spin électronique. L'amplitude de l'écho de Hahn A_e est représentée en fonction du délai 2τ pour plusieurs températures de spin. Les données sont ajustées avec la décroissance de l'écho en $\exp\{-(2\tau/T_2)^x\}$, modulée par le couplage dipolaire de l'erbium avec le spin nucléaire des tungstènes voisins (ESEEM). L'ajustement à 23 mK donne $T_2 = 1.3$ ms, à 50 mK, $T_2 = 300$ μs, à 100 mK, $T_2 = 110$ μs et à 500 mK, $T_2 = 40$ μs. **c. & d.** Largeur de diffusion spectrale Γ_{SD} et taux de flip-flop R des isotopes à spin nucléaire nul de l'erbium et de l'ytterbium en fonction de la température des spins. Ces données (symboles colorés) sont obtenues en ajustant des mesures de décroissance d'écho stimulé avec le modèle de "sudden-jump". Elles sont ici ajustées avec des fonctions proportionnelles à $\mathrm{sech}^2[\mathrm{g}_{\mathrm{eff},\beta}\mu_B B_0/(2k_B T)]$, où $\mathrm{g}_{\mathrm{eff},\beta}$ est le facteur g effectif de l'erbium et de l'ytterbium respectivement (lignes pointillées colorées).

en température. Les données du couplage d'ensemble sont modélisées quantitativement par la dépendence en température de la population sur la transition concernée. Cela indique en particulier une bonne thermalisation du spin des ions erbium au réseau cristallin, au moins jusqu'à environ 25 mK.

Le chapitre 11 présente des mesures pulsées. En particulier, le temps de cohérence de l'erbium est étudié sur la transition hyperfine $m_I = 3/2$. Cette transition est très peu peuplée à basse température, de sorte que la diffusion instantanée ne limite pas le temps de cohérence. Cela nous permet de réaliser une étude détaillée de la diffusion spectrale se produisant dans ce cristal. Les résultats principaux sont résumés dans la figure 6. Des courbes de décroissance d'écho de Hahn sont mesurées à des températures variées (voir figure 6a et b). Les oscillations sont dues à l'interaction de l'erbium avec le bain de spins nucléaires (ESEEM) et sont quantitativement modélisées. La décroissance dépend fortement de la température, de 1.3 ms à 23 mK jusqu'à 40 μs à 600 mK. Pour mieux comprendre l'effet de la diffusion spectrale paramagnétique, nous mesurons également la décroissance d'échos stimulés. Celle-ci est ajustée avec le modèle de "sudden-jump", décrit dans le chapitre 4. De cette façon, nous obtenons à chaque température deux paramètres : le taux de flip-flop R et la largeur de diffusion spectrale Γ_{SD} des deux bains dominants de spins électroniques,

qui sont les ions erbium et ytterbium à spin nucléaire nul. La figure 6c et d montre leur dépendence en température, qui suit les lois attendues en $\mathrm{sech}^2[g_{\mathrm{eff},\beta}\mu_B B_0/(2k_B T)]$, où $g_{\mathrm{eff},\beta}$ est le facteur g effectif de l'erbium et de l'ytterbium respectivement.

Chapter 1

Introduction

Today's computers rely on transistors which process classical information, encoded in two states 0 and 1. Their computational power is directly related to the number of transistors on a single processor chip. Since 50 years, computers got more and more powerful, following Moore's law, which predicted in 1965 a doubling of the number of transistors on a chip every year [Moo06]. This was made possible by the shrinking of transistors size, reaching nanometer scales nowadays. However, at this scale, quantum effects, such as electron tunneling through a potential barrier, need to be taken into account and new architectures have to be envisioned to pursue Moore's law.

Alternatively, the realization of a new kind of computer, based on quantum mechanics, has raised a worldwide interest for its capacity to solve certain types of problems much more efficiently than a classical computer. In quantum computers, the information is encoded on the basis states $|0\rangle$ and $|1\rangle$ of a quantum-mechanical two-level system. An arbitrary qubit state is written $|\psi\rangle = \alpha\,|0\rangle + \beta\,|1\rangle$, where α and β are complex numbers such that $|\alpha|^2 + |\beta|^2 = 1$. When applied to a large qubit register, the superposition principle can lead to massively parallel computation. The most famous quantum algorithm was invented by Shor in 1994. His algorithm factorizes a large integer number into prime numbers in a time polynomial in the number size [Sho94], whereas the best known classical algorithm scales exponentially. The difficulty to factorize a number into its prime numbers is at the heart of current encryption systems, which are used constantly to secure our information. Quantum computers would thus be able to break this encryption system and new cryptographic schemes would have to be implemented. Following Shor's algorithms, many others were proposed, promising quantum speedup in a number of fields, such as quantum chemistry calculations, or optimization problems. This motivates a worldwide research effort to actually build such a machine.

Quantum computers have not been demonstrated yet, because quantum information is very fragile. Indeed the interactions of the qubits with their environment are very detrimental to quantum coherence. Protection against decoherence will require complex quantum error correction schemes, which puts stringent demands on the quality of the physical qubits.

In the quest for quantum processors, several qubit platforms have emerged. In the solid-state, two prominent systems are superconducting qubits, where quantum information is encoded in the quantum state of an electrical circuit, and spin qubits, where quantum information is encoded in the spin state of a solid-state defect. Each of them has advantages and drawbacks.

Superconducting circuits are easy to control and fabricate in large numbers, while they easily interact with each other. Google and IBM have already demonstrated quantum processors up to about 100 qubits [Aru+19]. Despite recent progress, the finite qubit

coherence time (1 ms for the longest reported value [Som+21]) remains the limiting factor of superconducting quantum processors.

On the other hand solid-state defects have electron and nuclear spin transitions with record coherence times: nitrogen-vacancy (NV) centers in diamonds, donors in silicon and rare-earth ions in solids have all demonstrated coherence times approaching or exceeding one second [Bar+13; Tyr+12; Ran+18]. But contrary to superconducting circuits, spin qubits are difficult to control and entangle. The most advanced spin-qubit platform, consisting in individual phosphorus donors in silicon, has demonstrated single-spin control almost a decade ago, while qubit entanglement remains a major challenge [Pla+12; Tos+17] (note that we will not discuss in this thesis spin qubits based on electrons trapped in lithographically-defined quantum dots).

Because of all these limitations, hybrid quantum systems, which combine different types of qubits in order to take all their advantages, have been thought as a promising architecture for quantum information processing [Xia+13]. As an example, superconducting qubits can be coupled to spin ensembles, where superconducting circuits are the processing unit while the spin ensemble is the memory. For this to work, the spin ensemble must have a coherent transition at gigahertz frequencies, corresponding to the typical frequency of superconducting circuits, while it should be able to strongly couple to superconducting resonators to efficiently exchange microwave photons. Superconducting qubits and spin ensembles can be coupled via a quantum bus, provided by a superconducting resonator, which links the superconducting qubit to the spin ensemble.

Many different solid-state defects have been investigated. A proof-of-concept, coupling a superconducting qubit to a spin ensemble via a quantum bus, was achieved for NV centers in diamonds [Kub+11], while bismuth donors in silicon have demonstrated storage of quantum microwave fields up to 100 ms [Ran+20b]. Other candidates for such applications are erbium ions embedded in crystals. Indeed, erbium ions have an effective electron spin half which can be magnetically coupled to superconducting resonators. Moreover, erbium ions have the extra advantage of possessing an optical transition at 1.5 μm which is optimal for low-loss transmission in optical fibers [Sag+15]. There is thus a strong interest for erbium doped crystals in the perspective of a future quantum internet, where quantum information will need to travel between distant superconducting quantum processors. For these two reasons, erbium ions have been proposed for several hybrid architectures, such as microwave quantum memories [Afz+13; Pro+15] and microwave-to-optical transduction schemes [WCL14; Fer+15], where the erbium spin ensemble is coupled to a superconducting resonator. One specific advantage of erbium ions is their strong magnetic moment which enables efficient coupling to other quantum systems. Detection of single erbium ions coupled to nanophotonic cavities has been very recently achieved in optics [Che+20].

These proposals for erbium-based hybrid quantum systems rely on a long coherence time of the erbium electron spin transition and this has so far been missing. Indeed, previous measurements of erbium doped crystals demonstrated electron spin coherence times less than 50 μs [Pro+15; Ber+07], except for clock transitions where a coherence time of 1.5 ms was reported [Rak+20].

In this thesis, we investigate the electron spin dynamics of erbium ions in scheelite crystals ($CaWO_4$) to understand the mechanisms leading to the electron spin decoherence. The experiments are performed at sub-Kelvin temperatures, using superconducting micro-resonators patterned on the sample surface for spin detection. Three samples with vastly different erbium concentrations are studied (two with about 1 ppb -part per billion- and one with 20 ppm -part per million-). One of the main results of this thesis is that the erbium electron spin coherence time improves considerably by cooling the samples down

to millikelvin temperatures, reaching up to 1 ms in the highly-concentrated sample and up to 30 ms in the lowest-concentrated samples. This is due to the quenching of spectral diffusion caused by paramagnetic impurities because of their progressive polarization at low temperatures. This last value represents an improvement by nearly three orders of magnitude for erbium ions in $CaWO_4$ [Ber+07] and by one order of magnitude for any electron spin transition in natural abundant crystals, on a magnetically-sensitive transition [Li+20]. Moreover, in the lowest-concentrated sample, a narrow inhomogeneous linewidth of 1 MHz is reported, which is particularly interesting for microwave to optical transduction schemes [Fer+15]. Finally, we also demonstrate that erbium ions can reach the so-called Purcell regime, where spin relaxation is dominated by the spontaneous emission of microwave photons instead of phonons.

This thesis is divided in three parts. The first part gives the necessary background to understand the experiments. The second part presents results obtained with the two low-doped samples, and the third one the high-doped sample. The content of the chapters is described in more details below.

1.1 Background

Erbium belongs to a class of atoms known as rare-earths, which have very similar properties. In particular, half of them, including erbium, are Kramers ions, with a ground state doublet that behaves as an effective electron spin $1/2$. The spectroscopic properties of rare-earth ions are introduced in Chapter 2, with an emphasis on the properties of erbium ions in $CaWO_4$.

The ground state doublet of Kramers ions can be split with a bias magnetic field such that the effective electron spin transition reaches a typical frequency of 5 GHz with a moderate magnetic field of 100 mT, which is compatible with superconducting circuits. We use superconducting resonators to detect the spins, allowing for a record sensitivity [Bie+16b; Ran+20a]. Chapter 3 describes the coupling of electron spins to the superconducting resonator used for detection in the quantum regime.

The principle of the experiment is shown in Figure 1.1. The unit cell of $CaWO_4$ with one erbium ion replacing a calcium atom is shown in subplot a. Due to the tetragonal symmetry of the scheelite matrix, the erbium electron spin has an anisotropic **g**-tensor, with $g_c = g_\parallel = 1.247$ and $g_{a/b} = g_\perp = 8.38$. To detect the erbium electron spin with magnetic resonance, a niobium resonator consisting in an interdigitated finger capacitor shunted by a narrow inductance wire, of typically a few micrometers width, is patterned directly on the $CaWO_4$ sample (subplot b). The electron spin is coupled to the resonator via the magnetic field $\boldsymbol{B_1}$ generated around the inductive wire, which oscillates at the resonator frequency ω_0. This magnetic coupling induces Rabi oscillations of the spin at a frequency $\Omega_R = \sqrt{\Delta^2 + (2g_0\alpha)^2}$, where Δ is the frequency detuning between the spin and the resonator, α the intra-resonator field and g_0 the spin-resonator coupling constant. However, due to the decay of $\boldsymbol{B_1}$ in typically r^{-1}, where r is the distance of the spin from the inductive wire, the coupling constant g_0 is very anisotropic and so is the Rabi frequency. The 2D map of the coupling constant is shown in subplot b for two crystal orientations, either with c out-of-plane or with c in plane and perpendicular to the inductive wire. In the latter case, spins below the resonator are weakly coupled due to the lower value of the **g**-tensor in the direction of $\boldsymbol{B_1}$, whereas it is the opposite in the former case.

The experimental setup is sketched in subplot c. The sample with its niobium resonator is placed in a dilution refrigerator which can reach down to 10 mK. Either continuous-wave fields or pulses can be sent to the resonator. The output signal is amplified at several stages, including a low-noise parametric amplifier at 10 mK. The main pulse sequence used

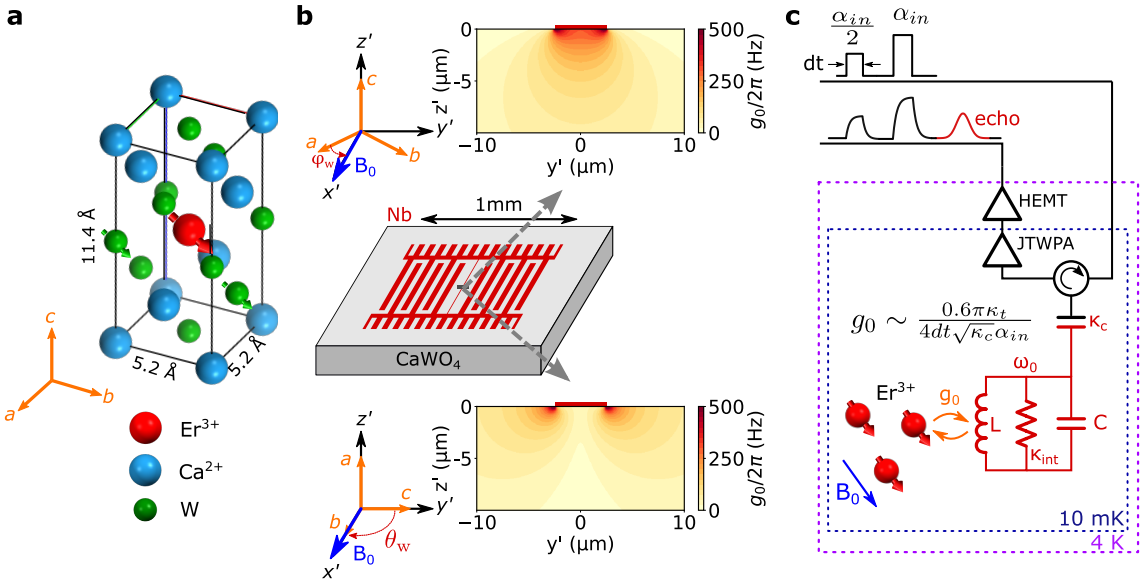

Figure 1.1 – **Electron spin resonance setup for probing erbium ions at 10 mK. a.** $CaWO_4$ unit cell with a central erbium ion replacing a calcium atom. Oxygen atoms are removed for clarity. Erbium ions have an effective electron spin half while a fraction of tungsten atoms (14%) has a nuclear spin half. **b.** Typical design of a superconducting niobium resonator, patterned on a $CaWO_4$ sample. The erbium electron spin is coupled magnetically to the resonator via the coupling constant g_0. This coupling constant is shown over a cross-section below the resonator inductance wire, with the magnetic field applied along the wire axis. It is displayed for two different crystal orientations, either with c pointing out of plane (top) or with c in plane and perpendicular to the wire axis (bottom). These two configurations will be encountered in the thesis. **c.** Schematics of the experiment. Microwaves are sent to the resonator which is located on the 10 mK plate of a dilution refrigerator. The most common pulse sequence is the Hahn-echo sequence consisting in two pulses of length dt with amplitudes $\alpha_{in}/2$ and α_{in}. These pulses trigger a spin echo which probes mostly spins whose coupling constant is $g_0 \sim 0.6\pi\kappa_t/(4dt\sqrt{\kappa_c}\alpha_{in})$. The echo signal is first amplified by a Josephson traveling wave parametric amplifier (JTWPA) at 10 mK, and then by a high-electron mobility transitor (HEMT) at 4 K, followed by further amplification at room temperature (not shown on this sketch).

in this work is the Hahn-echo sequence, where two microwave pulses of amplitude $\alpha_{in}/2$ and α_{in} are sent to the device. It can be shown that the echo signal generated by the spins is dominated by the contribution of those which undergo a $0.6\pi/2$ and a 0.6π nutations [Ran+20c]. This corresponds to spins whose coupling constant is $g_0 \sim 0.6\pi\kappa_t/(4dt\sqrt{\kappa_c}\alpha_{in})$. This relation implies that strong pulse amplitudes α_{in} probe weakly coupled spins, located in the bulk of the crystal, while low pulse amplitudes α_{in} probe strongly coupled spins, which are located closer to the resonator. Most of the measurements in the thesis are performed at high power, and therefore probe spins in the bulk.

With this setup, we are interested in studying the coherence time of erbium electron spins in scheelite, measured by varying the inter-pulse delay τ of a Hahn-echo sequence. Decoherence of dilute paramagnetic spins in crystals comes mainly from dipolar interactions with a spin bath. Chapter 4 reviews the various processes leading to electron spin decoherence. Three main processes are relevant in this thesis (see Figure 1.2):

- A measured spin interacts with other spins at the same frequency (other orange spins in the figure). They are also flipped by the refocusing pulse of the Hahn echo

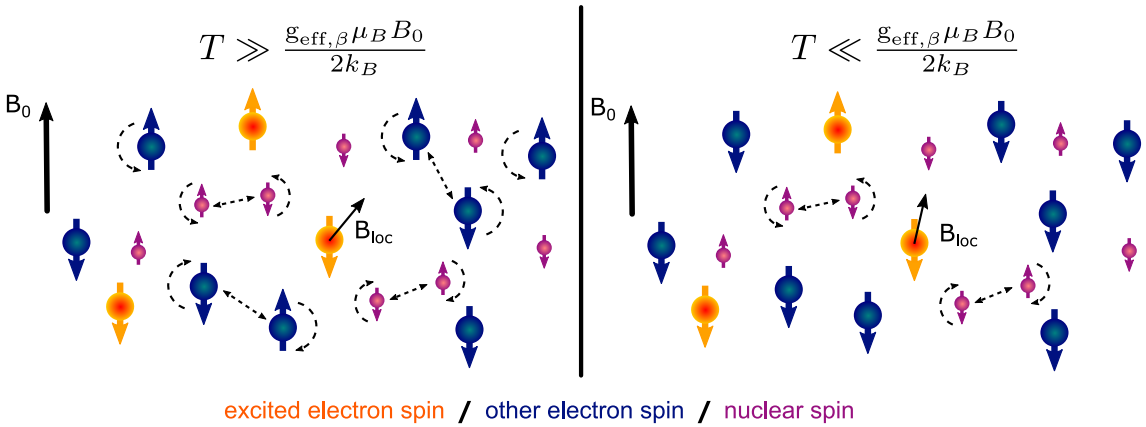

Figure 1.2 – **Spectral diffusion.** A central electron spin (orange spins) is excited by the input microwaves. Because of other electron and nuclear spins (blue and purple spins respectively), each probed spin sees a local magnetic field which fluctuates due to spin flips in its environment. However, the temperature can be decreased low enough so that the electron spin bath (of g-factor $g_{eff,\beta}$) is fully polarized, while nuclear spins remain unpolarized due their much lower energy splitting.

sequence, which leads to decoherence. This process is called instantaneous diffusion (ID).

- Paramagnetic impurities at other frequencies (blue spins in the figure) also lead to decoherence because their state evolves in time due to flip-flops or spin flip relaxation events. This is spectral diffusion (SD) by the paramagnetic impurity bath.

- Finally, nuclear spins (purple spins in the figure) lead to decoherence because their state evolves in time due to flip-flops with other nuclear spins of the bath. This is SD by the nuclear spin bath.

Spectral diffusion can be reduced by two means, the first one being the reduction of the concentration of paramagnetic impurities and nuclear spins. This motivates the choice of pure $CaWO_4$ as the host matrix. Second, paramagnetic spectral diffusion can be suppressed to a large extent by polarizing the paramagnetic impurities into their ground state at sufficiently low temperatures. Note that nuclear spin spectral diffusion cannot be quenched, as the temperature to reach would be much lower than the one reached in a dilution cryostat.

1.2 Experiment 1: spin dynamics of erbium ions in pure $CaWO_4$ crystals

The second part is devoted to the study of pure scheelite samples, where traces of rare-earth ions, including erbium, of the order of ppb concentrations are present. Chapter 5 describes the two nominally undoped scheelite samples used in the experiment, the superconducting resonator design and the experimental setup.

Figure 1.3 and Figure 1.4 show the main results of this experiment. The sample used to take these data is oriented such that the magnetic field can be rotated in the (a, b)-plane. First we measure the erbium inhomogeneous linewidth as a function of φ, the angle of the magnetic field with respect to the crystal a-axis (see subplot a). The FWHM linewidth is found to vary by a factor 20 in the (a, b)-plane (subplot b). This is due to the angular dependence of the gyromagnetic ratio sensitivity to inhomogeneous electric fields present

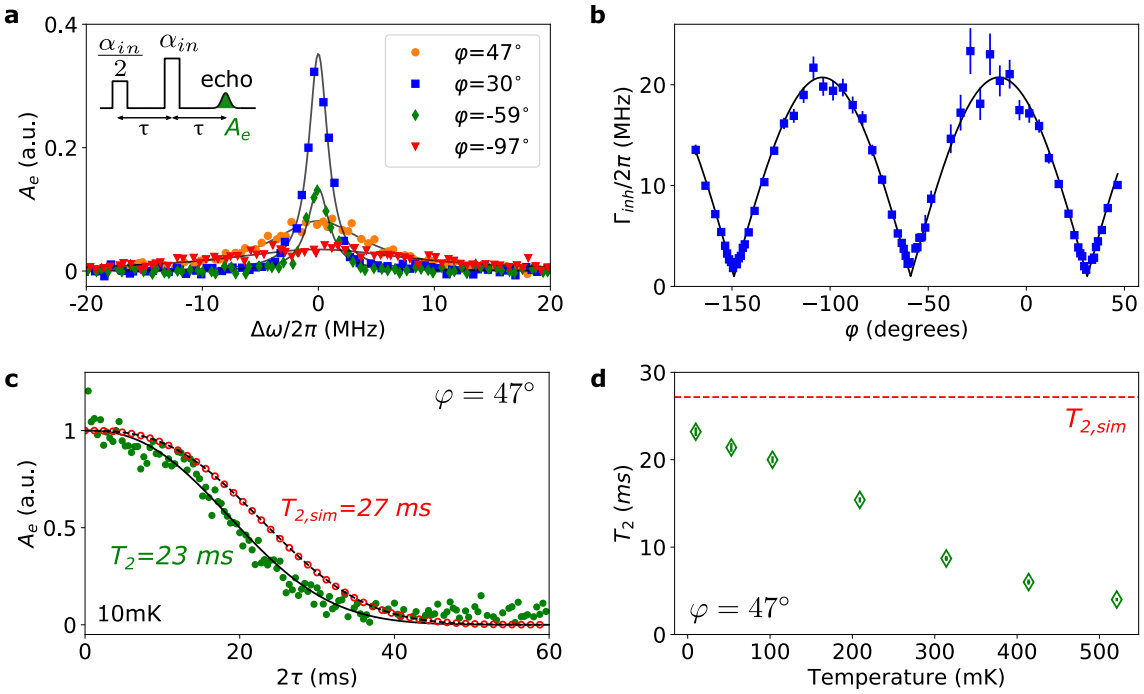

Figure 1.3 – **Spectroscopy and coherence time of erbium ions in pure $CaWO_4$.** The sample studied here has the c-axis out of plane and the magnetic field can be applied with an arbitrary direction in the crystal (a, b)-plane. **a.** Spectroscopy over the erbium electron spin transition where the amplitude of a Hahn-echo A_e is measured as a function of the magnetic field amplitude B_0. The x-axis is rescaled into a frequency detuning $\Delta\omega$. The magnetic field is applied with different angles φ from the crystal a-axis. The data (colored symbols) are fitted with a Lorentzian distribution (solid grey line). **b.** Fitted erbium full-width-at-half-maximum (FWHM) linewidth Γ_{inh} as a function of the magnetic field angle φ. The data are fitted with a model taking into account typical electric field gradients along the c-axis of 32 kV/cm. **c.** Coherence time measurement at 10 mK cryostat temperature and $\varphi = 47°$. The data (green circles) are the Hahn-echo amplitude as a function of the time interval 2τ. The fit of the echo decay yields a coherence time of $T_2 = 23$ ms. The data are compared with a cluster-correlation expansion (CCE) simulation, predicting a coherence time of $T_{2,\text{sim}} = 27$ ms. **d.** Temperature dependence of the fitted coherence time (green diamonds) at $\varphi = 47°$. The CCE simulated $T_{2,\text{sim}}$, which is constant within our temperature range, is indicated with a dashed red line.

in the crystal. It vanishes at an angle $\varphi = 31°$, where the linewidth reaches 1 MHz. This is to our knowledge the narrowest erbium electron spin inhomogeneous linewidth, which is interesting in the context of microwave-to-optical transduction schemes [WCL14]. These spectroscopic measurements are detailed in Chapter 6.

The coherence time of the erbium electron spins is studied in Chapter 7. The echo amplitude is measured as a function of the delay 2τ, and is found to decay with a time constant $T_2 = 23$ ms at 10 mK. Additionally, calculations of the echo decay due to nuclear spin spectral diffusion predict a time constant of 27 ms (see Figure 1.3c). The similarity of both decays indicates that the coherence time at low temperature is mostly limited by nuclear spin spectral diffusion. Moreover, the coherence time is seen to decrease rapidly with increasing temperature (subplot d). This is due to paramagnetic spectral diffusion, which takes place at higher temperatures. By measuring a second pure sample with the c-axis in plane, we also reach a longer coherence time of 30 ms at 10 mK, by applying the magnetic field along the crystal c-axis.

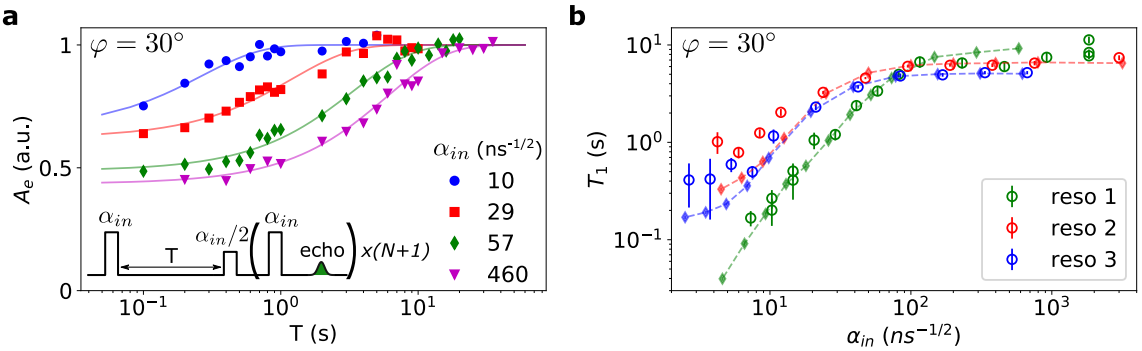

Figure 1.4 – **Relaxation time of erbium ions in pure $CaWO_4$ and Purcell effect. a.** Echo amplitude A_e generated by an inversion recovery sequence consisting of an inversion pulse of amplitude α_{in}, followed after a delay T by a Hahn-echo sequence of same amplitude. The last pulse is repeated for enhanced signal averaging. The echo amplitude is plotted as a function of the delay T for several pulse amplitudes α_{in} (colored symbols) and the data are fitted with exponential curves (solid lines). These measurements are performed at $\varphi = 30°$. **b.** Fitted relaxation time as a function of the pulse amplitude α_{in}, measured for the three resonators patterned on the sample (empty circles). Colored diamonds result from simulations where the only free parameters are the spin-lattice relaxation time and the input line attenuation.

Chapter 8 focuses on spin relaxation measurements, using an inversion recovery sequence. The results are shown in Figure 1.4a, for different input amplitudes α_{in}. T_1 is seen to strongly depend on α_{in} for all superconducting resonators patterned on the sample (see Figure 1.4b). At low input power, T_1 becomes shorter with a quadratic dependence on α_{in}. This is a signature of the Purcell effect, where at resonance $T_1 = \kappa_t/(4g_0^2)$ and, in our setup, g_0 is roughly inversely proportional to α_{in}. At high input power, relaxation is dominated by spin-lattice relaxation. By reducing the power, we thus observe a cross-over between spin-lattice and Purcell relaxations. Purcell-enhanced relaxation of electron spins in solids has been observed for the first time for bismuth donors in silicon [Bie+16a] and we are here reporting the first observation for rare-earth ions embedded in crystals.

1.3 Experiment 2: spin dynamics of erbium ions in a highly doped $CaWO_4$ crystal

The third part presents measurements performed with a much more doped scheelite crystal (20 ppm erbium, 10 ppm ytterbium). Chapter 9 presents the sample, device and setup. The setup is very similar to the previous experiment.

Continuous-wave spectroscopy measurements are presented in Chapter 10. Figure 1.5a shows the measurement of the resonator transmission coefficient S_{21} as the magnetic field is swept along the a-axis. Due to the high concentration, the resonator-erbium ensemble is in the high cooperativity regime, manifested by the appearance of avoided level crossings. The strongest avoided crossing originates from the zero-nuclear spin erbium isotopes (with 0.77 natural abundance), while eight smaller signals correspond to the hyperfine transitions of ^{167}Er. Moreover, other visible avoided crossings are due to a similar concentration of ytterbium ions in the crystal. By fitting the spectra with a model presented in Chapter 10, we extract the ensemble coupling and the inhomogeneous linewidth of several erbium transitions. Their temperature dependence is shown in Figure 1.5b and c. The ensemble coupling data are quantitatively understood by the temperature dependence of the population on the relevant transition. This indicates in particular a good thermalization

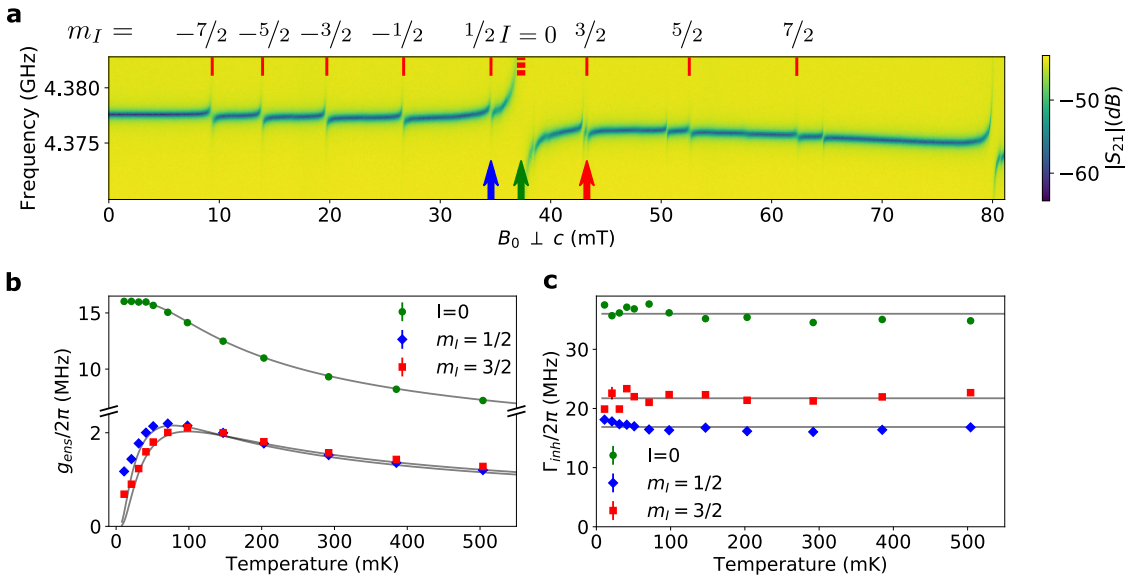

Figure 1.5 – **Spectroscopy of erbium ions with a 20 ppm concentration in $CaWO_4$.** **a.** Continuous-wave spectroscopy at 100 mK. The resonator transmission coefficient S_{21} is measured as a function of the magnetic field amplitude B_0, which is applied along the crystal a-axis. Most of the avoided crossings are attributed to erbium electron spin transitions, labelled by their nuclear spin state. Other visible signals come from ytterbium. **b & c.** Fitted values of the ensemble coupling g_{ens} and inhomogeneous linewidth Γ_{inh} as a function of cryostat temperature for the three erbium transitions marked with a colored arrow in subplot a.

of the erbium ion spin to the lattice, at least down to approximately 25 mK.

Chapter 11 presents pulsed spin measurements. In particular, the erbium coherence time is studied on the hyperfine $m_I = 3/2$ transition. This transition is very little populated at low temperature so that instantaneous diffusion does not limit the coherence time. Therefore, it enables us to conduct a detailed study of the spectral diffusion occurring in this crystal. The main results are summarized in Figure 1.6. Hahn echo decay curves are measured at various temperatures (see Figure 1.6a and b). The oscillations are due to interactions with the nuclear spin bath (ESEEM), and are quantitatively modelled. The decay is seen to strongly depend on temperature, from 1.3 ms at 23 mK to 40 μs at 600 mK. To gain further insight into paramagnetic spectral diffusion, we also measure the decay of stimulated echoes. It is fitted with the sudden jump model, described in Chapter 4. In this way, we obtain at each temperature two parameters: the flip-flop rate R and the spectral diffusion linewidth Γ_{SD} of the two dominant electron spin baths which are the zero-nuclear-spin erbium and ytterbium ions. Their temperature dependence is shown in Figure 1.6c and d and follows the expected laws in $\text{sech}^2[g_{\text{eff},\beta}\mu_B B_0/(2k_B T)]$, where $g_{\text{eff},\beta}$ is the effective g-factor of erbium or ytterbium respectively.

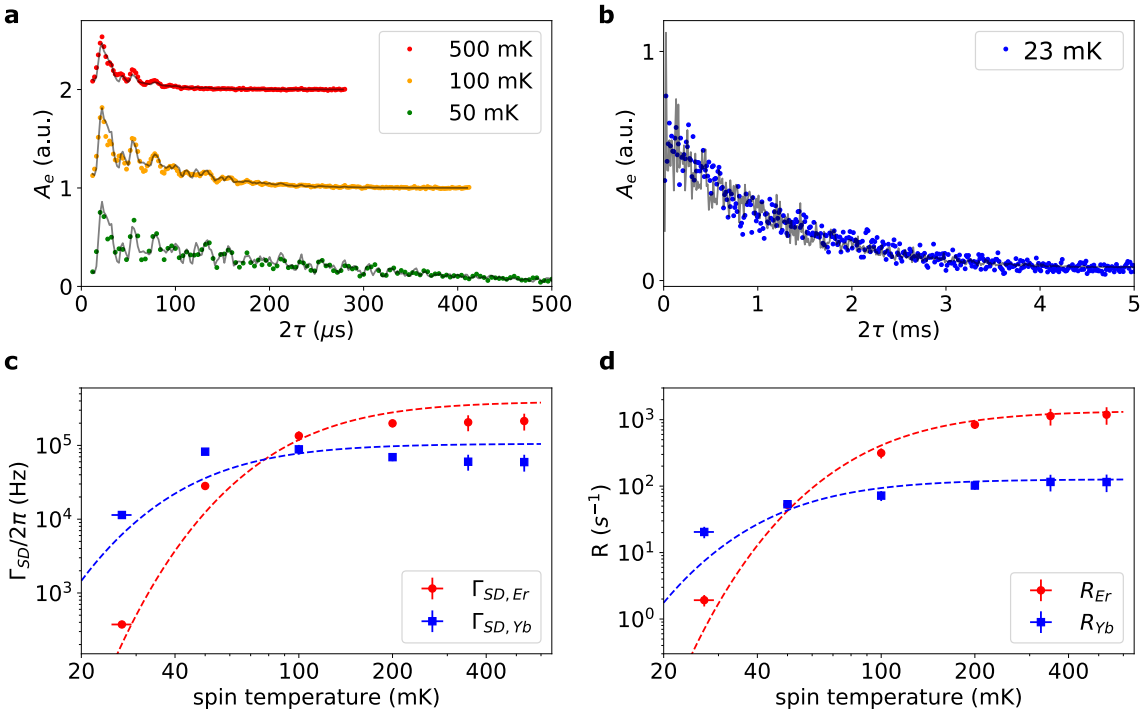

Figure 1.6 – **Coherence time and spectral diffusion study on the erbium $m_I = 3/2$ hyperfine transition. a. & b.** Electron spin coherence time measurement. The Hahn-echo amplitude A_e is plotted as a function of the delay 2τ for several spin temperatures. The data are fitted with the echo decay $\exp\{-(2\tau/T_2)^x\}$, modulated by the dipolar coupling of erbium to neighboring tungsten nuclear spins (ESEEM). The fit at 23 mK yields $T_2 = 1.3$ ms, at 50 mK, $T_2 = 300$ μs, at 100 mK, $T_2 = 110$ μs and at 500 mK, $T_2 = 40$ μs. **c. & d.** Spectral diffusion linewidth Γ_{SD} and flip-flop rate R of the zero-nuclear-spin isotopes of erbium and ytterbium as a function of spin temperature. These data (colored symbols) are obtained by fitting stimulated echo decay measurements with the sudden-jump model. They are fitted with functions proportional to $\mathrm{sech}^2[g_{\mathrm{eff},\beta}\mu_B B_0/(2k_B T)]$, where $g_{\mathrm{eff},\beta}$ is the effective g-factor of erbium and ytterbium respectively (colored dashed lines).

Part I

Background

Chapter 2

Erbium dopants in scheelite

Erbium belongs to a class of 15 atoms known as lanthanides. In solids, these atoms become usually tri-positive ions whose common property is their partially filled $4f$ electronic shell. Their electronic structure is based on xenon -$1s^2 2s^2 2p^6 3s^2 3p^6 4s^2 3d^{10} 4p^6 5s^2 4d^{10} 5p^6$- plus N additional electrons on the $4f$ shell, where N varies from 0 for lanthanum to 14 for lutetium. Erbium ions have an odd number of $4f$ electrons with $N = 11$. Associated to scandium ([Ar]$4s^2 3d^1$) and yttrium ([Kr]$5s^2 4d^1$), the lanthanides form the rare-earth elements (see Table 2.1).

Rare-earth ions (REIs) have very similar properties. Because of their narrow optical linewidth, they are widely used for many optical applications including fluorescent lamps, solid-state lasers or optical amplifiers in fiber optics [LJ06]. In this chapter we will introduce the general properties of rare-earth ions based on several textbooks ([Wei12] for general atomic spectroscopy and [AB12; Wyb65; LJ06] for rare-earth ion spectroscopy).

Atomic number	Rare-earth element	Electronic configuration of the trivalent rare earth ion (RE^{3+})	Ground state (Russell-Saunders notation)
21	Sc Scandium	$3d^0$	$^1S_0$
39	Y Yttrium	$4d^0$	$^1S_0$
57	La Lanthanum	$4f^0$	$^1S_0$
58	Ce Cerium	$4f^1$	$^2F_{5/2}$
59	Pr Praseodymium	$4f^2$	$^3H_4$
60	Nd Neodymium	$4f^3$	$^4I_{9/2}$
61	Pm Promethium	$4f^4$	$^5I_4$
62	Sm Samarium	$4f^5$	$^6H_{5/2}$
63	Eu Europium	$4f^6$	$^7F_0$
64	Gd Gadolinium	$4f^7$	$^8S_{7/2}$
65	Tb Terbium	$4f^8$	$^7F_6$
66	Dy Dysprosium	$4f^9$	$^6H_{15/2}$
67	Ho Holmium	$4f^{10}$	$^5I_8$
68	Er Erbium	$4f^{11}$	$^4I_{15/2}$
69	Tm Thulium	$4f^{12}$	$^3H_6$
70	Yb Ytterbium	$4f^{13}$	$^2F_{7/2}$
71	Lu Lutetium	$4f^{14}$	$^1S_0$

Table 2.1 – **Trivalent rare-earth ion properties.** List of rare-earth elements with their electronic configuration in the trivalent ion state and the corresponding ground state label in the Russell-Saunders notation (see Section 2.1.1.3).

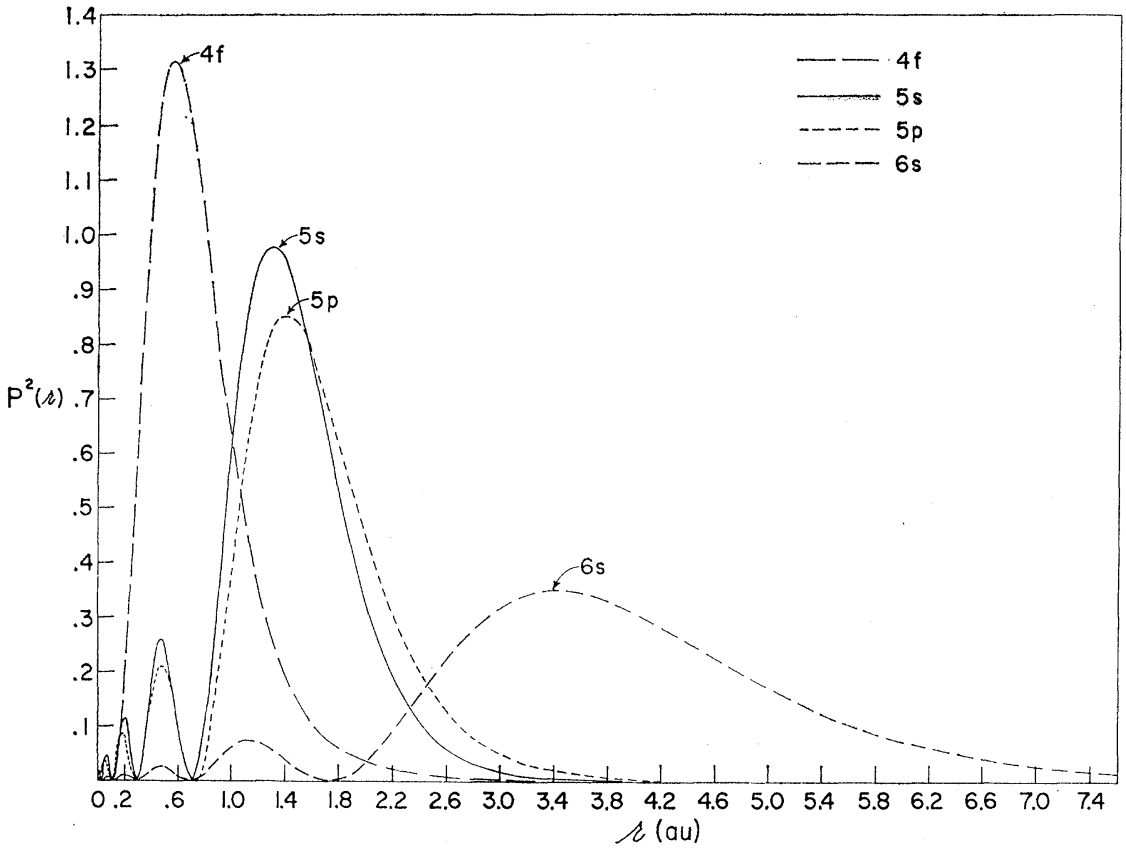

Figure 2.1 – **Electronic shell distribution for Gd^{+}.** Radial probability distribution for the $4f$, $5s$, $5p$ and $6s$ shells of Gd^{+}, copied from [FW62]. In trivalent rare-earth ions, the $6s$ shell is empty but the $5s$ and $5p$ shells are fully populated.

Interaction type	Energy (GHz)
Configuration splitting $4f^N$ to $4f^{N-1}5d^1$	10^6
Splitting within the $4f^N$ configuration:	
- Non central electrostatic field	10^5
- Spin-orbit coupling	10^4
- Crystal-field interaction	10^3
- Hyperfine splitting	$10^{-2} - 1$
- Superhyperfine interaction (ion-ligand)	$10^{-3} - 10^{-1}$

Table 2.2 – **Typical energy scales involved in rare-earth level structure.** Table adapted from [LJ06]. The configuration splitting down to the spin-orbit coupling are properties of the free ion, while from the hyperfine splitting it concerns the spin Hamiltonian.

2.1 Introduction to rare-earth ions

The similarity amongst rare-earth elements comes from the fact that $4f$ electrons are shielded by electrons in the $5s$ and $5p$ closed shells from interacting with ligand electrons and lattice vibrations. Figure 2.1 shows a plot of the theoretical probability distribution of the outer electronic shells of Gd^{+}, calculated using Hartree Fock calculation [FW62]. The $4f$ shell is seen to be closer to the nucleus than the $5s$ and $5p$ shells.

For this reason, the electronic level structure of rare-earth ions can be first approximated by the free-ion energy levels using atomic spectroscopy. The interaction with the host crystal ("crystal-field") can be treated as a perturbation of the free ion.

The total Hamiltonian of any rare-earth ion can be divided into three terms, ordered with decreasing energy scales (see Table 2.2):

$$\mathcal{H} = \mathcal{H}_{FI} + \mathcal{H}_{CF} + \mathcal{H}_{spin} \tag{2.1}$$

where $\mathcal{H}_{FI}$ is the free-ion Hamiltonian, $\mathcal{H}_{CF}$ the crystal-field Hamiltonian and $\mathcal{H}_{spin}$ the spin Hamiltonian. We will now focus on each term separately.

2.1.1 Free-ion level structure

The Hamiltonian describing an N-electron ion without any external field can be decomposed as follows:

$$\mathcal{H}_{FI} = \mathcal{H}_0 + \mathcal{H}_C + \mathcal{H}_{SO}, \tag{2.2}$$

where

$$\mathcal{H}_0 = -\sum_{i=1}^{N} \frac{\hbar^2}{2m}\nabla_i^2 - \sum_{i=1}^{N} \frac{Ze^2}{r_i} \tag{2.3}$$

is the sum of the kinetic energy and the potential energy of the electrons in the field of the nucleus,

$$\mathcal{H}_C = \sum_{i<j}^{N} \frac{e^2}{r_{ij}} \tag{2.4}$$

is the Coulomb repulsion between pairs of electrons and

$$\mathcal{H}_{SO} = \sum_{i=1}^{N} \xi(r_i)\boldsymbol{l_i}.\boldsymbol{s_i} \tag{2.5}$$

is the spin-orbit interaction.

The spin-orbit term is relatively small and can be treated as a perturbation. However, the Coulomb interaction cannot be neglected in front of the first term $\mathcal{H}_0$. Because this Coulomb repulsion term couples pairs of electrons, the motion of each electron depends on the other $N-1$ electrons and there exist no solution of the corresponding Schrödinger equation for $N > 1$. In order to solve the Schrödinger equation, the central field approximation must be used.

2.1.1.1 Central-field approximation

The central-field aproximation consists in rewritting the Hamiltonian of Equation 2.2 with a solvable dominant part and additional terms which can be treated as perturbations:

$$\mathcal{H}_{FI} = \mathcal{H}_0' + \mathcal{H}_C' + \mathcal{H}_{SO}. \tag{2.6}$$

Here,

$$\mathcal{H}_0' = -\sum_{i=1}^{N} \left[\frac{\hbar^2}{2m}\nabla_i^2 + U(r_i)\right], \tag{2.7}$$

where $U(r_i)$ is a potential energy function with spherical symmetry. It approximates the potential energy of electron i in the field of the nucleus and the $N-1$ other electrons such that

$$\sum_{i=1}^{N} U(r_i) = -\sum_{i=1}^{N} \frac{Ze^2}{r_i} + \langle \sum_{i<j}^{N} \frac{e^2}{r_{ij}} \rangle, \tag{2.8}$$

where the second term is the spherically averaged Coulomb term and includes most of the inter-electron repulsion.

Then the remaining part of the Coulomb interaction is put in $\mathcal{H}'_C$,

$$\mathcal{H}'_C = \sum_{i<j}^{N} \frac{e^2}{r_{ij}} - \langle \sum_{i<j}^{N} \frac{e^2}{r_{ij}} \rangle, \tag{2.9}$$

which is now small enough to be treated as a perturbation in addition to the spin-orbit term.

Let's focus on the dominant term $\mathcal{H}'_0$. This Hamiltonian describes the independent motion of N electrons and the Schrödinger equation can be solved for each electron i with

$$\left[-\frac{\hbar^2}{2m} \nabla_i^2 + U(r_i) \right] \psi_i = E_i \psi_i. \tag{2.10}$$

Equation 2.10 is very similar to the equation for an hydrogen atom with a single electron. Only the spherical potential differs and is more complex here than for hydrogen. Similarly to hydrogen, each electron's state is determined by four quantum numbers (n, l, m_l, m_s): its principal quantum number n, its angular momentum quantum number l ($0 \leq l < n-1$), its magnetic quantum number m_l ($-l \leq m_l \leq l$) and its spin quantum number $m_s = \pm 1/2$. However, contrary to hydrogen, the energy of each electron will not only depend on n but also on l [Wei12]. Each (n, l) energy level is called a configuration. Here we focus of the $4f$ configuration, with $n = 4$ and $l = 3$.

In order to satisfy Pauli's exclusion principle, the N-electron eigenfunctions of $\mathcal{H}'_0$ are obtained as antisymmetric linear combinations of the single electron wavefunctions. The actual computation of the N-electron wavefunction is performed with the Hartree-Fock method (see [Wei12; FW62] for more details).

The goal of this central field approximation is to provide basis sets in order to calculate the matrix elements of the pertubative terms, namely $\mathcal{H}'_C$ and $\mathcal{H}_{SO}$. From the next section, we will focus only on the $4f$-configuration. Adding each perturbation will lift the degeneracy within this configuration.

2.1.1.2 Non-central part of the Coulomb interactions

To treat the remaining non-central Coulomb interaction term, the most common approach consists in computing the matrix elements of $\mathcal{H}'_C$ in a basis where it is diagonal. This can be achieved by noticing that $\mathcal{H}'_C$ commutes with the atomic orbital momentum: $\boldsymbol{L} = \sum_{i=1}^{N} \boldsymbol{l_i}$ and the atomic spin momentum: $\boldsymbol{S} = \sum_{i=1}^{N} \boldsymbol{s_i}$. As these two operators also commute with $\mathcal{H}'_0$, L and S are good quantum numbers to describe the eigenstates of $\mathcal{H}'_0 + \mathcal{H}'_C$. Therefore, to compute the matrix elements of the pertubative $\mathcal{H}'_C$, a natural basis is the set of eigenvectors of $\boldsymbol{L}^2$ and $\boldsymbol{S}^2$. This basis choice is called the LS or Russell-Saunders coupling scheme. The calculation of $\mathcal{H}'_C$ in this basis induces a splitting of the $4f$ configuration into terms associated to specific values of L and S.

2.1.1.3 Spin-orbit coupling

The last term of the free-ion Hamiltonian is the spin-orbit coupling. Let's assume that the spin-orbit term is much smaller than the non-central Coulomb term treated above. $\mathcal{H}_{SO}$ does not commute with neither $\boldsymbol{L}$ nor $\boldsymbol{S}$ but it commutes with $\boldsymbol{J} = \boldsymbol{L} + \boldsymbol{S}$. Therefore, the spin-orbit splits the LS terms into levels associated to a specific value of J, where each level is a $(2J+1)$ degenerate multiplet labelled with the Russell-Saunders notation ${}^{2S+1}L_J$.

The LS coupling scheme applies however better for light atoms than heavy. When the atomic number Z increases, the spin-orbit coupling increases much faster than the Coulomb interaction. In rare-earth ions, they are typically of same magnitude. As a consequence, L and S are not good quantum numbers anymore and the LS coupling scheme must be

replaced by the so-called intermediate coupling scheme which includes mixing of energy terms with different L and S by the spin-orbit interaction [LJ06]. The final energy levels are $(2J+1)$ degenerate multiplets characterized by quantum number J only. Nevertheless, rare-earth energy levels are usually still labelled with the Russell-Saunders notation ${}^{2S+1}L_J$. This remains accurate for low energy states which are relatively pure in L and S, as ground multiplets are usually greater than 90% pure LS states. This is not accurate anymore to describe high energy states as discussed by Wybourne [Wyb65]. For erbium, the ground state of the free ion corresponds to ${}^4I_{15/2}$, I corresponding to $L = 6$. The first excited level is ${}^4I_{13/2}$ and the transition between these two levels is an optical transition at 1.5 μm which is perfectly suited for low loss transmission into optical fibers and is responsible for the attractivity of erbium doped crystals.

2.1.2 Crystal-field interactions

When embedded in a crystal, the rare-earth ion's environment produces electric fields which break the spherical symmetry of the electronic structure developed above. However, as the $4f$ electrons have very localized states, the crystal-field interaction can be simply treated as a perturbation of the free-ion energy levels. Figure 2.2 shows the energy level diagram of each trivalent lanthanide in LaF_3, where the main structure originates from the free ion levels while the crystal field splitting is only responsible for each level thickness.

The crystal-field Hamiltonian may by written using Wybourne's formalism [Wyb65; LJ06]:

$$\mathcal{H}_{CF} = \sum_{k,q,i} B_q^{(k)} C_q^{(k)}(i) = \sum_{k=2,4,6} \sum_{q=-k}^{k} B_q^{(k)} O_q^{(k)}, \tag{2.11}$$

where $B_q^{(k)}$ are crystal field parameters, $C_q^{(k)}(i)$ are operators proportional to the spherical harmonics of the i^{th} electron and $O_q^{(k)}$ are Stevens operator equivalents [Ste52]. This equation can be further simplified using symmetry rules depending on the crystal. The effect of the Stevens operators $O_q^{(k)}$ is to mix states with different numbers J and J_z. The J-mixing is however much smaller than the mixing within the J-multiplet due to the large splitting between J-levels.

The $(2J+1)$ degeneracy of each J-multiplet may be partially or completely removed by the crystal-field Hamiltonian, depending on the site symmetry. Importantly, Kramers' theorem [Kra30] states that if the number of electrons of the $4f$ shell is odd, then all crystal field levels are at least doubly degenerate. This is the case for erbium with $N = 11$.

As shown on Table 2.2, typical crystal-field interactions are of the order of 1 THz. This corresponds to a temperature of roughly 50 K. Consequently, in our temperature range (10 mK to 1 K), only the ground state crystal field level is populated. Applying these concepts to erbium (see Figure 2.3), as already said, the ground state is ${}^4I_{15/2}$. There are $2J+1 = 16$ levels within this J-multiplet. Due to Kramers degeneracy, they are split into 8 doublets by the crystal-field interaction (labelled Z_1 ... Z_8). The energy scale between the Z_1 and Z_2 doublets is 0.57 THz for erbium in $CaWO_4$ [Enr71]. Therefore, at sub-Kelvin temperatures, only the ground state doublet Z_1 is populated. This is the effective spin-$1/2$ that we will be focusing on in this thesis.

2.1.3 Kramers doublets and effective spin Hamiltonian

In this section, we focus on Kramers doublets. Under a magnetic field $\boldsymbol{B_0}$, each doublet, denoted $(|+\rangle, |-\rangle)$, is split by the Zeeman interaction according to

$$\mathcal{H}_{spin} = \mu_B \boldsymbol{B_0} \cdot (\boldsymbol{L} + g_s \boldsymbol{S}) = g_J \mu_B \boldsymbol{B_0} \cdot \boldsymbol{J}, \tag{2.12}$$

where $g_s = 2$ and g_J is the Landé g-factor. For the ${}^4I_{15/2}$ erbium levels, $g_J = 6/5$.

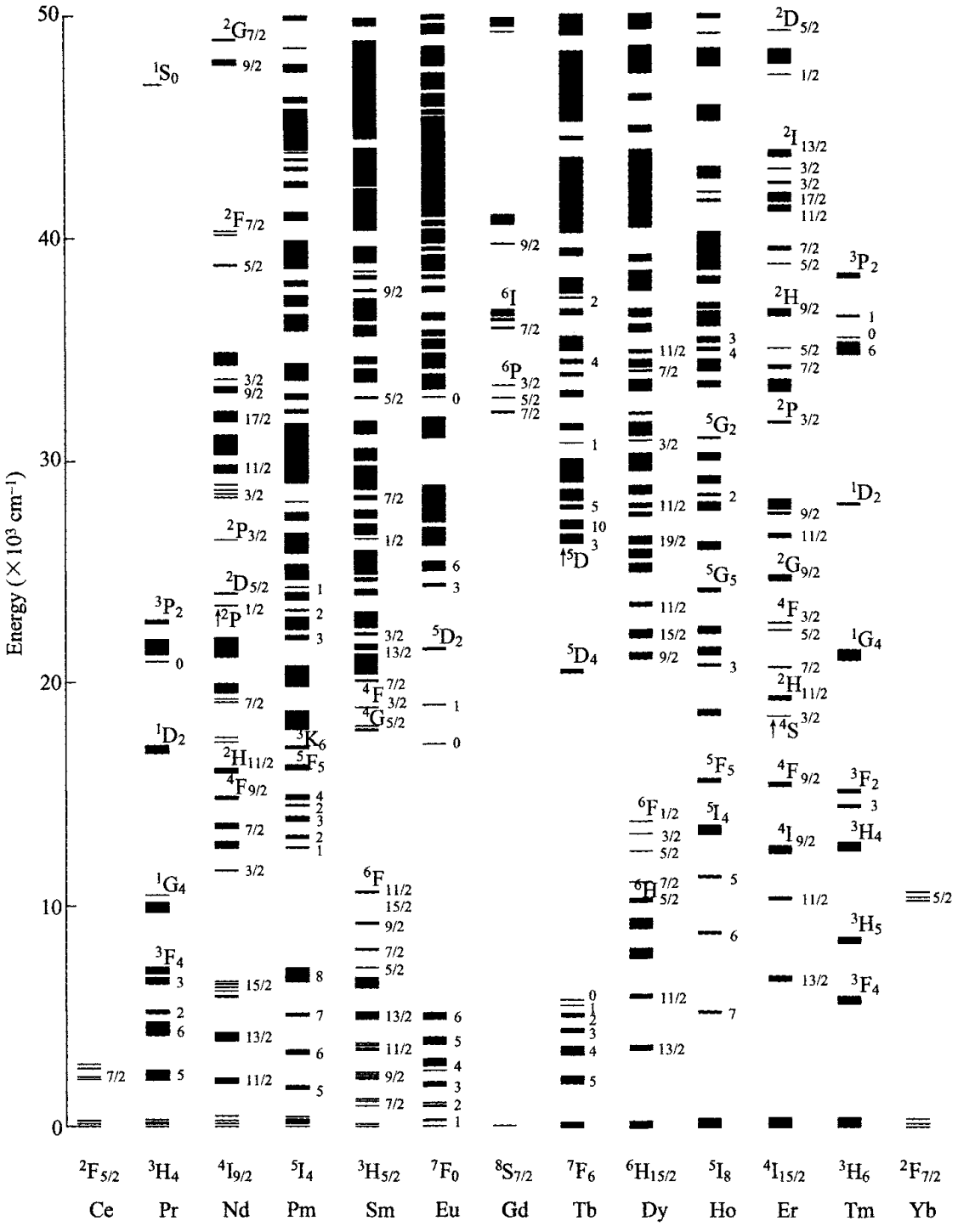

Figure 2.2 – **Theoretical energy level structure of trivalent lanthanide ions in LaF_3.** This diagram, taken from [Car+89], labels each state with $^{2S+1}$L and/or J, depending on the dominant character of the levels, whether rather pure *LS* state or not. The tickness of each level depends on the crystal field splitting of the free-ion multiplets.

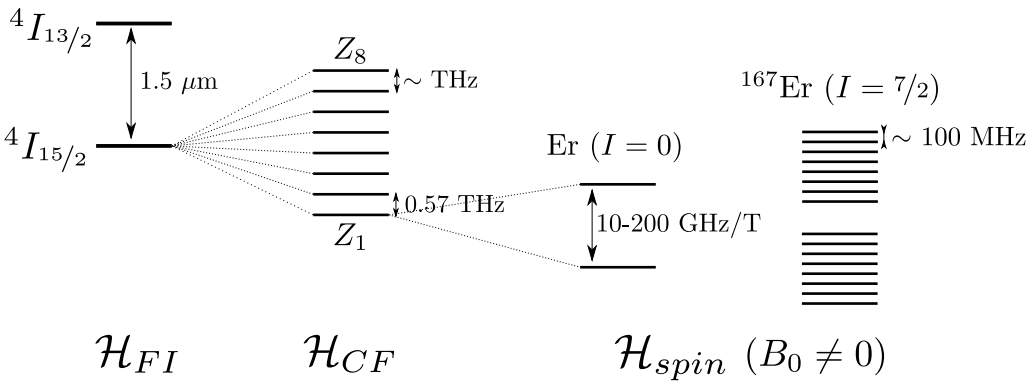

Figure 2.3 – **Lowest energy levels of Er^{3+} embedded in a crystal and with non-zero magnetic field.** The crystal field interaction splits the free ion ground state multiplet $^4I_{15/2}$ into doubly degenerate Kramers doublets (labelled Z_1, Z_2... Z_8). Under a non-zero magnetic field $\boldsymbol{B_0}$, this doublet behaves as an effective spin $S = 1/2$, which also has a hyperfine structure if the erbium isotope has a non-zero nuclear spin I. Note that the energy difference of 0.57 THz between the Z_1 and Z_2 levels is specific to $CaWO_4$ as a host. All other values are general to any host.

This Zeeman interaction can be interpreted as the interaction between the magnetic field $\boldsymbol{B_0}$ and an effective spin $S = 1/2$ with an anisotropic g-factor. This interpretation remains valid while the magnetic field strength is small enough such that the doublet splitting, of order 10-200 GHz/T, is smaller than the crystal-field splitting (typically THz). Because of the crystal field, the **g**-tensor depends on the host crystal and reflects the symmetry of the rare-earth ion site. For example, in case of a host crystal with tetragonal symmetry, the **g**-tensor has one parallel component around the rotation axis z and one perpendicular component which are given by [AB12]

$$\begin{aligned} \mathrm{g}_{\parallel} &= 2\mathrm{g}_J \langle + | J_z | + \rangle \\ \mathrm{g}_{\perp} &= \mathrm{g}_J \langle + | J_+ | - \rangle . \end{aligned} \tag{2.13}$$

This is the case for REIs located at the calcium site of $CaWO_4$, as will be discussed below.

The effective spin Hamiltonian of any Kramers ion with zero nuclear spin contains only the Zeeman interaction, which in general is given by

$$\mathcal{H}_{spin} = \mathcal{H}_{Ze} = \mu_B \boldsymbol{B_0} \cdot \mathbf{g} \cdot \hat{\boldsymbol{S}} = \mu_B \begin{pmatrix} B_x & B_y & B_z \end{pmatrix} \begin{pmatrix} \mathrm{g}_{xx} & \mathrm{g}_{xy} & \mathrm{g}_{xz} \\ \mathrm{g}_{yx} & \mathrm{g}_{yy} & \mathrm{g}_{yz} \\ \mathrm{g}_{zx} & \mathrm{g}_{zy} & \mathrm{g}_{zz} \end{pmatrix} \begin{pmatrix} \hat{S}_x \\ \hat{S}_y \\ \hat{S}_z \end{pmatrix} \tag{2.14}$$

where $\boldsymbol{B_0}$ is the magnetic field vector, **g** the effective **g**-tensor and $\hat{\boldsymbol{S}}$ the effective spin operator,

$$\hat{S}_x = \frac{1}{2}\begin{pmatrix} 0 & 1 \\ 1 & 0 \end{pmatrix}, \quad \hat{S}_y = \frac{1}{2}\begin{pmatrix} 0 & -i \\ i & 0 \end{pmatrix}, \quad \hat{S}_z = \frac{1}{2}\begin{pmatrix} 1 & 0 \\ 0 & -1 \end{pmatrix}. \tag{2.15}$$

However, REIs may have isotopes with a nuclear spin as it is the case for ^{167}Er with $I = 7/2$. In that case, the effective spin Hamiltonian contains more terms,

$$\mathcal{H}_{spin} = \mathcal{H}_{Ze} + \mathcal{H}_{HF} + \mathcal{H}_{Q} + \mathcal{H}_{Zn}, \tag{2.16}$$

where $\mathcal{H}_{Ze}$ is the electronic Zeeman interaction as described above. The second term is the hyperfine interaction, $\mathcal{H}_{HF} = \hat{\boldsymbol{S}} \cdot \boldsymbol{A} \cdot \hat{\boldsymbol{I}}$, which describes the magnetic coupling between the nuclear magnetic moment and the local field degenerated by the surrounding

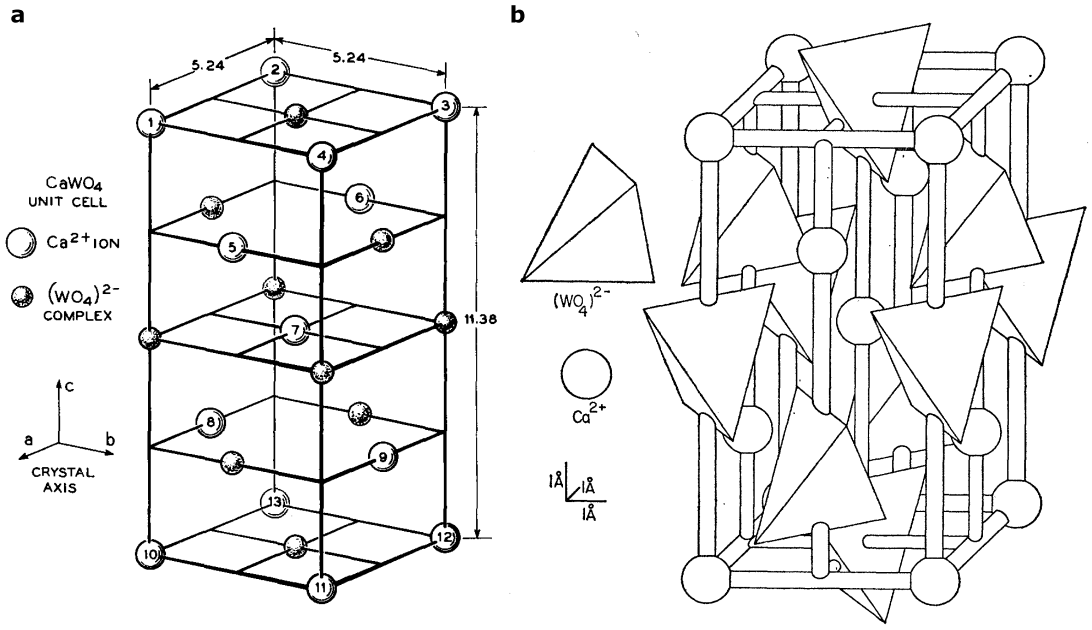

Figure 2.4 – **$CaWO_4$ unit cell. a.** Drawing extracted from [MG67]. The unit cell contains four calcium atoms and has a volume $V \approx 310\ \mathring{A}^3$. The WO_4 complex is shown as a single sphere. On this drawing, the symmetry of the calcium site appears as D_{2d}. In reality, the oxygens tetrahedrons reduce this symmetry to S_4. **b.** Drawing extracted from [RV64]. Here the oxygen tetrahedra are presented schematically.

electrons. Hence the $\boldsymbol{A}$-tensor follows the same symmetry as the $\mathbf{g}$-tensor. The third term, $\mathcal{H}_Q = \hat{\boldsymbol{I}} \cdot \boldsymbol{Q} \cdot \hat{\boldsymbol{I}}$, comes into play when $I \geq 1$ and is the nuclear electric quadrupole interaction with an electric field gradient at the nucleus due to the anisotropic electric charge distribution. The last term is the nuclear Zeeman interaction, $\mathcal{H}_{Zn} = -\mu_N \boldsymbol{B_0} \cdot \mathbf{g}^{(n)} \cdot \hat{\boldsymbol{I}}$, where the anisotropy of $\mathbf{g}^{(n)}$ comes from the shielding of the external magnetic field by the electrons [AB12]. The three last terms, which depend all on the nuclear spin, determine what is called the hyperfine structure. Note that the last two terms are much smaller than the electron Zeeman and hyperfine interactions and are thus often neglected. Lastly, the dipolar coupling between the electron spin and ligand nuclear spins, called superhyperfine coupling, may also shift the energy levels but its effect is neglected here. The energy level structure of trivalent erbium ions is summarized in Figure 2.3

2.2 Effective spin Hamiltonian of several Kramers ions in $CaWO_4$

2.2.1 $CaWO_4$ crystal

The host matrix used in this work is calcium tungstate ($CaWO_4$). This crystal has a tetragonal structure and belongs to the $I4_1/a$ space group [ZT64; Ber+09]. The lattice constants of its unit cell are $a = b = 0.524$ nm and $c = 1.138$ nm as shown in Figure 2.4a. Rare-earth ions substitute for Ca^{2+}. However, their 3+ charge does not match the calcium 2+ charge and compensation occurs in the crystal. Charge compensation can occur "naturally" during growth by creation of calcium vacancies, or is sometimes achieved "on purpose" by doping with Na^+ ions [MG67]. This charge compensation contributes to the existence of large inhomogeneous electric fields in the crystal, which has measurable consequences in our experiments as will be explained in more detail in Section 2.5.

Looking at Figure 2.4a, the symmetry of the calcium site appears to be D_{2d}. However, once we add the oxygen atoms forming tetrahedra around each tungsten atom, the point symmetry is reduced to S_4 (see Figure 2.4b). This means that the calcium site is identical under a combination of a rotation by 90° around the c-axis, followed by a reflection in the (a, b)-plane. There are two inequivalent calcium sites which are the inversion image of each other. On subplot a, the sites labelled 1-4, 7, 10-13 are equivalent and are related by inversion symmetry to the equivalent sites 5, 6, 8, 9.

Since rare earth ions substitute to calcium, their spin Hamiltonian is also expected to satisfy the S_4 site symmetry. The effective **g**-tensor is diagonal along the a, b, c-axes, with a parallel component along c, $g_{\parallel}$, and a perpendicular component along a and b, $g_{\perp}$, due to the fact that the a and b-crystal axes are equivalent. In fact, all spin Hamiltonian parameters, including for example the hyperfine tensor $\boldsymbol{A}$, have the same axial symmetry around the c-axis and the two inequivalent calcium sites are not distinguishable regarding the properties of REIs occupying them. One may wonder whether charge compensation would perturb this S_4 symmetry. This was shown to be the case when charge compensation occurs right next to the REI, giving rise in some samples to EPR lines that do not obey the S_4 symmetry [GM64; RV64; MG67] in addition to the main REI EPR lines which do obey indeed S_4. As will be shown later, in our spectra, we see some non-S_4 lines, which could possibly originate from such "charged-REIs". Note also that other paramagnetic impurities, like Fe^{3+}, may also go in interstitial sites, instead of substituting for calcium [GKT78; CTM97; MT85].

The dopant concentration is often given in percent, ppm or ppb, corresponding to the fraction of calcium atoms replaced by REIs. The unit cell of $CaWO_4$ shown in Figure 2.4 has four calcium sites and a volume $V_{\text{unit cell}} \sim 310\ \mathring{A}^3$. Thus, the conversion factor of the dopant concentration to cm^{-3} is $4/V_{\text{unit cell}} \sim 1.3 \times 10^{22}\ \text{cm}^{-3}$. The dominant nuclear spin contribution in this crystal comes from tungsten atoms, where the isotope ^{183}W, with 0.145 natural abundance, has a nuclear spin $I = 1/2$ and a gyromagnetic ratio of $\gamma_W/2\pi = 1.8$ MHz/T (corresponding to a nuclear g-factor of g = 0.236). These numbers lead to a relatively low magnetic moment density for $CaWO_4$ compared to other hosts, due to both the low nuclear abundance of the ^{183}W isotope and the small gyromagnetic ratio of its nuclear spin. This comparison to other host crystals will be detailed at the end of Chapter 4.

2.2.2 Zero nuclear spin Kramers ions in $CaWO_4$

Following the above discussion, the **g**-tensor of erbium in this crystal has an axial symmetry around the c-axis and is given by [Ber+07]

$$\mathbf{g} = \begin{pmatrix} g_{\perp} & 0 & 0 \\ 0 & g_{\perp} & 0 \\ 0 & 0 & g_{\parallel} \end{pmatrix}_{(a,b,c)} = \begin{pmatrix} 8.38 & 0 & 0 \\ 0 & 8.38 & 0 \\ 0 & 0 & 1.247 \end{pmatrix}_{(a,b,c)} \tag{2.17}$$

This **g**-tensor has a remarkably strong component in the (a, b)-plane, which is about 4 times larger that the free electron g-factor of $g_e = 2$. This large value originates from the strong total angular momentum of the ground state Kramers doublet of erbium, $J = 15/2$, which is the maximum J value for any rare-earth ion (see Table 2.1). Stronger components of the **g**-tensor of erbium can be obtained in other crystals like Y_2SiO_5 with $g_{\text{max}} = 15$. Depending on the magnetic field orientation, erbium ions can therefore be more sensitive to their magnetic environment than a typical g= 2 electron spin. This is an advantage for coupling to other systems like superconducting circuits, but a possible difficulty for reaching long coherence times as will be discussed in Chapter 4.

The **g**-tensor of several other Kramers ions in $CaWO_4$ is given in Table 2.3.

Ion	Er^{3+}	Yb^{3+}	Ce^{3+}	Nd^{3+}
$g_\parallel$	1.247	1.05	2.92	2.03
$g_\perp$	8.38	3.93	1.43	2.52

Table 2.3 – **g-tensor of four Kramers ions in $CaWO_4$.** These values are taken from [Mim65]. The more precise values of erbium are taken from [Ber+07].

The anisotropy of the **g**-tensor has an effect on the electron-spin spectrum of erbium, as discussed in [AB12]. Expanding the scalar product of Equation 2.14 in the (x, y, z) basis corresponding to the crystal (a, b, c) axes gives

$$\mathcal{H}_{spin} = \mu_B B_0 (g_\perp \sin\theta \cos\varphi \hat{S}_x + g_\perp \sin\theta \sin\varphi \hat{S}_y + g_\parallel \cos\theta \hat{S}_z), \tag{2.18}$$

where θ and φ characterise the magnetic field orientation in spherical coordinates.

Because of the axial symmetry around the c-axis, the (x, y, z) basis can be rotated such that $\varphi = 0$. Then,

$$\begin{aligned} \mathcal{H}_{spin} &= \mu_B B_0 (g_\perp \sin\theta \hat{S}_x + g_\parallel \cos\theta \hat{S}_z) \\ &= g_{\text{eff}} \mu_B B_0 \left(\frac{g_\perp \sin\theta}{g_{\text{eff}}} \hat{S}_x + \frac{g_\parallel \cos\theta}{g_{\text{eff}}} \hat{S}_z \right) \\ &= g_{\text{eff}} \mu_B B_0 (\sin\theta' \hat{S}_x + \cos\theta' \hat{S}_z) \\ &= g_{\text{eff}} \mu_B B_0 \hat{S}'_z, \end{aligned} \tag{2.19}$$

where $g_{\text{eff}} = \sqrt{(g_\perp \sin\theta)^2 + (g_\parallel \cos\theta)^2}$. Everything happens as if a magnetic field directed along θ' would be applied on a spin with isotropic g-factor g_{eff}.

We have

$$\begin{cases} \hat{S}'_x & = \hat{S}_x \cos\theta' - \hat{S}_z \sin\theta' \\ \hat{S}'_y & = \hat{S}_y \\ \hat{S}'_z & = \hat{S}_z \cos\theta' + \hat{S}_x \sin\theta' \\ \sin\theta' & = \sin\theta \times g_\perp / g_{\text{eff}} \\ \cos\theta' & = \cos\theta \times g_\parallel / g_{\text{eff}}. \end{cases} \tag{2.20}$$

The eigenstates of the spin Hamiltonian are the eigenstates of the operator $\hat{S}'_z$ with quantization axis along θ'. Note that the erbium spin is polarized along the magnetic field orientation only if the latter is applied along a principal axis of the **g**-tensor, i.e. when $\theta = 0$ or $\theta = \pi/2$.

2.2.3 Non-zero nuclear spin Kramers ions in $CaWO_4$

The **g**-tensor is the only parameter needed to characterize the spin Hamiltonian of Kramers ions with zero nuclear spin. This applies to most stable isotopes of erbium, namely ^{164}Er (1.5% natural abundance), ^{166}Er (33.5%), ^{168}Er (27%) and ^{170}Er (15%). The last stable isotope, ^{167}Er (23%), has a nuclear spin $I = 7/2$. Its spin Hamiltonian thus contains two terms, the electronic Zeeman and the hyperfine interactions, the other terms of Equation 2.16 being negligible [Ber+09].

The hyperfine interaction is parametrized by a tensor which has the same principal axes as **g**,

$$\mathbf{A} = h \frac{A_J}{g_J} \mathbf{g}, \tag{2.21}$$

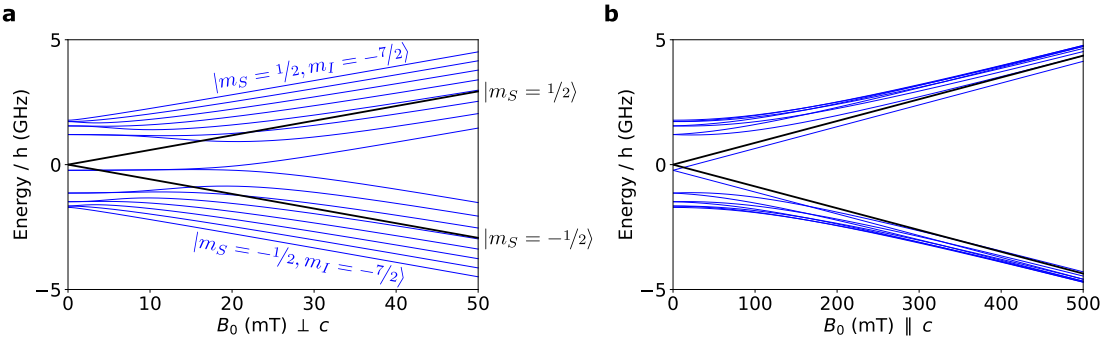

Figure 2.5 – **Energy levels of Er^{3+}:$CaWO_4$ with the magnetic field oriented along the principal axes of the g-tensor.** The black lines show the spectrum of the zero nuclear spin isotopes whereas the blue lines correspond to ^{167}Er. Note the difference of x-axis scale between the two plots. **a.** Magnetic field applied in the (a, b)-plane. **b.** Magnetic field applied along the c-axis.

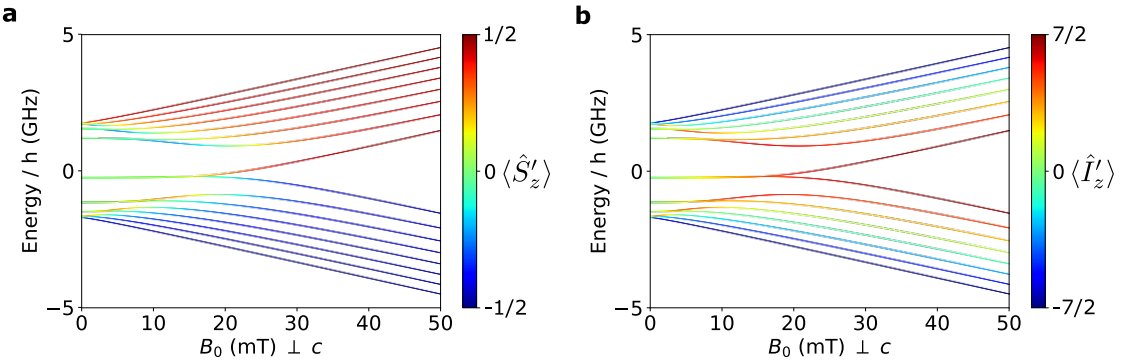

Figure 2.6 – **Spin matrix element of each hyperfine level when the magnetic field B_0 is applied perpendicular to the c-axis. a.** $\langle \hat{S}'_z \rangle$. **b.** $\langle \hat{I}'_z \rangle$. The identification of the levels with quantum numbers $|m_S, m_I\rangle$ applies only in the high-field limit, where the electronic Zeeman energy is greater than the hyperfine interaction.

where $g_J = 6/5$ and $A_J = -125$ MHz [AB12]. The complete spin Hamiltonian,

$$\mathcal{H}_{^{167}\mathrm{Er}} = \mu_B \boldsymbol{B_0} \cdot \mathbf{g} \cdot \hat{\boldsymbol{S}} + \hat{\boldsymbol{S}} \cdot \boldsymbol{A} \cdot \hat{\boldsymbol{I}}, \tag{2.22}$$

splits the Kramers doublet into $(2S + 1)(2I + 1) = 16$ energy levels. The energy level structure of erbium is plotted as a function of magnetic field in Figure 2.5. The zero nuclear spin erbium isotopes have two levels separated by a linear Zeeman splitting. The ^{167}Er hyperfine level structure is more complex and can be split in two regimes: the low-field regime, where the hyperfine interaction is larger than the electronic Zeeman interaction, and high-field regime, where the electronic Zeeman interaction dominates.

In the latter case, the electron spin quantum number $m_S = \pm 1/2$ is well defined, as well as the nuclear spin quantum number m_I. If the magnetic field is applied along a principal axis of the **g**-tensor, the effect of the hyperfine interaction is simply to add a frequency shift of the m_I level as $\hbar\Delta\omega \sim m_S A_{\parallel/\perp} m_I$, depending on the magnetic field orientation. Figure 2.6 and Figure 2.7 show the spin matrix element $\langle \hat{S}'_z \rangle$ and $\langle \hat{I}'_z \rangle$ for each hyperfine level. In the high-field limit, they are equal to m_S and m_I respectively. In the low-field limit, the labelling of each level with $|m_S, m_I\rangle$ is not valid anymore.

Throughout this thesis, we will need to compute the hyperfine level structure of ^{167}Er. We will also encounter the non-zero nuclear spin isotopes of ytterbium, ^{171}Yb and ^{173}Yb. As for ^{167}Er with Equation 2.22, their spin Hamiltonian contains two terms, the electronic

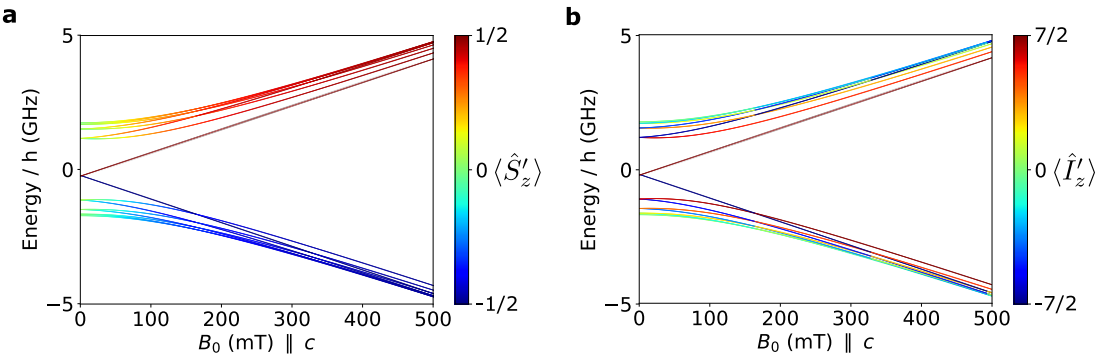

Figure 2.7 – **Spin matrix element of each hyperfine level when the magnetic field B_0 is applied along the c-axis.** m_S and m_I are not good quantum numbers at low field due to the hyperfine interaction. **a.** $\langle \hat{S}'_z \rangle$. **b.** $\langle \hat{I}'_z \rangle$.

Isotope	Nuclear spin	Nat. abund.	$g_\parallel$	$g_\perp$	$A_\parallel/h$ (MHz)	$A_\perp/h$ (MHz)
Er ($I=0$)	0	0.77	1.247	8.38	0	0
^{167}Er	7/2	0.23			-130	-873
Yb ($I=0$)	0	0.7			0	0
^{171}Yb	1/2	0.14	1.05	3.92	788	3082
^{173}Yb	5/2	0.16			-216	-851

Table 2.4 – **Spin Hamiltonian parameters for Er^{3+} and Yb^{3+} in $CaWO_4$.** The erbium parameters are taken from [Ber+07]. The ytterbium parameters are taken from the measurement of [SN70] for the absolute values and the calculation of [Zhe+04] for the sign of the hyperfine coupling. This sign influences the hyperfine levels labelling, where the lowest spin state in the high-field limit is $|-S,-I\rangle$ if $A<0$ and $|-S,+I\rangle$ is $A>0$.

Zeeman and hyperfine interactions. The other terms are negligible [SN70]. The full spin Hamiltonian parameters of both erbium and ytterbium are summarized in Table 2.4.

2.2.4 Concentration and polarization

A consequence of the hyperfine structure is that the non-zero nuclear spin isotopes are distributed among all hyperfine levels and their Boltzmann distribution is temperature dependent. In the high field limit, where the $|m_S, m_I\rangle$ labels are well defined, the concentration of the $|m_I\rangle$ levels of ^{167}Er is given by

$$c(T) = [^{167}\mathrm{Er}^{3+}] \frac{\exp\left[-E_{|g\rangle}/(k_B T)\right] + \exp\left[-E_{|e\rangle}/(k_B T)\right]}{\sum_n \exp[-E_n/(k_B T)]}, \tag{2.23}$$

where $[^{167}\mathrm{Er}^{3+}] = 0.23[\mathrm{Er}^{3+}]$ is the absolute concentration of the ^{167}Er isotope, E_n is the energy of level n of ^{167}Er, $|g\rangle = |-1/2, m_I\rangle$ is the ground state and $|e\rangle = |1/2, m_I\rangle$ the excited state. The occupation factor,

$$\frac{c(T)}{[^{167}\mathrm{Er}^{3+}]} = \frac{\exp\left[-E_{|g\rangle}/(k_B T)\right] + \exp\left[-E_{|e\rangle}/(k_B T)\right]}{\sum_n \exp[-E_n/(k_B T)]}, \tag{2.24}$$

is plotted in Figure 2.8a and b for all hyperfine levels as a function of temperature. The magnetic field is applied perpendicular to c, with magnitude 43 mT. At high temperature, when the eight hyperfine levels are equally populated, the relative concentration reaches a plateau at 1/8. At zero temperature, only the lowest hyperfine level, $|-7/2\rangle$, is populated and the occupation factor of all other transitions is zero.

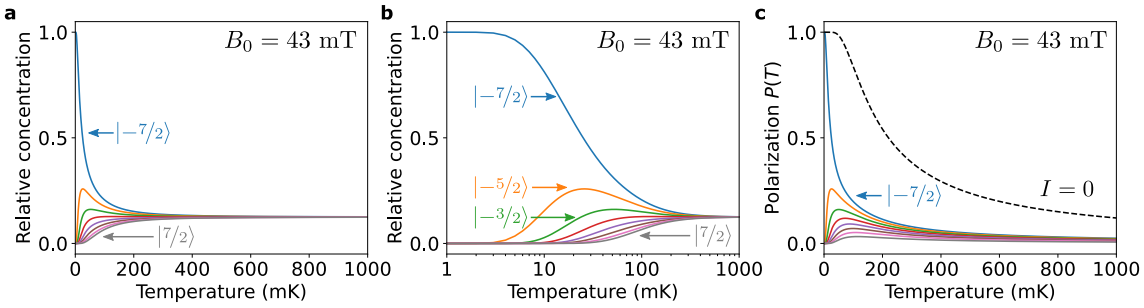

Figure 2.8 – **Relative concentration of the hyperfine levels and polarization.** The energy level spectra are computed with $\boldsymbol{B_0} \perp c$ and $B_0 = 43$ mT. **a.** Relative concentration of the hyperfine levels, computed as the fraction of the total ^{167}Er concentration, as a function of temperature. The hyperfine levels are labelled with their nuclear spin projection $|m_I\rangle$ from $|-7/2\rangle$ to $|7/2\rangle$. The relative concentration decreases with m_I due to the higher energy of the $|-1/2, m_I\rangle$ level. **b.** Same data with the temperature represented in logarithmic scale. **c.** Polarization $P(T)$ as a function of temperature. The polarization of the hyperfine levels (colored solid lines) are compared with the erbium $I = 0$ polarization (dashed black line).

Another important quantity is the polarization $P(T)$ of each transition, defined as $P(T) = (N_{|g\rangle} - N_{|e\rangle})/N$,

$$P(T) = \frac{\exp\left[-E_{|g\rangle}/(k_B T)\right] - \exp\left[-E_{|e\rangle}/(k_B T)\right]}{\sum_n \exp[-E_n/(k_B T)]}, \tag{2.25}$$

where E_n is the energy of level n of the multiplet.

For the $I = 0$ electron spin transition, the polarization function simplifies in

$$P(T) = \tanh\left(\frac{g_{\text{eff}}\mu_B B_0}{2k_B T}\right). \tag{2.26}$$

These functions are plotted with the same magnetic field conditions ($\boldsymbol{B_0} \perp c$ and $B_0 = 43$ mT) as a function of temperature in Figure 2.8c. We note that $P(T)$ reaches 1 at $T = 0$ K when it applies to a transition involving the multilevel ground state, for example the $I = 0$ transition or the $|-7/2\rangle$ transition of ^{167}Er. $P(0\ K) = 0$ for all other hyperfine transitions. All polarization functions go to 0 at high temperature because the ground state and excited levels are equally populated.

2.3 Spin-spin interactions

Everything derived until now concerns individual erbium ions in a crystal. We now discuss the interaction of the erbium spin with other spins in the crystal, which can be of the exchange type or dipolar magnetic. Note that this discussion applies more generally to any electron or nuclear spins.

2.3.1 Exchange interaction

The exchange interaction can be written as

$$\mathcal{H}_{\text{exch}} = \boldsymbol{S_1} \cdot \boldsymbol{J} \cdot \boldsymbol{S_2} \tag{2.27}$$

[AB12] and couples two electron spins with coupling strength tensor $\boldsymbol{J}$. This interaction is significant only when the wavefunctions of the two unpaired spins overlap. In solids, this

happens if the distance between the two spins is below typically 1.5 nm or if the wavefunctions are strongly delocalized [SJ01]. In the case of rare-earth ions, the wavefunctions are very localized. Moreover, in the samples we are studying here, the inter-ion distance is larger than 10 nm. Therefore, the exchange interaction can be neglected.

2.3.2 Magnetic dipole-dipole interaction

The second mechanism of spin-spin interaction is the magnetic coupling between the two magnetic moments of the spins, $\boldsymbol{\mu_1}$ and $\boldsymbol{\mu_2}$, with Hamiltonian

$$\mathcal{H}_{dd} = \frac{\mu_0}{4\pi} r^{-3} [\boldsymbol{\mu_1}.\boldsymbol{\mu_2} - 3r^{-2}(\boldsymbol{\mu_1}.\boldsymbol{r})(\boldsymbol{\mu_2}.\boldsymbol{r})] \tag{2.28}$$

[AB12], where $\boldsymbol{r}$ is the vector separating the two magnetic moments. This Hamiltonian can be seen as the interaction between one spin and the local magnetic field generated by the other one and vice-versa.

Due to the anisotropy, the spin is not necessarily aligned with the direction of the magnetic field $\boldsymbol{B_0}$ and the magnetic moment $\boldsymbol{\mu}$ is related to the spin $\boldsymbol{S}$ with the relation $\boldsymbol{\mu} = -\mu_B \mathbf{g} \cdot \hat{\boldsymbol{S}}$. Note that the magnetic moment can also come from a nuclear spin in the bath which is often described with an isotropic g-factor g_N as $\boldsymbol{\mu} = \mathrm{g}_N \mu_N \hat{\boldsymbol{I}}$.

The dipolar coupling Hamiltonian can be decomposed in six terms (where $\hat{S}$ can be replaced by $-\mu_N/\mu_B \hat{I}$ in case of a nuclear spin):

$$\begin{aligned}
\mathcal{H}_{dd} = \mu_B^2 \frac{\mu_0}{4\pi} r^{-3} \, [& \mathrm{g}_{x1}\mathrm{g}_{x2}\hat{S}_{x1}\hat{S}_{x2}(1 - 3\sin^2\theta_r \cos^2\phi_r) \\
& + \mathrm{g}_{y1}\mathrm{g}_{y2}\hat{S}_{y1}\hat{S}_{y2}(1 - 3\sin^2\theta_r \sin^2\phi_r) \\
& + \mathrm{g}_{z1}\mathrm{g}_{z2}\hat{S}_{z1}\hat{S}_{z2}(1 - 3\cos^2\theta_r) \\
& - 3\sin^2\theta_r \cos\phi_r \sin\phi_r (\mathrm{g}_{x1}\mathrm{g}_{y2}\hat{S}_{x1}\hat{S}_{y2} + \mathrm{g}_{y1}\mathrm{g}_{x2}\hat{S}_{y1}\hat{S}_{x2}) \\
& - 3\sin\theta_r \cos\phi_r \cos\theta_r (\mathrm{g}_{x1}\mathrm{g}_{z2}\hat{S}_{x1}\hat{S}_{z2} + \mathrm{g}_{z1}\mathrm{g}_{x2}\hat{S}_{z1}\hat{S}_{x2}) \\
& - 3\sin\theta_r \sin\phi_r \cos\theta_r (\mathrm{g}_{y1}\mathrm{g}_{z2}\hat{S}_{y1}\hat{S}_{z2} + \mathrm{g}_{z1}\mathrm{g}_{y2}\hat{S}_{z1}\hat{S}_{y2}) \,]
\end{aligned} \tag{2.29}$$

where θ_r and ϕ_r are the spherical coordinates of the vector $\boldsymbol{r}$ separating the two spins.

Let's pause to give orders of magnitude, in case of an erbium bath of concentration 1 ppm within $CaWO_4$. The dipolar interaction between erbium spins 1 and 2 induces a shift of the Zeeman energy of spin 1 which is very roughly in absolute value

$$\hbar|\Delta\omega_1| = \mu_B^2 \frac{\mu_0}{4\pi} \frac{2\mathrm{g}_{\mathrm{eff},1}|m_{z1}|\mathrm{g}_{\mathrm{eff},2}|m_{z2}|}{r^3}. \tag{2.30}$$

A 1 ppm erbium concentration corresponds to $c \sim 10^{16}$ cm^{-3} and to a mean distance between two erbium ions of $d = [3/(4\pi c)]^{1/3} \sim 30$ nm. The resulting frequency shift is calculated in Table 2.5 for two magnetic field orientations ($\theta = 0$ and $\theta = \pi/2$), as well as the shift due to the erbium coupling to its nearest tungsten nuclear spin. We see that the strength of the dipolar coupling to other spins strongly depends on the $\boldsymbol{B_0}$ orientation. Effectively, the erbium magnetic moment is 7 times lower when $\boldsymbol{B_0} \parallel c$ than when $\boldsymbol{B_0} \perp c$. The impact is maximum for the erbium-erbium interaction, which changes by a factor 40 for the same distance r between ions. One can thus expect that coherence times strongly depend on the $\boldsymbol{B_0}$ orientation, as we will see later.

As calculated in Table 2.5, the dipolar interaction is negligible in front of the Zeeman energy of the erbium transition and can be considered as a small perturbation. For a tungsten nuclear spin nearest neighbor of an erbium ion, on the other hand, the dipolar interaction with erbium is of comparable magnitude as the Zeeman interaction.

Interaction	**Energy** for $\theta = 0$, $B_0 = 100$ mT	**Energy** for $\theta = \pi/2$, $B_0 = 100$ mT
Zeeman		
- Erbium $I = 0$ isotopes ($S = 1/2$)	1.7 GHz	11.7 GHz
- Tungsten ^{183}W ($I = 1/2$)	0.18 MHz	0.18 MHz
dipolar		
- Er-Er (d=30 nm)	0.4 kHz	17 kHz
- Er-^{183}W (first neighbor, d=0.4 nm)	16 kHz	110 kHz
- ^{183}W-^{183}W (d=0.5 nm)	1 Hz	1 Hz

Table 2.5 – **Typical dipolar interactions for erbium ions in $CaWO_4$ with a concentration of 1 ppm.** The concentration c affects the mean distance between erbium ions such that the dipolar interaction with their nearest neighbor increases proportionally to c.

From the above considerations, Equation 2.29 can be greatly simplified. Two cases need to be distinguished: either the two spins coupled by the dipolar interaction are of the same kind (either two electron spins or two nuclear spins) or they are of different kinds (one electron spin and one nuclear spin).

2.3.2.1 Secular approximation for two coupled electron spins or nuclear spins

Let's consider two electron spins coupled by the dipolar interaction. The derivation is identical for nuclear spins. We showed in Table 2.5 that this interaction is negligible in front of the Zeeman interaction and can be considered as a perturbation. The unperturbed Zeeman Hamiltonian is

$$\mathcal{H}_Z = \mathrm{g}_{\mathrm{eff},1}\mu_B B_0 \hat{S}'_{z1} + \mathrm{g}_{\mathrm{eff},2}\mu_B B_0 \hat{S}''_{z2}, \tag{2.31}$$

where here the sign $''$ stresses the fact that for an arbitrary orientation of the magnetic field, the two spins are not necessarily aligned. This unperturbed Hamiltonian lifts the degeneracy of both spin states according to their quantum numbers m_{s1} and m_{s2} if $\mathrm{g}_{\mathrm{eff},1} \neq \mathrm{g}_{\mathrm{eff},2}$ and $m_{s1} + m_{s2}$ if $\mathrm{g}_{\mathrm{eff},1} = \mathrm{g}_{\mathrm{eff},2}$.

Equation 2.29 can be rewritten by changing the operators (S_{x1}, S_{y1}, S_{z1}) into $(S_{+1}, S_{-1}, S'_{z1})$ where $S_{+1} = (S'_{x1} + iS'_{y1})/2$ and $S_{-1} = (S'_{x1} - iS'_{y1})/2$ for spin 1 and equivalently into $(S_{+2}, S_{-2}, S''_{z2})$ for spin 2. In this way, Equation 2.29 splits into several terms, factors of $S'_{z1}S''_{z2}$, $S'_{z1}S_{+2}$, $S'_{z1}S_{-2}$, $S_{+1}S_{+2}$, $S_{+1}S_{-2}$, $S_{-1}S_{-2}$, plus the terms reverting 1 and 2. All these terms do not perturb equally the eigenstates of the Zeeman Hamiltonian of Equation 2.31. Indeed, at first order, perturbation theory keeps only terms conserving the quantum numbers $m_{s1} + m_{s2}$ if $\mathrm{g}_{\mathrm{eff},1} = \mathrm{g}_{\mathrm{eff},2}$ or m_{s1} and m_{s2} if $\mathrm{g}_{\mathrm{eff},1} \neq \mathrm{g}_{\mathrm{eff},2}$ [Abr61]. Here, only the term in $S'_{z1}S''_{z2}$ keeps both m_{s1} and m_{s2} while the terms in $S'_{z1}S''_{z2}$, $S_{+1}S_{-2}$ and $S_{-1}S_{+2}$ conserve $m_{s1} + m_{s2}$. All the other terms can be neglected at first order of perturbation theory, this is called the **secular approximation**.

The prefactor of each of these secular terms can be complex due to the anisotropy of the **g**-tensor. However, the equations are simple if the magnetic field is oriented along a principal axis of $CaWO_4$, either along the c-axis ($\theta = 0$) or in the (a, b)-plane ($\theta = \pi/2$), which is mostly the case in our experiments. Indeed, in this case, both spins are aligned with the magnetic field and $\hat{S}''_{z2}$ can be written $\hat{S}'_{z2}$. As a consequence, if the spins are of

different species ($g_{\text{eff},1} \neq g_{\text{eff},2}$), the dipolar interaction simply reduces to

$$\mathcal{H}_{dd} = \mu_B^2 \frac{\mu_0}{4\pi} r^{-3} g_{\text{eff},1} g_{\text{eff},2} (1 - 3\cos^2\theta_r) \hat{S}'_{z1} \hat{S}'_{z2}, \tag{2.32}$$

where θ_r has been redefined as the angle between $\boldsymbol{r}$ and $\boldsymbol{B_0}$. In the following, we call it the ZZ interaction term, as it involves only the spin longitudinal component. Note that $g_{\text{eff},i}$ equals $g_{\parallel,i}$ if $\boldsymbol{B_0} \parallel c$ and $g_{\perp,i}$ if $\boldsymbol{B_0} \perp c$. If the spins are of the same species ($g_{\text{eff},1} = g_{\text{eff},2}$), the dipolar interaction in the secular approximation consists in the term above, plus a term in $(S_{+1}S_{-2} + S_{-1}S_{+2})$ which describes possible "flip-flop" between resonant spins. We call this term $XX + YY$ as it concerns only the spin transverse components.

2.3.2.2 Secular approximation for an electron spin coupled to a nuclear spins

Considering now the dipolar interaction between an electron and a nuclear spin, the scenario is slightly different because the dipolar interaction is not necessarily negligible compared to the nuclear Zeeman interaction (see Table 2.5). The total Hamiltonian is

$$\mathcal{H} = g_{\text{eff}} \mu_B B_0 \hat{S}'_z - g_N \mu_N B_0 \hat{I}''_z + \mathcal{H}_{dd}. \tag{2.33}$$

Without the dipolar interaction, the nuclear spin would be aligned with the magnetic field orientation because its g-factor is isotropic while the electron spin is not necessarily.

The last two terms are small compared to the electronic Zeeman interaction. Hence the secular approximation for the electron spin is valid. When developing the dipolar Hamiltonian as a function of (S'_x, S'_y, S'_z) and (I''_x, I''_y, I''_z), all terms in S'_x and S'_y can be neglected so that the total Hamiltonian in the secular approximation is

$$\mathcal{H} = g_{\text{eff}} \mu_B B_0 \hat{S}'_z - g_N \mu_N B_0 \hat{I}''_z + A \hat{S}'_z \hat{I}''_z + B \hat{S}'_z \hat{I}''_x + C \hat{S}'_z \hat{I}''_y, \tag{2.34}$$

where A, B and C are constants depending on the **g**-tensor and on the vector $\boldsymbol{r}$ separating the spins.

2.4 Spin relaxation

When out of thermal equilibrium, spins relax by exchanging energy with a bath at temperature T_0. There are two thermal baths with which spins can exchange energy: either they relax by emitting microwave photons (radiative relaxation), or they relax by emitting phonons (non-radiative relaxation). In this section, we follow the derivation found in [AB12].

Let's consider Kramers ions whose ground state doublet ($|g\rangle$, $|e\rangle$) splits under a magnetic field $\boldsymbol{B_0}$ with Zeeman energy $\hbar\omega = g_{\text{eff}} \mu_B B_0$. The populations of each level are called n_g and n_e respectively. They are coupled to a bath of infinite heat capacity such that its temperature is always at T_0. Note that in the case of phonons, this assumption is not always valid. In fact, the heat capacity of phonons is often smaller than the one of the spins and this can lead to an effect called phonon bottleneck, where the phonon temperature increases due to spin relaxation.

2.4.1 Direct process

We first consider the direct process where each spin exchanges one resonant phonon or photon with the bath. The population difference between the two spin levels evolves according to the following differential equation,

$$\frac{d(n_g - n_e)}{dt} = (w_- + w_+) \left[(N_g - N_e) - (n_g - n_e) \right], \tag{2.35}$$

where w_+ and w_- are the transition rates from $|g\rangle$ to $|e\rangle$ and from $|e\rangle$ to $|g\rangle$ respectively and N_g and N_e are the equilibrium level populations. The transition rates are related to Einstein coefficients with

$$\begin{aligned} w_+ &= B\rho \\ w_- &= A + B\rho = B\rho e^{\hbar\omega/(k_B T_0)}, \end{aligned} \tag{2.36}$$

where B is the coefficient of stimulated absorption or emission, A is the coefficient of spontaneous emission and ρ is the energy density of the bath,

$$\rho d\omega \propto \frac{\omega^3}{v^3} \frac{d\omega}{\exp\{\hbar\omega/(k_B T_0)\} - 1}. \tag{2.37}$$

v is the light velocity $c = 3 \times 10^8$ m.s^{-1} in the case of photons, or the phonon velocity, which is typically $v = 3 \times 10^3$ m.s^{-1}.

The solution of Equation 2.35 is thus

$$n_e - n_g = (N_e - N_g) + [(n_e - n_g)_{t=0} - (N_e - N_g)]e^{-t/T_1} \tag{2.38}$$

where

$$\frac{1}{T_1} = w_+ + w_- = A + 2B\rho \propto \frac{\omega^3}{v^3} B \coth \frac{\hbar\omega}{2k_B T_0}. \tag{2.39}$$

2.4.1.1 Radiative relaxation

It can be shown that the relaxation rate of Equation 2.39 by direct absorption and emission of photons from the electromagnetic radiation field in free space is given by

$$\frac{1}{T_1} = \frac{\mu_0}{4\pi} \frac{2(g\mu_B/\hbar)^2}{3} \frac{\hbar\omega^3}{c^3} \coth \frac{\hbar\omega}{2k_B T_0}. \tag{2.40}$$

Computing this equation for $\omega/2\pi = 5$ GHz, g= 2 and $T_0 = 10$ mK gives $T_1 = 4 \times 10^{12}$ s. Therefore, radiative relaxation in free space can be neglected. However, photon emission can be greatly enhanced via the coupling of the spin to a high-quality-factor microwave resonator. This is called the Purcell effect and will be discussed in Chapter 3.

2.4.1.2 Non-radiative relaxation

Because radiative relaxation is negligible, spin relaxation in crystals occurs dominantly by exchange of phonons with the lattice. We now describe qualitatively the mechanism leading to spin relaxation by phonon emission in REIs, based on [AB12; LJ66a; LJ66b]. Lattice ion vibration leads to a modulation of the crystal field, which couples to the REI magnetic moment via the spin-orbit interaction. In Kramers ions, this process is completely suppressed at zero field by Kramers degeneracy. However it becomes allowed at finite $\boldsymbol{B_0}$, because the levels $|g\rangle$ and $|e\rangle$ then slightly hybridize with other crystal fields levels (in particular with Z_2 which is the closest in energy). This rescales the Einstein coefficient B by a factor $(B_0/\Delta)^2$, where $\Delta/h = 0.57$ THz is the energy separation between Z_1 and Z_2 for erbium in $CaWO_4$ and B_0 is the magnetic field strength. As a consequence, it can be shown that for a Kramers ion, the spin-lattice relaxation rate is

$$\frac{1}{T_1} = \alpha_D \omega^3 B_0^2 \coth \frac{\hbar\omega}{2k_B T_0}, \tag{2.41}$$

where α_D is an anisotropic constant coming from the anisotropy of the Zeeman interaction [LJ66a; LJ66b].

We note that, for isotopes with a non-zero nuclear spin, the hyperfine levels can add an additional direct process,

$$\frac{1}{T_1} = R_d^{\text{hfs}} \coth \frac{\hbar\omega}{2k_B T_0}, \tag{2.42}$$

where $R_d^{\text{hfs}} \propto (I(I-1) - m^2)$.

2.4.2 Two-phonon processes

In addition to the direct phonon process, REI spin relaxation can occur via two-phonon processes (Orbach or Raman).

2.4.2.1 Orbach process

The Orbach process involves a third level $|c\rangle$, which belongs to an excited Kramers doublet. If the phonon energy density is higher at its energy Δ compared to the Zeeman energy $\hbar\omega$, it will be more likely that, in order to relax from $|e\rangle$ to $|g\rangle$, a phonon is first absorbed such that $|e\rangle$ is excited to $|c\rangle$ and then state $|c\rangle$ emits a phonon and relaxes to $|g\rangle$.

It can be shown that the Orbach relaxation rate is

$$\frac{1}{T_1} = R_O \Delta^3 \frac{1}{e^{\Delta/k_B T_0} - 1}. \tag{2.43}$$

2.4.2.2 Raman process

The Raman process is a two-phonon process which involves a continuum of states within the phonon energy density. Unlike the Orbach process, it involves virtual phonon states which are not specifically resonant with transitions of the magnetic ion. From this virtual level, a phonon can be emitted again such that the electron spin relaxes to $|g\rangle$.

This relaxation can be modelled by two separate mechanisms and the Raman relaxation rate has thus two contributions,

$$\frac{1}{T_1} = R_R T_0^9 + R'_R \left(\frac{\hbar\omega}{k_B}\right)^2 T_0^7. \tag{2.44}$$

2.4.3 State of the art for Er^{3+}:$CaWO_4$

Figure 2.9 shows previous measurements of the relaxation time of Er^{3+}:$CaWO_4$ from 1 K to 20 K with the field applied in the crystal (a, b)-plane [Ant+68]. The experimental data, measured at two frequencies, 9.4 GHz and 36 GHz, are fitted with $1/T_1 = AT_0 + B_1 e^{-\Delta_1/T_0} + B_2 e^{-\Delta_2/T_0}$. The first term in AT_0 corresponds to the temperature dependence of the direct phonon process in the high temperature limit (when $\hbar\omega \ll 2k_B T_0$). The good agreement between the data and the fit shows that the Raman process is negligible in this temperature range. Moreover, there is a visible cross-over between the relaxation through the direct phonon process and through the Orbach process at a typical temperature of 2-3 K depending on the frequency. These data demonstrate that at sub-Kelvin temperature, all multi-phonon processes are quenched and the spin-lattice relaxation is dominated by the direct phonon process. The ratio of the direct process coefficients is expected to change as $(B_{0,36\text{ GHz}}/B_{0,9.4\text{ GHz}})^4 = 219$ according to Equation 2.41 in the high temperature limit. The fits give a ratio $A_{36\text{ GHz}}/A_{9.4\text{ GHz}}$ of 78 which is in qualitative agreement, although off by a factor of 3. This may be linked to the spin-lattice anisotropy in the (a, b)-plane (coefficient α_D in Equation 2.41) as the authors do not specify the orientation of the magnetic field within this plane.

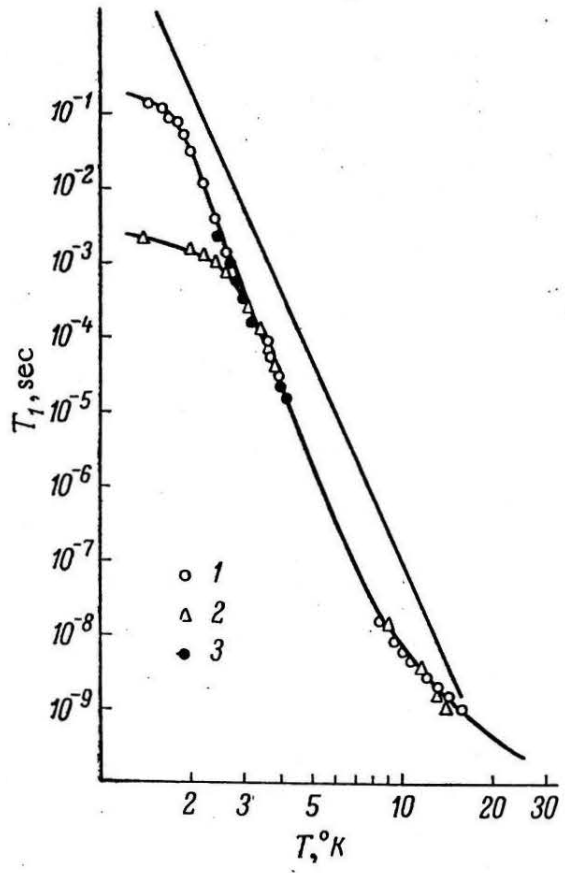

Figure 2.9 – **Relaxation time measurement of Er:$CaWO_4$.** This plot is taken from [Ant+68] and represents the temperature dependence of the spin-lattice relaxation time of Er^{3+} in $CaWO_4$ with the magnetic field applied perpendicular to the c-axis. The experimental data is measured at 9.4 GHz and 80 mT (label 1, circles), at 36 GHz and 310 mT (2, triangles) and at 6.7 GHz (label 3, dots, measured in another paper). The data are fitted using the direct process (in the high temperature limit) and two Orbach processes, with $1/T_1 = AT_0 + B_1 e^{-\Delta_1/T_0} + B_2 e^{-\Delta_2/T_0}$ (solid black lines). The coefficient A is frequency and field dependent according to Equation 2.41 and the fit yields $A = 4.6$ at 9.4 GHz and $A = 357$ at 36 GHz. The straight line shows the expected dependence of a Raman process, with $T_1^{-1} \propto T^9$, which does not match the data. The contribution of Raman processes is therefore neglected.

2.5 Homogeneous and inhomogeneous linewidths

Any transition of the magnetic ion has a given shape with a finite width, ultimately limited by the excited state lifetime. The linewidth is due to several mechanisms which can be divided into two groups, homogeneous broadening and inhomogeneous broadening.

2.5.1 Homogeneous broadening

Homogeneous broadening accounts for the linewidth of the transition of each spin individually. This linewidth is limited by decoherence phenomena happening in the environment of the spin (see Chapter 4). The homogeneous linewidth Γ_h (in rad.s^{-1}) can be related to the coherence time T_2 with $\Gamma_h = 2/T_2$. This coherence time has two origins, pure dephasing and relaxation $1/T_2 = 1/T_\phi + 1/(2T_1)$.

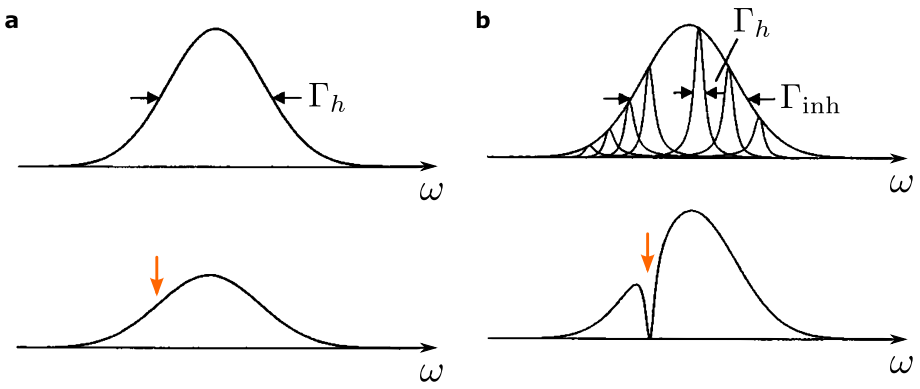

Figure 2.10 – **Homogeneous and inhomogeneous linewidths. a.** Superposition of spin packets of homogeneous width Γ_h and same center frequency. Irradiation at the frequency indicated with the orange arrow reduces the whole line intensity. **b.** Superposition of spin packets of homogeneous width Γ_h with different center frequencies leading to an inhomogeneously broadened line of width Γ_{inh}. Irradiation at the frequency indicated with the orange arrow burns a hole of width Γ_h. This figure is taken from [SJ01].

2.5.2 Inhomogeneous broadening

In a crystal, spins experience different local environments. This causes a static shift of the spin resonance frequency. Therefore, the spin line is inhomogeneously broadened and the inhomogeneous linewidth Γ_{inh} is generally much larger than Γ_h. Spins with the same local environment form spin packets of width Γ_h which behave independently from the other packets (see Figure 2.10).

2.5.2.1 Dipolar linewidth

Static spin frequency shifts can have several origins. We saw in Section 2.3 that the magnetic dipole-dipole interaction shifts the frequency of an electron spin via the ZZ interaction term. Thus it causes inhomogeneous broadening of the spin ensemble. Dipole interactions are of two types: either with the nuclear spins of the host crystals, or with paramagnetic impurities. It can be shown that dipolar coupling leads to a Lorentzian lineshape. Its full-width-at-half-maximum (FWHM) linewidth is called the dipolar linewidth Γ_{dd} ([MDS82], see Appendix B for its derivation). We consider only the case where the magnetic field is aligned with a principal axis of the host crystal ($\theta = 0°$ or $\theta = 90°$ for $CaWO_4$).

In the case of dipolar coupling of an electron spin with the tungsten nuclear spin bath of $CaWO_4$, the dipolar linewidth (in rad.s^{-1}) is

$$\Gamma_{dd,\mathrm{W}} = \frac{2\pi\mu_0\mu_B \mathrm{g}_{\mathrm{eff},\alpha}\mu_N \mathrm{g}_{\mathrm{W}} c_{\mathrm{W}}}{9\sqrt{3}\hbar}, \tag{2.45}$$

where α characterizes the electron spin under study. If it is erbium, when $\boldsymbol{B_0} \perp c$, $\mathrm{g}_{\mathrm{eff,Er}} = 8.38$ and $\Gamma_{dd,\mathrm{W}}/2\pi = 130$ kHz. When $\boldsymbol{B_0} \parallel c$, $\mathrm{g}_{\mathrm{eff,Er}} = 1.247$ and the linewidth reduces to 20 kHz.

The dipolar linewidth due to paramagnetic impurities is given by

$$\Gamma_{dd,\beta} = \frac{2\pi\mu_0\mu_B^2 \mathrm{g}_{\mathrm{eff},\alpha}\mathrm{g}_{\mathrm{eff},\beta} c_\beta}{9\sqrt{3}\hbar}, \tag{2.46}$$

where $\mathrm{g}_{\mathrm{eff},\beta}$ and c_β are the effective g-factor and the concentration of the considered paramagnetic impurities in the bath. For a 1 ppm erbium concentration, the erbium dipolar linewidth due to the erbium bath is $\Gamma_{dd,\mathrm{Er}}/2\pi = 60$ kHz when $\boldsymbol{B_0} \perp c$ and 1 kHz when $\boldsymbol{B_0} \parallel c$.

2.5.2.2 Charge defects

Another less intuitive broadening mechanism is the frequency shift caused by inhomogeneous electric field gradients in the crystal. Due to the time-reversal symmetry of Kramers doublets, electric fields do not induce any Stark shift (equivalent of the Zeeman effect with an electric field). However, when a magnetic field is applied, this time-reversal symmetry is broken and magneto-electric interactions with the electron spin may induce shifts in the **g**-tensor [Kie66]. Indeed, Mims and Gillen show that when the magnetic field $\boldsymbol{B_0}$ is applied in the (a, b) plane, the c-axis component E_c of an electric field lifts the degeneracy of the g-factor $g_\perp$, while electric fields applied perpendicular to c have no effect. If the magnetic field makes an angle φ from the crystal a-axis, the shift in the g-factor can be expressed as

$$\delta g_\perp^2 = 2g_\perp \delta g_\perp = \alpha \sin(2\varphi - 2\varphi_0) E_c, \tag{2.47}$$

where α and φ are constants which depend on the Stevens operators of the ion and are therefore ion-dependent. In particular φ_0 corresponds to the angle where this electric field sensitivity vanishes. In the case of Er^{3+}:$CaWO_4$, $\alpha = (11 \pm 0.6) \times 10^{-6}$ $(V/cm)^{-1}$ and $\varphi_0 = 31 \pm 1°$ [Mim65].

The shift in resonance frequency is then

$$\delta\omega = \delta g_\perp \frac{\mu_B}{\hbar} B_0, \tag{2.48}$$

yielding the sensitivity of the spin-transition frequency to electric fields as

$$\frac{\partial\omega}{\partial E_c} = \frac{\alpha \sin(2\varphi - 2\varphi_0)}{2g_\perp} \frac{\mu_B}{\hbar} B_0. \tag{2.49}$$

This sensitivity has been demonstrated experimentally as shown in Figure 2.11 when applying an external electric field along the c-axis.

Now, if each of the erbium ion sees a random electric field of the order of ΔE_c along the c-axis, the FWHM linewidth of the spin-ensemble broadens such that

$$\Gamma_{\text{inh}} \sim \Gamma_{\text{min}} + \left| \frac{\partial\omega}{\partial E_c} \right| \Delta E_c. \tag{2.50}$$

Mims and Gillen estimate the typical electric field to be of the order of 50 kV/cm [MG66].

We will see below that this mechanism is the dominant source of inhomogeneous broadening in our sample, as was the case in [MG66]. The existence of inhomogeneous electric fields in $CaWO_4$ crystals is possibly linked to the charge compensation effects already discussed earlier.

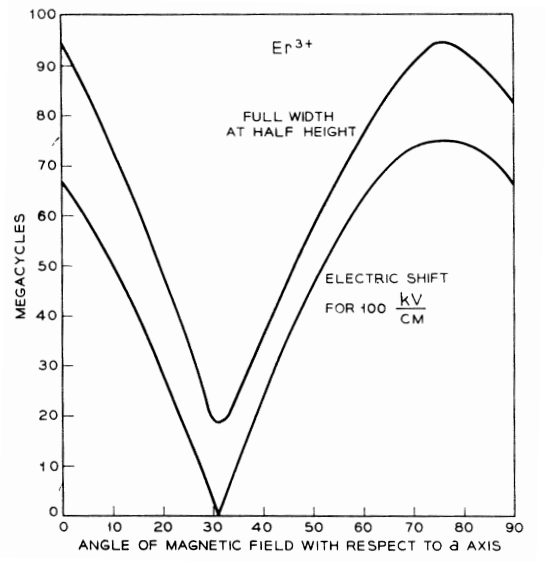

Figure 2.11 – **Inhomogeneous linewidth of erbium ions in $CaWO_4$.** This figure comes from [MG66] The top solid line shows the measured inhomogeneous linewidth, $\Gamma_{\text{inh}}/2\pi$ in MHz, of Er^{3+}:$CaWO_4$ as a function of φ. The magnetic field is applied in the (a, b)-plane and makes an angle φ from the a-axis. The erbium concentration is $c = 4 \times 10^{17}$ cm^{-3}. The bottom solid line is the measured resonance frequency shift (in absolute value) with the same magnetic field conditions and when an electric field of 100 kV/cm is applied along c. Electric fields along a and b have no effect when $\boldsymbol{B_0}$ is in the (a, b)-plane.

Chapter 3

Electron spin resonance with quantum circuits

The technique used in this work to detect electron spins in $CaWO_4$ is electron spin resonance (ESR) spectroscopy, also called electron paramagnetic resonance (EPR) spectroscopy. It consists in applying a static magnetic field to the sample, inserted in a microwave resonator. When the electron spin transition is resonant with the detection resonator, the spin can absorb and emit microwave energy.

One specificity of our experiments is to use a superconducting planar resonator and superconducting amplifiers to detect the spin signal. This has been shown to yield a high sensitivity in recent experiments performed in our group with donors in silicon [Bie+16b; Pro+17].

3.1 Superconducting microwave resonators

A schematic representation of our resonator design is shown in Figure 3.1b. A capacitor (in blue) is shunted by a wire that acts as an inductor (in red). They are patterned on top of the $CaWO_4$ sample. To the representation of this LC resonator must also be added a parallel resistance which accounts for internal losses (see Figure 3.1a for the schematics).

3.1.1 LC resonator: classical modeling

In the experiments presented here, the resonators are probed in two different ways as shown in Figure 3.2:

- in part II, the $CaWO_4$ sample is installed in a copper box. An antenna placed into the box is capacitively coupled to the resonator. This resonator is probed in **reflection** via one port.
- in part III, the resonator is capacitively coupled to a transmission line that is patterned on the sample and connected to a microwave printed circuit board (PCB). It is probed in **transmission** via two ports with a geometry called **hanger geometry**.

The modeling of these two ways of probing the resonator by the outside is shown in Figure 3.3a. The RLC resonator is capacitively coupled with capacitance $C_c \ll C$ to semi-infinite lines of impedance Z_c which is typically 50 Ω. In the reflection type measurement, there is one single port and the switch is open, while in the hanger type measurement, there are two ports, corresponding to the two sides of the 50 Ω feedline, and the switch is closed.

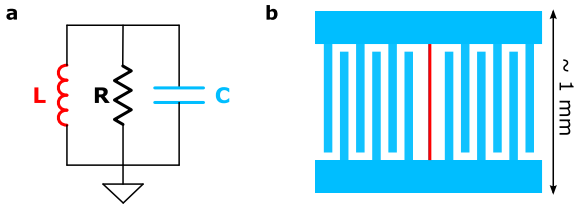

Figure 3.1 – **LC resonator. a.** Schematics of an RLC parallel resonator. **b.** Typical physical implementation. The design includes a capacitor (in blue) in parallel with an inductance (in red). The parallel resistance R comes from internal losses of the material on which the resonator is patterned.

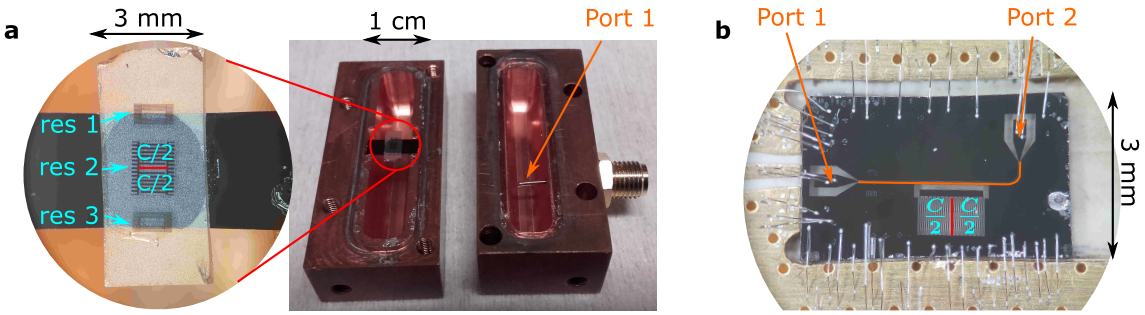

Figure 3.2 – **Physical implementations of LC-circuits. a.** Resonator design for part II. Three resonators are patterned on the $CaWO_4$ sample which is placed inside a 3D copper box with a copper pin probing the resonator. **b.** Resonator design for part III. One resonator is patterned on the $CaWO_4$ sample, surrounded by a ground plane and a transmission line (in orange) with two ports allowing to probe the resonator.

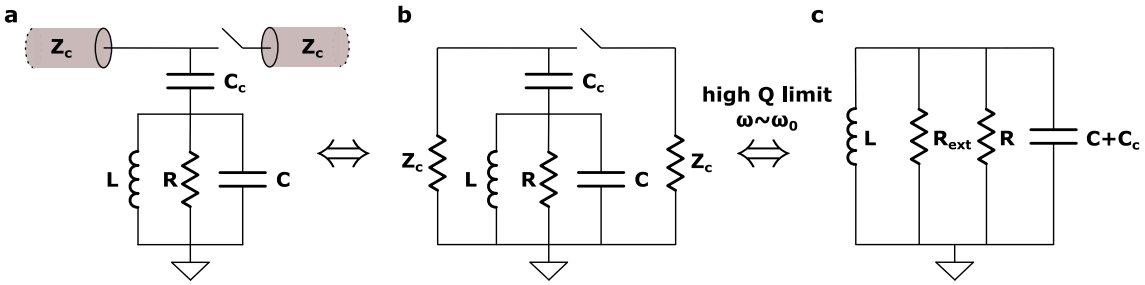

Figure 3.3 – **Equivalent RLC circuit when probed by the outside. a.** RLC circuit connected to the outside by a capacitor C_c and one or two semi-infinite lines of impedance Z_c, depending whether the resonator design is probed in reflection or by shunting a transmission line (hanger geometry, switch closed). **b.** Equivalent circuit when no input voltage is applied to any port. **c.** Equivalent circuit in the high Q limit and in the vicinity of the resonance frequency.

3.1.1.1 Equivalent RLC circuit

The equivalent circuit (in the undriven case) is shown in Figure 3.3b. The coupling of the LC resonator to transmission lines modifies slightly the frequency $\omega_0 = 1/\sqrt{LC}$ and impedance $Z_0 = \sqrt{L/C}$ of the bare RLC circuit.

The total impedance of this circuit is

$$\begin{aligned}\frac{1}{Z_t} &= \frac{1}{R} + iC\omega + \frac{1}{iL\omega} + \frac{1}{Z'_c + \frac{1}{iC\omega}} \\ &= \frac{1}{R} + \frac{Z'_c C_c^2 \omega^2}{1 + (Z'_c C_c \omega)^2} + i\left[\left(C + \frac{C_c}{1 + (Z'_c C_c \omega)^2}\right)\omega - \frac{1}{L\omega}\right]\end{aligned} \tag{3.1}$$

where $Z_c' = Z_c$ in the reflection measurement and $Z_c' = Z_c/2$ in the hanger-type measurement.

In general, $Z_c' C_c \omega \ll 1$, corresponding to the high quality factor limit. Moreover, in the vicinity of ω_0, this impedance can be seen associated to an $R'L'C'$ parallel circuit with

$$\begin{aligned} L' &= L \\ C' &= C + \frac{C_c}{1 + (Z_c' C_c \omega_0)^2} \sim C + C_c \\ \frac{1}{R'} &= \frac{1}{R} + \frac{1}{R_{\text{ext}}} \\ R_{\text{ext}} &= Z_c' \left[1 + \frac{1}{(Z_c' C_c \omega_0)^2} \right] \sim \frac{1}{Z_c' (C_c \omega_0)^2} \end{aligned} \tag{3.2}$$

The resonance frequency of the isolated resonator is seen to be slightly modified, $\omega_0' \sim 1/\sqrt{L(C + C_c)}$, as well as its impedance, $Z_0' \sim \sqrt{L/(C + C_c)}$. Such a parallel $R'L'C'$-circuit can be characterized by a quality factor $Q = R'\sqrt{C'/L'}$ describing how slowly energy stored in the resonator will be dissipated in the environment [Poz11]. This quality factor is related to the energy damping rate $\kappa_t = \omega_0'/Q$, which has two distinct contributions: the internal damping rate $\kappa_{\text{int}} = \omega_0'/Q_{\text{int}} = \omega_0'/R \times \sqrt{L'/C'}$ and the coupling rate $\kappa_c = \omega_0'/Q_c = \omega_0'/R_{\text{ext}} \times \sqrt{L'/C'}$. We note that in the hanger-type measurement, the coupling rate κ_c is twice smaller than in the reflection measurement.

In the following, we keep the notations ω_0 and Z_0 for characterising the resonator, which take into account this renormalization by the transmission line.

3.1.1.2 Scattering matrix coefficients

These resonators are probed by sending an input microwave power via one of the ports and measuring either the reflected signal or the transmitted signal to another port. The reflection and transmission coefficients are given by a scattering matrix which can be measured using a vector network analyzer (VNA).

For a one port system, it is simply defined as

$$V_1^- = S_{11} V_1^+. \tag{3.3}$$

For a two port system, the scattering matrix is a 2×2 matrix [Poz11]

$$\begin{pmatrix} V_1^- \\ V_2^- \end{pmatrix} = \begin{pmatrix} S_{11} & S_{12} \\ S_{21} & S_{22} \end{pmatrix} \begin{pmatrix} V_1^+ \\ V_2^+ \end{pmatrix}, \tag{3.4}$$

where $V_i^+ = (V_i + Z_c I_i)/2$ is the incident voltage on port i and $V_i^- = (V_i - Z_c I_i)/2$ is the reflected voltage from port i (see Figure 3.4). Here the resonator dimensions are small compared to the wavelength and all propagation effects are neglected.

The scattering coefficients are defined by

$$S_{ij} = \left. \frac{V_i^-}{V_j^+} \right|_{V_{k \neq j}^+ = 0} \tag{3.5}$$

It can be shown (see [Poz11; Che+21a] and Appendix A) that

- for reflection measurements,

$$S_{11} \approx 1 - \frac{2Q/Q_c}{1 + 2iQ(\omega - \omega_0)/\omega_0} \approx 1 - \frac{2\kappa_c}{\kappa_t + 2i(\omega - \omega_0)}, \tag{3.6}$$

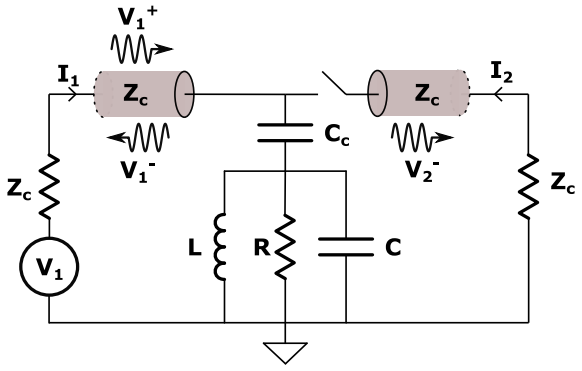

Figure 3.4 – **Probing a resonator from port 1**

- for hanger measurements,

$$S_{21} \approx 1 - \frac{Q/Q_c}{1 + 2iQ(\omega - \omega_0)/\omega_0} \approx 1 - \frac{\kappa_c}{\kappa_t + 2i(\omega - \omega_0)}, \tag{3.7}$$

where the $\approx$ sign means that this approximation is valid in the limit of high quality factors and in the vicinity of the resonance frequency.

In practice, the measured reflection and transmission coefficients always include a background which comes from the whole setup, in particular from all the attenuation and amplification in the line and the finite length of the wiring. This background multiplies to the previous ideal scattering coefficients such that the measured coefficient is $S_{\text{real}} = \text{Background} \times S_{\text{ideal}}$ and it is taken into account in the fit of the resonance.

3.1.2 Quantum description

We now turn to the quantum-mechanical description of a resonator coupled to a measurement line.

3.1.2.1 Hamiltonian of the isolated LC circuit

Here, we go back to the isolated parallel LC-circuit of Figure 3.1, disregarding its internal resistance R. This circuit can be quantized with two conjugate operators, the flux in the inductance $\hat{\Phi}$ and the charge accumulated in the capacitor $\hat{Q}$, with $[\hat{\Phi}, \hat{Q}] = i\hbar$ [Dev+95].

The Hamiltonian of this resonator is

$$\mathcal{H}_r = \frac{\hat{Q}^2}{2C} + \frac{\hat{\Phi}^2}{2L}. \tag{3.8}$$

This can be rewritten using the ladder operators

$$\mathcal{H}_r = \hbar\omega_0 \left(\hat{a}^\dagger \hat{a} + \frac{1}{2}\right), \tag{3.9}$$

where the creation and annihilation operators are

$$\begin{aligned} \hat{a}^\dagger &= \frac{1}{\sqrt{2\hbar Z_0}}(\hat{\Phi} - iZ_0\hat{Q}) \\ \hat{a} &= \frac{1}{\sqrt{2\hbar Z_0}}(\hat{\Phi} + iZ_0\hat{Q}), \end{aligned} \tag{3.10}$$

with $\omega_0 = 1/\sqrt{LC}$ and $Z_0 = \sqrt{L/C}$. The ladder operators $\hat{a}$ and $\hat{a}^\dagger$ satisfy the usual commutation relation $[\hat{a}, \hat{a}^\dagger] = 1$. The eigenstates of $\hat{a}$ are the coherent states $|\alpha\rangle$.

This Hamiltonian has eigenvalues $E_n = \hbar\omega_0(n+1/2)$, where n is the number of photons in the resonator and its eigenstates are the Fock states $|n\rangle$.

The voltage and current in the resonator are linked to the conjugate variables $\hat{\Phi}$ and $\hat{Q}$ such that

$$\begin{aligned} \hat{V} = \frac{\hat{Q}}{C} &= i\omega_0\sqrt{\frac{\hbar Z_0}{2}}(\hat{a}^\dagger - \hat{a}) = i\delta V(\hat{a}^\dagger - \hat{a}) \\ \hat{I} = \frac{\hat{\Phi}}{L} &= \omega_0\sqrt{\frac{\hbar}{2Z_0}}(\hat{a}^\dagger + \hat{a}) = \delta I(\hat{a}^\dagger + \hat{a}) \end{aligned} \tag{3.11}$$

where $\delta V = \omega_0\sqrt{\hbar Z_0/2}$ and $\delta I = \omega_0\sqrt{\hbar/(2Z_0)}$ are the root-mean-square (rms) vacuum fluctuations of the voltage and current. These voltage and current induce electric and magnetic fields in the resonator which can be described as

$$\begin{aligned} \hat{\boldsymbol{E}}_\mathbf{1}(\boldsymbol{r}) &= i\boldsymbol{\delta E}(\boldsymbol{r})(\hat{a}^\dagger - \hat{a}) \\ \hat{\boldsymbol{B}}_\mathbf{1}(\boldsymbol{r}) &= \boldsymbol{\delta B}(\boldsymbol{r})(\hat{a}^\dagger + \hat{a}) \end{aligned} \tag{3.12}$$

These quantities are spatially dependent and the electric field will be mostly produced between the capacitor plates while the magnetic field will be generated around the inductance wire. $\boldsymbol{\delta E}(\boldsymbol{r})$ and $\boldsymbol{\delta B}(\boldsymbol{r})$ are rms vacuum fluctuations of the electric and magnetic fields at position $\boldsymbol{r}$.

3.1.2.2 Input-output theory

The classical scattering matrix approach of Section 3.1.1.2 has a quantum equivalent with the input-output formalism developed by Gardiner and Collet [CG84; GC85] describing the evolution of the intra-resonator field $\hat{a}$ as a function of the input and output fields on port i, $\hat{a}_{\text{in},i}$ and $\hat{a}_{\text{out},i}$. These operators can be seen as the quantum analogs of the classical input and output waves $a_{\text{in},i} = V_i^+/\sqrt{Z_c} = (V_i + Z_c I_i)/(2\sqrt{Z_c})$ and $a_{\text{out},i} = V_i^-/\sqrt{Z_c} = (V_i - Z_c I_i)/(2\sqrt{Z_c})$.

Here we need to distinguish the two cases of reflection and hanger measurements.

Reflection measurement

For a resonator probed with a single port, the master equation of the intra-resonator field is

$$\frac{\partial\hat{a}}{\partial t}(t) = \frac{i}{\hbar}[\mathcal{H}_r, \hat{a}(t)] - \frac{\kappa_t}{2}\hat{a}(t) - \sqrt{\kappa_c}\hat{a}_{\text{in}}(t) - \sqrt{\kappa_{\text{int}}}\hat{a}_{\text{int}}(t), \tag{3.13}$$

[Che+21b], where $\kappa_t = \kappa_c + \kappa_{\text{int}}$. $\hat{a}_{\text{int}}$ can be seen as an input field which is actually the vacuum state and arrives at an additional port to account for the internal losses of the resonator. Moreover, this master equation comes along with a continuity relation at the input of the resonator stating that

$$\hat{a}_{\text{in}}(t) = \hat{a}_{\text{out}}(t) + \sqrt{\kappa_c}\hat{a}(t). \tag{3.14}$$

In our experiments, the drive field is coherent and can be written as $\hat{a}_{\text{in}}(t) = \alpha_{\text{in}}e^{-i\omega t}$, where $|\alpha_{\text{in}}|^2$ is the number of photon per second at the resonator input and $P = \hbar\omega|\alpha_{\text{in}}|^2$ is the input power.

Rewriting the master equation for the mean intra-resonator field $\alpha(t) = \langle\hat{a}(t)\rangle$ gives

$$\frac{\partial\alpha}{\partial t}(t) = -i\omega_0\alpha(t) - \frac{\kappa_t}{2}\alpha(t) - \sqrt{\kappa_c}\alpha_{\text{in}}(t), \tag{3.15}$$

taking into account that $\langle\hat{a}_{\text{int}}(t)\rangle = 0$.

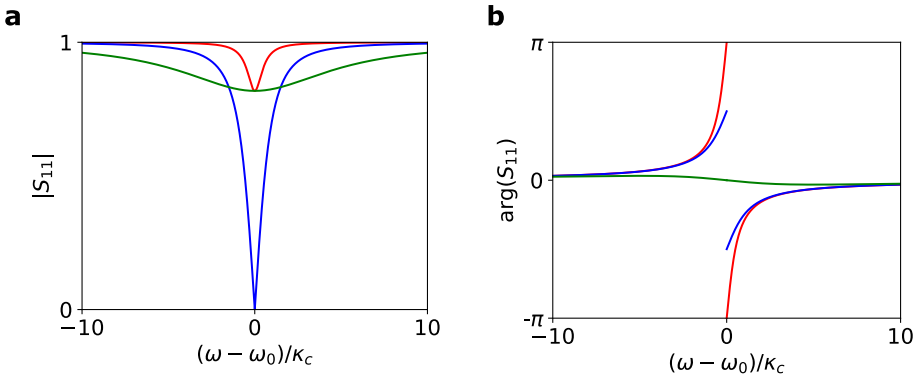

Figure 3.5 – **Calculated reflection coefficient. a.** $|S_{11}|$. **b.** phase of S_{11}. This is computed in three different scenarii: red color corresponds to $\kappa_{\text{int}} = 0.1\kappa_c$, blue to $\kappa_{\text{int}} = \kappa_c$ and green to $\kappa_{\text{int}} = 10\kappa_c$.

Taking the Fourier transform of this expression leads to

$$\alpha(\omega) = -\frac{i\sqrt{\kappa_c}}{(\omega - \omega_0) + i\frac{\kappa_t}{2}}\alpha_{\text{in}}(\omega). \tag{3.16}$$

At resonance, the intra-resonator photon number n is given by

$$n = |\alpha|^2 = \frac{4\kappa_c}{\hbar\omega_0\kappa_t^2}P, \tag{3.17}$$

where $P = \hbar\omega_0|\alpha_{\text{in}}|^2$ is the input power.

Finally the reflection coefficient S_{11} can be calculated as

$$S_{11} = \frac{\alpha_{\text{out}}}{\alpha_{\text{in}}} = \frac{\alpha_{\text{in}} + \sqrt{\kappa_c}\alpha}{\alpha_{\text{in}}} = 1 - \frac{i\kappa_c}{(\omega - \omega_0) + i\frac{\kappa_t}{2}}. \tag{3.18}$$

This is identical to Equation 3.6, with the difference that it is the complex conjugate. This reflection coefficient is computed in Figure 3.5.

Three cases can be distinguished:

- the **over-coupled regime** where $\kappa_c \gg \kappa_{\text{int}}$ hence $\kappa_t \sim \kappa_c$. The reflection coefficient is approximately 1 while the phase undergoes a 2π phase shift at resonance.
- the **critical coupling condition** where $\kappa_c \sim \kappa_{\text{int}}$. The reflection coefficient goes to 0 at resonance while the phase undergoes a π discontinuity.
- the **under-coupled regime** where $\kappa_c \ll \kappa_{\text{int}}$, hence $\kappa_t \sim \kappa_{\text{int}}$. Then the magnitude and phase show a small dip and shift respectively, which width is determined by κ_{int}.

Hanger transmission measurement

For a resonator probed with two ports in hanger mode, the master equation of the intra-resonator field is [Che+21b]

$$\frac{\partial\hat{a}}{\partial t}(t) = \frac{i}{\hbar}[\mathcal{H}_r, \hat{a}(t)] - \frac{\kappa_t}{2}\hat{a}(t) - \sqrt{\frac{\kappa_c}{2}}(\hat{a}_{\text{in},1}(t) + \hat{a}_{\text{in},2}(t)) - \sqrt{\kappa_{\text{int}}}\hat{a}_{\text{int}}(t) \tag{3.19}$$

The two continuity relations at the input of the resonator are

$$\begin{aligned}\hat{a}_{\text{out},2}(t) &= \hat{a}_{\text{in},1}(t) + \sqrt{\frac{\kappa_c}{2}}\hat{a}(t)\\ \hat{a}_{\text{out},1}(t) &= \hat{a}_{\text{in},2}(t) + \sqrt{\frac{\kappa_c}{2}}\hat{a}(t).\end{aligned} \tag{3.20}$$

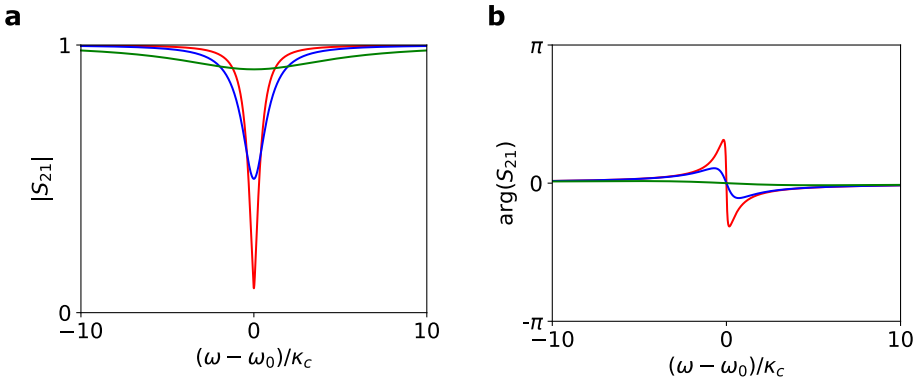

Figure 3.6 – **Calculated transmission coefficient in the hanger geometry. a.** $|S_{21}|$. **b.** phase of S_{21}. This is computed in three different scenarii: red color corresponds to $\kappa_{\text{int}} = 0.1\kappa_c$, blue to $\kappa_{\text{int}} = \kappa_c$ and green to $\kappa_{\text{int}} = 10\kappa_c$.

At resonance, similarly to the reflection case, the intra-resonator photon number n when the resonator is only driven from port 1 is given by

$$n = |\alpha|^2 = \frac{2\kappa_c}{\hbar\omega_0\kappa_t^2}P, \tag{3.21}$$

where $P = \hbar\omega_0|\alpha_{\text{in},1}|^2$ is the input power at port 1.

Also, the transmission coefficient S_{21} can be calculated

$$S_{21} = \left.\frac{\alpha_{\text{out},2}}{\alpha_{\text{in},1}}\right|_{\alpha_{\text{in},2}=0} = \frac{\alpha_{\text{in},1} + \sqrt{\kappa_c/2}\alpha}{\alpha_{\text{in},1}} = 1 - \frac{i\kappa_c/2}{(\omega-\omega_0) + i\frac{\kappa_t}{2}}. \tag{3.22}$$

This is identical to Equation 3.7, with the difference that it is the complex conjugate. This transmission coefficient of the hanger geometry is computed in Figure 3.6.

Three cases can be distinguished, which differ slightly from the reflection case:

- the **over-coupled regime** where $\kappa_c \gg \kappa_{\text{int}}$ hence $\kappa_t \sim \kappa_c$. The transmission coefficient goes to nearly 0 at resonance while the phase shifts at resonance.
- the **critical coupling condition** where $\kappa_c \sim \kappa_{\text{int}}$. The transmission coefficient goes to 0.5 at resonance while the phase shift at resonance is reduced.
- the **under-coupled regime** where $\kappa_c \ll \kappa_{\text{int}}$, hence $\kappa_t \sim \kappa_{\text{int}}$. The magnitude and phase show a small dip and shift respectively, which width is determined by κ_{int}.

3.2 Coupling a superconducting circuit to one spin

3.2.1 System Hamiltonian

Here we consider a LC-circuit coupled to an electron spin $S = 1/2$. Interactions with the environment are neglected in a first step.

The total Hamiltonian describing this isolated system is

$$\mathcal{H} = \mathcal{H}_r + \mathcal{H}_{spin} + \mathcal{H}_{r-s}, \tag{3.23}$$

where $\mathcal{H}_{r-s}$ accounts for the interaction between the resonator and the spin.

Let's detail each of the terms:

- As described in Section 3.1.2.1, the resonator Hamiltonian is

$$\mathcal{H}_r = \hbar\omega_0 \left(\hat{a}^\dagger \hat{a} + \frac{1}{2}\right). \tag{3.24}$$

- The spin has two energy levels, its ground state $|g\rangle$ and its excited state $|e\rangle$, separated by the Zeeman energy $\hbar\omega_s = \mathrm{g}\mu_B B_0$ where g is an effective g-factor depending on the field orientation.

  The Zeeman Hamiltonian of this two-level system can be written using the Pauli matrices $(\hat{\sigma}_x, \hat{\sigma}_y, \hat{\sigma}_z) = 2 \times \hat{\mathbf{S}}$ such that

$$\mathcal{H}_{spin} = \mu_B \boldsymbol{B_0} \cdot \mathbf{g} \cdot \hat{\boldsymbol{S}} = \hbar \frac{\omega_s}{2} \hat{\sigma}_z, \tag{3.25}$$

  where z is the spin quantization axis. Note that due to the **g**-tensor anisotropy, the spin quantization axis is not necessarily aligned with the magnetic field (see Section 2.2.2).

- The interaction term comes from the magnetic coupling of the spin magnetic moment with the oscillating field $\hat{\boldsymbol{B}}_\mathbf{1}$ which is generated by the current flowing in the resonator inductance wire (see Section 3.1.2.1). The interaction Hamiltonian is thus

$$\mathcal{H}_{r-s} = \mu_B \hat{\boldsymbol{B}}_\mathbf{1} \cdot \mathbf{g} \cdot \hat{\boldsymbol{S}} = \mu_B \boldsymbol{\delta B}(\mathbf{r}) \cdot \mathbf{g} \cdot \hat{\boldsymbol{S}} (\hat{a} + \hat{a}^\dagger). \tag{3.26}$$

Expanding the scalar product on the basis $(|g\rangle, |e\rangle)$ gives

$$\mathcal{H}_{r-s} = \hbar(\hat{a} + \hat{a}^\dagger)[\alpha_e |e\rangle \langle e| + \alpha_g |g\rangle \langle g| + g_0 \hat{\sigma}_+ + g_0^* \hat{\sigma}_-], \tag{3.27}$$

where

$$\begin{aligned} \alpha_e &= \frac{\mu_B}{\hbar} \boldsymbol{\delta B} \cdot \mathbf{g} \cdot \langle e| \hat{\boldsymbol{S}} |e\rangle, \qquad \alpha_g = \frac{\mu_B}{\hbar} \boldsymbol{\delta B} \cdot \mathbf{g} \cdot \langle g| \hat{\boldsymbol{S}} |g\rangle \\ g_0 &= \frac{\mu_B}{\hbar} \boldsymbol{\delta B} \cdot \mathbf{g} \cdot \langle e| \hat{\boldsymbol{S}} |g\rangle, \qquad g_0^* = \frac{\mu_B}{\hbar} \boldsymbol{\delta B} \cdot \mathbf{g} \cdot \langle g| \hat{\boldsymbol{S}} |e\rangle \end{aligned} \tag{3.28}$$

To treat these terms, the basis $(|g\rangle, |e\rangle)$ can first be modified such that $g_0 = g_0^*$. Moreover, using the interaction picture and applying the rotating wave approximation leads to [HR06]

$$\mathcal{H}_{r-s} = \hbar g_0 (\hat{\sigma}_+ \hat{a} + \hat{\sigma}_- \hat{a}^\dagger). \tag{3.29}$$

Finally, the total Hamiltonian is transformed into the so-called Jaynes-Cummings Hamiltonian

$$\mathcal{H} = \frac{\hbar\omega_s}{2} \hat{\sigma}_z + \hbar\omega_0 \left(\hat{a}^\dagger \hat{a} + \frac{1}{2}\right) + \hbar g_0 (\hat{\sigma}_+ \hat{a} + \hat{\sigma}_- \hat{a}^\dagger). \tag{3.30}$$

Order of magnitude

To give an order of magnitude of g_0, we first need to approximate the vacuum fluctuations of the magnetic field $\hat{\boldsymbol{B}}_\mathbf{1}$. This can be done using Biot-Savart law, which is valid in the near-field regime, where a spin is in the vicinity of the inductance wire and their distance is smaller than the field wavelength. Then, if the wire is infinitely narrow and infinitely long [Gri99]

$$\hat{\boldsymbol{B}}_\mathbf{1}(\mathbf{r}) = \mu_0 \frac{\hat{I}}{2\pi r} \boldsymbol{e_\theta}, \tag{3.31}$$

where $\boldsymbol{e_\theta}$ is the azimuthal unit vector at the spin location in the cylindrical coordinate system. This enables us to relate the vacuum fluctuations of the magnetic field to those of the current

$$|\boldsymbol{\delta B}(\boldsymbol{r})| = \mu_0 \frac{\delta I}{2\pi r} = \mu_0 \frac{\omega_0}{2\pi r} \sqrt{\frac{\hbar}{2Z_0}} \tag{3.32}$$

Let's consider an electron spin with isotropic g= 2, distant from the wire by a distance $r \sim 1$ μm, and a resonator with $\omega_0/2\pi \sim 7$ GHz and $Z_0 \sim 50$ Ω. The coupling strength of this spin to the resonator is

$$\frac{g_0}{2\pi} = \frac{\mathrm{g}\mu_B}{h}\delta B \langle e|\hat{S}|g\rangle = \frac{\mathrm{g}\mu_B}{h}\mu_0 \frac{\omega_0}{2\pi r}\sqrt{\frac{\hbar}{2Z_0}}0.5 \sim 100 \text{ Hz}. \tag{3.33}$$

This approximation of the vacuum fluctuations of the field using Biot-Savart law gives a rough scaling of the coupling constant with the distance r between the spin and the inductance wire as $\propto 1/r$. This means that g_0 is strongly dependent on the spin location and that it decreases rapidly with the spin distance to the resonator.

3.2.2 Interaction with the environment

In practice, the spin and the resonator both interact with their environment, which needs to be taken in account for describing their dynamics. The resonator energy is damped with rate κ_t and the spin looses its coherence with rate $\Gamma_h = 2/T_2$ (see Section 2.5). Two regimes can be distinguished:

- if $g_0 \gg \kappa_t$ & Γ_h, coherent oscillations induced by the Jaynes-Cummings Hamiltonian can take place between the spin and the cavity. This is the strong coupling regime.
- if $g_0 \ll \kappa_t$ or Γ_h, the system is damped before coherent oscillations can take place. This is the weak coupling regime.

As discussed above, for a single spin coupled to a resonator, $g_0/2\pi \sim 100$ Hz $\ll \kappa_t/2\pi \sim$ 100 kHz-1 MHz; we are therefore in the weak spin-resonator coupling regime. The rest of this section will focus on the consequences of the weak coupling regime on the spin dynamics.

3.2.2.1 Purcell effect

A first consequence of the weak coupling regime is that the resonator enhances the spontaneous photon emission by the spin via the Purcell effect. A simplified derivation can be found in [HR06]. The spin emits photons with the Purcell rate,

$$\Gamma_P(\Delta) = \frac{g_0^2\kappa_t}{\Delta^2 + (\kappa_t/2)^2}. \tag{3.34}$$

where $\Delta = \omega_0 - \omega_s$. Spin measurements are mostly performed at resonance, such that $\Gamma_P(\Delta = 0) = 4g_0^2/\kappa_t$. Therefore, increasing Γ_P requires increasing the quality factor of the resonator. With $g_0/2\pi \sim 100$ Hz and $\kappa_t/2\pi \sim 100$ kHz, one gets $\Gamma_P \sim 3$ s^{-1}. This is twelve orders of magnitude larger than free-space radiation, and close to the non-radiative relaxation rates discussed earlier (see Section 2.4.3). Increasing g_0 further should therefore enable to reach the Purcell regime for REIs, as we will see later in this manuscript. The Purcell enhanced relaxation of an electron spin in a solid coupled to a superconducting micro-resonator has been observed for the first time in [Bie+16a] with donors in silicon (see Figure 3.7).

3.2.2.2 Bloch equations and magnetic resonance

Another consequence of weak coupling is that the entanglement between the spin and the photon dynamics can be neglected. In practice, it means that the spin dynamics can be computed using only the mean field value of $\hat{a}$ which is replaced by a classical variable

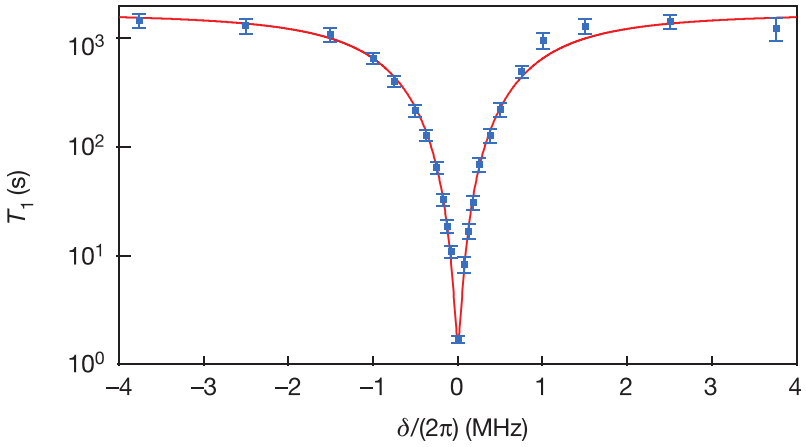

Figure 3.7 – **Demonstration of the Purcell effect for bismuth electron spins in silicon.** This figure is taken from [Bie+16a] The blue dots show the measured relaxation time T_1 as a function of δ, the frequency detuning between the spins and the resonator. The solid red line is a fit with $T_1^{-1} = (\Gamma_P(\delta) + \Gamma_{NR})^{-1}$, where $\Gamma_P(\delta) = \kappa_t g_0^2/(\kappa_t^2/4 + \delta^2)$ is the Purcell decay rate and Γ_{NR} is the non-radiative decay rate. The fit yields $\Gamma_{NR}^{-1} = 1600$ s. The measured T_1 at $\delta = 0$ is 1.7 s.

$\alpha e^{-i\omega_0 t}$. The Hamiltonian of the spin dynamics in the rotating frame at frequency ω_0 is thus

$$\mathcal{H} = -\frac{\hbar\Delta}{2}\hat{\sigma}_z + \hbar g_0(\alpha\hat{\sigma}_+ - \alpha^*\hat{\sigma}_-), \tag{3.35}$$

where $\Delta = \omega_0 - \omega_s$. Note that in the experiment, rotating fields $\alpha e^{-i\omega_0 t}$ are replaced by oscillating fields $2\alpha\cos(\omega_0 t)$ [Abr61]. The cosine function can be decomposed in two fields rotating in opposite directions $\pm\omega_0$. However, in the Hamiltonian written above, only the slow frequency part, rotating at $\omega_s - \omega_0$, will affect the system dynamics and the $\omega_s + \omega_0$ frequency component can be neglected (this is again the rotating wave approximation). Therefore, oscillating instead of rotating fields do not change any conclusion achieved here.

Computing the spin dynamics is achieved in the framework of the so-called master equation, which describes the evolution of the spin density matrix ρ_s,

$$\dot{\rho}_s = -\frac{i}{\hbar}[\mathcal{H}, \rho_s] + \sum_\alpha L_\alpha \rho_s L_\alpha^\dagger - \frac{1}{2}(L_\alpha^\dagger L_\alpha \rho_s + \rho_s L_\alpha^\dagger L_\alpha), \tag{3.36}$$

where each dissipation channel α is taken into account by introducing a jump operator L_α. Note that this description assumes that the spin environment is markovian which implies that any relaxation process is exponential. This is usually inaccurate to model spin dephasing as we will see in Chapter 4. There are three dissipation channels for the spins:

- **non-radiative relaxation**: The phonon jump operators are $L_{1,-} = \sqrt{\Gamma_1(1+n_{ph})}\hat{\sigma}_-$ and $L_{1,+} = \sqrt{\Gamma_1 n_{ph}}\hat{\sigma}_+$. Γ_1 is the direct phonon relaxation rate at zero temperature, which corresponds to the rate of spontaneous emission of a phonon. $n_{ph} = 1/(e^{\hbar\omega_s/(k_B T_{ph})} - 1)$ is the average thermal phonon number per mode at the spin frequency ω_s.

- **radiative relaxation**: The Purcell jump operators, derived by adiabatic elimination of the resonator, are $L_{P,-} = \sqrt{\Gamma_P(\Delta)(1+n_{th})}\hat{\sigma}_-$ and $L_{P,+} = \sqrt{\Gamma_P(\Delta) n_{th}}\hat{\sigma}_+$ [JM12b; WWM05]. $n_{th} = 1/(e^{\hbar\omega_0/(k_B T_0)} - 1)$ is the average thermal photon number per mode at frequency ω_0. In general, the spin and resonator frequencies are close as well as the phonon and photon bath temperature so $n_{ph} \sim n_{th}$. We will assume that they are equal in the following.

- **dephasing** $L_2 = \sqrt{\Gamma_\phi/2}\hat{\sigma}_z$. This jump operator describes the pure spin dephasing with rate $\Gamma_\phi = 1/T_\phi$.

The spin density matrix ρ_s can be expressed as a function of the magnetization vector $\boldsymbol{M}$: $\rho_s = 1/2(\mathbb{1} + \boldsymbol{M}.\hat{\boldsymbol{\sigma}})$. Note that $M_i = \mathrm{Tr}[\hat{\rho}_s\hat{\sigma}_i] = \langle\hat{\sigma}_i\rangle$.

Solving the master equation of Equation 3.36 results in

$$\dot{\boldsymbol{M}} = \begin{pmatrix} \langle\dot{\hat{\sigma}}_x\rangle \\ \langle\dot{\hat{\sigma}}_y\rangle \\ \langle\dot{\hat{\sigma}}_z\rangle \end{pmatrix} = \begin{pmatrix} 0 & \Delta & -2g_0\,\mathrm{Im}[\alpha] \\ -\Delta & 0 & -2g_0\,\mathrm{Re}[\alpha] \\ 2g_0\,\mathrm{Im}[\alpha] & 2g_0\,\mathrm{Re}[\alpha] & 0 \end{pmatrix} \boldsymbol{M} - \begin{pmatrix} \Gamma_\perp\langle\hat{\sigma}_x\rangle \\ \Gamma_\perp\langle\hat{\sigma}_y\rangle \\ \Gamma_\parallel\left(\langle\hat{\sigma}_z\rangle + \frac{1}{1+2n_{th}}\right) \end{pmatrix} \tag{3.37}$$

where the longitudinal relaxation time is $\Gamma_\parallel = [\Gamma_1+\Gamma_P](1+2n_{th}) = 1/T_1$ while the transverse relaxation time is $\Gamma_\perp = \Gamma_\phi+\Gamma_\parallel/2 = 1/T_2$. We note that $1+2n_{th} = \coth\left[\hbar\omega_0/(2k_BT_0)\right]$ and we recover the temperature dependence of the spin relaxation rate of Equation 2.39. The term $\langle\hat{\sigma}_z\rangle + 1/(1+2n_{th})$ accounts for the fact that the z-component of the magnetization vector does not decay towards zero but towards the thermal equilibrium state.

This differential equation for the magnetization vector corresponds to the classical **Bloch equations** with the slight difference that the Purcell effect, which originates from the quantum interaction between the spin and the resonator, has been included in the spin longitudinal relaxation. Let's simplify Equation 3.37 in particular cases:

- If the relaxation is neglected and $\alpha = 0$, we have

$$\dot{\boldsymbol{M}} = \begin{pmatrix} 0 & \Delta & 0 \\ -\Delta & 0 & 0 \\ 0 & 0 & 0 \end{pmatrix} \boldsymbol{M} \tag{3.38}$$

  $\boldsymbol{M}$ rotates around $-z$ at frequency Δ (in blue in Figure 3.8).

- If the relaxation is neglected, $\Delta = 0$ and α is real, we have

$$\dot{\boldsymbol{M}} = \begin{pmatrix} 0 & 0 & 0 \\ 0 & 0 & -2g_0\alpha \\ 0 & 2g_0\alpha & 0 \end{pmatrix} \boldsymbol{M} \tag{3.39}$$

  $\boldsymbol{M}$ rotates around $-x$ at frequency $2g_0\alpha$ (in red in Figure 3.8). This is the magnetic resonance condition where the spin magnetic moment is completely reverted by the oscillating field.

- More generally, if the relaxation can be neglected and the axis changed such that α is real,

$$\dot{\boldsymbol{M}} = \begin{pmatrix} 0 & \Delta & 0 \\ -\Delta & 0 & -2g_0\alpha \\ 0 & 2g_0\alpha & 0 \end{pmatrix} \boldsymbol{M} \tag{3.40}$$

  $\boldsymbol{M}$ rotates around the axis $-2g_0\alpha\boldsymbol{e_x} - \Delta\boldsymbol{e_z}$ at frequency $\Omega_R = \sqrt{\Delta^2 + (2g_0\alpha)^2}$ which is the Rabi frequency. These dynamics are completely classical and are the basis of magnetic resonance.

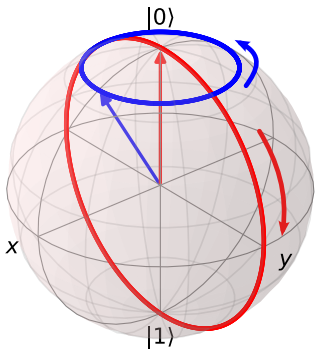

Figure 3.8 – **Spin dynamics on the Bloch sphere.** Bloch sphere with the magnetization vector rotating around $-z$ (blue) where $\alpha = 0$ and with an initial angle from the z-axis of 30° and around $-x$ (red) when $\Delta = 0$ and the magnetization vector is initially along z.

3.2.3 Spin detection through field observables

The variable detected in our measurements is the output-resonator field $\hat{a}_{\text{out}}$. To relate $\hat{a}_{\text{out}}$ to the spins, we go back to the input-output formalism introduced in Section 3.1.2.2. We use Equation 3.13 and Equation 3.19, where the Hamiltonian is now the Jaynes-Cummings Hamiltonian.

In the frame rotating at frequency ω_0 and without any drive term, the differential equation simplifies into

$$\langle \dot{\hat{a}} \rangle = -\frac{\kappa_t}{2}\langle \hat{a} \rangle - ig_0 \langle \hat{\sigma}_- \rangle, \tag{3.41}$$

whose solution is

$$\langle \hat{a}(t) \rangle = -ig_0 \int_{-\infty}^{t} e^{-\frac{\kappa_t}{2}(t-t')} \langle \hat{\sigma}_-(t') \rangle dt'. \tag{3.42}$$

We also note that in the limit of low quality factors, corresponding to the resonator damping rate much faster than the spin dynamics which happen at the Rabi frequency, $\kappa_t \gg \Omega_R$, the exponential term in the integral can be replaced by a Dirac function such that the resonator follows adiabatically the spin dynamics. In this limit,

$$\langle \hat{a}(t) \rangle = -ig_0 \langle \hat{\sigma}_-(t) \rangle. \tag{3.43}$$

Once the intra-resonator mean field value is calculated, the output field is computed using the continuity relation of Equation 3.14 and Equation 3.20. When there is no drive, the mean field value of $\hat{a}_{\text{out}}$ is simply proportional to the mean-field value of $\hat{a}$, with coefficient $\sqrt{\kappa_c}$ in the reflection case and $\sqrt{\kappa_c/2}$ in the hanger case.

This links the output resonator field to the spin state and can be compared to Faraday's law where an oscillating magnetization generates an output electric field. This detection technique is called "inductive detection" of the spin.

3.3 Coupling a superconducting circuit to a spin ensemble

In reality, our measurements address an ensemble of spins. The Jaynes-Cummings Hamiltonian, for a single spin, depends on its frequency ω_s and its coupling strength to the resonator g_0. We saw in Section 2.5 that the spin frequency is actually distributed according to an inhomogeneously broadened lineshape. Moreover, we saw in Section 3.2.1 that the ensemble coupling is also distributed, according to the position of the spin with respect to the resonator. Therefore, when considering an ensemble of N spins, we must consider the frequency ω_k and the coupling g_k of each spin k.

The Jaynes Cummings Hamiltonian becomes the Tavis-Cummings Hamiltonian:

$$\mathcal{H} = \frac{\hbar}{2}\sum_{k=1}^{N}\omega_k\hat{\sigma}_z^{(k)} + \hbar\omega_0\left(\hat{a}^\dagger\hat{a} + \frac{1}{2}\right) + \hbar\sum_{k=1}^{N} g_k\left(\hat{\sigma}_+^{(k)}\hat{a} + \hat{\sigma}_-^{(k)}\hat{a}^\dagger\right). \tag{3.44}$$

3.3.0.1 Modified scattering matrix coefficients

The scattering matrix coefficients described in Section 3.1.2.2 are modified in the presence of the spin ensemble. They can be analytically computed in the limit where the number of excitations in the spin ensemble is small compared to the number of spins, which corresponds to neglecting saturation effects.

In this limit, the spin operators $\hat{\sigma}_\pm^{(k)}$ of Equation 3.44 can be transformed into bosonic operators $\hat{s}_k$ verifying the usual commutation relation for bosons $[\hat{s}_k, \hat{s}_k^\dagger] = 1$. $\hat{\sigma}_-^{(k)}$ is replaced by $\hat{s}_k$, $\hat{\sigma}_+^{(k)}$ by $\hat{s}_k^\dagger$ and $\hat{\sigma}_z^{(k)}$ by $-1 + 2\hat{s}_k^\dagger\hat{s}_k$. This is the Holstein-Primakov approximation which transforms the N spins into harmonic oscillators. With these new operators, the Tavis-Cummings Hamiltonian of Equation 3.44 translates into [KWM11]

$$\mathcal{H} = \hbar\omega_s\sum_{k=1}^{N}\left(\hat{s}_k^\dagger\hat{s}_k - \frac{1}{2}\right) + \hbar\omega_0\left(\hat{a}^\dagger\hat{a} + \frac{1}{2}\right) + \hbar\sum_{k=1}^{N} g_k\left(\hat{s}_k^\dagger\hat{a} + \hat{s}_k\hat{a}^\dagger\right). \tag{3.45}$$

In the case of a reflection measurement, Equation 3.13 can be evaluated again with this Hamiltonian. This gives for the mean intra-resonator field $\alpha(t)$

$$\frac{\partial\alpha}{\partial t}(t) = -\left(i\omega_0 + \frac{\kappa_t}{2}\right)\alpha(t) - i\sum_{k=1}^{N} g_k\langle\hat{s}_k(t)\rangle - \sqrt{\kappa_c}\alpha_{\text{in}}. \tag{3.46}$$

In the same way, the differential equation for the mean value of the spin operator $\hat{s}_k$ is

$$\frac{\partial\langle\hat{s}_k\rangle}{\partial t}(t) = -\left(i\omega_k + \frac{\Gamma_h}{2}\right)\langle\hat{s}_k(t)\rangle - ig_k\alpha(t), \tag{3.47}$$

where $\Gamma_h = 2/T_2$ is the decoherence rate of the individual spins.

The Fourier transform of this equation gives

$$\langle\hat{s}_k(\omega)\rangle = -\frac{ig_k}{i(\omega_k - \omega) + \Gamma_h/2}\alpha(\omega), \tag{3.48}$$

which can be included in the equation for $\alpha(\omega)$,

$$\alpha(\omega) = -\frac{\sqrt{\kappa_c}}{i(\omega_0 - \omega) + \frac{\kappa_t}{2} + \sum_k \frac{g_k^2}{i(\omega_k - \omega) + \Gamma_h/2}}\alpha_{\text{in}}(\omega). \tag{3.49}$$

Finally, the reflection coefficient of Equation 3.18 becomes [Din+11]

$$S_{11} = 1 - \frac{i\kappa_c}{(\omega - \omega_0) + i\frac{\kappa_t}{2} - \sum_k \frac{g_k^2}{(\omega - \omega_k) + i\Gamma_h/2}} = 1 - \frac{i\kappa_c}{(\omega - \omega_0) + i\frac{\kappa_t}{2} - W(\omega)} \tag{3.50}$$

From this equation emerges a new quantity, the ensemble coupling g_{ens} which can be defined as $g_{\text{ens}} = \sqrt{\sum g_k^2} = \sqrt{\int g^2\rho(g)dg}$, where $\rho(g)$ is the coupling distribution.

$W(\omega)$ is a function which takes into account the inhomogeneous broadening of the spin, with spectral density defined as $\rho(\omega) = \sum_k g_k^2\delta(\omega - \omega_k)/g_{\text{ens}}^2$:

$$W(\omega) = g_{\text{ens}}^2\int_{-\infty}^{+\infty}\frac{\rho(\omega')d\omega'}{\omega - \omega' + i\Gamma_h/2}. \tag{3.51}$$

In the case where the coupling distribution is decorrelated from the spin frequency distribution, which is assumed to be always the case, the spectral density defined above is simply the spin frequency distribution $\rho(\omega) = \sum_k \delta(\omega - \omega_0)$, which is given by the spin inhomogeneous lineshape. For a Lorentzian distribution, the spectral density distribution ρ depends on its FWHM linewidth Γ_{inh}, and its center frequency ω_s as

$$\rho(\omega) = \frac{\Gamma_{\text{inh}}/2}{\pi} \frac{1}{(\Gamma_{\text{inh}}/2)^2 + (\omega - \omega_s)^2}, \tag{3.52}$$

and the W function simplifies into [Din+11]

$$W(\omega) = \frac{g_{\text{ens}}^2}{(\omega - \omega_s) + i(\Gamma_h + \Gamma_{\text{inh}})/2}. \tag{3.53}$$

By analogy to the reflection case, the hanger geometry transmission coefficient of Equation 3.22 becomes

$$S_{21} = 1 - \frac{i\kappa_c/2}{(\omega - \omega_0) + i\frac{\kappa_t}{2} - W(\omega)}. \tag{3.54}$$

Impact on the resonator properties

Developing the denominator of Equation 3.50 and Equation 3.54 leads to

$$\omega - \omega_0 - \frac{g_{\text{ens}}^2(\omega - \omega_s)}{(\omega - \omega_s)^2 + (\Gamma_{\text{inh}}/2)^2} + i\left(\frac{\kappa_t}{2} + \frac{g_{\text{ens}}^2\Gamma_{\text{inh}}/2}{(\omega - \omega_s)^2 + (\Gamma_{\text{inh}}/2)^2}\right), \tag{3.55}$$

where the spin damping rate Γ_h has been neglected in front of Γ_{inh}.

- In the limit where $g_{\text{ens}} < \Gamma_{\text{inh}}/2$, it can be shown that the term $\omega - \omega_s$ can be approximated by $\Delta = \omega_0 - \omega_s$ [Abe+11]. Then the coupling between the resonator and the spin ensemble results in a shift of the resonator frequency such that the new frequency is

  $$\tilde{\omega_0} = \omega_0 + \frac{g_{\text{ens}}^2(\omega_0 - \omega_s)}{(\omega_0 - \omega_s)^2 + (\Gamma_{\text{inh}}/2)^2} \tag{3.56}$$

  and a change in internal quality factor such that the new damping rate is

  $$\tilde{\kappa}_t = \kappa_c + \tilde{\kappa}_{\text{int}} = \kappa_c + \kappa_{\text{int}} + \frac{g_{\text{ens}}^2\Gamma_{\text{inh}}}{(\omega_0 - \omega_s)^2 + (\Gamma_{\text{inh}}/2)^2}. \tag{3.57}$$

  At resonance, the change in damping rate becomes

  $$\tilde{\kappa}_t = \kappa_t\left(1 + \frac{4g_{\text{ens}}^2}{\kappa_t\Gamma_{\text{inh}}}\right) = \kappa_t(1 + C). \tag{3.58}$$

  The dimensionless quantity, $C = 4g_{\text{ens}}^2/(\kappa_t\Gamma_{\text{inh}})$, is called the cooperativity [JM12a]. In the high cooperativity regime ($C \gg 1$), the resonator is strongly affected when crossing the spin frequency. Its internal losses increase by several orders of magnitude at resonance and this is accompanied with a visible avoided crossing of the resonator frequency. In the low cooperativity regime ($C \ll 1$), the resonator is weakly affected by the presence of resonant spins. Its internal loss rate shows a small bump at resonance and the frequency is little shifted. Both regimes, with in addition the regime of near unity cooperativity, are shown in Figure 3.9.

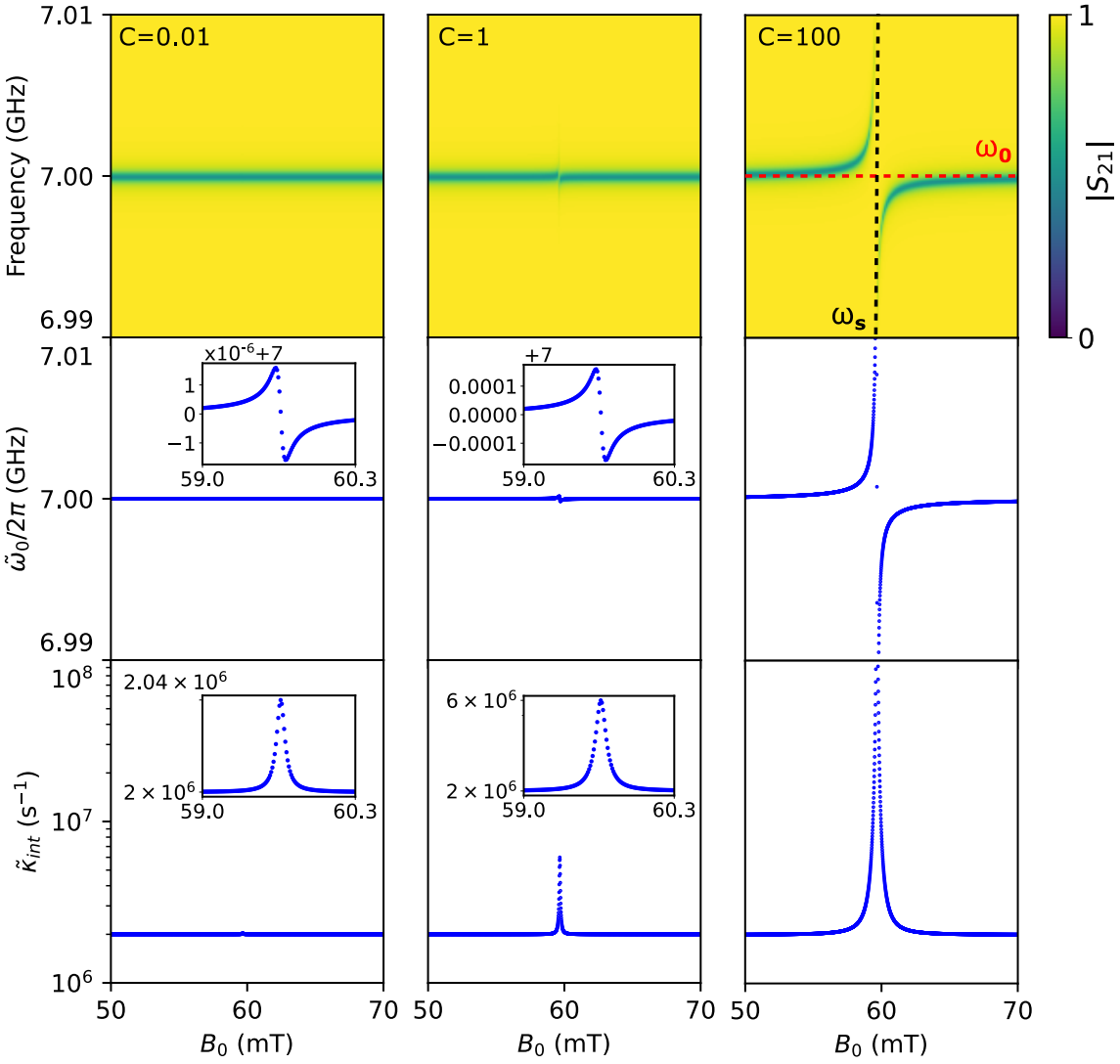

Figure 3.9 – **Transmission coefficient S_{21} when crossing an electron spin transition, in the hanger case, when $g_{\text{ens}} \lesssim \Gamma_{\text{inh}}$ Top.** Magnitude of the transmission coefficient S_{21} computed with Equation 3.54 for three cooperativity regimes: $C = 0.01$, 1 , 100. The resonator parameters are its frequency $\omega_0/2\pi = 7$ GHz, its coupling and internal loss rates $\kappa_c = \kappa_{\text{int}} = 2 \times 10^6$ s^{-1}. The electron spin transition parameters are its g-factor g= 8.38, its inhomogeneous linewidth $\Gamma_{\text{inh}}/2\pi = 10$ MHz and its ensemble coupling g_{ens} which varies depending on the chosen value of the cooperativity. The spin transition frequency is given by $\omega_s = g\mu_B B_0$. The low cooperativity, $C = 0.01$, corresponds to $g_{\text{ens}}/2\pi \sim 0.13$ MHz, the unity cooperativity, $C = 1$, to $g_{\text{ens}} \sim 1.3$ MHz, and the high cooperativity, $C = 100$, to $g_{\text{ens}} \sim 13$ MHz. Guidelines with $\omega_0(B_0)$ and $\omega_s(B_0)$ are shown on the figure at high cooperativity. **Middle.** Shifted resonator frequency, $\tilde{\omega}_0$, as a function of B_0, computed with Equation 3.56. Insets zoom on the avoided crossings. **Bottom.** Modified internal loss rate, $\tilde{\kappa}_{\text{int}}$, as a function of B_0, computed with Equation 3.57. The y-axis is in logarithmic scale. Insets zoom on the internal loss peak at resonance.

- If $g_{\text{ens}} > \Gamma_{\text{inh}}/2$ and $\kappa_t/2$, when the spin and the resonator are resonant, the spectrum shows two dips separated by $2g_{\text{ens}}$. This strong coupling regime was not achieved in our experiments.

The usual regime for magnetic resonance is the low cooperativity regime. Both high cooperativity and strong coupling regimes have been achieved a few years ago with superconducting circuits [Sch+10; Kub+10; Ran+13; Pro+13].

Saturation effects

By describing the spins with bosonic operators, this derivation discards any spin saturation. However, at finite temperature, a non-negligible fraction of the spins is in the excited state following Boltzmann distribution law. This should be taken into account in the definition of the ensemble coupling constant, defined earlier as $g_{\text{ens}} = \sqrt{\sum g_k^2}$. The sum, instead of being performed on the total number of spins N of the ensemble, is in fact performed over the difference of population between the ground and excited states, $N_{|g\rangle} - N_{|e\rangle}$. As a consequence, the definition of the ensemble coupling must be rescaled manually by a factor $\sqrt{P(T)}$, where $P(T)$ is the polarization of the spin ensemble, defined as $P(T) = (N_{|g\rangle} - N_{|e\rangle})/N$ (see Section 2.2.4).

3.3.1 Spin detection using spin echoes

The detection of the spin ensemble via their impact on the bare resonator scattering matrix is difficult when the cooperativity is too small. Another more sensitive detection technique uses microwave pulses to trigger spin-echoes which can be measured in the output resonator field. This technique is more sensitive because the spin signal appears at a time when no drive is applied to the resonator.

3.3.1.1 Hahn-echo sequence

The most common pulse sequence is the Hahn-echo sequence (see Figure 3.10). At $t = 0$, a first pulse, applied along x, makes the spins rotate by an angle $\pi/2$ on the Bloch sphere. Due to the inhomogeneous broadening of the spins, they rotate in the equatorial plane at different speeds, depending on their detuning Δ from the center frequency ω_s. After a delay time τ, a π pulse is applied along y, which can be seen as a time-reversal action and the spins refocus at a time 2τ after the first excitation pulse. This refocusing on the equatorial plane yields a non-zero term in $\langle\hat{\sigma}_-\rangle = \sum_k \langle\hat{\sigma}_-^{(k)}\rangle$. Therefore, according to Equation 3.42, the output field contains a signal at $t = 2\tau$ which is called spin echo. Moreover, immediately after the $\pi/2$ pulse, at $t = 0$, the spins are in phase such that there is also a spin signal in the output field of the cavity. This signal, called free induction decay (FID), decays with rate $1/T_2^* = \Gamma_{\text{inh}}/2$ if not dominated by the cavity damping rate κ_t. It is not easily observable as it happens immediately after the microwave excitation while the echo signal is well isolated in time.

3.3.1.2 Hahn-echoes with an inhomogeneous coupling constant

So far, we have considered ideal pulses, which instantaneously rotate the spins by a given angle. The rotation angle of each spin is $\theta = \Omega_R dt$, where $\Omega_R = \sqrt{\Delta^2 + (2g_0|\alpha|)^2}$ is its Rabi frequency (see Equation 3.40) and dt is the pulse duration. The intra-resonator field α is related to the input field amplitude α_{in}. Taking Equation 3.16 at resonance yields $\alpha = 2\sqrt{\kappa_c}\alpha_{\text{in}}/\kappa_t$ in the reflection case and $\alpha = \sqrt{2\kappa_c}\alpha_{\text{in}}/\kappa_t$ in the hanger case. If the spin detuning Δ is small compared to $2g_0|\alpha|$, the Rabi frequency is simply $\Omega_R = 2g_0|\alpha| \propto g_0|\alpha_{\text{in}}|$.

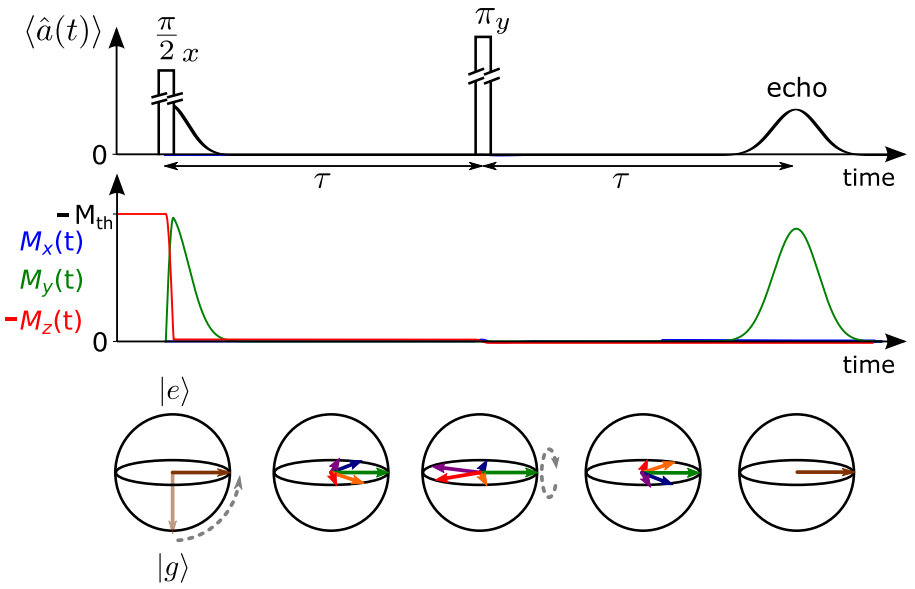

Figure 3.10 – **Hahn-echo sequence.** z is the polarization axis of the spins under a magnetic field $\boldsymbol{B_0}$. The thermal equilibrium magnetization of the spin ensemble is denoted M_{th}. A $\pi/2$ pulse applied along x brings the spins along y. All spins have a different detuning from their center frequency ω_s. Therefore, in the frame rotating at ω_s, the spins rotate with different speeds, those being exactly at ω_s staying along y. A π pulse applied along y acts as a time-reversal event, where all spins refocus in an echo along y at time 2τ after the initial pulse. *Top.* Field in the resonator. The control pulses are much larger than the spin signal which is indicated by the cuts in the rectangular shapes. *Middle.* Magnetization components in the rotating frame at frequency ω_s in absolute value. *Bottom.* Sketch of the spin dynamics on the Bloch sphere at the corresponding time of the sequence.

Moreover, we know that the coupling constant g_0 is roughly proportional to r^{-1}, where r is the distance between the spin and the inductance wire (see Equation 3.33). Due to its spatial inhomogeneity, the Rabi frequency is itself very inhomogeneous. Therefore, it is not possible in bulk-doped samples to rotate all the spins by a constant angle with such simple rectangular shaped pulses. Achieving well-defined Rabi angles is nevertheless possible using more elaborated chirped pulses [OSu+21], which was not attempted in our work.

However, it is worth noticing that in fact any combination of flipping angles θ_1 and θ_2 produce an echo, except if they are 0 or multiples of π and 2π respectively. This makes any two-pulse echo sequence with arbitrary pulse amplitudes a very robust technique for spin detection.

In the following we provide a simple model to describe the spin-echo in the situation where the Rabi frequency is spread. We follow the analysis of [Ran+20c].

If the spin line is narrow in front of the pulse excitation bandwidth ($\Gamma_{\text{inh}} \ll \kappa_t$), it can be shown that the echo amplitude is proportional to $\sin\theta_1 \sin^2(\theta_2/2)$ [SJ01]. As a consequence, if we apply two pulses of real amplitude $\alpha_{\text{in}}/2$ and α_{in}, with same pulse duration dt, the magnetization component of spin k contributing to the echo at $t = 2\tau$, $M_y^{(k)}$, is proportional to $\sin^3(2\alpha g_k dt)$, where α is the intra-resonator mean field during the first pulse.

Moreover, input-output theory yields that in the adiabatic limit, the output field at the echo time is proportional to $\sum_k g_k M_y^{(k)}$, which is itself proportional to $\int g\rho(g)\sin^3(2\alpha g dt)dg$. As the coupling constant g scales roughly as r^{-1} (see Equation 3.33), the density $\rho(g)$ is proportional to g^{-3} in our bulk-doped crystals. By changing variable with $\theta_1 = 2\alpha g dt$,

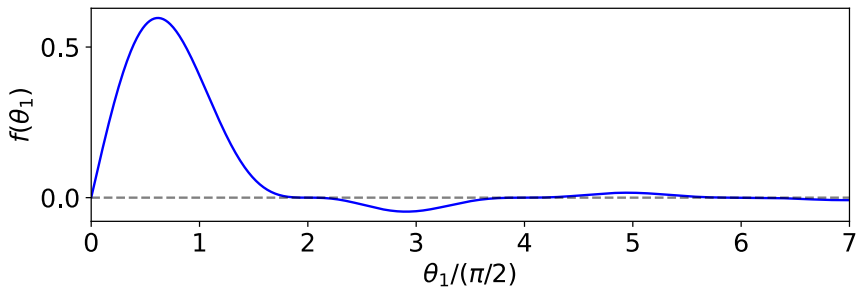

Figure 3.11 – **Calculated relative echo contribution.** The plotted function is $f(\theta_1) = \theta_1^{-2} \sin^3 \theta_1$, representing the contribution to the echo signal from spins with different Rabi angles θ_1, copied from [Ran+20c].

this integral becomes proportional to $\int f(\theta_1) d\theta_1$ where $f(\theta_1) = \theta_1^{-2} \sin^3 \theta_1$. Each spin has a different Rabi angle θ_1, which is the angle by which it is rotated after the first pulse. Computing the function $f(\theta_1)$ enables to understand which Rabi angles θ_1 contribute most to the Hahn-echo signal. This is performed in Figure 3.11, where it is clear that the spins contributing to most of the signal are those which rotate by nearly $\pi/2$, and hence π after the second pulse. The maximum of $f(\theta_1)$ occurs actually around $0.6\pi/2$. Interestingly, spins which rotate by $\pi/2 + 2k\pi$ where $k > 0$ do not contribute significantly to the Hahn echo because they are less numerous than spins rotating by exactly $\pi/2$. We can compute the single spin coupling constant of the spins which rotate by $0.6\pi/2$ during the first pulse: $\theta_1 = \theta_2/2 = 0.6\pi/2$ corresponds to

$$g_0 = \frac{0.6\pi\kappa_t}{4\sqrt{\kappa_c}\alpha_{\text{in}} dt}, \tag{3.59}$$

where α_{in} is the input pulse amplitude of the second pulse.

In reality, the spin line is much broader than the cavity linewidth. To get a complete model, the dynamics of each spin k should be computed using the Bloch equations which depend on its coupling constant g_k and its frequency detuning Δ_k. This is done numerically, using a simulation program that was developed by our group.

3.3.2 Spin excitation bandwidth

In our experiments, the spin inhomogeneous linewidth $\Gamma_{\text{inh}}/2\pi$, of the order of 20 MHz, is generally much larger that the resonator bandwidth $\kappa_t/2\pi$, which is typically 100 kHz-1 MHz. The resonator fixes the maximum spin bandwidth that can be excited by the microwave pulses.

From the resonator properties and the pulse length, it is possible to extract the intra-resonator averaged field $\alpha(t) = \langle \hat{a}(t) \rangle$ using input-output theory. In the low cooperativity regime, it is possible to neglect the back-action of the spins on the intra-cavity field. Equation 3.46 is thus computed by neglecting the coupling between the spins and the resonator in the Hamiltonian $\mathcal{H}$.

For a reflection measurement, the differential equation of $\alpha(t)$ in the frame rotating at ω_0 is

$$\dot{\alpha} = -i\omega_0\alpha - \frac{\kappa_t}{2}\alpha + \sqrt{\kappa_c}\alpha_{\text{in}}, \tag{3.60}$$

which solution is analog to Equation 3.42,

$$\alpha(t) = \sqrt{\kappa_c} \int_{-\infty}^{t} e^{-\frac{\kappa_t}{2}(t-t')} \alpha_{\text{in}}(t') dt'. \tag{3.61}$$

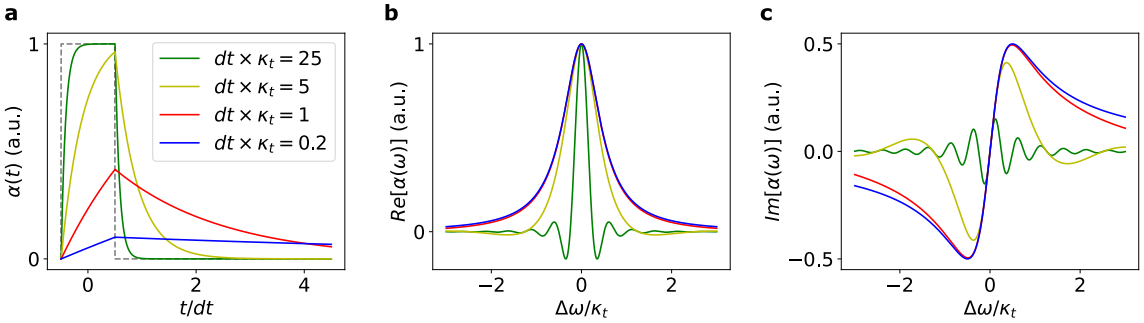

Figure 3.12 – **Pulse excitation profile in the cavity.** Normalized time (**a**) and frequency (real part in **b**, imaginary part in **c**) response of the intra-cavity field for a rectangular input pulse of duration dt and with a resonator of bandwidth κ_t.

Note that for a hanger-type measurement, κ_c is replaced by $\kappa_c/2$.

In the case of a rectangular input pulse, starting at $t = -dt/2$, of duration dt and amplitude α_{in}, this becomes

$$\alpha(t) = \sqrt{\kappa_c}\alpha_{\text{in}} \int_{-\frac{dt}{2}}^{\max(t,\frac{dt}{2})} e^{-\frac{\kappa_t}{2}(t-t')} dt'. \tag{3.62}$$

This is computed in Figure 3.12a for different values of the product $dt \times \kappa_t$. More interestingly is to compute the spectral response of the intra-resonator field to a rectangular pulse. Taking the Fourier transform of Equation 3.60 implies that (we recover Equation 3.16)

$$\alpha(\omega) = \frac{i\sqrt{\kappa_c}}{(\omega - \omega_0) + i\frac{\kappa_t}{2}} \alpha_{\text{in}}(\omega). \tag{3.63}$$

Therefore, the spectral response of a rectangular pulse inside the cavity is given by

$$\begin{aligned} \alpha(\omega) &= \left[\frac{\sqrt{\kappa_c}\kappa_t/2}{(\omega-\omega_0)^2 + (\kappa_t/2)^2} + i\frac{\sqrt{\kappa_c}(\omega-\omega_0)}{(\omega-\omega_0)^2 + (\kappa_t/2)^2} \right] \times |\alpha_{\text{in}}(\omega)| \\ &= \left[\frac{\sqrt{\kappa_c}\kappa_t/2}{(\omega-\omega_0)^2 + (\kappa_t/2)^2} + i\frac{\sqrt{\kappa_c}(\omega-\omega_0)}{(\omega-\omega_0)^2 + (\kappa_t/2)^2} \right] \times \left[\alpha_{\text{in}} dt \frac{\sin\left(dt(\omega-\omega_0)/2\right)}{dt(\omega-\omega_0)/2} \right]. \end{aligned} \tag{3.64}$$

The real and imaginary parts of $\alpha(\omega)$ are plotted in Figure 3.12b and c. The real part of the intra-cavity field has a FWHM linewidth $\Delta\omega$ (in rad.s^{-1}). Figure 3.12b shows that if $dt \times \kappa_t \gg 1$, $\Delta\omega$ is determined by the pulse FWHM linewidth: $\Delta\omega/2\pi \sim 1.2/dt$. On the contrary, if $dt \times \kappa_t \ll 1$, $\Delta\omega$ is determined by the cavity bandwidth: $\Delta\omega \sim \kappa_t$. In practice, the pulse length is often chosen to roughly match the cavity bandwidth, $dt \times \kappa_t \sim 1$. If the spins were a linear system, their excitation linewidth would be determined by the intra-cavity field linewidth $\Delta\omega$, but in general, the spin excitation linewidth has to be calculated using Bloch equations (see Equation 3.40). Nevertheless, $\Delta\omega$ will be used in this thesis as an order of magnitude estimate of the spin excitation linewidth [SJ01].

3.3.2.1 Hahn-echoes for studying spin coherence and relaxation

In this work, we are interested not only in detecting spins but mostly in understanding their dynamics, in particular their relaxation and coherence properties. This is achieved using the Hahn-echo detection described above.

Coherence time measurement

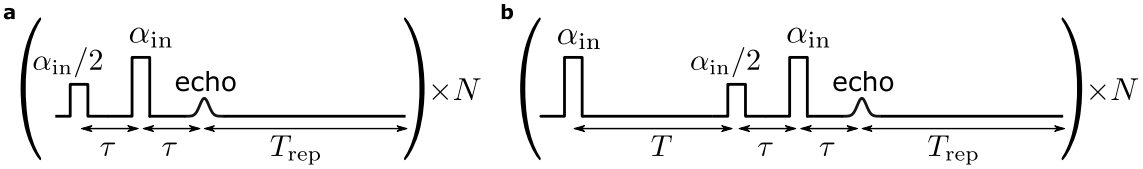

Figure 3.13 – **Pulse sequences for coherence and relaxation time measurements. a.** The coherence time T_2 is measured by varying the inter-pulse delay τ of a Hahn-echo sequence. The sequence is repeated after a waiting time T_{rep} which is typically of the order of T_1. **b.** The relaxation time T_1 is measured with an inversion recovery sequence. An initial inversion pulse is applied, followed after a delay T by a Hahn-echo sequence of fixed inter-pulse delay τ. The echo is measured as a function of the delay T.

The natural way for measuring the spin coherence time T_2 is to measure the amplitude of the Hahn-echo as a function of the delay 2τ between the first excitation pulse and the echo (see Figure 3.13a). Indeed, Equation 3.37 predicts an exponential decay of the transverse magnetisation as $M_x, M_y \propto \exp\{-2\tau/T_2\}$. In reality, the decoherence processes are usually non-Markovian because they involve interactions with a spin bath. Therefore, the decay is not always exponential and this measurement yields a decay of the equatorial magnetization components as $M_x, M_y \propto \exp\{-(2\tau/T_2)^x\}$, where x is a stretching exponent. Typically this exponent is between 1 (exponential decay) and 2 (Gaussian decay). More emphasis on the decoherence processes leading to this kind of echo shapes will be put in Chapter 4. To enhance the SNR, the spin echo sequence is repeated N times in order to average the signal. The optimal repetition time in-between two Hahn-echo sequences is typically the spin relaxation time T_1.

Relaxation time measurement

The relaxation time measurement makes also use of the Hahn-echo with one additional pulse in order to revert the spins at the beginning of the sequence. The sequence, called inversion recovery sequence, consists in one initial pulse of amplitude α_{in} and time dt (see Figure 3.13b). The spins which have the corresponding Rabi frequency rotate by an angle π. Then, according to Bloch equation (see Equation 3.37), they relax exponentially towards thermal equilibrium with rate $1/T_1$. After a varying time T, a Hahn echo sequence, of pulse length dt, amplitude $\alpha_{\text{in}}/2$ and α_{in} and fixed inter-pulse delay τ, triggers a spin echo at time $t = T + 2\tau$ and measures the longitudinal polarization at delay T after application of the first pulse. The equatorial magnetization components M_x, M_y decay as $\exp\{-T/T_1\}$. The Hahn-echo inter-pulse delay is chosen sufficiently low such that the impact of decoherence on M_x and M_y is small.

3.3.2.2 Relaxation time simulations in the low cooperativity regime

The decay of the relaxation measurement can be complex due to the fact that the spins have all a different coupling constant to the resonator and therefore a different Purcell relaxation rate. The development of Section 3.3.1.2 showed that the signal can be roughly seen as originating from the spins which flip as $0.6\pi - T - 0.6\pi/2 - \tau - 0.6\pi -$ echo. However it is also possible to simulate the dynamics of each spin packet to get a more accurate result, which takes into account inhomogeneous broadening.

In the low cooperativity regime, the back-action of the spin on the intra-cavity field can be neglected. Hence the simulation is performed in three steps [Ran+20c]:

- First, the intra-cavity field is computed from the input-output expressions of Equation 3.46 by neglecting the spins.

- Second, the spin dynamics are solved for each spin separately according to the Bloch equations derived in Equation 3.37. These simulations are mostly helpful for simulating relaxation and the coherence time T_2 is taken identical for all spins. $1/T_1^{(k)}$ is taken as the sum of the spin-lattice relaxation rate $1/T_{1,\text{phonon}}$, which is the same for all spins, and the Purcell relaxation rate $\Gamma_P^{(k)}$, which on the contrary depends on the coupling and detuning of each spin. The initial spin state is $P_g^{(k)} |g\rangle + \left(1 - P_g^{(k)}\right) |e\rangle$, where $P_g^{(k)} = 1 - 1/2e^{-T_{\text{rep}}/T_1^{(k)}}$ and T_{rep} is the waiting time before the sequence is repeated.
- Last, the output field is computed using input-output theory with the simulated spin dynamics included with Equation 3.42.

Chapter 4

Spin dynamics in solids

In this chapter, we investigate the different mechanisms leading to electron spin decoherence. As explained in Chapter 3, coherence time is measured by varying the delay τ of a Hahn-echo sequence ($\pi/2$-τ-π-τ-echo), where the π pulse compensates for the static inhomogeneity of the spin frequencies. The coherence time is thus limited by changes in the local spin environment within the delay 2τ, which are mainly due to dipolar interactions with a bath of spins (see Section 2.3.2). Spins in the bath can be of three kinds (see Figure 4.1): either electron spins which are being probed by the experiment (group A), all the other paramagnetic ions (group B), or nuclear spins (group C).

4.1 Decoherence mechanisms

We begin this chapter with a qualitative description of the main decoherence mechanisms for an electron spin embedded in a crystal. More quantitative results will be derived in the following sections. We consider only the case where the magnetic field is aligned with a principal axis of the host crystal ($\theta = 0°$ or $\theta = 90°$ for $CaWO_4$), which will be mostly the case in our experiments.

The decoherence mechanisms of a central spin (CS, in orange in Figure 4.1) are summarized in Figure 4.2 and listed below:

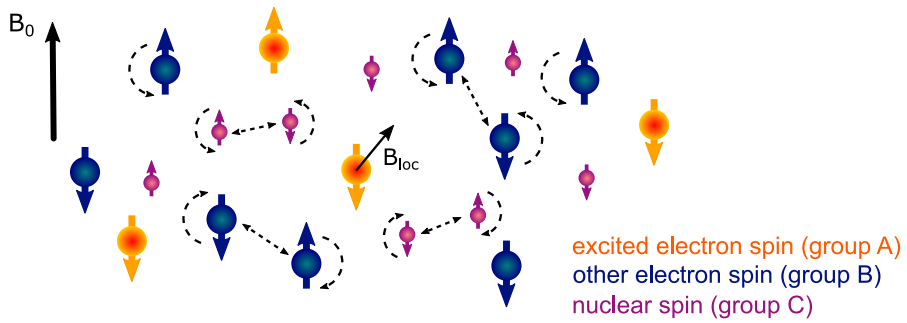

Figure 4.1 – **Probed electron spin with its magnetic environment.** The neighboring spins can be divided into three groups: electron spins being probed by the measurement (group A), any other electron spins, either of the same species as group A or not (group B), and nuclear spins, which come mostly from the host crystal (group C). This spin environment affects locally the magnetic field which is applied to the probed electron spin, both from a static point of view (with dipolar broadening) and a dynamic point of view (with decoherence).

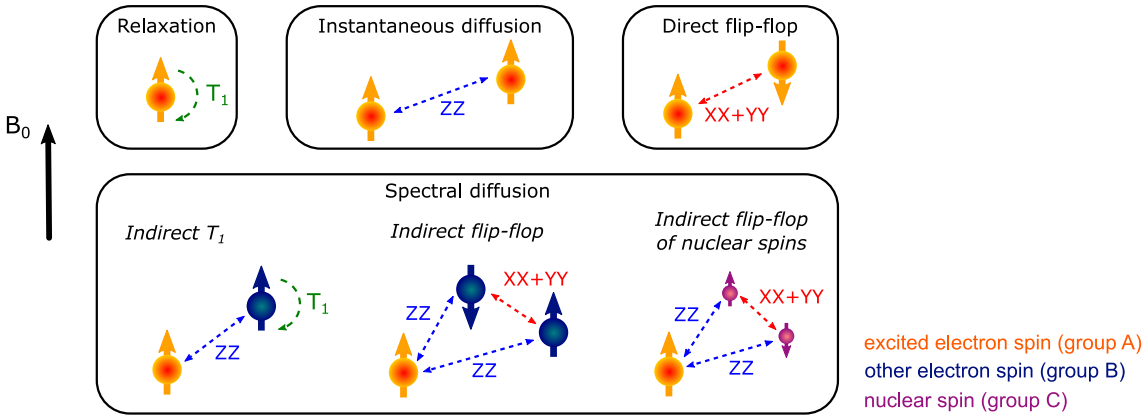

Figure 4.2 – **Decoherence mechanisms.** There are four main decoherence mechanisms, as described in text: relaxation, instantaneous diffusion, direct flip-flop and spectral diffusion. The decoherence is ultimately limited by the twice the relaxation time T_1. Other decoherence mechanisms come from the magnetic dipole-dipole interaction, where spins interact either via their longitudinal component (ZZ interaction, where Z is the spin quantization axis) or via their transverse component ($XX + YY$ interaction). Note that we use the special case where the magnetic field is applied along a principal axis of the **g**-tensor, such that spins are all polarized along the same direction, corresponding the magnetic field orientation. Otherwise, different spin species might not have the same quantization axis due to the **g**-tensor anisotropy.

- The coherence time T_2 is ultimately limited by twice the **relaxation** time T_1, such that $1/T_2 = 1/(2T_1) + 1/T_\phi$, where T_ϕ is the pure dephasing time.

- With spins of group A, which are all excited by the microwave pulses, the CS interacts with both the ZZ and $XX + YY$ interaction terms of the dipolar coupling (see Section 2.3.2). The former makes the CS sensitive to the spin flip of its neighbors during the refocusing π pulse of the Hahn-echo sequence. This is called **instantaneous diffusion (ID)**. The latter implies that the CS may undergo a flip-flop with a neighboring resonant spin. This is called **direct flip-flop**. For the concentrations and linewidths that we are considering in this work, this process is negligible. It was shown to become dominant in the special case of clock transitions [Wol+13].

- Electron spins of group B are not resonant with the CS. Thus they are coupled to the CS via the ZZ term only. Changes of neighboring spin B state cause an effective magnetic noise acting on the central spin, leading to dephasing. This process is called **spectral diffusion (SD)** by paramagnetic impurities. Spin B state changes via two processes: either due to spin-lattice relaxation (so-called indirect T_1 process) or due to flip-flops within the spin B bath (indirect flip-flop through the $XX + YY$ interaction).

- Regarding the coupling to the nuclear spins (group C), two different effects can be identified, depending on the magnitude of their hyperfine coupling constants A, B, C (which were defined in Section 2.3.2). For the nuclear spins closest to the electron, A, B and C are of the same magnitude as the nuclear Zeeman term. These spins have a strong impact on the electron spin dynamics, leading to a phenomenon called **ESEEM**, which will be described in more details below. On the other hand, the frequency of these spins is shifted compared to the bulk nuclear spins due to the hyperfine coupling, and as a result they are protected against flip-flops. Spins further away have lower hyperfine coupling, and do not cause any ESEEM. However, they

undergo some dynamics due to flip-flops with their neighbors ($XX+YY$ interactions), and this leads to **spectral diffusion** from the nuclear spins via the ZZ interaction with the CS.

4.2 Spectral diffusion

In this section, we focus on spectral diffusion, which is usually the dominant decoherence mechanism in our experiments. As explained above, spectral diffusion is due to spin-flips from either electron spins (group B) or nuclear spins (group C). The spin-flip probability depends on the spin polarization of groups B and C. Indeed, if the spins are polarized in their ground state, spin-flips and thus spectral diffusion are suppressed. Electron spins (group B) get frozen in their ground state below $T \sim g\mu_B B_0/k_B$, which, for a typical $g = 2$ and $B_0 = 100$ mT, gives $T \sim 130$ mK. This regime is achievable experimentally and spectral diffusion from group B can be quenched (alternatively, this can be achieved at ~ 1 K by increasing the magnetic field up to $\sim 7-8$ T [Tak+08]). For nuclear spins, due to the much lower gyromagnetic ratio, the equivalent temperature falls in the tens of microkelvin range and group C is thus always unpolarized in our experiments.

First, we present a spectral diffusion model which will be used in Chapter 11 to describe some of our measurements. We then discuss numerical methods known as CCE that can tackle accurately the phenomenon. They are particularly useful to describe nuclear spin spectral diffusion, where the nuclear spin concentration is known to a high precision and accurate predictions are therefore possible.

4.2.1 Echo sequences

Spectral diffusion can be evidenced in Hahn-echo measurements. During the pulse sequence, each spin i of group A rotates in the equatorial plane of the Bloch sphere by acquiring a phase $\phi_i = \omega_i t$. If a neighboring spin j flips state during the time interval 2τ, the frequency of spin i is changed by $\Delta\omega_{ij}$, which is given by the ZZ interaction term of the dipolar coupling. This change induces a dephasing which is not refocused by the π pulse and leads to the decay of the spin-echo.

There is another pulse sequence which is particularly suited to study spectral diffusion. It is called the stimulated echo or three pulse echo sequence. This sequence is sketched in Figure 4.3 and consists in three $\pi/2$ pulses where the first two are separated by τ and the third one happens after a waiting time T_w. The first two pulses create a frequency grating of $\langle \hat{S}'_z \rangle$ with period $1/\tau$, where some spins are excited whereas others are in the ground state. The third pulse stimulates an echo which should be seen as the free induction decay (FID) of the polarization grating [SJ01]. In fact, the grating period $1/\tau$ delays the FID signal, occurring at time τ after the third pulse. This sequence is useful to study the evolution of the polarization grating during the waiting time T_w. If spectral diffusion is present, the grating blurs due to frequency shifts of individual spins. This happens with increasing speed as τ increases, due to the smaller grating period, and the stimulated echo decays faster. When there is no spectral diffusion, the grating goes back to equilibrium with relaxation time T_1. Therefore, this stimulated echo sequence enables us to probe spectral diffusion over timescales as long as T_1, which is an advantage over Hahn-echo measurements which are limited by the coherence time T_2.

4.2.2 Uncorrelated sudden-jump model

Spectral diffusion with two and three pulse echoes has first been observed experimentally in the 60s by Mims [MNM61], while the first models arised from Portis [Por56], Mims [Mim68], Klauder and Anderson [KA62]. These theories have been united by Hu and

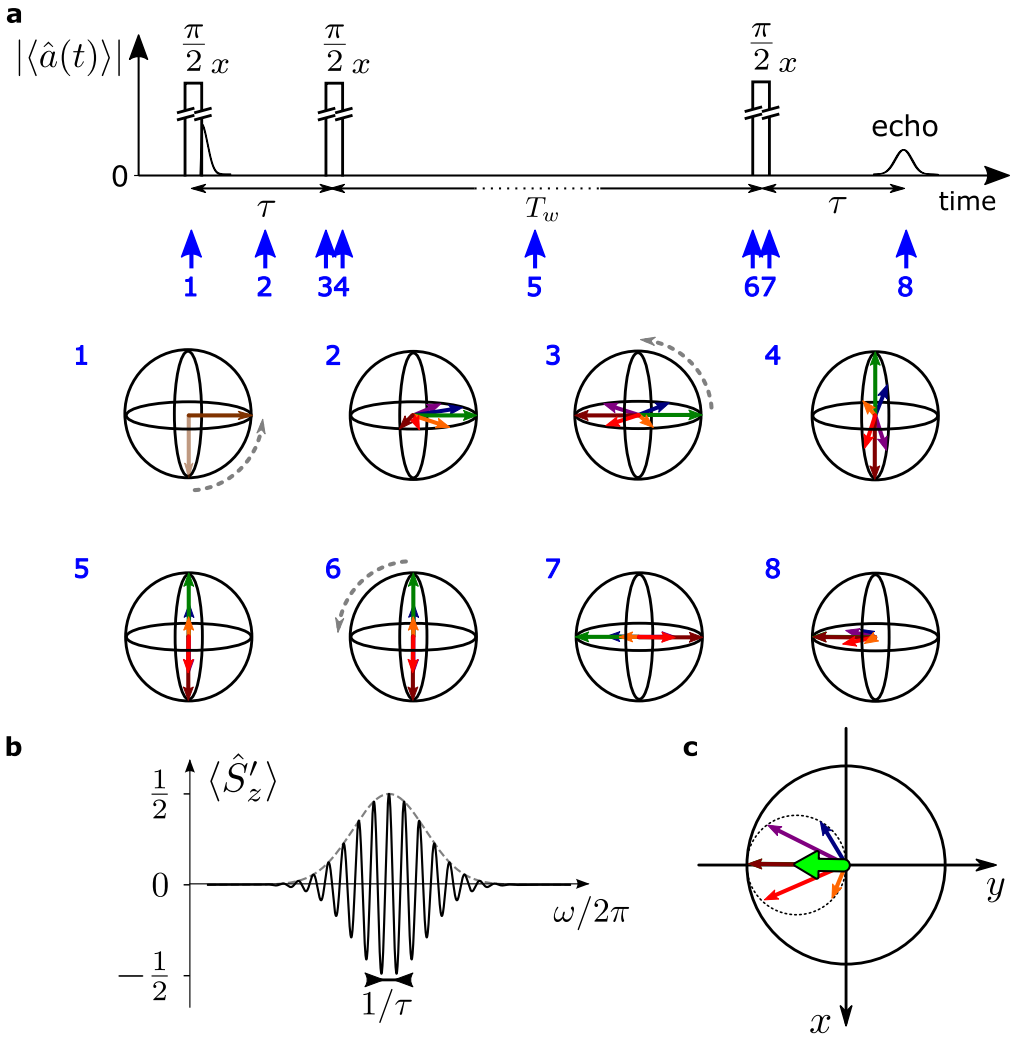

Figure 4.3 – **Stimulated echo sequence. a.** Description of the sequence which consists in three identical $\pi/2$ pulses applied along x and is therefore also called three-pulse echo sequence. The first two pulses are separated by τ and the last two are separated by the waiting time T_w. A stimulated echo appears at time τ after the last pulse. The plot shows the intra-resonator mean field $\langle\hat{a}(t)\rangle$, which contains the control rectangular pulses and the spin signal. The latter includes the FID at $t = 0$ and the stimulated echo at time $T_w + 2\tau$. The rectangular control pulses are cut to indicate that their amplitude is much larger than the echo signal. Below is shown the spin evolution on the Bloch sphere, in the rotating frame at ω_s, at the times indicated by the blue arrows. The first $\pi/2$ pulse brings the spins on the equatorial plane (1). This gives rise to a FID signal which decays due to the dephasing of the spins at frequency $\Delta\omega_s$ (2). At time τ, a second $\pi/2$ pulse brings the spins in the (y, z)-plane (3 to 4). During the waiting time T_w, the spins loose their coherence in a time T_2 and keep only their z-component, until they relax back to equilibium within T_1 (5). The last $\pi/2$ pulse brings the spins back to the equatorial plane (6 to 7). At time $T_w + 2\tau$, the spins partially align along $-y$ forming the stimulated echo signal. **b.** Polarization grating (solid black line) created along z during T_w (4 to 6), in the case of a narrow line compared to the excitation bandwidth (dashed grey line). This grating has a period $1/\tau$. **c.** Top view of the Bloch sphere at the time of the echo, $T_w + 2\tau$. The individual spin arrows point at a circle of radius 1/2, centered at $(0, -1/2)$ (dotted line). The resulting spin signal is the bigger green arrow which length is 1/2. Thus the stimulated echo amplitude is twice smaller than the Hahn-echo amplitude [SJ01].

Hartmann [HH74] to build up the so called "uncorrelated-sudden-jump model" which is based on several assumptions:

- the spins are randomly located,
- the spins of group A are isolated from each other,
- the local field fluctuation for spins of group A is due to the dipolar coupling to the perturbing spins (group B or C) which are flipping state or "jumping" at an average rate R,
- All spins can be seen as spin 1/2 particles.

An important consequence of the third assumption is that this model assumes that the perturbing spins (groups B and C) are weakly coupled spins and can therefore be taken as statistically independent. This describes well sudden jumps induced by a T_1 flip, but the applicability to flip-flops is less obvious.

Based on these assumptions, and following Bai and Fayer [BF89], we derive in Appendix B predictions for the stimulated echo dependence on τ and T_w, for an electron spin bath (group B). These predictions can be also found in [Böt+06]. The main result is that (in the limit where there is at most one jump during time τ, i.e. $R\tau \ll 1$), the 2- and 3-pulse echo decay is given by

$$V(2\tau + T_w) = V_0 \exp\left\{-\frac{T_w}{T_1}\right\} \exp\left\{-\tau \left[\Gamma_0 + \frac{\Gamma_{\mathrm{SD}}}{2}\left(R\tau + 1 - e^{-RT_w}\right)\right]\right\}, \tag{4.1}$$

where V_0 is the echo amplitude (which may be modulated by ESEEM as we will see later in Section 4.4), Γ_0 is the linewidth in the absence of spectral diffusion, including instantaneous diffusion and relaxation, Γ_{SD} is the spectral diffusion linewidth and R the spin flip rate. The spectral diffusion linewidth Γ_{SD} is given by

$$\Gamma_{\mathrm{SD}} = \Gamma_{dd} \operatorname{sech}^2 \frac{\Delta E}{2k_B T}, \tag{4.2}$$

where Γ_{dd} is the dipolar linewidth of Equation 2.46 and $\Delta E = \mathrm{g}_{\mathrm{eff},\beta}\mu_B B_0$ is the transition energy of the flipping spins. We observe that the spectral diffusion linewidth goes to zero at low temperature, when the perturbing spin bath is fully polarized, while it saturates at Γ_{dd} at high temperature, when the spin bath is fully unpolarized.

Looking at Equation 4.1 in the limit $T_w \to +\infty$ and remembering that $R\tau \ll 1$, the effective echo decay rate becomes $\Gamma_0 + \Gamma_{\mathrm{SD}}/2$, which means that at very long times, an initial spin homogeneous linewidth Γ_0 broadens into a line of width $\Gamma_0 + \Gamma_{\mathrm{SD}}$ due to spectral diffusion. The factor $1/2$ accounts for the fact that spectral diffusion affects only the last time interval τ and not the first one. At low temperature, Γ_{SD} goes to zero and spectral diffusion is quenched.

Note that if group B contains multiple spin species, each contribution of one subgroup is modeled with Equation 4.1 and then multiplied with the others,

$$V(2\tau + T_w) = V_0 \exp\left\{-\frac{T_w}{T_1}\right\} \exp\left\{-\tau \left[\Gamma_0 + \sum_\beta \frac{\Gamma_{\mathrm{SD},\beta}}{2}\left(R_\beta\tau + 1 - e^{-R_\beta T_w}\right)\right]\right\}. \tag{4.3}$$

In particular, this equation allows us to compute T_2 by taking $T_w = 0$,

$$V(2\tau) = V_0 \exp\left\{-\Gamma_0\tau - \sum_\beta \frac{R_\beta \Gamma_{\mathrm{SD},\beta}}{2}\tau^2\right\} = \exp\left\{-\left(\frac{2\tau}{T_2}\right)^x\right\}. \tag{4.4}$$

The coherence time T_2 is defined as the time when the echo decay equals $1/e$ and is derived by solving the corresponding second degree polynomial equation, yielding

$$T_2 = \frac{2}{\sum_\beta \Gamma_{\mathrm{SD},\beta} R_\beta}\left(-\Gamma_0 + \sqrt{\Gamma_0^2 + 2\sum_\beta \Gamma_{\mathrm{SD},\beta} R_\beta}\right). \tag{4.5}$$

Equation 4.4 shows that a two pulse echo experiment does not allow for extracting separately R and Γ_{SD}, which is possible with a three pulse echo experiment. If the residual decoherence rate Γ_0 can be neglected in front of spectral diffusion, the echo amplitude decay is Gaussian with coherence time

$$T_2 = \frac{2\sqrt{2}}{\sqrt{\sum_\beta R_\beta \Gamma_{\mathrm{SD},\beta}}}. \tag{4.6}$$

4.2.3 Spin flip rate

The spin-flip rate R of spins of group B is a parameter of the sudden-jump model. Physically, the jumps occur via either of two processes: either spin-flips due to relaxation (in which case $R = 1/T_1$), or flip-flops (in which case $R = R_{\mathrm{ff}}$). Depending on the concentration of B spins, the temperature and the applied magnetic field, flip-flops or spin-flips may be the dominant process. Although the sudden-jump model does not apply in theory to flip-flops, we include both rates in the model, with $R = 1/T_1 + R_{\mathrm{ff}}$ (see [Böt+06; Böt+09]).

Spin-lattice flip rate

As explained in Section 2.4, relaxation is dominated by the direct phonon process in our temperature range. If the perturbing spins are Kramers ions, their T_1 spin flip rate is

$$\frac{1}{T_1} = \alpha_D \mathrm{g}_{\mathrm{eff},\beta}^3 B_0^5 \coth\frac{\mathrm{g}_{\mathrm{eff},\beta}\mu_B B_0}{2k_B T}, \tag{4.7}$$

where α_D is an anisotropic term, dependent on the Kramers ion considered.

Flip-flop rate

The flip-flop rate can be estimated following the analysis done in [Car+19]. Fermi's golden rule states that

$$R_{\mathrm{ff}} \approx \frac{2\pi}{\hbar}\langle|\langle +-|\,\mathcal{H}_{dd,\text{spin i-spin j}}\,|-+\rangle|^2\rangle_{\mathrm{avg}}\frac{1}{\hbar\Gamma_{\mathrm{inh},\beta}}, \tag{4.8}$$

where $|+\rangle$ and $|-\rangle$ are the eigenvectors of the spin Hamiltonian, $1/(\hbar\Gamma_{\mathrm{inh},\beta})$ is the density of final states and $\langle ...\rangle_{\mathrm{avg}}$ is the average over all spin pairs. This average can be approximated by separating the angular average from the radial one,

$$\langle|\langle +-|\,\mathcal{H}_{dd,\text{spin i-spin j}}\,|-+\rangle|^2\rangle_{\mathrm{avg}} \approx \left(\frac{\mu_0}{4\pi}\mu_B\right)^2 \times \Xi(\mathbf{g}_\beta, \boldsymbol{B_0}) \times \left\langle\frac{1}{r^6}\right\rangle_{\mathrm{avg}}. \tag{4.9}$$

The angular averaging function, $\Xi(\mathbf{g}_\beta, \boldsymbol{B_0})$, depends only on the $\mathbf{g}$-tensor anisotropy and is calculated in [Car+19]. Here, we consider two specific cases. If $\boldsymbol{B_0} \parallel c$, $\Xi(\mathbf{g}_\beta, \boldsymbol{B_0}) =$

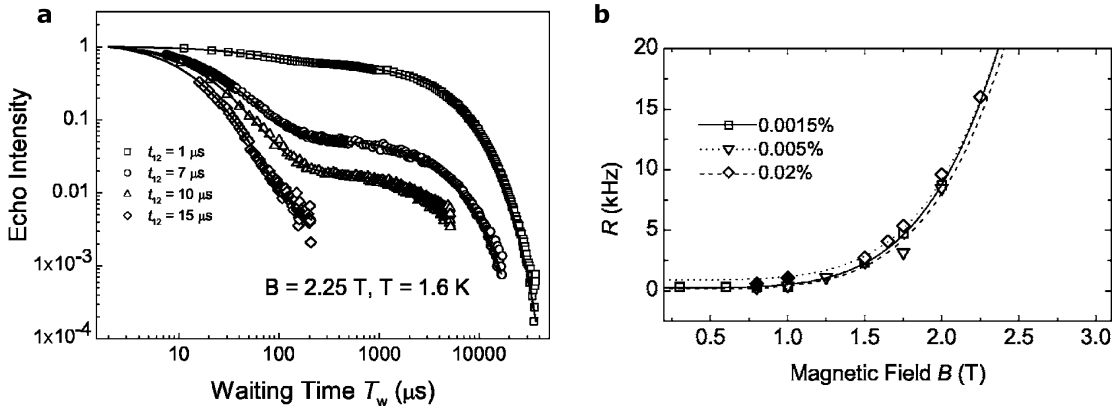

Figure 4.4 – **Stimulated echo measurements.** This figure is taken from [Böt+06], where the samples under study are Er^{3+}:Y_2SiO_5 with various erbium concentrations at $T = 1.6$ K. These measurements are done on the optical transition of erbium, from the ground state of the $^4I_{15/2}$ multiplet to the ground state of the $^4I_{13/2}$ multiplet, at 1.5 μm. **a.** Stimulated echo decay as a function of T_w, for various values of $t_{12} = \tau$ between 1 and 15 μs. The erbium doping concentration is 0.02% and $B_0 = 2.25$ T. The echo decay curves are normalized to the intensity of their first point. The solid lines are fits with Equation 4.1. **b.** Spin-flip rate R as a function of B_0, extracted from stimulated echo decays, measured with samples of various erbium doping concentrations: 0.0015, 0.005 and 0.02%. The data are fitted with $R = R_0 + 1/T_1$.

$g^4_{\perp,\beta}/20$, while if $\boldsymbol{B_0} \perp c$, $\Xi(\mathbf{g}_\beta, \boldsymbol{B_0}) = 1/20(g^4_{\parallel,\beta} + g^4_{\perp,\beta} - g^2_{\parallel,\beta}g^2_{\perp,\beta})$. For the case of erbium in $CaWO_4$, as $g_\perp$ is much greater than $g_\parallel$, $\Xi(\mathbf{g}, \boldsymbol{B_0}) \sim g^4_\perp/20$ as well.

Simplifying the radial average leads to

$$R_{\text{ff}} = \frac{1}{12\hbar^2}\mu_0^2\mu_B^4\Xi(\mathbf{g}_\beta, \boldsymbol{B_0})\frac{c_\beta^2}{\alpha_0\Gamma_{\text{inh},\beta}}, \tag{4.10}$$

where α_0 is a free parameter of order unity. This derivation holds for the high temperature limit, when the spin bath is unpolarized. At lower temperature, the flip-flop rate is rescaled by the probability of finding a pair of spins with opposite direction, in $\text{sech}^2[g_{\text{eff},\beta}\mu_B B_0/(2k_B T)]$. This implies, as expected, that the flip-flop rate vanishes at zero temperature, when the spins are fully polarized in their ground state.

Finally, the flip-flop rate is

$$R_{\text{ff}} = \alpha_{\text{ff}}\frac{\Xi(\mathbf{g}_\beta, \boldsymbol{B_0})c_\beta^2}{\Gamma_{\text{inh},\beta}}\,\text{sech}^2\,\frac{g_{\text{eff},\beta}\mu_B B_0}{2k_B T}, \tag{4.11}$$

where $\alpha_{\text{ff}} = \mu_0^2\mu_B^4/(12\hbar^2\alpha_0)$.

The sudden-jump model was used successfully to describe optical coherence time measurements performed on Er^{3+}:Y_2SiO_5 at $T = 1.6$ K by Böttger *et al.* [Böt+06]. Some of their results are reproduced in Figure 4.4. In subplot a, the decay of stimulated echoes is shown as a function of T_w, measured for various values of $t_{12} = \tau$ at $B_0 = 2.25$ T. We observe that the echo intensity decay strongly depends on τ, and therefore on the periodicity of the polarization grating. This is a signature of spectral diffusion. The data are fitted with Equation 4.1, which reproduces well the data. The experiment is repeated for various magnetic field amplitudes B_0 and for different samples with various erbium concentrations. Subplot b shows that the extracted values of R have a magnetic field dependence which is well fitted by the T_1 spin flip rate, with $R = R_0 + 1/T_1$ and T_1

Host crystal	$CaWO_4$	Si	Y_2SiO_5		YVO_4	
nuclear spin i	^{183}W	^{29}Si	^{89}Y	^{29}Si	^{89}Y	^{51}V
natural abundance	0.145	0.047	1	0.047	1	1
g-factor g_i	0.236	-1.111	-0.275	-1.111	-0.275	1.471
nuclear spin I_i	1/2	1/2	1/2	1/2	1/2	7/2
density n_i (cm^{-3})	1.9×10^{21}	2.3×10^{21}	1.8×10^{22}	4.2×10^{20}	1.2×10^{22}	1.2×10^{22}
$\overline{\mu}/\mu_N$ (cm^{-3})	2.0×10^{20}	1.3×10^{21}	2.7×10^{21}		6.4×10^{22}	
$T_2(g_e = 2)$ (ms)	17	1.2	1.4		0.02	
$T_2(g_e = 8.38)$ (ms)	10	0.7	0.8		0.01	

Table 4.1 – **Predicted nuclear spin limited coherence time for several host crystals of rare-earth ions.** Comparison between four host crystals: $CaWO_4$, Si, Y_2SiO_5 and YVO_4. The nuclear magnetic properties of $CaWO_4$ were already given in Section 2.2.1. The properties of the other crystals are taken from easyspin.org and materialsproject.org. Only non-zero nuclear spin isotopes with more that 1% natural abundance are considered. These properties are used to calculate the magnetic density, defined as $\overline{\mu}/\mu_N = \sum_i |g_i| I_i n_i$, and the coherence time predicted by Equation 4.12 for a g_e=2 and a g_e=8.38 electron spin. These values are estimated with a 10% uncertainty.

is the direct phonon relaxation time, given in Equation 4.7. The fit shows that at this temperature, the direct phonon process is dominant over two-phonon processes above 1 T. In this experiment, spectral diffusion is thus dominated by T_1 spin flips. We will do a similar analysis on the erbium spectral diffusion in Chapter 11.

4.2.4 Cluster correlation expansion - numerical approach

Beyond the uncorrelated sudden-jump model, a more recent numerical technique, called cluster-correlation expansion (CCE), has emerged [WSD05; YL08]. It consists in dividing the spin bath into subsets or clusters of interacting spins. This numerical approach has proven to be successful in simulating the spectral diffusion caused by a nuclear spin bath [Ma+14]. CCE calculations of the tungsten nuclear spin bath in $CaWO_4$ were performed by our collaborators Sen Lin and Ren Bao Liu at the Chinese university of Hong Kong and will be presented and discussed in Chapter 7.

Approximate scaling for a nuclear spin bath

Recently, Kanai *et al.* [Kan+21] proposed a phenomenological "universal formula" to compute the coherence time due to nuclear spin spectral diffusion in an arbitrary crystal. It is based on the assumption that dilute nuclear spins (of concentration below 10^{22} cm^{-3}) can be taken as randomly distributed (thus, neglecting the details of the crystal structure), and on an observed scaling of the CCE calculation with the nuclear spin parameters (density n_i in cm^{-3}, quantum number I_i, g-factor g_i), leading to

$$T_{2,i} = 1.5 \times 10^{18} |g_i|^{-1.6} I_i^{-1.1} n_i^{-1.0}. \tag{4.12}$$

This equation holds for an electron spin $S = 1/2$ with g-factor $g_e = 2$. For an electron spin with effective g-factor g_{eff}, the coherence time is rescaled by approximately $(2/g_{\text{eff}})^{0.39}$. When a crystal contains several nuclear spin species, the contribution of all nuclear spin baths to the coherence time is computed as

$$T_2 = \left(\sum_i T_{2,i}^{-\eta_i} \right)^{-1/\eta'} \tag{4.13}$$

a

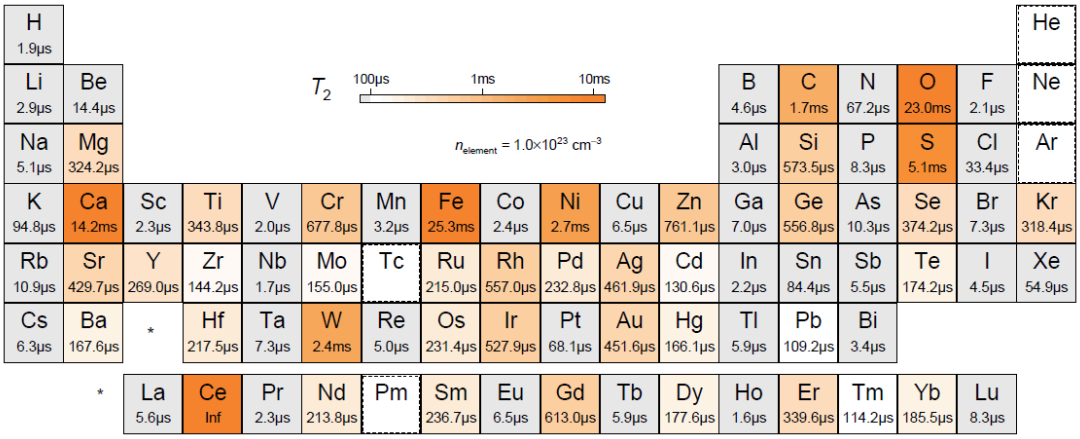

b

#	Material	T_2 (ms)	#	Material	T_2 (ms)	#	Material	T_2 (ms)
1	CeO_2	47	12	CaS	23	23	WS_2	11
2	FeO	36	13	Ca_2NiWO_6	19	24	$Sr_2Si(S_2O_7)_4$	11
3	CaO	34	14	S	19	25	$Sr_2Ge(S_2O_7)_4$	11
4	$CaSO_4$	29	15	$CaWO_4$	18	26	$CaCO_3$	11
5	$Ce(SO_4)_2$	29	16	CS_{14}	18	27	FeS_2	10
6	SO_3	29	17	Fe_2NiO_4	18			
7	$FeSO_4$	28	18	S_8O	17	138	SiO_2	2.7
8	CaS_3O_{10}	28	19	$FeWO_4$	16	298	ZnO	1.9
9	Ca_3WO_6	27	20	$NiSO_4$	15	709	SiC	1.1
10	WS_2O_9	25	21	WO_3	13	936	diamond	0.89
11	Ca_2FeWO_6	24	22	$NiWO_4$	12	1125	MgO	0.60

Figure 4.5 – **Predicted coherence times from CCE calculations of nuclear spin baths.** This figure is taken from [Kan+21]. **a.** Periodic table where each element is associated with its CCE-simulated coherence time for a g= 2 electron spin in a hypothetical material with natural abundance of a single species with element density $n = 1.0\times10^{23}$ cm^{-3}. The colors correspond to the simulated T_2 in logarithmic scale. The materials in white were not simulated as they are either difficult to make compounds from or they have no stable isotope. **b.** 12,000 host materials were simulated and the table makes a list of all simulated materials with $T_2 > 10$ ms and bandgap > 1 eV, with their corresponding simulated T_2.

where η_i and η' are stretching exponents close to 2. Using both formulas allows one to quickly estimate the nuclear spin limited coherence time of an electron spin in any host crystal.

Table 4.1 compares different host crystals for rare-earth ions, regarding their magnetic properties. Two quantities are calculated for each material: its nuclear magnetic moment density, defined as $\overline{\mu} = \sum_i |\mu_i| n_i$, where $\mu_i = |g_i|\mu_N I_i$, and their coherence time predicted by the model presented above. The coherence time is calculated for both $g_e = 2$ and $g_e = 8.38$ electron spins, which rescales the first number by 0.6. For $CaWO_4$, we get $T_2(g_e = 2) = 17$ ms and $T_2(g_e = 8.38) = 10$ ms. These coherence times are one order of magnitude larger than for Si and Y_2SiO_5 and three orders of magnitude larger than for YVO_4. This is due to its lower nuclear magnetic moment density $\overline{\mu}$. In fact, in the work of Kanai *et al.*, $CaWO_4$ is listed as one of the best out of 12,000 host crystals with natural abundance of isotopes (see Figure 4.5).

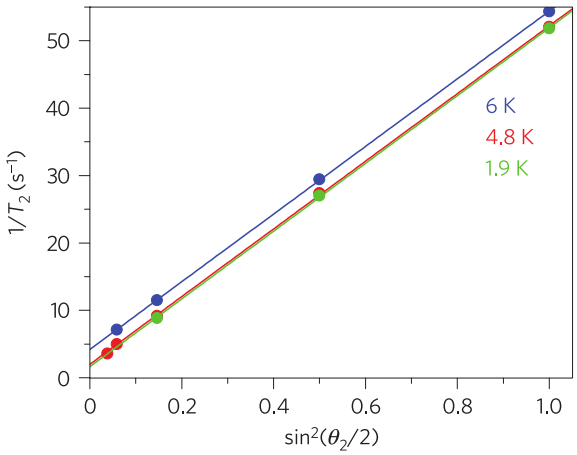

Figure 4.6 – **Electron spin coherence time of phosphorus donors in ^{28}Si crystal with 50 ppm ^{29}Si.** This figure is taken from [Tyr+12]. The donor concentration is $c = 1.2 \times 10^{14}$ cm^{-3}. The coherence times T_2 are fitted from Hahn-echo decay curves measured at several temperatures, 1.9, 4.8 and 6 K. The pulse amplitude is calibrated such that the initial pulse makes the spins rotate by $\theta_1 = 90°$ and the refocusing pulse makes the spins rotate by θ_2 which varies for different measurements. The data at each temperature are fitted with a linear function as $1/T_2 = a + b \sin^2(\theta_2/2)$. The extrapolated value at $\theta_2 = 0$ gives the remaining coherence time when ID is fully suppressed.

4.3 Instantaneous diffusion

Instantaneous diffusion (ID) is a decoherence process occurring within the spins of group A. It is a consequence of the fact that all spins A are resonant with the refocusing pulse and may thus be flipped. The resulting frequency shift of each spin due to the ZZ dipolar interaction term is not refocused by the Hahn-echo sequence and leads to the echo decay. Instantaneous diffusion can be suppressed by reducing the refocusing angle θ_2 [Tyr+12]. Indeed, if θ_2 is less that π, an echo will still form at time $t = 2\tau$, although of lower amplitude, and the chances of flipping spins A are reduced, which leads to a longer coherence time.

This phenomenon, if dominant, leads to the exponential decay of the echo as

$$\begin{aligned} V(2\tau) &= V_0 \exp\left\{-\frac{2\tau}{T_{2,\mathrm{ID}}}\right\} \\ \frac{1}{T_{2,\mathrm{ID}}} &= \frac{\pi}{9\sqrt{3}}\mu_0 \frac{(\mathrm{g}_{\mathrm{eff},\alpha}\mu_B)^2}{\hbar} c_\alpha \sin^2\frac{\theta_2}{2}, \end{aligned} \tag{4.14}$$

where c_α is the concentration of the spins in group A and $\mathrm{g}_{\mathrm{eff},\alpha}$ their effective g-factor [KI92; SJ01]. If the whole electron spin line is excited by the microwave pulses, then c_α is the concentration c of the electron spin transition under study. However, most of the time, the spin excitation bandwidth $\Delta\omega$ (defined in Section 3.3.2) is much smaller than the spin inhomogeneous linewidth $\Gamma_{\mathrm{inh},\alpha}$ and the concentration of spins A is approximated by $c_\alpha = \Delta\omega/\Gamma_{\mathrm{inh},\alpha} \times c$. The proportionality of the decoherence rate to $\sin^2(\theta_2/2)$ has been demonstrated experimentally by Tyryshkin *et al.* [Tyr+12] (see Figure 4.6).

4.4 Electron spin echo envelope modulation

The last phenomenon to be discussed in this chapter is electron spin echo envelope modulation (ESEEM). It is different from the previous ones because it does not lead to decoherence but simply modulates the echo shape. In Er:$CaWO_4$, ESEEM takes place at

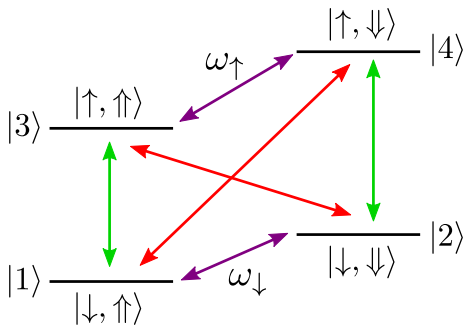

Figure 4.7 – **Energy level diagram involved in the ESEEM phenomenon.** The dipolar coupling between one electron and one nuclear spins gives rise to four energy levels, $|1\rangle, |2\rangle, |3\rangle, |4\rangle$. The states are labelled with $|\uparrow / \downarrow, \Uparrow / \Downarrow\rangle$, where the single arrow characterizes the electron spin $|S = \pm 1/2\rangle$ and the double arrow the nuclear spin $|I = \pm 1/2\rangle$. Note that this labelling is valid only in the high field limit, where ESEEM is not present because the nuclear spin projection is well defined. In the intermediate field regime, the nuclear spin quantization axis depends on the electron spin state. Therefore, not only the two $\Delta m_S = \pm 1$, $\Delta m_I = 0$ are allowed (green arrows) but also the two cross-transitions where $\Delta m_S = \pm 1$, $\Delta m_I = \pm 1$ (red arrows). All four transitions lie within the excitation bandwidth of the resonator and are simultaneously excited. This induces beatings in the echo decay with frequencies $\omega_{\uparrow/\downarrow}$.

small to moderate magnetic fields, typically < 100 mT. Here, we give a brief description of the phenomenon, following [Car+18; Pro+20].

For simplicity, we consider a system consisting of one electron spin coupled to one nuclear spin by the dipolar interaction. Its Hamiltonian in the secular approximation has already been derived in Section 2.3.2.2 (see Equation 2.34). The diagonalization of this Hamiltonian gives four eigenstates $(|1\rangle, |2\rangle, |3\rangle, |4\rangle)$ where $(|1\rangle, |2\rangle)$ are associated to electron spin $|S = -1/2\rangle$ and $(|3\rangle, |4\rangle)$ to the opposite $|S = +1/2\rangle$ (see Figure 4.7). Within these two subspaces, the nuclear spin has a different quantization axis, which implies that all four transitions become allowed, to some extent.

The splitting within the two subspaces, $\omega_\uparrow$ and $\omega_\downarrow$, are of the order of the nuclear Zeeman splitting ω_I which is small compared to the spin excitation bandwidth $\Delta\omega$. Therefore, all four transitions are excited by the microwave pulses. This simultaneous excitation leads to beating between these frequencies which modulates the echo amplitude.

The echo modulation has an analytical expression, which in the case of a two pulse echo is given by [SJ01]

$$V_{2p}(2\tau) = 1 - \frac{k}{4}\left[2 - 2\cos\omega_\uparrow\tau - 2\cos\omega_\downarrow\tau + \cos\left(\omega_\uparrow - \omega_\downarrow\right)\tau\right) + \cos\left(\omega_\uparrow + \omega_\downarrow\right)\tau\right], \quad (4.15)$$

where $k = 4R/(1+R)^2$ is the branching contrast and $R = |\langle 2|3\rangle|^2 / |\langle 1|3\rangle|^2 = |\langle 1|4\rangle|^2 / |\langle 2|4\rangle|^2$ is the branching ratio, characterizing how well the cross-transitions are allowed [Car+18].

For N nearest neighbors, the modulation effects are multiplicative, and the echo amplitude of a two-pulse echo sequence is

$$V(2\tau) = V_0 \exp\left\{-\left(\frac{2\tau}{T_2}\right)^x\right\} \prod_{i=1}^{N} V_{2p,i}(2\tau), \quad (4.16)$$

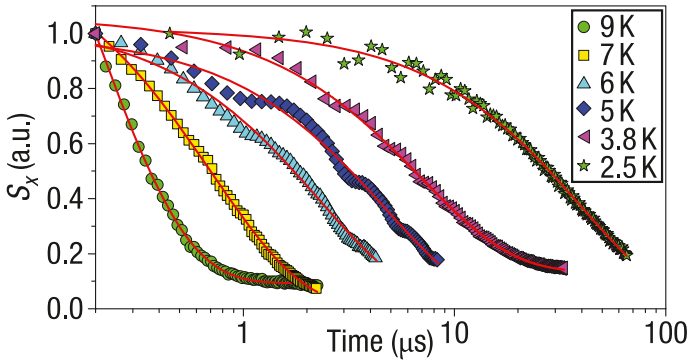

Figure 4.8 – **Coherence time of Er^{3+}:$CaWO_4$ at 2.5 K.** Hahn-echo measurements at various temperatures, with $B_0 = 0.5$ T applied along the c-axis. The decay at the lowest temperature of 2.5 K gives an electron spin coherence time of $T_2 \sim 50$ μs. Extracted from [Ber+07].

where

$$V_{2p,i}(2\tau) = 1 - \frac{pk_i}{4}\left[2 - 2\cos\omega_{\uparrow,i}\tau - 2\cos\omega_{\downarrow,i}\tau + \cos\left(\omega_{\uparrow,i} - \omega_{\downarrow,i}\right)\tau\right) + \cos\left(\omega_{\uparrow,i} + \omega_{\downarrow,i}\right)\tau\right]. \tag{4.17}$$

Note that the probability p that the atom i has a spin $I = 1/2$ is taken into account as a pre-factor [RHM65].

For a three pulse echo sequence, the modulation is [SJ01]

$$V_{3p,i}(2\tau+T_w) = 1-\frac{pk_i}{4}\left[(1-\cos\omega_{\downarrow,i}\tau)(1-\cos\omega_{\uparrow,i}(T_w+\tau)) + (1-\cos\omega_{\uparrow,i}\tau)(1-\cos\omega_{\downarrow,i}(T_w+\tau))\right]. \tag{4.18}$$

Both two-pulse and three-pulse ESEEM will be used in Chapter 7 and Chapter 11 to analyze our experimental data.

Resonator filtering

In our measurements, the resonator bandwith $\kappa_t/2\pi$ may be narrow enough to filter out the high frequencies of the ESEEM signal. Modeling this filtering is complex, because it occurs both during the spin excitation, where the linewidth is limited by the combination of the resonator and the pulse bandwidths (see Section 3.3.2), and also during the echo detection, where the output signal is filtered by the resonator bandwidth. We did not attempt to model this effect but we observe some filtering of the ESEEM frequencies in our measurements (see Chapter 7 and Chapter 11).

4.5 State of the art of the electron spin coherence of erbium dopants

Previous experiments on erbium doped crystals have reported its electron spin coherence time in various crystal matrices. Here we call coherence time the decay time measured with a Hahn-echo sequence, as introduced in Section 3.3.1, which is the most widespread method to characterize coherence.

Our system, Er^{3+}:$CaWO_4$, has previously been measured at temperatures of a few Kelvin. In particular, Bertaina *et al.* reported a coherence time of 50 μs at 2.5 K [Ber+07]. Figure 4.8 shows the experimental results, where the coherence time is measured at various

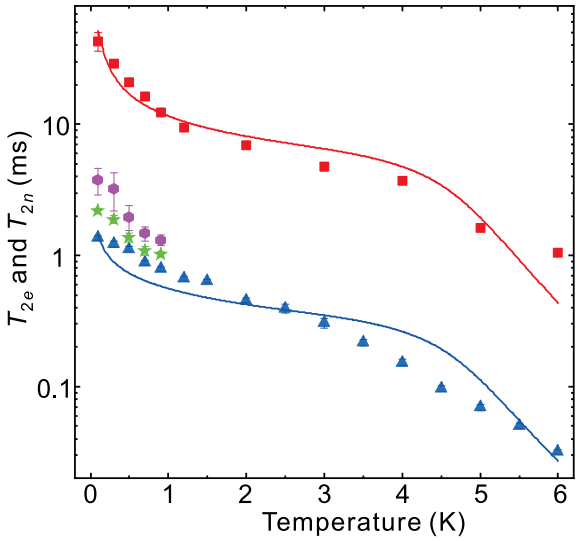

Figure 4.9 – **Electron and nuclear spin coherence time of $^{143}Nd^{3+}$:Y_2SiO_5 down to 100 mK.** Red squares are measured nuclear coherence times. Blue triangles are measured electron coherence times with 700 ns long pulses. Green stars are measurements with 200 ns long pulses. Purple hexagons are extrapolated coherence times where the instantaneous diffusion contribution is removed. The longest measured electron spin coherence time is $T_2 = 2.18 \pm 0.09$ ms, with stretching exponent $x = 1.42 \pm 0.09$ (green star at 100 mK). Solid lines are fits with a model including ID and SD contributions. Extracted from [Li+20].

temperatures, from 9 K down to 2.5 K. The coherence time varies by two orders of magnitude, increasing from about 0.5 μs at 9 K to 50 μs at 2.5 K.

This result can be compared to coherence time measurements of other Kramers ions in solid state. The longest coherence time reported for rare-earth electron spins, on a magnetically-sensitive transition, is 2 ms for Nd^{3+} in Y_2SiO_5 at 100 mK [Li+20]. The experimental data of Li *et al.* are presented in Figure 4.9. The nuclear and electron spin coherence times are measured as a function of temperature. Both quantities show a two order of magnitude increase between 6 K and 100 mK. The temperature dependence of the electron spin T_2 is fitted with a model including instantaneous diffusion and spectral diffusion from Nd^{3+} T_1-spin flips. When the temperature decreases, spectral diffusion from Nd^{3+} is quenched and the coherence time is limited by ID. This 2-ms T_2 is the longest electron spin coherence time measured on a magnetically-sensitive transition in a natural-abundance crystal. Other solid-state electron spin systems, as donors in silicon and nitrogen-vacancy centers in diamonds, have demonstrated coherence times up to 0.6 ms with natural-abundance crystals and on magnetically-sensitive transitions [Tyr+03; ZHL12]. Extending these coherence times can be achieved by isotopic purification, consisting in removing non-zero nuclear spin isotopes from the host crystal, and electron spin coherence times up to about one second have been reported for low doped phosphorus donors in ^{28}Si [Tyr+12].

The coherence time of rare-earth ions has already been measured down to 10 mK. At this temperature, Probst *et al.* measured a coherence time of 5 μs for Er^{3+}:Y_2SiO_5 [Pro+15] and Dold *et al.* reported coherence times of 0.4 ms for $^{145}Nd^{3+}$:Y_2SiO_5 and 1.2 ms for $^{171}Yb^{3+}$:Y_2SiO_5 [Dol20].

We stress that all these measurements are performed on magnetically-sensitive transitions. Indeed, the hyperfine structure of non-zero nuclear spin isotopes can lead to electron spin transitions where $\partial\omega/\partial B_Z \sim 0$, making the transition magnetically-insensitive. These

transitions are called zero-first-order-Zeeman (ZEFOZ) or clock transitions. In that case, all decoherence processes based on the ZZ dipolar interaction are strongly suppressed, leading to longer coherence times. On such transitions, coherence times of a few milliseconds have been measured for rare-earth doped crystals [Ort+18; Rak+20] and of 90 ms and 2.7 s for bismuth donors in natural silicon and isotopically purified silicon respectively [Wol+13].

Beyond these electron spin T_2, long coherence times have been measured on the optical transition of Er^{3+}:Y_2SiO_5 (which is also magnetically sensitive) at 7 T and 1.5 K, with $T_{2,\text{opt}} = 4$ ms [Böt+09] and on the nuclear spin transition of $^{167}Er^{3+}$:Y_2SiO_5 with $T_{2,n} = 1$ s at 1.4 K and 7 T [Ran+18].

Part II

Experiment 1: spin dynamics of erbium ions in pure $CaWO_4$ crystals

Chapter 5

Devices and experimental setup

This second part is devoted to the study of the properties and dynamics of erbium ions in nominally undoped crystals. This study has been conducted with two pure $CaWO_4$ samples which are presented in the following section.

5.1 Sample characterization

5.1.1 Crystal growth

The two $CaWO_4$ samples used for this experiment are cut from larger $CaWO_4$ crystals, also called boules, which are grown with the Czochralski method using oxides of different qualities:

- sample A is cut from a $CaWO_4$ crystal, which we call boule A, grown in the Walther-Meißner-Institut by Andreas Erb and Jean-Côme Lanfranchi. This crystal, described in detail in [EL13], was fabricated for particle detection applications and was therefore optimized to minimize radioactive impurities, but not necessarily paramagnetic impurities. It has been prepared by solid state reaction from $CaCO_3$ and WO_3 with purities of 99.999 atomic % (at%) and 99.998 at% respectively.
- sample B is cut from a $CaWO_4$ crystal, which we call boule B, grown at ChimieParis-Tech by Alban Ferrier and Philippe Goldner for our experiments. It originates from less pure oxides, with $CaCO_3$ of 99.95 at% purity, specified with less than 400 ppm of manganese, and WO_3 with 99.9 at%.

5.1.2 Characterization by ESR spectroscopy at 8-9 K

To pre-characterize these samples, continuous-wave ESR spectroscopy was performed by Sylvain Bertaina at IM2NP in Marseille, using a Bruker EMX spectrometer operating at 9.63 GHz. One sample from boule A, sample 1, and two samples from boule B, sample 2, extracted from the middle of the boule, and sample 3, extracted from the beginning of the boule, were studied.

5.1.2.1 Rotation in the (a, c)-plane

Identification of paramagnetic species is done using angular dependence spectroscopy in the crystal (a, c)-plane, θ being the angle of the magnetic field with respect to the c-axis. The sample is rotated using an automatic goniometer with a relative resolution of $< 1°$.

As explained in Section 2.4, spin relaxation of paramagnetic impurities can be strongly temperature dependent. As a result, the measured ESR spectrum can change drastically

when varying the sample temperature: an impurity would be invisible at too high temperature (due to a short T_1), but also at low temperature (due to a long T_1 leading to saturation). For REIs, a temperature of 8-9 K is found to be a good compromise.

Figure 5.1 and Figure 5.2 show the angular spectroscopy of all three samples. Several lines are observed, some of them dependent on θ, and others not. Sample 1 is measured twice, with different temperatures and powers, which makes the line intensities vary. Among the θ-dependent lines, we identify four paramagnetic Kramers ions (Er^{3+}, Ce^{3+}, Yb^{3+}, Nd^{3+}) based on their known **g**-tensor in $CaWO_4$ (see Table 2.3). The imperfect agreement is attributed to a slight misalignment. They are found in all three samples. The variation of the line intensities depends both on the ion concentration and on the temperature which impacts differently the relaxation of these Kramers ions.

The spectra also present a number of different features. Sample 1 shows a strong and narrow isotropic line at $B_0 = 160\,\mathrm{mT}$, which is attributed to Fe^{3+} [GKT78]. This line is also present in the other spectra albeit much weaker and broader. In sample 1, we observe weak lines at low field (below 50 mT) which are attributed to Tb^{3+}, with $I = 3/2$ in 100% abundance (in $CaWO_4$ it has an effective spin $S = 1/2$ with effective **g**-tensor $g_{\parallel} \sim 18$ and $g_{\perp} \sim 0$ [FH62]). These lines are also visible in sample 2, although at a lower concentration. Most spectra show a broad signal around $B_0 = 340$ mT, which corresponds to g= 2 spins, and is due to the sample holder.

We thus have a roughly complete assignment of the lines visible in sample 2. Note that around the Yb I=0 line, a pair of satellite lines clearly belong to the ^{171}Yb isotope (which has a nuclear spin $I = 1/2$, see Table 2.4). A remarkable feature is that the ratio between the ^{171}Yb and I=0 lines is not the same as in sample 1, and is also visibly larger than the natural abundance (14%). We are thus led to conclude that part the ytterbium traces present in samples 2 and 3 originates from a crystal growth performed one year before by P. Goldner's group, where material isotopically enriched in the ^{171}Yb isotope was used.

In samples 1 and 3 on the other hand, other lines are visible that have not been assigned. They show a strong dependence in θ, but with a symmetry that deviates from the REI S_4. In sample 1 we observe two strong lines with a θ-dependence and a gyromagnetic ratio that resemble Ce^{3+} in symmetry S_4, but shifted. In sample 3 we observe four additional lines, with a θ-dependence and gyromagnetic ratio resembling Er^{3+} in symmetry S_4, but here again shifted. A possible explanation of these lines is that they originate from REIs (possibly Ce^{3+} in sample 1 and Er^{3+} in sample 3) having a charge next to them on the lattice, either 2+ if the charge compensation is done by Ca^{2+} vacancy, or 1+ if it is done by a monovalent ion such as Na^{+}. As explained in Section 2.2.1, such satellite lines have been reported in $CaWO_4$ samples [GM64; RV64], and their features seem in agreement with our observations.

By scanning more precisely over the different lines, the relative concentration of several defects was calculated by our colleague Sylvain Bertaina in samples 1 and 3. To do so, the EPR signal, which is the derivative of the absorption, is integrated twice in order to calculate the spin susceptibility. This quantity is proportional to the number of spins. The susceptibilities are then renormalized by the experimental parameters (gain, temperature, sample mass), the electron spin g-factor in the direction of the microwave and the natural abundance of the measured isotope. Additionally, we will show in Chapter 6 that the absolute erbium concentration in sample A is 0.7 ± 0.1 ppb and in sample B it is 3.1 ± 0.2 ppb. Assuming that the erbium concentration in samples 1 and A is identical as they originate from the same boule, we use this value to calculate the absolute concentrations in sample 1, which are presented in Table 5.1. We follow the same hypothesis regarding samples 3 and B. In particular, sample 3 appears to contain less paramagnetic impurities than sample 1 which is surprising as sample 3 was grown from less pure oxides.

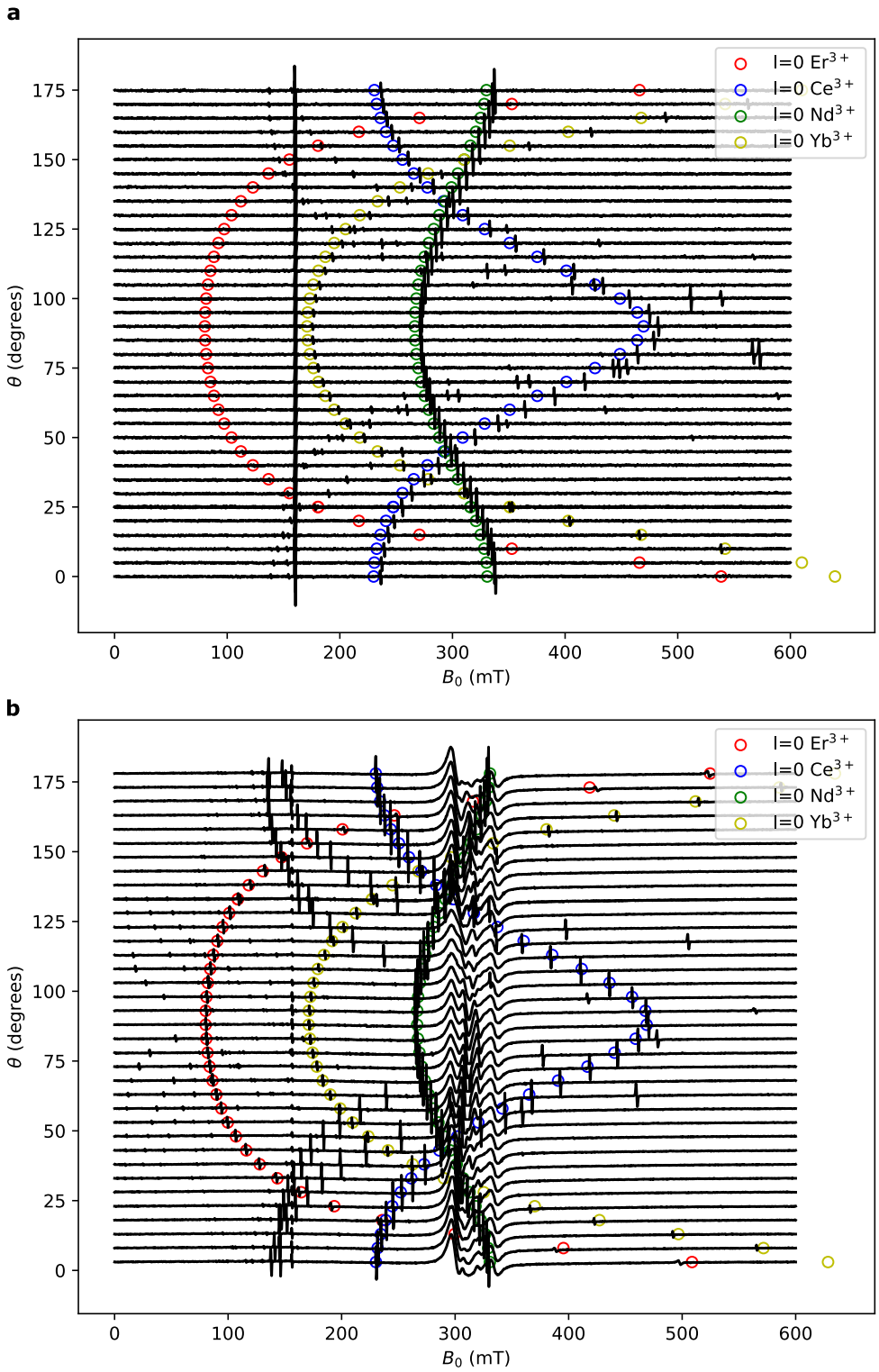

Figure 5.1 – **ESR spectroscopy of sample 1 (from boule A) with a Bruker spectrometer operating at $\omega_0/2\pi = 9.63$ GHz. a.** Spectrum recorded at low power and 8 K. **b.** Spectrum recorded at high power (+30 dB) and 9.5 K. Both spectra are taken in different runs and the strong and broad signal around 340 mT in subplot b mostly originates from the sample holder. Four Kramers ions are identified (open circles): erbium, cerium, neodymium and ytterbium, whose **g**-tensors in $CaWO_4$ are given in Table 2.3. The strong signal at 160 mT could be iron ions [GKT78]. The angular-dependent signals at low magnetic field (below 50 mT) are attributed to Tb^{3+} [FH62].

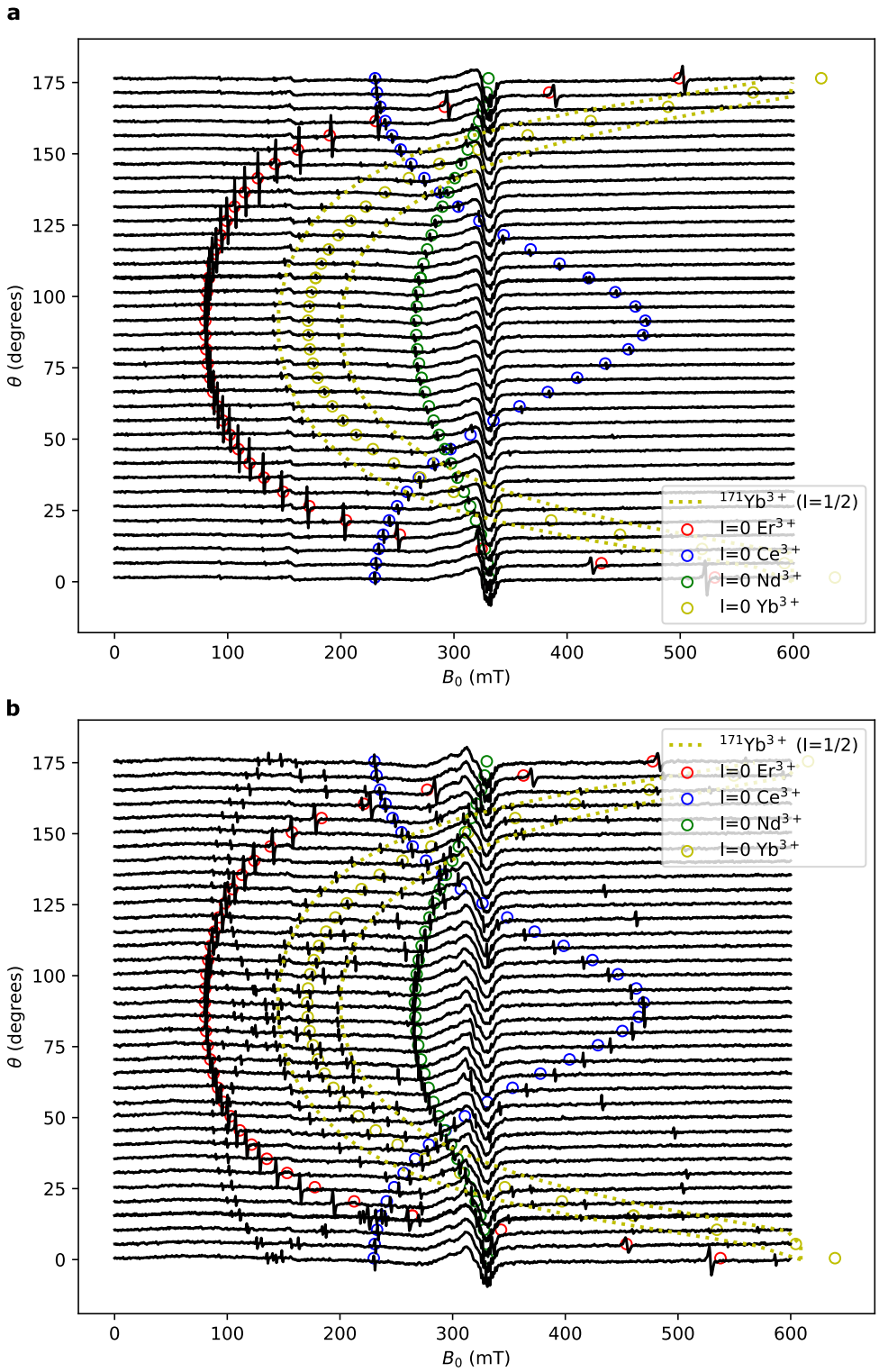

Figure 5.2 – **ESR spectroscopy of samples 2 and 3 (from boule B) with a Bruker spectrometer operating at $\omega_0/2\pi = 9.63\,\mathrm{GHz}$. a.** Sample 2, from the middle of the boule. **b.** Sample 3, from the beginning of the boule. Both spectra are measured at high power and 9 K. Four Kramers ions are identified (open circles): erbium, cerium, neodymium and ytterbium. Two satellite lines around the $I = 0$ ytterbium ions match with the ^{171}Yb isotope ($I = 1/2$) and are thus identified with the same color (dotted lines). Its Hamiltonian is computed using the parameters of Table 2.4. The broad signal around 340 mT corresponds to g= 2 spins and mostly originates from the sample holder.

Spin	Er^{3+}	Ce^{3+}	Yb^{3+}	Nd^{3+}	Fe^{3+}
Sample 1	0.7	2.7	38	12	11
Sample 3	3.1	0.7	0.04	0.31	/

Table 5.1 – **Absolute concentration in part per billion (ppb) with an uncertainty of 20%.** The relative concentrations are estimated from spectra measured with the Bruker spectrometer. The absolute erbium concentration of samples A and B is calculated in Chapter 6. It is assumed to be identical in sample 1 and sample 3 respectively, as these samples come from the same boule. The iron line in sample 3 is much broader and weaker and its concentration could therefore not be estimated. The concentrations take into account only spins located in sites with the usual S_4 symmetry.

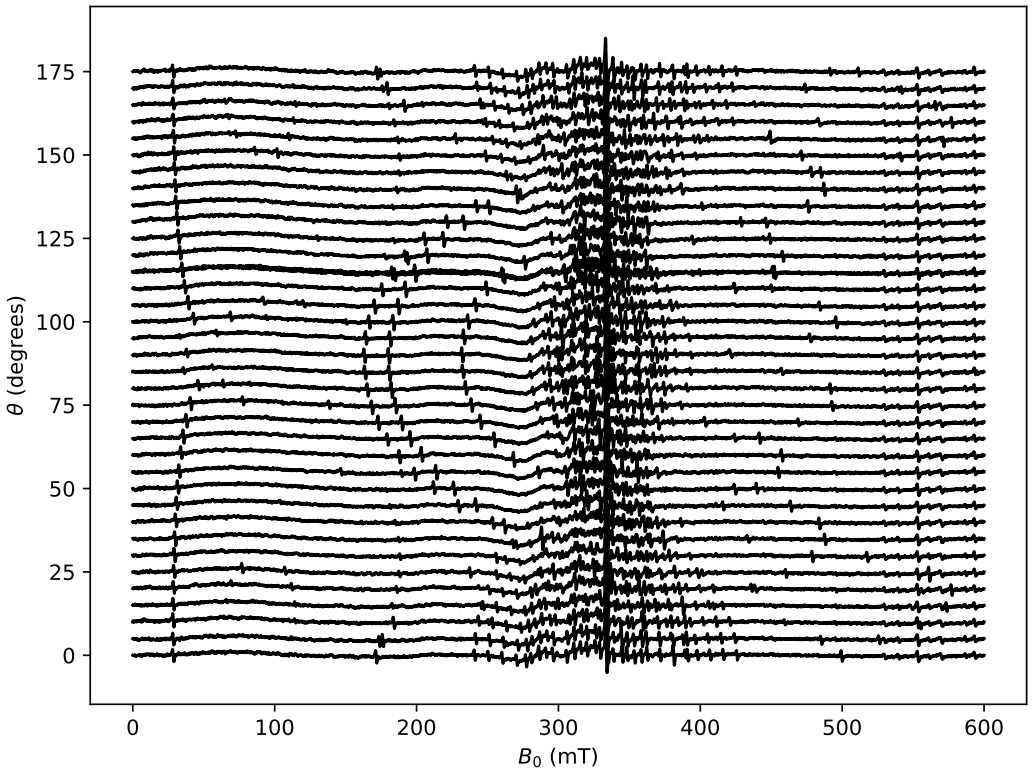

Figure 5.3 – **ESR spectrosopy of sample 3 at room temperature with a Bruker spectrometer operating at $\omega_0/2\pi = 9.63$ GHz.** The spectrum is measured at high power. We attribute most of the spin transitions to Mn^{2+} and Gd^{3+} [HB60], although we did not attempt to fit the spectrum.

Figure 5.3 shows a spectrum of sample 3 recorded at room temperature. The anisotropic lines varying close to $B_0 = 340$ mT (corresponding to g$\sim$ 2 spins) are attributed to manganese ions, Mn^{2+}, with $S = I = 5/2$. Other more anisotropic lines, especially at low fields, are attributed to gadolinium, Gd^{3+}, with $S = 7/2$ and several isotopes with different nuclear spins [HB60]. Its spectrum is thus complex and we did not attempt to compute it.

5.1.2.2 Rotation in the (a, b)-plane

Sample 1 was also measured with the field rotated in the crystal (a, b)-plane. Figure 6.1 shows the spectroscopy performed at two temperatures, 7.8 and 9.5 K, by varying the magnetic field angle φ in the (a, b)-plane. The iron line (at 160 mT) is visible in both spectra. The erbium line (at 80 mT) is slightly visible in subplot a. Its reduced intensity

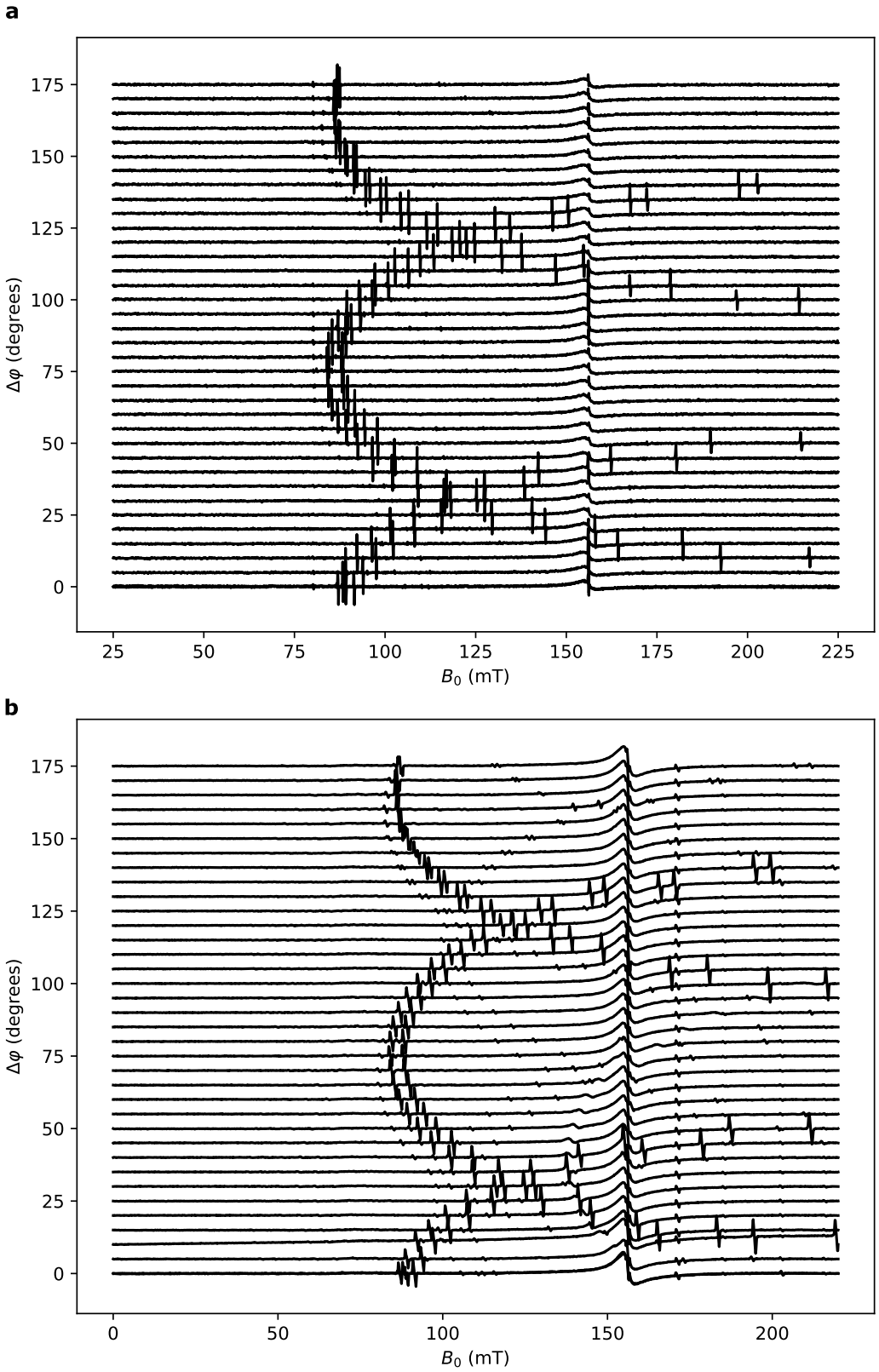

Figure 5.4 – **ESR spectroscopy in the (a, b)-plane of sample 1 (from boule A) with a Bruker spectrometer operating at $\omega_0/2\pi = 9.63$ GHz. a.** Spectrum recorded at high power and 7.8 K. **b.** Spectrum recorded at high power and 9.5 K. The isotropic line at $B_0 \sim 160$ mT is attributed to iron. The erbium line at $B_0 \sim 80$ mT is slightly visible in subplot a.

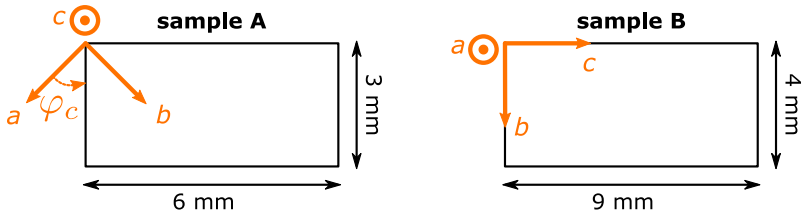

Figure 5.5 – **Orientation of the two undoped $CaWO_4$ samples studied in this second part.** *Left.* Sketch of sample A which has a rectangular surface of 3×6 mm^2 and the c-axis pointing out-of-plane. The a-axis makes an angle φ_c with the sample short edge. *Right.* Sketch of sample B which has a rectangular surface of 4×9 mm^2. The surface short edge is aligned with the b-axis and the long edge is aligned with the c-axis.

compared to Figure 5.1 is explained by the fact that in this configuration, the oscillating magnetic field $\boldsymbol{B_1}$ is along the c-axis and the erbium **g**-tensor is minimum along this orientation, which affects the line intensity.

The most visible feature in these spectra is a set of four lines with a strong angular dependence in the (a, b)-plane. They therefore originate from a paramagnetic center that does not obey the S_4 symmetry. The lines are arranged by pairs of two lines close in frequency, brought in correspondence with the other pair by a 90° rotation. The gyromagnetic ratio along the b-axis is low, which explains why these lines are not visible in the (a, c)-plane spectra of Figure 5.1, since the $\boldsymbol{B_1}$ field was then oriented along b. There are also several other pairs of less intense lines with a similar angular dependence. Although we cannot assign these lines with certainty, it is notable that their gyromagnetic ratio along one axis is close to the one of erbium; moreover their saturation curve also is similar to erbium (S. Bertaina, private communication).

5.1.3 Crystal orientation with X-Ray diffraction pattern

Samples A and B are cut from $CaWO_4$ boules A and B into rectangular slabs. Figure 5.5 shows sketches of the two samples. Sample A has dimensions $3 \times 6\,\text{mm}^2$ with 0.5 mm thickness in the c-axis direction, while sample B has dimensions $4 \times 9\,\text{mm}^2$, with the c-axis parallel to the 9 mm edge, and 0.5 mm thickness in the a-axis direction. X-ray diffraction enables us to determine the orientation of the crystal before cutting it according to a chosen orientation.

The surface of sample A was randomly oriented within the (a, b)-plane. X-Ray diffraction was later used to determine the orientation of the crystal a-axis (or equivalently b-axis) with respect to the sample edges. The diffraction pattern of Figure 5.6 indicates that the crystal a-axis makes an angle $\varphi_c = 46.5°$ from the sample short edge and an angle of 3.5° from the out-of-plane direction, due to a small misalignment of the surface with respect to the (a, b)-plane. These angles are measured with a precision of $\pm 2°$.

After being cut, the samples are polished on the face where the superconducting resonator will be patterned. Polishing was either performed at ChimieParisTech or by a company called SurfaceNet. The surface roughness after polishing is typically 0.5 nm.

5.2 Superconducting resonator design

In order to target slightly different frequencies, several micro-resonators are designed with frequencies between 7 and 8 GHz using Ansys HFSS software. Figure 5.7 shows the resonator design consisting in two lumped elements: an inter-digitated finger capacitor C shunted by a few micron-wide central inductance wire L. Table 5.2 lists the resonator

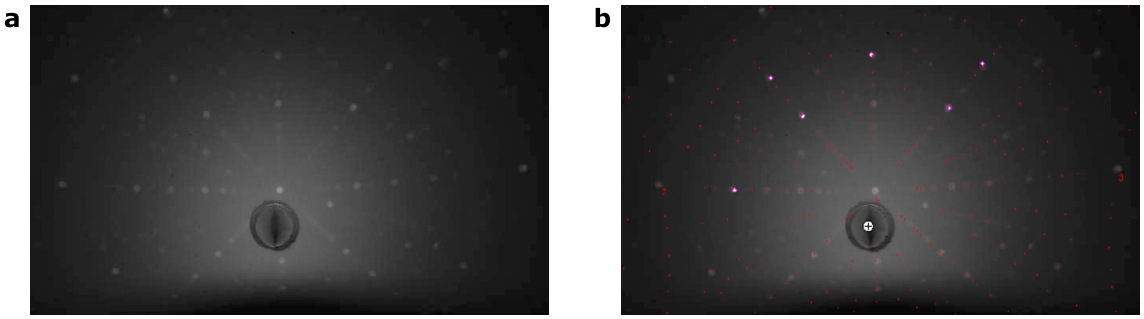

Figure 5.6 – **X-ray diffraction. a.** X-ray diffraction pattern of sample A. **b.** Same pattern superposed with the angular fit in red.

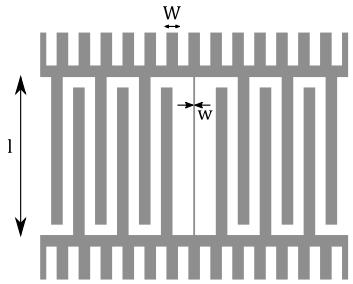

Figure 5.7 – **Example resonator design (resonator 2) with key tunable design parameters W, w and l labelled.**

resonator design	reso 0 (sample B only)	reso 1	reso 2	reso 3
w (μm)	2	2	5	5
l (μm)	720	630	720	630
W (μm)	50	10	50	10
N	6	8	6	8

Table 5.2 – **Resonator geometric properties.** Three resonators are pattern on sample A (reso 1-3) and all four are patterned on sample B.

geometric properties: wire width w, wire length l, finger width W and number of pairs of interdigitated fingers N. These parameters were adjusted to target specific frequencies.

For this experiment, a 3D geometry is chosen such that the resonator is coupled to the fundamental mode of a 3D box. This geometry minimizes the surface of superconducting metal as there is no need for a superconducting ground plane. This geometry is thus interesting for magnetic field resilience. The finger pattern in the two pads is an attempt to further improve this resilience by reducing the metallic area of the pads. This design shows good resilience properties up to 0.5 T, as will be shown in Section 6.1.2, but was not compared to the same resonator with full pads.

5.2.1 Electromagnetic simulations

The dielectric constant of $CaWO_4$ is similar to silicon with a slight anisotropy. Measurements at 1.6 kHz and room temperature gave $\epsilon_{a,b} = 11.7 \pm 0.1$ and $\epsilon_c = 9.5 \pm 0.2$ [BF67], which was later confirmed at 1 MHz [TA75]. Due to the dielectric constant anisotropy, the simulated frequencies depend on the crystal orientation. For film thicknesses and width that are used in our experiment, the kinetic inductance contribution is expected to be negligible and is not taken into account in the resonator design.

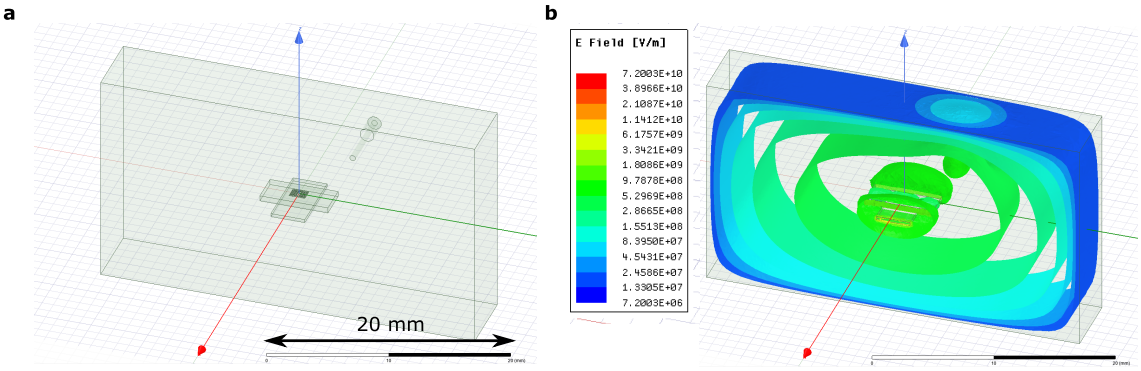

Figure 5.8 – **HFSS simulation**. **a.** Drawing in HFSS showing the rectangular metallic box (of dimensions $33 \times 19 \times 6$ mm^3), the metallic antenna and the silicon chip which holds the $CaWO_4$ sample where one resonator is patterned. **b.** Electric field in logarithmic scale with 1 Joule applied in the box fundamental mode.

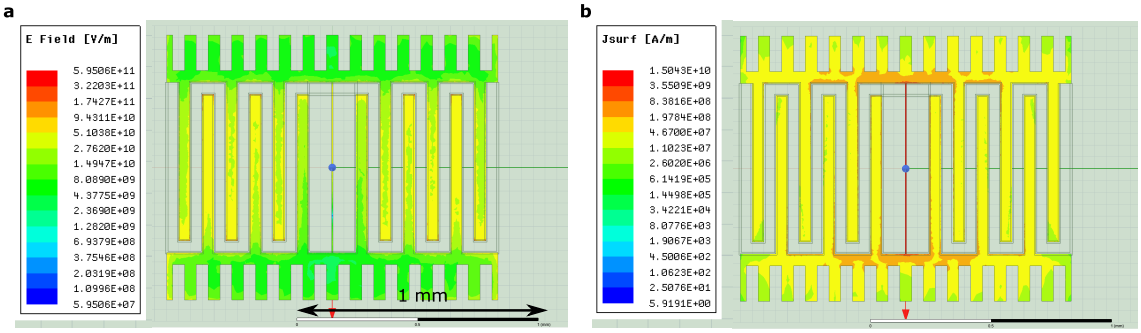

Figure 5.9 – **HFSS simulation of resonator 2 on sample A**. **a.** Electric field in logarithmic scale with 1 Joule applied in the resonator mode. **b.** Surfacic current in logarithmic scale with 1 Joule applied in the resonator mode.

The HFSS layout is presented in Figure 5.8a. The simulation has five elements:

- the copper box,
- the copper antenna,
- a silicon piece which fits in the copper box and is used for holding the sample of interest,
- the $CaWO_4$ sample which is stacked on the silicon sample,
- and the superconducting resonator which is drawn a 2D layer on the $CaWO_4$ top surface.

All copper and superconducting materials are taken as perfect electrical conductors.

The HFSS simulation solves the eigenmodes of the system. We run independent simulations for each resonator design. Figure 5.8b shows the electric field with 1 Joule in the box mode and Figure 5.9 shows the electric field and surfacic current with 1 Joule in the resonator mode. The simulation yields the eigenmode data of each resonance, with its frequency and coupling rate, which are summarized in Table 5.3 and Table 5.4. Similar frequencies and quality factors are found for the orientations of samples A (c out-of-plane) and B (c in-plane and perpendicular to the wire).

The impedance Z_0 of these resonators is determined by adding a small lumped inductance of typically 50 pH in series with the inductance wire. Using a linear expansion

resonator property	box	reso 1	reso 2	reso 3
$\omega_0/2\pi$ (GHz)	8.51	7.23	7.38	7.62
κ_c ($\times 10^6$ s^{-1})	440	0.14	1.23	0.38

Table 5.3 – **Resonator properties simulated with HFSS for sample A (*c* out-of-plane).**

resonator property	box	reso 0	reso 1	reso 2	reso 3
$\omega_0/2\pi$ (GHz)	8.24	6.95	7.29	7.32	7.78
κ_c ($\times 10^6$ s^{-1})	350	0.91	0.37	2.53	2.36

Table 5.4 – **Resonator properties simulated with HFSS for sample B (*c* in-plane, perpendicular to the wire).**

of the frequency as a function of inductance ($-2d\omega_0/\omega_0 \sim dL/L$), the impedance of our resonators is found to be $Z_0 = L\omega_0 = 35 \pm 2\ \Omega$.

5.2.2 Fabrication recipe

The superconducting resonators are fabricated out of niobium which has a critical temperature of 9.2 K and a bulk critical field of 0.2 T. The fabrication process contains sputtering of a thin layer of niobium (typically 50 nm) before dry etching using SF_6.

Prior to resonator fabrication, the etching rate of $CaWO_4$ with SF_6 was measured by making a simple pattern with resist, without metal deposition, and was found to be less than 10 nm/min. This boundary is set by the precision of the profilometer and the total etching time of 2' used in this test. This etching rate is much smaller than for silicon and enables us to neglect overetching of the crystal.

The step-by-step process is:

- **Substrate cleaning:** 5' in acetone with ultrasounds then 1' in isopropanol (IPA) and ultrasounds. Rinse in another bath of IPA for 30" and blow dry. Sample B has an extra step of cleaning in piranha (H_2SO_4:H_2O_2 3:1) for 10', followed by a rinse in three water beakers, then with IPA before blowing dry. Indeed, tests with piranha cleaning show a slight increase of the resonator internal quality factor. Both samples are then put on a hot plate at 115°C for 5' to remove any water left on the surface.

- **Metal deposition:** deposit 50±3 nm of niobium by sputtering. Niobium is deposited at a rate of 2 nm/s. During deposition, the $CaWO_4$ sample is surrounded by silicon rectangular pieces of same thickness (0.5 mm) to prevent metal deposition on the sample sides.

- **Resist coating:** clean the sample without ultrasounds because niobium does not stick as well on $CaWO_4$ as on silicon: 3' in acetone while moving the chip with tweazers, then twice 30" in IPA. The sample is then placed 3' on a hot plate at 110°C. Spin nLOF2020 resist: 4" at 8000 rpm (revolutions per minute) acceleration 4000, then 60" at 4000 rpm acceleration 1000. Soft bake for 90" at 110°C.

- **Optical lithography:** using Heidelberg μMLA (with dose 45 mJ/cm^2 and defoc 5). The nLOF resist is negative such that only parts of the sample where the metal needs to stay is exposed. This writing step takes a few seconds.

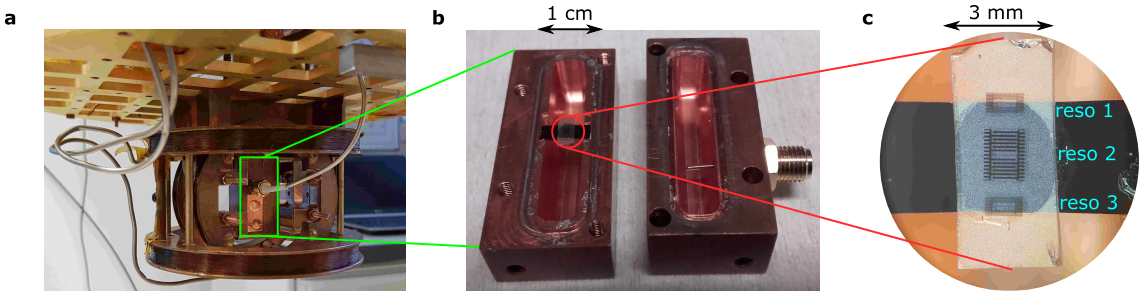

Figure 5.10 – **Sample A placed inside the 3D box a.** 3D box inside the Helmholtz coils which are anchored on the mixing chamber plate. **b.** Inside the 3D box. A copper antenna with tunable length couples to the box and resonator modes. **c.** Zoom on $CaWO_4$ sample A, with its three niobium resonators. The sample is glued on a silicon piece with vacuum grease.

- **Resist development:** post exposition bake 90" at 110°C. Then 1' in MF319 before rinsing for 1' in water.

- **Dry etching:** reactive ion etching at a base pressure of 12 μbar, with 10 sccm (standard cubic centimeters per minute) of Ar, 20 sccm of SF_6 and at a power of 50 W. Laser reflectometry indicates that the niobium is etched in 39". An overetch time of 11" is used. Silicon pieces are put around the $CaWO_4$ sample to avoid a plasma border effect where the sample borders are etched more slowly than its center.

- **Resist removal:** 15' in remover P1331 at 50-60°C. Rinse twice in water for 30". Clean again with 3' in acetone then twice 30" in IPA before putting the sample in the fridge.

5.2.3 Resonator microwave characterization at 10 mK

After resonator fabrication, the $CaWO_4$ sample is glued with vacuum grease on a silicon piece which size fits in the 3D copper box as shown in Figure 5.10c. The latter is beforehand glued on two notches on the sides of the cavity. An antenna consisting of a copper rod soldered on an SMA female connector enables us to measure the modes inside the cavity. Its length within the cavity can be adjusted which tunes the coupling rate κ_c of the box mode and hence on the resonator mode.

When cooled down to 10 mK, the resonator properties are measured with a VNA which displays the reflection coefficient S_{11} of the resonators. Figure 5.11 shows the measured reflection coefficient for resonator 3 of sample A. In particular, the internal loss rate κ_{int} decreases with power due to saturation of defects called two level systems or TLS [Wan+09].

Table 5.5 and Table 5.6 indicate the frequency ω_0, the coupling rate κ_c, the internal loss rate κ_{int} at single photon intra-resonator field, and total damping rate $\kappa_t = \kappa_c + \kappa_{\text{int}}$, all measured at 10 mK and zero magnetic field. These parameters were found to slightly vary from one experimental run to another.

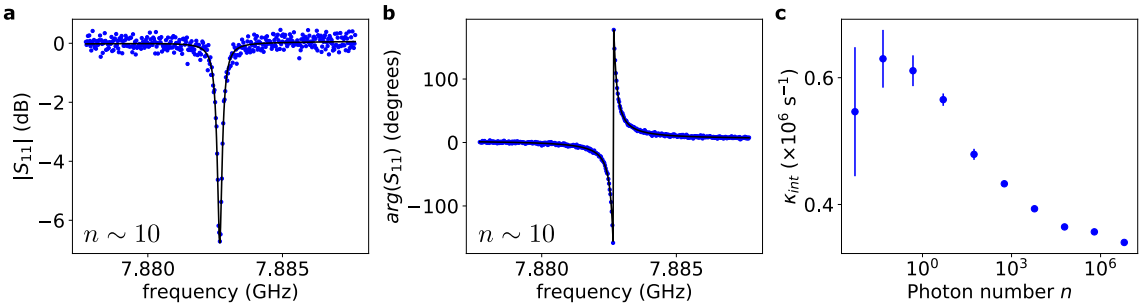

Figure 5.11 – **Measured reflection coefficient for resonator 3 of sample A. a.** and **b.** The reflection coefficient S_{11} is measured with about 10 photons in the resonator (blue dots). The black line shows a fit with Equation 3.6 multiplied by a linear background. **c.** Internal loss rate κ_{int} as a function of the number of photons in the resonator. These parameters were found to slightly vary from one run to another.

resonator property	reso 1	reso 2	reso 3
$\omega_0/2\pi$ (GHz)	7.025	7.508	7.881
κ_c ($\times 10^6$ s^{-1})	0.2	3.2	1.7
κ_{int} ($\times 10^6$ s^{-1})	1.0	0.6	0.6
κ_t ($\times 10^6$ s^{-1})	1.2	3.8	2.3

Table 5.5 – **Resonator properties of sample A measured at 10 mK and zero magnetic field.** The internal loss rate κ_{int} is given at single photon level. These values slightly vary from one run to another.

resonator property	reso 0	reso 1	reso 2	reso 3
$\omega_0/2\pi$ (GHz)	6.524	6.852	7.419	7.853
κ_c ($\times 10^6$ s^{-1})	0.3	0.1	5.7	5.7
κ_{int} ($\times 10^6$ s^{-1})	0.5	0.4	0.5	0.5
κ_t ($\times 10^6$ s^{-1})	0.8	0.5	6.2	6.2

Table 5.6 – **Resonator properties of sample B measured at 10 mK and zero magnetic field.** The internal loss rate κ_{int} is given at single photon level. These values slightly vary from one run to another.

The measured frequencies are slightly different from the simulated ones. We attribute these differences to two main reasons. First, optical lithography yields an uncertainty of ± 100 nm on the width of the features compared to the design, which may result in frequency shifts. Second, niobium kinetic inductance (which was neglected in the design) also adds a downwards frequency shift. One signature of the kinetic inductance contribution is that the frequency shift of resonators 0 and 1 appears to be larger than resonators 2 and 3, which is expected since the wire is also narrower.

5.2.4 Effect of the crystal orientation on the spin-resonator coupling constant g_0

These resonators allow us to detect electron spins located in the vicinity of the inductance wire. First the static magnetic field $\boldsymbol{B_0}$ must be applied such that the spin resonance frequency matches the resonator frequency. Then, we saw in Section 3.2.2.2 that the

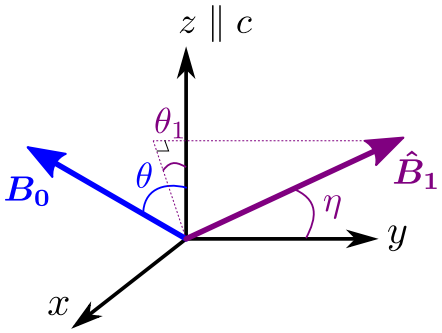

Figure 5.12 – **Choice of axes and angular coordinates for the magnetic fields.** z is aligned with the crystal c-axis and the x-axis is chosen such that $\boldsymbol{B_0}$ is in the (x, z)-plane. (x, y) is thus in the crystal (a, b)-plane. $\boldsymbol{B_0}$ makes an angle θ with the z-axis. The oscillating magnetic field $\hat{\boldsymbol{B}}_\mathbf{1}$ makes an angle η with the y-axis, and its projection in the (x, z)-plane, makes an angle θ_1 with the z-axis.

oscillating magnetic field $\hat{\boldsymbol{B}}_\mathbf{1}$ generated around the inductance wire of the resonator induces Rabi oscillations of the spins where, at resonance, the Rabi frequency is proportional to the spin-resonator coupling constant g_0.

The coupling constant g_0 can be be computed, taking into account the **g**-tensor anistropy. We use the same conventions as in Section 2.2.2, where the static magnetic field $\boldsymbol{B_0}$ makes an angle θ from the c-axis. The (x, y, z) coordinates are chosen such that z is along the c-axis and $\boldsymbol{B_0}$ is in the (x, z)-plane.

In the (x, y, z) basis, the magnetic fluctuations of the $\hat{\boldsymbol{B}}_\mathbf{1}$ field are defined by the following angles, according to Figure 5.12,

$$\delta\mathbf{B} = \delta B \begin{pmatrix} \sin\theta_1 \sin\eta \\ \cos\eta \\ \cos\theta_1 \sin\eta \end{pmatrix}. \tag{5.1}$$

We calculate analytically the coupling constant,

$$\begin{aligned} g_0 &= \frac{\mu_B}{\hbar} |\boldsymbol{\delta B} \cdot \mathbf{g} \cdot \langle e| \hat{\mathbf{S}} |g\rangle| \\ &= \frac{\mu_B}{\hbar} \delta B |\mathrm{g}_\parallel \langle e| \hat{S}_z |g\rangle \cos\theta_1 \sin\eta + \mathrm{g}_\perp (\langle e| \hat{S}_x |g\rangle \sin\theta_1 \sin\eta + \langle e| \hat{S}_y |g\rangle \cos\eta)| \\ &= \frac{\mu_B}{\hbar} \delta B |\mathrm{g}_\parallel \langle e| \cos\theta' \hat{S}'_z - \sin\theta' \hat{S}'_x |g\rangle \cos\theta_1 \sin\eta \\ &\quad + \mathrm{g}_\perp (\langle e| \cos\theta' \hat{S}'_x + \sin\theta' \hat{S}'_z |g\rangle \sin\theta_1 \sin\eta + \langle e| \hat{S}'_y |g\rangle \cos\eta)|. \end{aligned} \tag{5.2}$$

Now, if we consider the zero-nuclear-spin isotope of erbium, taking into account that $\langle e| \hat{S}'_z |g\rangle = 0$, $\langle e| \hat{S}'_x |g\rangle = 1/2$ and $\langle e| \hat{S}'_y |g\rangle = -i/2$, and replacing $\cos\theta' = \mathrm{g}_\parallel / \mathrm{g}_{\mathrm{eff}} \cos\theta$ and $\sin\theta' = \mathrm{g}_\perp / \mathrm{g}_{\mathrm{eff}} \sin\theta$,

$$g_0 = \frac{\mu_B \delta B}{2\hbar} |\frac{\mathrm{g}_\parallel \mathrm{g}_\perp}{\mathrm{g}_{\mathrm{eff}}} \sin\eta \sin(\theta_1 - \theta) - i\mathrm{g}_\perp \cos\eta|. \tag{5.3}$$

The expression above implies that the coupling constant is maximum when $\theta_1 - \theta = \pi/2$ modulo π corresponding to the fact that $\boldsymbol{\delta B}$ is perpendicular to $\boldsymbol{B_0}$. On the contrary, minimum coupling is achieved when $\boldsymbol{\delta B}$ and $\boldsymbol{B_0}$ are parallel (when $\theta_1 = \theta$ and $\eta = \pm\pi/2$).

Note that for the ^{167}Er isotope, Equation 5.3 has to be corrected by the actual matrix elements, which are modified because of the electron-nuclear hyperfine interaction.

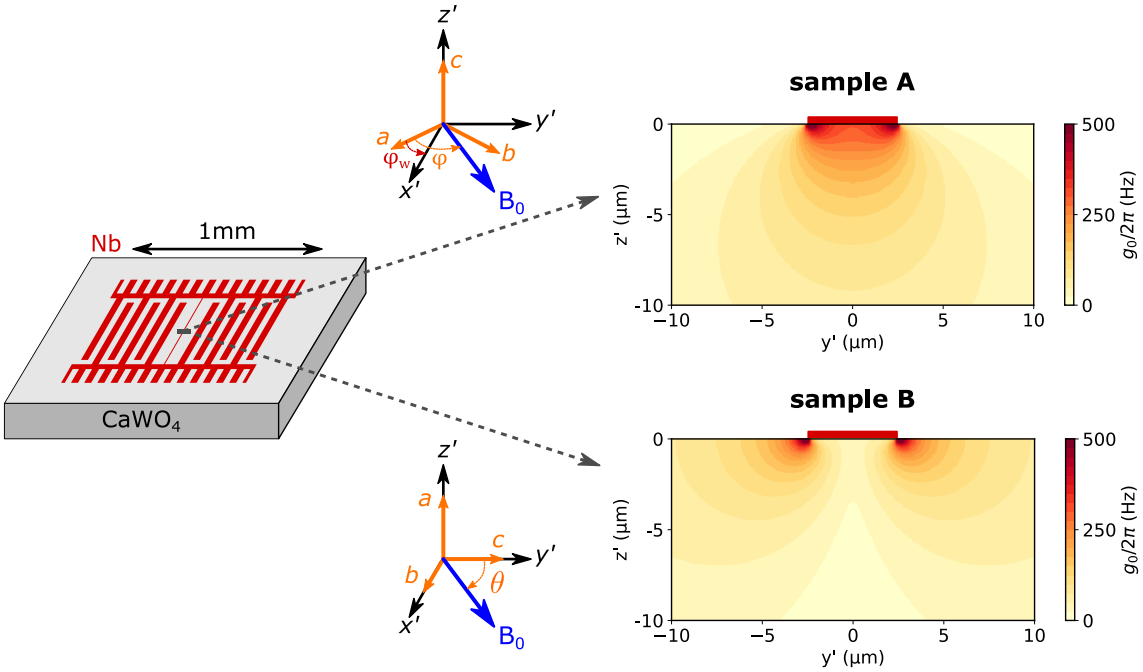

Figure 5.13 – **Coupling constant g_0** Sketch of one LC resonator patterned on top of the $CaWO_4$ sample. The cross-sections show the coupling g_0 between the resonator and erbium spins around a 5 μm-wide inductance wire when $\boldsymbol{B_0}$ is applied along its direction (x'-axis), with resonator frequency $\omega_0/2\pi = 7.881$GHz and impedance $Z_0 = 35\ \Omega$. *Top.* Sample A crystal orientation. The DC magnetic field $\boldsymbol{B_0}$ is applied in the (a, b) plane at an angle φ with respect to the a-axis, the resonator inductor making an angle φ_w with this axis. *Bottom.* Sample B crystal orientation. The DC magnetic field $\boldsymbol{B_0}$ is applied in the (b, c) plane at an angle θ with respect to the c-axis. The resonator inductor makes an angle $\theta_\mathrm{w} = \pi/2$.

The coupling constant for the $I = 0$ erbium spins can be computed according to the resonator orientation with respect to the crystal axes (see Figure 5.13). Due to the high aspect ratio of the inductance wire, the latter is considered as infinitely long and the oscillating field lies in the (y', z')-plane such that $\boldsymbol{\delta B} = \delta B_{y'}\boldsymbol{e_{y'}} + \delta B_{z'}\boldsymbol{e_{z'}}$

- for sample A, the static magnetic field $\boldsymbol{B_0}$ is always perpendicular to the c-axis such that $\theta = \pi/2$ and $\mathrm{g_{eff}} = \mathrm{g}_\perp$. The direction of $\boldsymbol{B_0}$ defines the x-axis. Hence $\boldsymbol{e_{z'}} = \boldsymbol{e_z}$ and $\boldsymbol{e_{y'}} = \cos\Delta\varphi\boldsymbol{e_y} + \sin\Delta\varphi\boldsymbol{e_x}$ where $\Delta\varphi = \varphi - \varphi_w$. The coupling constant expression simplifies into

$$g_0 = \frac{\mu_B}{2\hbar}\sqrt{(\mathrm{g}_\parallel\delta B_{z'})^2 + (\mathrm{g}_\perp\delta B_{y'}\cos\Delta\varphi)^2}. \tag{5.4}$$

- for sample B, $\boldsymbol{B_0}$ makes an angle θ from the c-axis which corresponds to $\boldsymbol{e_{y'}}$. Hence $\boldsymbol{e_{x'}} = \boldsymbol{e_x}$, $\boldsymbol{e_{y'}} = \boldsymbol{e_z}$, $\boldsymbol{e_{z'}} = -\boldsymbol{e_y}$ and $\theta_1 = 0$. The coupling constant expression simplifies into

$$g_0 = \frac{\mu_B}{2\hbar}\sqrt{\left(\frac{\mathrm{g}_\perp\mathrm{g}_\parallel}{\mathrm{g_{eff}}}\delta B_{y'}\sin\theta\right)^2 + (\mathrm{g}_\perp\delta B_{z'})^2}. \tag{5.5}$$

  In particular,

$$\begin{aligned} g_0(\theta = \pi/2) &= \frac{\mu_B}{2\hbar}\sqrt{(\mathrm{g}_\parallel\delta B_{y'})^2 + (\mathrm{g}_\perp\delta B_{z'})^2} \\ g_0(\theta = 0) &= \frac{\mu_B}{2\hbar}\mathrm{g}_\perp|\delta B_{z'}| \end{aligned} \tag{5.6}$$

These two cases can be actually expressed with the same formula

$$g_0 = \frac{\mu_B}{2\hbar}\sqrt{(\mathrm{g}_{z'}\delta B_{z'})^2 + (\mathrm{g}_{y'}\delta B_{y'}\cos\psi)^2}, \tag{5.7}$$

where x' is the wire direction, y' is the in-plane perpendicular axis, z' is pointing out-of-plane and ψ is defined as the angle between the in-plane magnetic field $\boldsymbol{B_0}$ and x'. For sample A, $\mathrm{g}_{z'} = \mathrm{g}_{\parallel}$, $\mathrm{g}_{y'} = \mathrm{g}_{\perp}$ and $\psi = \Delta\varphi$. For sample B, $\mathrm{g}_{z'} = \mathrm{g}_{\perp}$, $\mathrm{g}_{y'} = \mathrm{g}_{\parallel}\mathrm{g}_{\perp}/\mathrm{g}_{\mathrm{eff}}$ and $\psi = \pi/2 - \theta$.

To calculate the coupling constant g_0 for $I = 0$ erbium ions, the last step is to compute the vacuum fluctuations of the magnetic field $\boldsymbol{\delta B} = \delta B_{y'}\boldsymbol{e_{y'}} + \delta B_{z'}\boldsymbol{e_{z'}}$. This is done using COMSOL multiphysics, by computing the magnetic field generated by a current of 1 A, passing through a wire of 2 or 5 micron width depending on the resonator, and 50 nm thickness. This result is then rescaled by the ratio $\delta I/1\ A$ (with δI computed using Equation 3.11) to give $\boldsymbol{\delta B}$ which is inserted in Equation 5.7. Such a simulation result is shown in Figure 5.13 when the magnetic field is applied along the wire axis x'. For sample A, spins below the wire are more coupled to the resonator due to the larger g-factor. For sample B, spins on the side of the wire are more coupled.

5.3 Experimental setup for electron spin resonance at 10 mK

In this paragraph, we describe the experimental setup used for the measurements. It is a home-made ESR spectrometer operating between 10 mK and 1 K, with low-noise superconducting amplifiers, similar to the ones described in [Bie16; Bie+16b; Pro+17; Ran+20a].

5.3.1 Low temperature setup

The measurements are performed in a dilution refrigerator fabricated by the Finnish company Bluefors. This refrigerator is made of several plates thermalized at different temperatures which are shielded from each other with radiation shields. The bottom plate, called mixing chamber plate, is at the lowest temperature, which in normal operation mode is about 10 mK. A resistor placed on this plate enables to heat it up to typically 1 K by passing a small current.

Our microwave setup is shown in Figure 5.14. The input lines are filtered and attenuated at low temperature. A double circulator sends the input signal to the sample. Sample A is placed inside two perpendicular Helmholtz coils which generate a static magnetic field in the sample plane. With this setup, it is not possible to compensate for a small out-of-plane field component due to misalignment of the sample. Sample B was measured in an other Bluefors fridge with a 3D magnet, reaching up to 1 T on each axis, which enables to correct for sample misalignment with respect to the magnet axes.

The output signal is amplified by a superconducting parametric amplifier of the JTWPA type (for Josephson traveling-wave parametric amplifier) at 10 mK. For proper JTWPA operation, we found that it was necessary to isolate it using inner DC blocks. The output of the JTWPA is fed into a commercial high-electron-mobility transistor (HEMT) amplifier at 4 K, via a double circulator used to isolate the JTWPA from the microwave noise emitted by the HEMT. The microwave signal is finally amplified further at room-temperature using a Mini-Circuits amplifier. Two room temperature switches allow us to connect the setup to a VNA, for measuring the transmission coefficient, or to a pulse ESR setup which will be detailed in a following section.

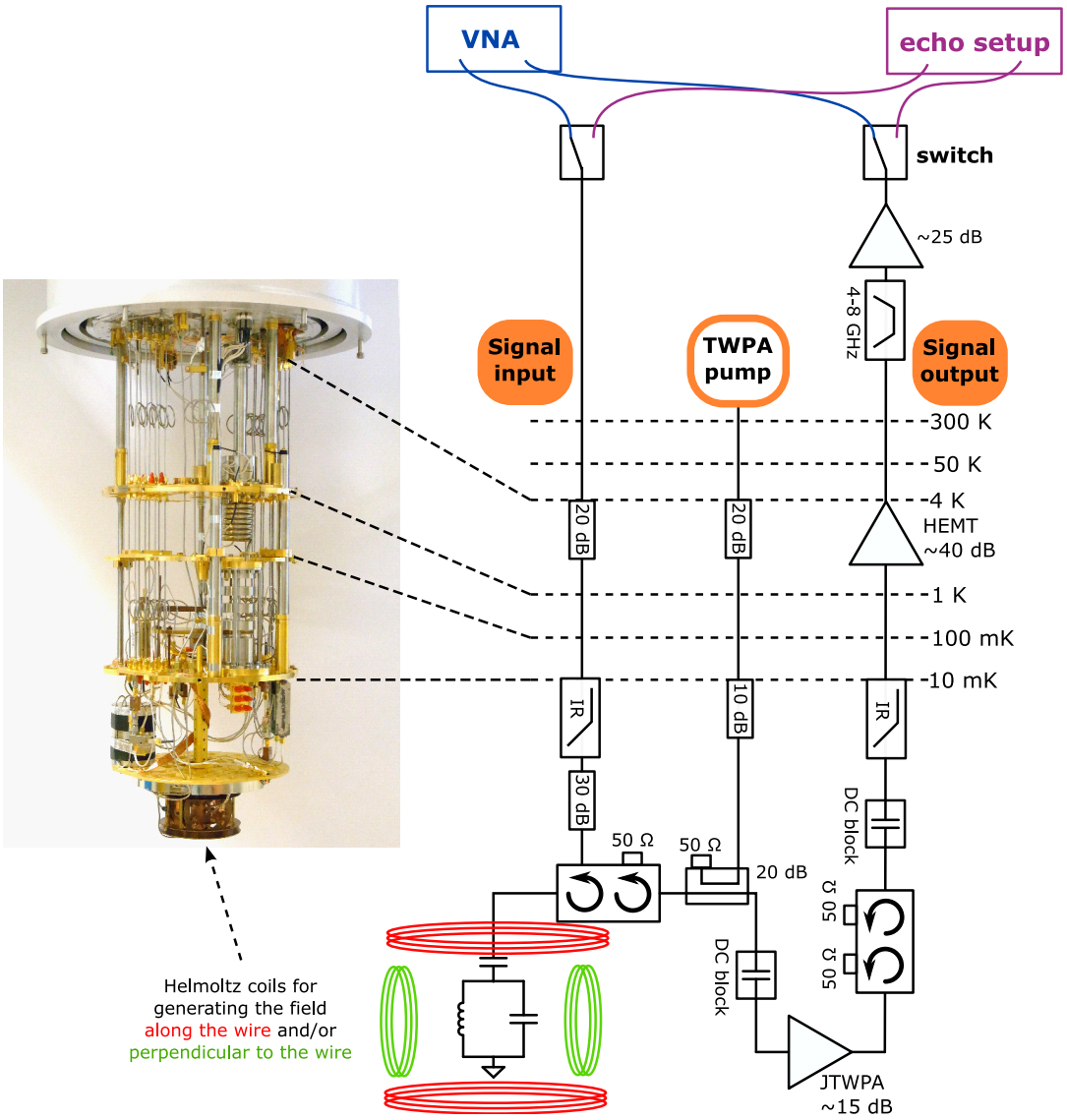

Figure 5.14 – **Microwave setup inside the Bluefors dilution refrigerator.** The input line is attenuated and filtered at low temperature before reaching the sample which is placed inside pairs of Helmholtz coils generating the static magnetic field $\boldsymbol{B_0}$. The output signal is amplified first at 10 mK using a Josephson traveling-wave parametric amplifier (JTWPA), then by a high electron mobility transistor (HEMT) and finally by an Mini-Circuits amplifier at room temperature. The JTWPA requires a microwave pump. At room-temperature, switches select whether the input and output ports are connected to a VNA or to a spin-echo setup.

5.3.2 JTWPA characterization

The JTWPA used in the setup was provided by Lincoln labs and enables signal amplification at 10 mK. Its working principle is described in [Mac+15]. It consists in a transmission line containing thousands of Josephson junctions. Gain is achieved by pumping the amplifier with a strong microwave signal at a frequency $\omega_p/2\pi \sim 6.0$ GHz. The effect of the pump is to modulate the Josephson inductance of the transmission line at $2\omega_p$, which leads to power gain by 4-wave mixing for signals having a frequency not too far from ω_p.

The JTWPA improves greatly the SNR. Indeed, the amplifying chain of the JTWPA, the HEMT and the room temperature (RT) amplifier provides a gain $G = G_{\text{JTWPA}} G_{\text{HEMT}} G_{\text{RT}}$

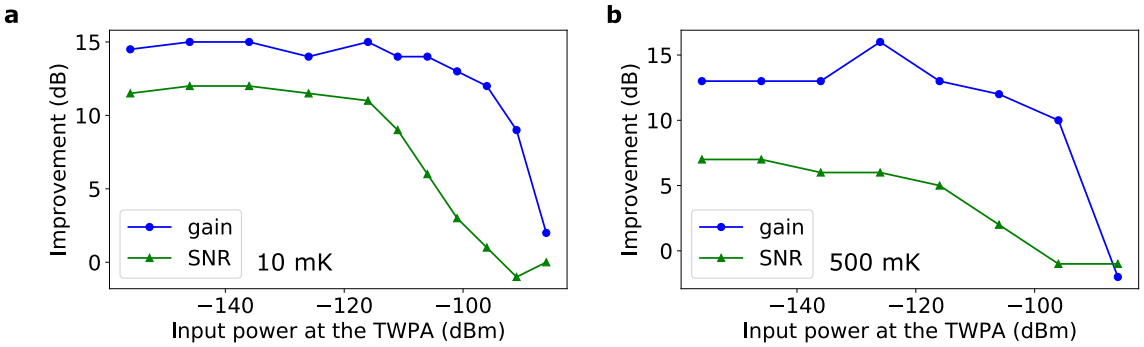

Figure 5.15 – **JTWPA characterization** Typical gain and SNR improvements measured with a spectrum analyzer when the JTWPA pump is switched on. This is measured at $\omega/2\pi = 7.88$ GHz. **a.** 10 mK measurement. **b.** 500 mK measurement. The JTWPA pump parameters (power and frequency) have been slightly adjusted for each temperature.

and a noise temperature of

$$T_N = T_{N,\mathrm{JTWPA}} + \frac{T_{N,\mathrm{HEMT}}}{G_{\mathrm{JTWPA}}} + \frac{T_{N,\mathrm{RT}}}{G_{\mathrm{JTWPA}} G_{\mathrm{HEMT}}}. \tag{5.8}$$

Therefore, if the gain of the JTWPA and the HEMT is sufficiently high, the noise temperature is dominated by the one of the JTWPA.

We show in Figure 5.15 the typical properties of the JTWPA. The gain curve is obtained by sending a continuous microwave tone at $\omega/2\pi = 7.88$ GHz and by measuring the power of the output microwave signal using a spectrum analyzer. The gain is the signal power enhancement when the JTWPA pump is turned on. We observe that the JTWPA gain is around 15 dB up to a certain input power (-100 dBm), above which the amplifier saturates.

The SNR is defined as the difference in dB between the output signal power at frequency ω and the background power level, measured for a given frequency bandwidth. The SNR improvement curve is obtained by comparing the SNR of the output signal when the JTWPA pump is turned on with the SNR when it is off, measured with the same frequency bandwidth. Figure 5.15 shows that the SNR improvement depends on the cryostat temperature and is about 12 dB at 10 mK and 7 dB at 500 mK. Moreover, the SNR improvement saturates at lower input power compared to the gain, at about -120 dBm.

From Figure 5.15 we can extract an approximate system noise temperature. According to its specifications, the HEMT input noise temperature is 4 K. The noise at the input of the amplifier chain can be neglected in front of the noise added by the amplifier chain itself. Thus an improvement of the SNR by 12 dB means that the noise temperature decreases by a factor 16 when turning the JTWPA pump on.

The measurement performed with samples A and B are done from 10 mK to 500 mK and the JTWPA shows a stable behaviour with positive gain up to the highest temperature. The pump frequency and power were adjusted at high temperature to find a good operational regime.

5.3.3 Magnetic field alignment in the 3D magnet for sample B

Sample A is placed inside two pairs of Helmholtz coils such that a magnetic field can be applied with an arbitrary orientation within the sample plane. However, there is no way to compensate for a small magnetic field out-of-plane component.

Sample B is measured inside an American Magnetics Inc (AMI) 3D magnet, which can apply a magnetic field along three perpendicular axes, X, Y, Z, and which can run in

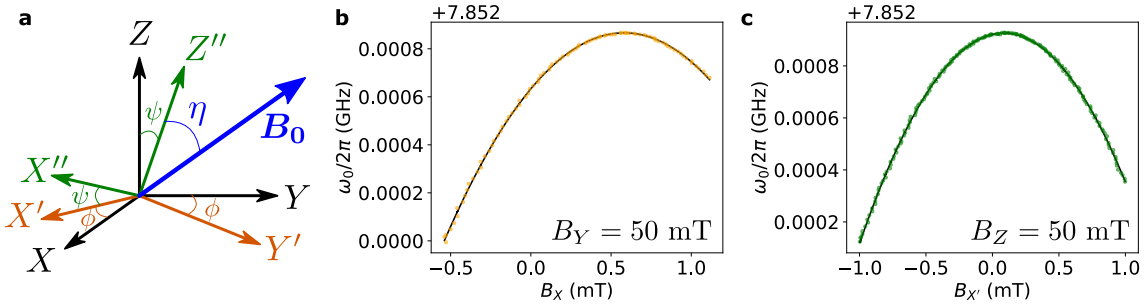

Figure 5.16 – **Magnetic field alignment of sample B in the 3D magnet. a.** Angles and axes notations used to align the magnetic field. The superconducting resonator plane corresponds to the $Y'Z''$ plane. The magnetic field $\boldsymbol{B_0}$ is applied in this plane with an angle η from the Z'' axis. **b.** Resonator frequency ω_0 as a function of a small magnetic field along X with 50 mT applied with magnet Y. The solid black is a parabolic fit in order to extract the correction field $B_{X,max} = 0.58$ mT at the maximum frequency, yielding $\phi = 0.67°$ ($\tan\phi = B_{X,max}/B_Y$). **c.** Resonator frequency ω_0 as a function of a small magnetic field applied along $X' = \cos\phi X - \sin\phi Y$ with 50 mT applied with magnet Z. The solid black is a parabolic fit, giving $B_{X',max} = 0.09$ mT, and thus $\psi = -0.10°$ ($\tan\psi = -B_{X',max}/B_Z$).

persistent mode. The sample is positioned such that its surface plane is approximately aligned with the YZ plane of the magnet. The magnetic field is precisely aligned within the sample plane with the following steps:

1. A magnetic field of typically 50 mT is applied with magnet Y.

2. The resonator frequency is measured as we sweep over a small magnetic field range with magnet X, typically between ±1 mT. The magnetic field is aligned with the superconducting resonator plane when the resonance frequency is maximum. This corresponds to a small correction angle ϕ. This step is illustrated in Figure 5.16b which shows the shift of the resonance frequency as a small correction field is applied in the X direction. After finding ϕ, the magnetic field is set back to zero field.

3. A magnetic field of typically 50 mT is applied with magnet Z.

4. The resonator frequency is measured as we sweep the magnetic field along the axis X', defined as $X' = \cos\phi X - \sin\phi Y$, where ϕ is the angle determined previously. The magnetic field value corresponding to the maximum of the resonance frequency yields the second correction angle ψ. This step is illustrated in Figure 5.16c which shows the shift of the resonance frequency as a small correction field is applied in the X' direction. Then the magnetic field is set back to zero.

5. Applying a magnetic field within the sample plane and making an angle η from the vertical direction is equivalent to applying the following field components on the X, Y, Z axes,

$$\boldsymbol{B_0} = B_0 \begin{pmatrix} -\cos\eta\sin\psi\cos\phi + \sin\eta\sin\phi \\ \cos\eta\sin\psi\sin\phi + \sin\eta\cos\phi \\ \cos\eta\cos\psi \end{pmatrix}_{X,Y,Z} \tag{5.9}$$

5.3.4 Homodyne setup for spin-echo measurements

The echo setup mentioned in Figure 5.14 is detailed in Figure 5.17. Microwave control pulses are generated with a microwave source (Rohde and Schwarz SMR20), at frequency ω_0 as local oscillator (LO), which output is mixed with pulses generated by an arbitrary

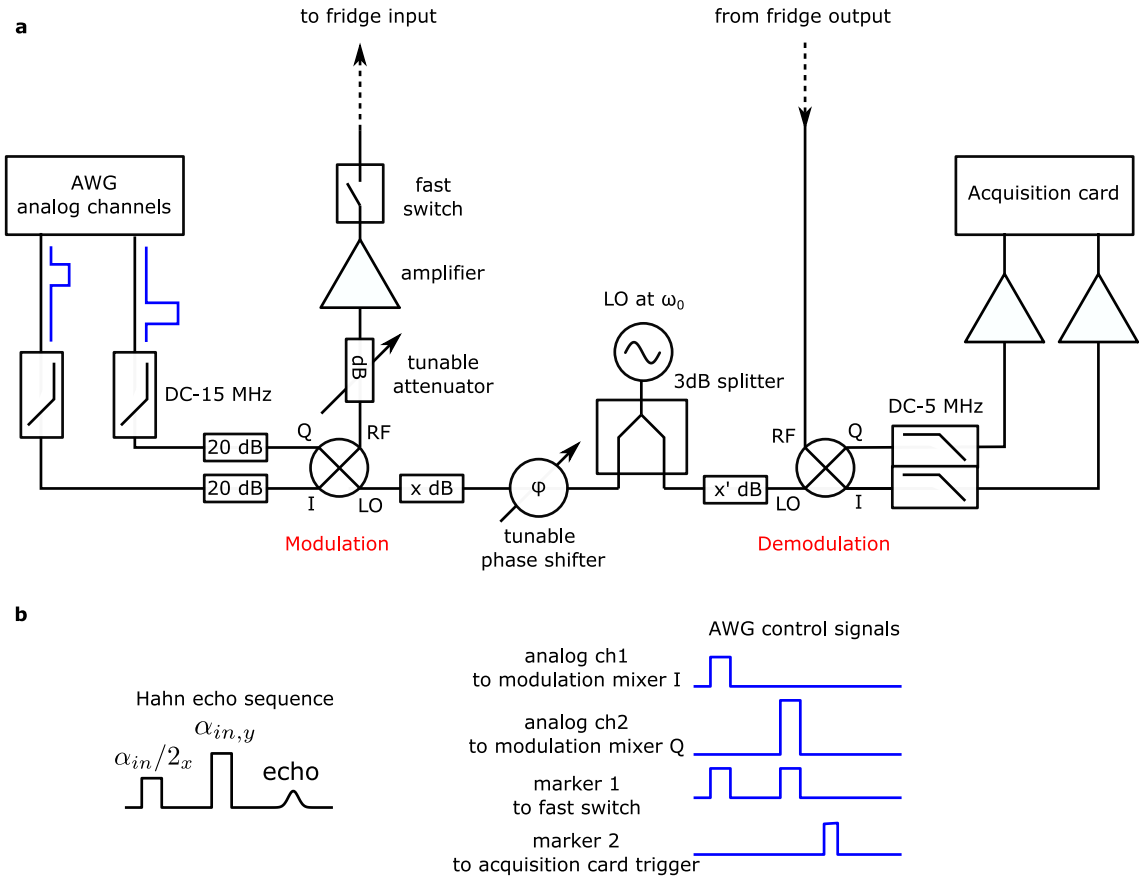

Figure 5.17 – **Spin-echo setup a.** Setup for sending microwave pulses to the resonator. DC pulse envelopes shaped by the arbitrary waveform generator (AWG) are modulated by an IQ mixer at the resonance frequency ω_0. This setup is called homodyne because the local oscillator (LO) is resonant with the resonator frequency. The output microwave signal from the fridge is demodulated to get a DC signal acquired by an acquisition card. The attenuation after the 3 dB splitter with x and x' dB is adjusted to match the IQ mixer specifications at the LO input. **b.** DC signals sent by the different AWG channels for a Hahn-echo sequence.

waveform generator (Tektronix AWG5014C) using an IQ mixer. Two analog AWG channels are used to drive the I and Q quadratures of the mixer, one marker AWG channel controls a fast switch which is closed only when pulses are sent to the fridge and remains open the rest of the time. One last marker AWG channel is used to trigger the acquisition. This setup is operated in homodyne mode, meaning that the pulse envelopes generated by the AWG are not modulated and that the radiofrequency (RF) signal sent to the fridge is at the same frequency as the LO.

After the IQ-mixer, the signal is attenuated with a variable attenuator and also amplified such that the maximum power arriving at the resonator input, achieved when the variable attenuator is set to 0 dB, is typically a few nW.

When the signal comes back from the fridge, it is demodulated with another IQ-mixer. After filtering and DC amplification, the signal is digitized with an acquisition card and saved on the measurement computer. The acquisition card records two quadratures, denoted $\tilde{I}(t)$ and $\tilde{Q}(t)$ which are in Volt unit. These quadratures are the sum of the output signal and a constant background, which is substracted in the data analysis, yielding $I(t)$ and $Q(t)$. These quadratures can be related to those of the output field $X_{out}(t)$ and $Y_{out}(t)$, defined as $X_{out} = \mathrm{Re}[\alpha_{out}]$ and $Y_{out} = \mathrm{Im}[\alpha_{out}]$, by the equation $I + iQ = \sqrt{G}(X_{out} + iY_{out})e^{i\phi}$,

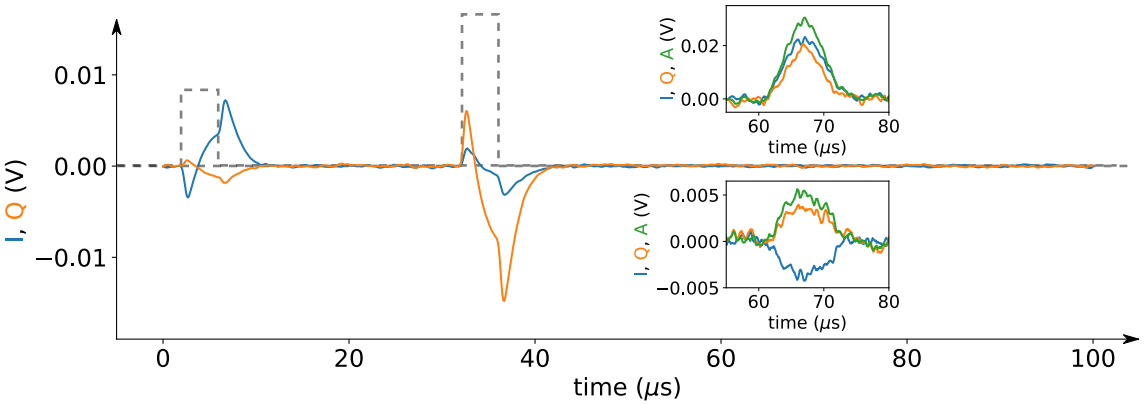

Figure 5.18 – **Echo measurement with a Hahn-echo sequence.** Measured I and Q quadratures. The AWG control pulses are shown in dashed grey lines (with arbitrary scale compared to the measurement). They consist in a first pulse of amplitude $V_{in}/2$ sent to the I port of the IQ-mixer and a second pulse of amplitude V_{in} sent to the Q port, spaced by $\tau = 30$ μs. The LO frequency matches the resonator frequency $\omega_0/2\pi = 7.88$ GHz. The reflected pulses (superposed with the control pulses) are measured with 72 dB added attenuation to avoid saturation of the amplifiers and the JTWPA pump is turned off. The sequence is repeated every 10 ms and averaged about 10^4 times. The insets show the spin echo occurring at time 2τ after the first pulse. They show the I and Q quadratures (in blue and orange respectively), plus the amplitude A (in green) defined as $A = \mathrm{Re}([I+iQ]e^{-i\phi_{\mathrm{echo}}})$. The top inset is measured with 36 dB input attenuation, 4 s repetition time, 100 averages, and the JTWPA pump is switched on. The bottom inset is measured with 36 dB input attenuation, 4 s repetition time, 300 averages, and the JTWPA pump is switched off.

G being the total gain of the measurement chain. As explained in Chapter 3, the field quadratures, X_{out} and Y_{out}, are related to the intra-resonator field via the input-output theory and therefore contain the spin-echo signal.

Typical $I(t)$ and $Q(t)$ quadratures obtained during a Hahn-echo measurement are shown in Figure 5.18. In general, the reflected control pulses saturate the amplifiers. In this figure, they are thus measured with 72 dB attenuation at the fridge input. The spin echoes are plotted in insets with just 36 dB input attenuation and with the JTWPA pump either turned on or off. For measuring the spin-echo, the repetition time of the Hahn-echo sequence needs to be adjusted according to the spin relaxation time, which is 4 s for this measurement.

IQ mixer calibration

An IQ mixer is a device with four ports: the LO, which receives continuous microwave power at a given frequency ω_0, the quadratures I and Q and the RF port. It is symmetric and can be used either for modulating the input I and Q signals at the LO frequency, or for demodulating an RF signal by deconvoluting the modulation at ω_0 from the RF input yielding the two quadratures I and Q.

When working in modulation mode, the RF output of an ideal IQ mixer is

$$V_{RF}(t) = V_I(t)\cos(\omega_0 t + \phi) + V_Q(t)\sin(\omega_0 t + \phi), \tag{5.10}$$

where ϕ is the phase of the LO. This phase can be adjusted with the tunable phase shifter (see Figure 5.17a). Note that the ideal Hahn-echo sequence consists in a first microwave pulse generating a rotation on the Bloch sphere around a transverse axis which we call x and a second pulse which applies a rotation around the perpendicular transverse axis y

(see Figure 3.10). This translates in applying two pulses where the second microwave pulse is dephased by $\pi/2$ from the first one, and this is achieved by sending the first pulse to I and the second one to Q.

However, the IQ-mixer has several imperfections:

- **offsets**: when I and Q are set to 0 V, there is an RF leakage which is corrected by adding a constant voltage offset on each channel on the AWG.
- **amplitudes**: when applying 1 V on I and Q separately, the RF microwave power is different. This is corrected by changing the relative amplitudes of the two analog channels on the AWG.
- **phase**: the relative phase offset added by the IQ-mixer on the Q quadrature is not exactly $\pi/2$. The phase offset can be measured by sending a modulated signal on I and Q as $V_I(t) = \sin(\Delta\omega t)$ and $V_Q(t) = \cos(\Delta\omega t + \psi)$. This generates two sidebands at $\omega_0 \pm \Delta\omega$. If the mixer was perfect, one of the sidebands should be suppressed at $\psi = 0$. In practice, this sideband is suppressed at finite ψ. To correct for this error, any pulse envelope, which can be characterized by a complex number Z in the ideal IQ-plane, is sent to the IQ-mixer with $V_I(t) = \mathrm{Re}[Z(t)] - \mathrm{Im}[Z(t)]/\tan\psi$ and $V_Q(t) = \mathrm{Im}[Z(t)]/\cos\psi$.

All these imperfections are measured by connecting the RF output of the IQ-mixer to a spectrum analyzer. The signals generated by the AWG are corrected to account for the measured errors. In particular, these imperfections are frequency dependent and must be changed when varying the LO frequency.

Echo amplitude averaging

In the IQ plane, the echo can be described with a time-dependent envelope and a constant phase, $A(t)e^{i\phi_{\mathrm{echo}}}$. The integrated echo amplitude A_e is the result of a time average over typically the FWHM T of the echo signal, $A_e = \mathrm{Re}\left(e^{-i\phi_{\mathrm{echo}}}\{(1/T)\int_t [I(t) + iQ(t)]dt\}\right)$.

To have sufficient signal-to-noise ratio (SNR), the echo amplitude is computed using an average of N individual echo traces as follows,

$$A_{e,\mathrm{phase}} = \mathrm{Re}\left(e^{-i\phi_{\mathrm{echo}}}\frac{1}{N}\sum_{n=1}^{N}\{\frac{1}{T}\int_t [I_n(t) + iQ_n(t)]dt\}\right). \tag{5.11}$$

This is called quadrature averaging. If the noise in each quadrature is a white noise, the SNR is expected to increase as $\sqrt{N}$.

Another way for computing the echo amplitude is to get rid of the echo phase and to average the echo signal in magnitude. We choose to define the magnitude-averaged echo amplitude as

$$A_{e,\mathrm{mag}} = \sqrt{\frac{1}{N}\sum_{n=1}^{N}\{\left[\frac{1}{T}\int_t I_n(t)dt\right]^2 + \left[\frac{1}{T}\int_t Q_n(t)dt\right]^2\}}. \tag{5.12}$$

It is worth noticing that this quantity, contrarily to the previous one, is always positive. In the limit of a large number of traces N and with white noise, the echo amplitude $A_{e,\mathrm{mag}}$ converges towards $\sqrt{S^2 + C}$, where S is the actual signal and C is a noise offset which equals $2\sigma_N^2/M$, where σ_N^2 is variance of the noise on each quadrature and M is the number of data points used for the time integral of each echo.

Chapter 6

Spectroscopy

In this chapter, we present spectroscopic characterization of the erbium spin magnetic properties at millikelvin temperatures, in the spectrometer described previously. We focus on its field-dependence, linewidth, and concentration. All measurements presented in this chapter are performed using high-power microwave pulses, thus probing spins in the bulk of the crystal.

6.1 Field-sweep echo spectroscopy and rotation pattern

In this section, we show field-sweep echo measurements of samples A and B over a large magnetic field amplitude and orientation range. Hahn-echoes are measured for each magnetic field value B_0, which is swept over a chosen range with a given orientation. For the pulse sequence, short delays of $\tau \sim$ 30-40 μs$\ll T_2$ are chosen. As explained in Chapter 5, the two samples have different crystal orientations. As a result, the field is rotated in the (a, b)-plane for sample A, and in the (b, c)-plane for sample B.

6.1.1 Sample A

Rotation pattern

A field rotation in the (a, b)-plane is performed with resonator 3 in Figure 6.1. We observe several lines, some of them being angular-independent in the (a, b)-plane, as expected from S_4 symmetry, and others not. In particular, the most intense lines follow a similar angular dependence as those observed in Figure 5.4. Thus they belong to two subgroups which effective **g**-tensors are shifted by 90°.

At the resonator frequency, $\omega_0/2\pi = 7.881$ GHz, the erbium in S_4 symmetry is expected at $B_0 = 67.2$ mT, which matches one of the angular-independent lines of the spectrum. Other angular-independent lines between 90 and 110 mT are observed. Interestingly, these lines were not visible in the 9 K spectrum of Figure 5.4. One hypothesis is that they belong to the hyperfine structure of Tb^{3+}, which was observed in Figure 5.1b and whose effective g-factor is very sensitive to a small $\boldsymbol{B_0}$ misalignment from the (a, b)-plane [FH62]. Moreover, it can be seen in Figure 6.1 that the linewidth of the S_4-symmetry lines is angular dependent and this will be studied in more detail in a following section.

Spectroscopy at $\varphi = 47°$

To confirm that the line at $B_0 = 67.2$ mT is indeed erbium, we measure its gyromagnetic ratio. For that, we compare spectra taken with the three resonators, in the vicinity of the expected erbium resonance. The data are taken with $\boldsymbol{B_0}$ parallel to the crystal short edge, i.e. $\varphi = \varphi_c = 47°$ (see Chapter 5).

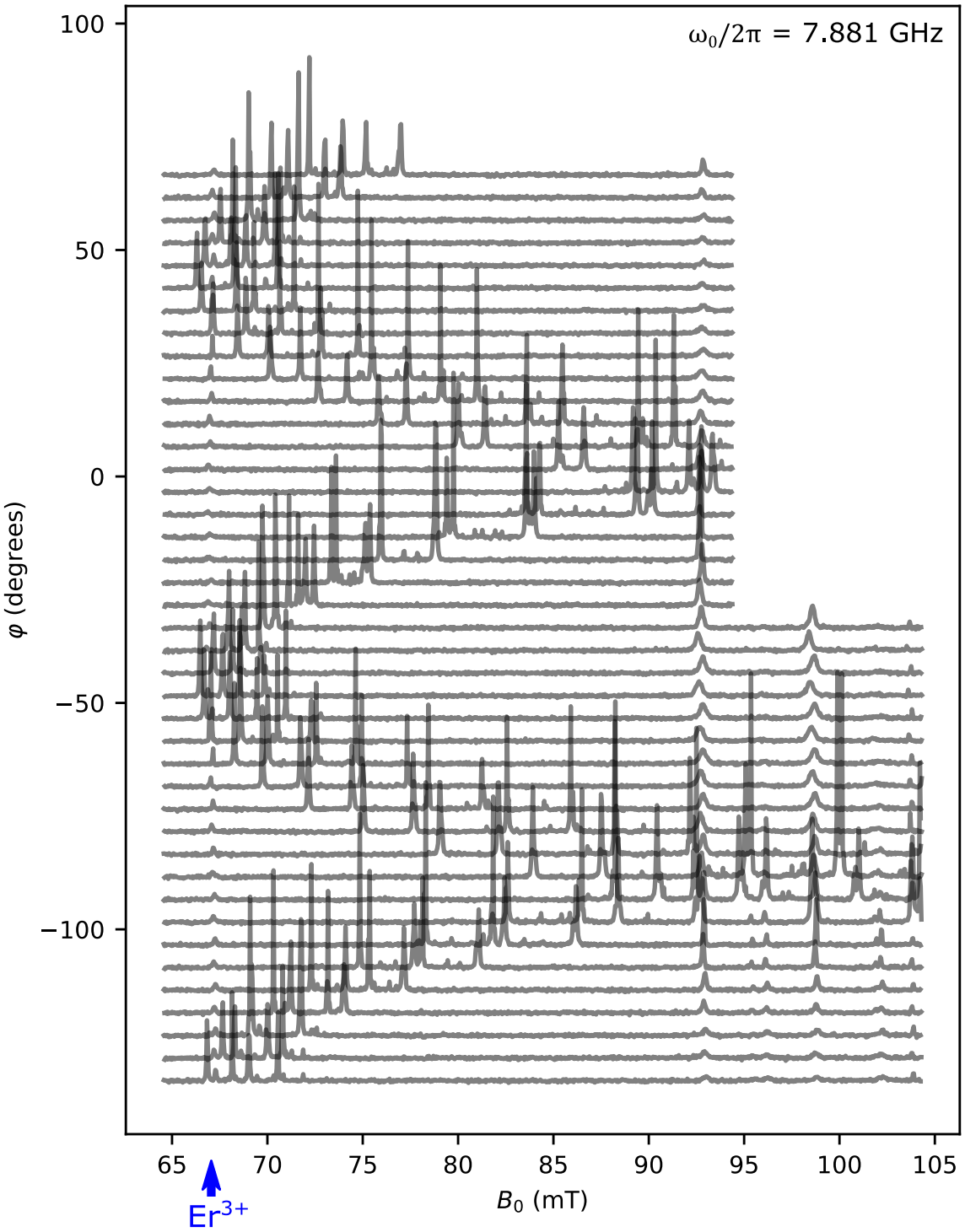

Figure 6.1 – **Rotation pattern of sample A in the (a, b)-plane with spin-echoes using resonator 3 at 10 mK.** The erbium line is the smaller peak at 67.2 mT and its resonance frequency is independent of φ as expected. A few intense lines demonstrate a strong angular dependence in the (a, b)-plane.

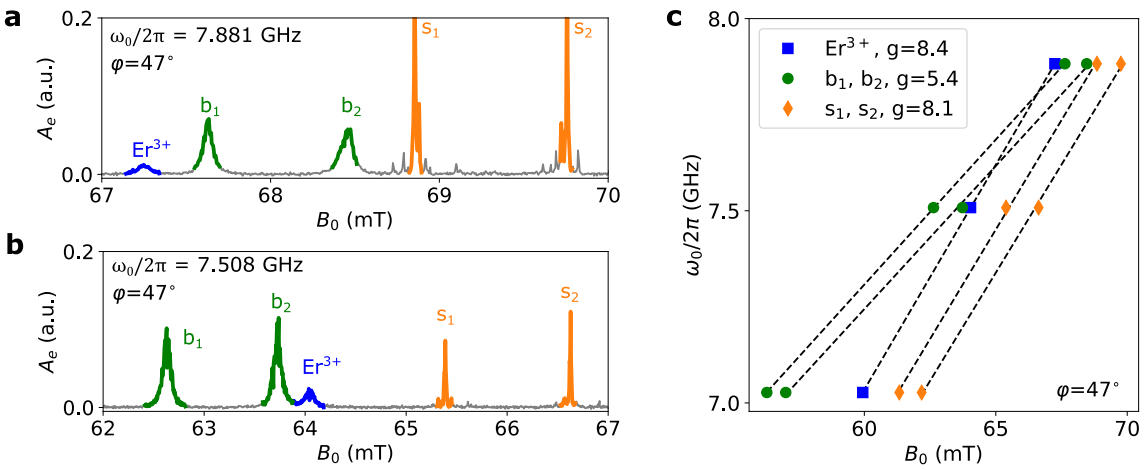

Figure 6.2 – **Hahn-echo spectroscopy in sample A at 10 mK with magnetic field angle $\varphi = 47°$. a.** Spectrum recorded with resonator 3, at frequency $\omega_0/2\pi = 7.881$ GHz. The erbium line is the peak at 67.2 mT. Pairs of broad peaks (b_1, b_2) and of sharp peaks (s_1, s_2) are observed. **b.** Spectrum recorded with resonator 2, at frequency $\omega_0/2\pi = 7.508$ GHz. **c.** Resonance frequency as a function of the magnetic field B_0 for each of the five transitions detected in a and b. Dashed lines are linear fits which give the g-factor shown in the legend within a standard error of 3%.

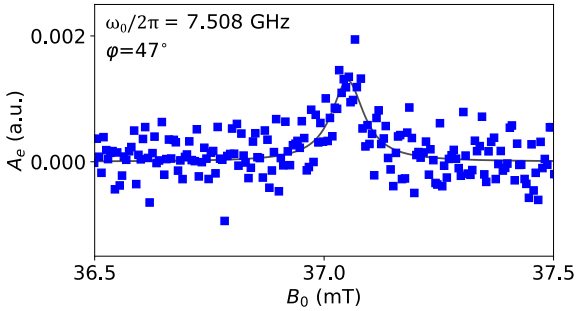

Figure 6.3 – **Hahn-echo spectroscopy of the first hyperfine transition of ^{167}Er in sample A at 10 mK.** The Lorentzian fit (solid line) gives a FWHM of 0.09 ± 0.01 mT which corresponds to an inhomogeneous linewidth of $\Gamma_{\text{inh}}/2\pi = 10 \pm 1$ MHz.

The field-sweep echo spectra are shown in Figure 6.2a and b. The echo integral is plotted as a function of B_0, for $\tau = 30$ μs, around the expected erbium resonance value. As expected from the previous rotation pattern at this orientation, we observe several resonance lines. Comparing the two spectra allows us to classify these resonances into one pair of broad peaks (labelled b_1, b_2), and one pair of sharp peaks (labelled s_1, s_2), each of these sharp peaks containing several narrow lines. These spectra, performed with all three resonators, are used to extract the effective g-factor of each transition for this $\boldsymbol{B_0}$ orientation from the dependence of their resonance magnetic field on the resonator frequency. As shown in Figure 6.2c, one peak is consistent with the g-factor of erbium $g_\perp$=8.38.

Moreover, a transition at $B_0 = 37.05$ mT is observed at $\varphi = 47°$ with resonator 2, at $\omega_0/2\pi = 7.508$ GHz. The spin-echo spectroscopy at 10 mK is shown in Figure 6.3. This transition is consistent with the first hyperfine level of ^{167}Er and we note that the FWHM linewidth of this hyperfine level is similar to that of the I=0 erbium spins.

The peaks (b_1, b_2, s_1, s_2) are the angular-dependent lines of Figure 6.1. A more detailed analysis, with relaxation and coherence time measurements, shows that the broad peaks (b_1, b_2) behave similarly to the erbium line while the sharp peaks (s_1, s_2) behave very

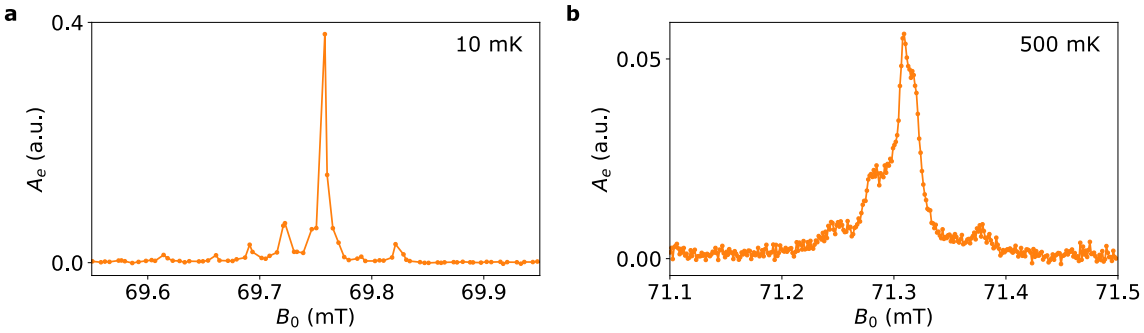

Figure 6.4 – **Hahn-echo spectroscopy in sample A of the sharp peak s_2, with $\varphi = 47°$, at 10 mK and 500 mK. a.** Spectrum recorded at 10 mK with resonator 3, at $\omega_0/2\pi = 7.881$ GHz. This spectrum is a zoom of the data plotted in Figure 6.2a. **b.** Spectrum recorded at 500 mK with the same resonator. The resonance magnetic field is slightly different compared to subplot a, due to a small change in the $\boldsymbol{B_0}$ orientation as the two data were taken in different runs.

differently. In particular, the signal of (s_1, s_2) saturates very quickly at 10 mK, suggesting that the relaxation time is much longer than for erbium. Therefore, it is possible that (b_1, b_2) correspond to rare-earth ions in non-tetragonal sites (and to the lines seen in Figure 5.4), whereas the origin of (s_1, s_2) is unknown.

Figure 6.4 shows two spectra of one of the sharp peaks, s_2, measured at 10 mK and 500 mK. At 10 mK, the line is saturated as the repetition time of 2 s between Hahn-echo sequences is not sufficient for the spins to relax. At 500 mK, the line relaxes faster, enabling proper measurement. In this measurement, the Hahn-echo sequence is repeated every second. The structure around the peak (visible both at 10 mK and 500 mK) is likely due to the hyperfine coupling with nearby tungsten nuclear spins.

6.1.2 Sample B

Rotation pattern

For sample B, we identify impurities with a rotation pattern in the (b, c)-plane. The field rotation spectrum is shown in Figure 6.5. As in the Bruker spectrometer measurements of Section 5.1.2, four Kramers ions are easily identified: Er^{3+}, Yb^{3+}, Ce^{3+} and Nd^{3+}. Contrarily to Figure 5.2, only one satellite of the zero-nuclear-spin ytterbium line is visible. This can be explained by the fact that only the lowest hyperfine level of ^{171}Yb is populated at 10 mK and confirms that this line is likely ^{171}Yb, despite its strong relative concentration with respect to its natural abundance. The group of six lines moving around 250 mT is Mn^{2+}. Note that manganese has an electron spin $S = 5/2$ and a nuclear spin $I = 5/2$, where only the electronic ground state is populated at 10 mK. The visible transitions therefore correspond to the six hyperfine transitions from $S = -5/2$ to $S = -3/2$. Contrarily to sample A, there is no other electron spin transition in the vicinity of the expected erbium line, the pairs of peaks (b_1, b_2, s_1, s_2) are not seen. Moreover, there is no trace of the isotropic iron line, expected at 130 mT, and all the isotropic peaks between 90 and 110 mT observed in sample A are absent. Overall, sample B seems to contain much less unknown impurities than sample A.

Moreover, the resonator reflection coefficient S_{11} is also measured for each magnetic field value of this rotation pattern. Figure 6.6 shows the resonator frequency and internal quality factor as the magnetic field is swept. The 3D magnet used for studying sample B enables us to align precisely the magnetic field with respect to the crystal surface (see Section 5.3.3) and the decrease of resonance frequency with magnetic field is attributed to

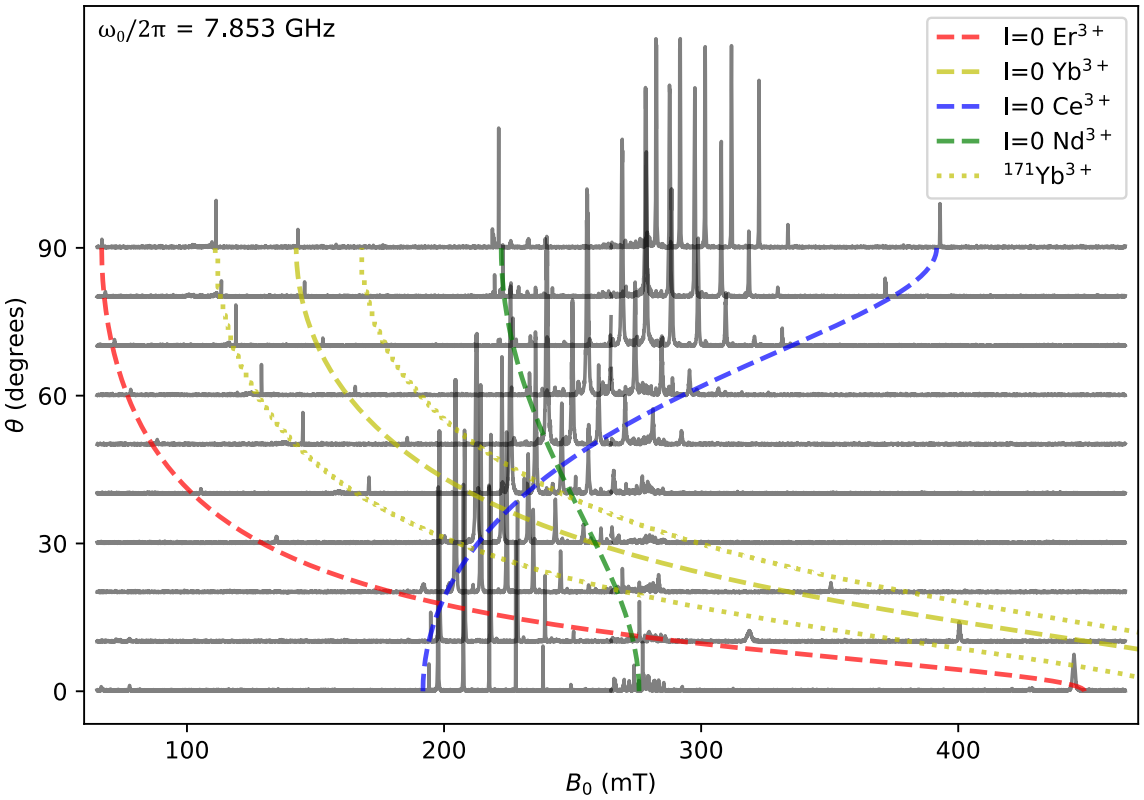

Figure 6.5 – **Rotation pattern of sample B with spin-echoes using resonator 3 at 10 mK.** Hahn-echo spectroscopy with the field rotated in the crystal (b, c)-plane. $\theta = 0°$ corresponds to the field aligned with the c-axis, which is perpendicular to the wire direction, while $\theta = 90°$ corresponds to the field aligned with the b-axis, which is in the wire direction. The same Kramers ions as in Figure 5.2 are identified. Interestingly the highest hyperfine transition of ^{171}Yb is not visible because most of these spins are in the lowest hyperfine level at 10 mK.

kinetic inductance [Hea+08]. The internal loss rate is rather stable up to 470 mT, with sharp peaks corresponding to intersections with electron spin transitions as explained in Section 3.3.0.1. In particular, the manganese lines of Figure 6.5 are very visible and are cut from the plot. Moreover, a broad peak is observed around 250 mT and corresponds roughly to g = 2 spins.

Magnetic field resilience up to 500 mT

The internal loss rate shown in Figure 6.6 is measured with resonator 3, which is over-coupled, with $\kappa_c = 5.7 \times 10^6$ s^{-1} (see Table 5.6). To get a better measurement of the internal loss rate, the continuous-wave spectroscopy is repeated with other under-coupled resonators. Figure 6.7 and Figure 6.8 show such measurements, performed with resonator 0, which coupling rate is $\kappa_c = 0.3 \times 10^6$ s^{-1}, and resonator 1, which coupling rate is $\kappa_c = 0.1 \times 10^6$ s^{-1}. The resonator frequency ω_0 and internal loss rate κ_{int} are plotted as a function of B_0 from 0 to 500 mT for several values of θ. Narrow peaks in the internal loss rate indicate the presence of an electron spin transition, in particular the manganese transitions which are very strong.

These measurements show that the internal loss rate does not increase up to 500 mT which demonstrates good magnetic field resilience properties of the niobium resonators. They confirm the presence of a broad peak around 230 mT which is noticeably stronger at $\theta = 90°$ than at $\theta = 0°$. This could be attributed to g$\sim$ 2 defects on the metallic surface of

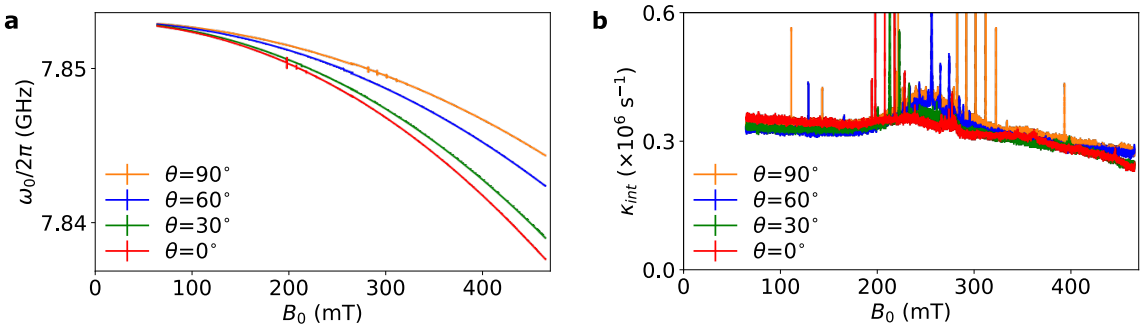

Figure 6.6 – **Rotation pattern of sample B with reflection coefficient measurements of resonator 3**. This data is measured simultaneously with the spectrum of Figure 6.5. **a.** Resonator frequency as a function of B_0 for several angles θ. **b.** Internal loss rate κ_{int} as a function of B_0 for several angles θ.

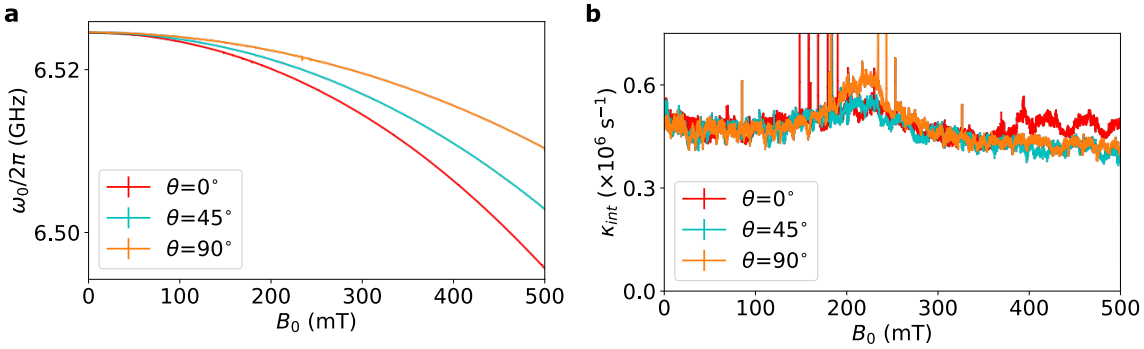

Figure 6.7 – **Rotation pattern of sample B with reflection coefficient measurements of resonator 0 a.** Resonator frequency as a function of B_0 for several angles θ. **b.** Internal loss rate κ_{int} as a function of B_0 for several angles θ.

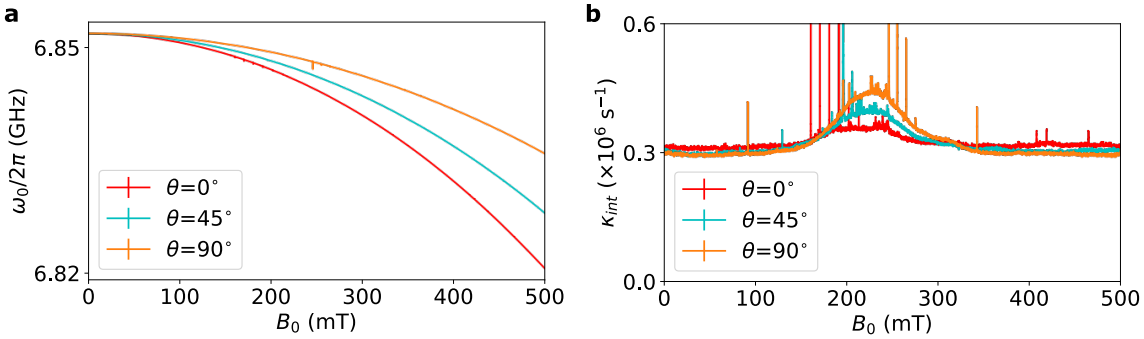

Figure 6.8 – **Rotation pattern of sample B with reflection coefficient measurements of resonator 1 a.** Resonator frequency as a function of B_0 for several angles θ. **b.** Internal loss rate κ_{int} as a function of B_0 for several angles θ.

the resonators which are not excited when the magnetic field is applied perpendicular to the wire axis. These measurements do not reproduce the slight decrease of κ_{int} with B_0 observed in Figure 6.6b.

6.2 Erbium linewidth

After identification of erbium in both samples, we focus on its lineshape. Sample A is particularly interesting for this study. Indeed, given its orientation, it is possible to

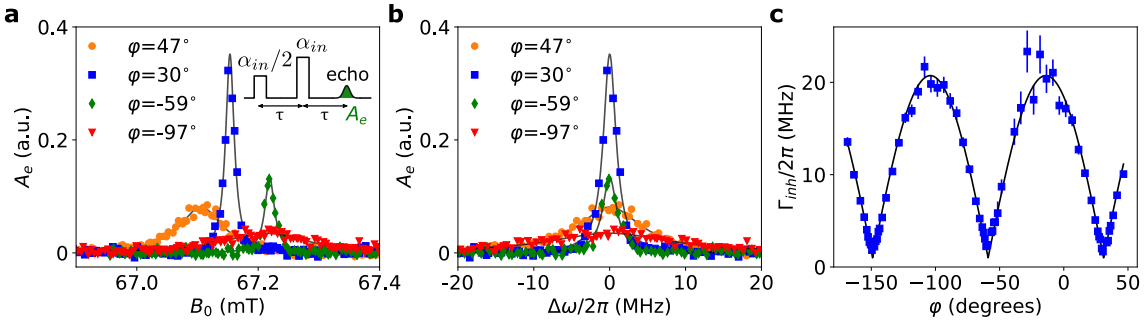

Figure 6.9 – **Erbium lineshape in sample A a.** Spin-echo integral A_e as a function of B_0, around 67.2 mT, measured with resonator 3. Each data point is averaged twice and the Hahn-echo sequence, with 4 μs pulses, is repeated every 4 s. Full symbols are measurements for various values of φ and solid lines are Lorentzian fits to the data. **b.** Same data where the x-axis is converted into a frequency detuning $\Delta\omega$. **c.** Full-width-at-half-maximum (FWHM) linewidth $\Gamma_{\text{inh}}/2\pi$ as a function of φ. The solid line is a fit following the model of [MG66; Mim65], yielding a typical magnitude of inhomogeneous electric fields along the c-axis of 32 kV/cm.

study the linewidth as a function of φ, at constant magnetic field amplitude B_0, which is convenient to identify broadening mechanisms.

6.2.1 Sample A

The measured erbium lineshapes at various angles φ are shown in Figure 6.9a. They are fitted using Lorentzian shapes with a FWHM linewidth Γ_{inh}. The resonance magnetic field slightly changes with the angle which is attributed to a small hysteresis of our applied magnetic field. The magnetic field axis can be converted into a frequency detuning $\Delta\omega$ using the erbium g-factor as shown in Figure 6.9b.

The fitted linewidth Γ_{inh} is plotted in Figure 6.9c as a function of φ and varies by a factor 20. Its angular dependence is fitted with Mims model described in Section 2.5. Equation 2.50 leads to $\Delta E_c = 32.0 \pm 0.6$ kV/cm. This value is approximately three times smaller than measured by Mims and Gillen in their ppm doped crystal [MG66]. We attribute this difference to our lower doping concentration and hence reduced charge defect density. Moreover, the fit yields $\varphi_0 = 31 \pm 0.2°$ which is the angle at which the spin transition frequency becomes insensitive to E_c and this is in agreement with Mims measurement and calculation.

Figure 6.10 shows the narrowest measured erbium linewidth, with $\Gamma_{\text{inh}}/2\pi = 1.5$ MHz. These data were measured with resonator 2, while the narrowest linewidth measured with resonator 3, in the data of Figure 6.9c, is 1.7 MHz. The fit to $\Gamma_{\text{inh}}(\varphi)$ gives a minimum residual linewidth $\Gamma_{\text{inh}}(\varphi_0)/2\pi = 1.0 \pm 0.2$ MHz (the corresponding line could unfortunately not be measured because of the fortuitous overlap of the erbium line with peaks b_1, b_2, s_1, s_2). To our knowledge, this is the narrowest inhomogeneous linewidth reported for erbium electron spins, supporting the application of erbium to microwave-optical conversion [WCL14]. This residual linewidth at φ_0 has several contributions: there is the dipolar coupling to nuclear spins, the dipolar coupling to paramagnetic species in the sample, the spin excitation bandwidth and the possibility of a residual sensitivity of the erbium g-factor to electric fields, due to a slight misalignment of $\boldsymbol{B_0}$ from the (a, b)-plane. We showed in Section 2.5.2.1 that the erbium dipolar linewidth from the tungsten nuclear spin bath when $\boldsymbol{B_0} \perp c$ is $\Gamma_{dd,\text{W}}/2\pi = 130$ kHz. The dipolar linewidth caused by paramagnetic impurities can be estimated using the concentrations of Table 5.1 in Equation 2.46 and summing all the contributions from different electron spins, yielding $\Gamma_{dd}/2\pi = 1.7$ kHz.

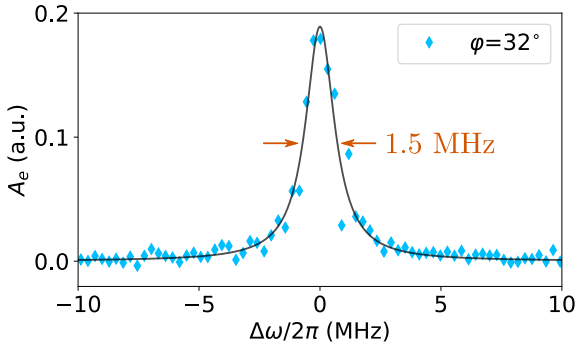

Figure 6.10 – **Erbium lineshape in sample A, measured at $\varphi = 32°$.** Spin-echo integral A_e as a function of B_0, around 64.6 mT, measured for resonator 2. Each data point is single-shot and the Hahn-echo sequence, with 1 μs pulses, is repeated every 6 s. Full symbols are measurements and the solid line is a Lorentzian fit, yielding a FWHM linewidth $\Gamma_{\text{inh}}/2\pi = 1.46 \pm 0.04$ MHz.

Note that this estimation takes into account only the impurities listed in Table 5.1 and excludes all spins which are not in an S_4 symmetry site. The contribution of paramagnetic spins might thus be slightly underestimated. Overall, the nuclear spin bath accounts for 13% of the residual linewidth and the pararamagnetic spin bath contribution is negligible. The spin excitation bandwidth, of about 0.25 MHz and 0.6 MHz for the data of Figure 6.9 and Figure 6.10 respectively, contributes to the measured inhomogeneous broadening and might contribute to the fitted value of 1 MHz. The remaining inhomogeneous linewidth may be due to a slight misalignment of $\boldsymbol{B_0}$ with respect to the (a, b)-plane, such that the electric field sensitivity of the spin frequency does not completely vanish at φ_0.

Moreover, this measurement allows us to determine the angle φ_{w} of the inductance wire with respect to the a-axis. The integral of the echo lineshape as a function of angle φ is plotted in Figure 6.11 and shows a variation which is different from the variation of the inhomogeneous linewidth and of the relaxation time T_1 (see explanations in Chapter 8). In fact this quantity depends on several parameters. First, the coupling constant of each single spin to the resonator is maximum when the magnetic field is aligned with the wire direction (see Equation 5.7 which is maximum when $\Delta\varphi = 0$). Second, the relaxation time plays a role as it is anisotropic in the (a, b)-plane and the Hahn-echo sequence for this measurement is repeated every 4 s, while T_1 varies between 4 s and 15 s. Thus, modelling exactly the data plotted in Figure 6.11 would require simulations. Here, we simply want to estimate the angle φ_{w} and the data is well fitted with $\sqrt{A + B\cos^2(\varphi - \varphi_{\text{w}})}$, which is the expected variation of the single-spin coupling constant g_0. The angle φ_{w} is determined from the maximum of the integrated echo lineshape as a function of φ, and corresponds to $\varphi_{\text{w}} = 51 \pm 3°$. Note that this angle is close but not equal to φ_c (46.5°), because the resonator inductance is not exactly parallel to the sample edge due to lithography alignment error.

6.2.2 Sample B

In sample B, the erbium lineshape is measured for two magnetic field orientations, $\theta = 0°$ and $\theta = 90°$. Figure 6.12 shows the Hahn-echo spectroscopy measured at 10 mK for these two orientations. The data are fitted with Lorentzian lineshapes with FWHM Γ_{inh}. At $\theta = 90°$, the fitted inhomogeneous linewidth is $\Gamma_{\text{inh}}/2\pi = 28$ MHz. This magnetic field orientation is equivalent to the data taken at $\varphi = 0°$ with sample A. The fit to the data shown in Figure 6.9c gives $\Gamma_{\text{inh}}/2\pi(\varphi = 0°) = 18$ MHz. Thus the inhomogeneous linewidth

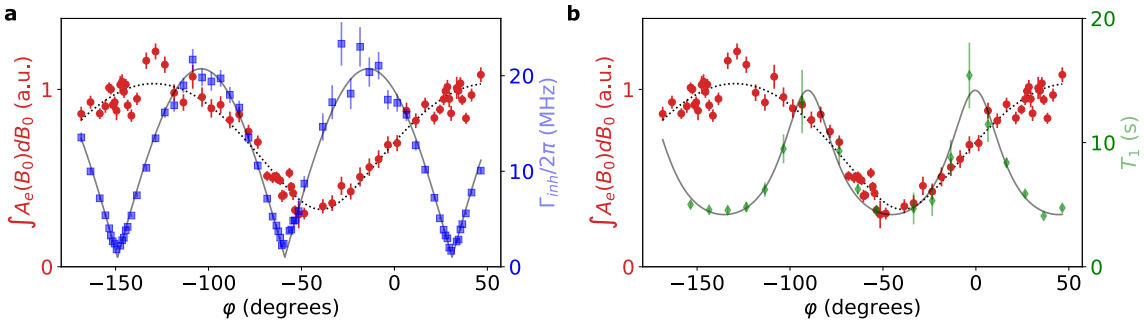

Figure 6.11 – **Angular dependence of the erbium lineshape integral in sample A.** Red circles are the integrated echo lineshapes for each angle φ. These integrals are calculated using the Lorentzian fits shown in Figure 6.9a and b. The dotted black line is a fit to the data with $\sqrt{A + B\cos^2(\varphi - \varphi_w)}$, which is proportional to the single-spin coupling constant g_0. The fit yields $\varphi_w = 50.5 \pm 1°$. These data are compared with other measured properties of the erbium line. **a.** The data in light blue squares are the inhomogeneous linewidth Γ_{inh} and its fit (solid grey curve). They reproduce the data of Figure 6.9c, showing that the angular dependence of the linewidth and the lineshape integral are not correlated. **b.** The data in light green diamonds are the measured relaxation time T_1 and its fit (solid grey line). They reproduce the data of Figure 8.1b.

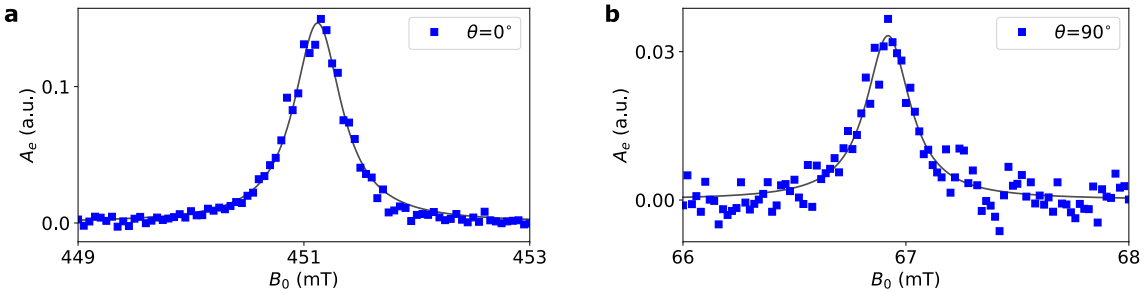

Figure 6.12 – **Erbium lineshape in sample B. a.** Hahn-echo spectroscopy when the field is perpendicular to the wire axis, $\theta = 0°$. The Lorentzian fit gives a FWHM of 0.51 ± 0.01 mT, corresponding to $\Gamma_{inh}/2\pi = 8.9 \pm 0.2$ MHz. **b.** Hahn-echo spectroscopy when the field is parallel to the wire axis, $\theta = 90°$. The Lorentzian fit gives a FWHM of 0.24 ± 0.01 mT, corresponding to $\Gamma_{inh}/2\pi = 28 \pm 1$ MHz.

measured with sample A is slighty narrower than in sample B, which indicates a larger concentration of charged impurities in sample B. At $\theta = 0°$, the Lorentzian fit to the data gives $\Gamma_{inh}/2\pi = 9$ MHz, also likely due to inhomogeneous internal electric fields.

6.3 Erbium concentration

6.3.1 Linking the ensemble coupling to the erbium concentration

As defined in Section 3.3.0.1, the ensemble coupling constant at zero temperature is

$$g_{ens} = \sqrt{\sum g_k^2} = \sqrt{\int g^2 \rho(g) dg} = \sqrt{c \int_V d\boldsymbol{r} g_0(\boldsymbol{r})^2}, \tag{6.1}$$

in the case of a homogeneous spin concentration c in a volume V.

The single-spin coupling g_0 for a $I = 0$ erbium ion has been calculated in Equation 5.7,

yielding

$$g_{\text{ens}} = \frac{\mu_B}{2\hbar}\sqrt{c\int_V d\boldsymbol{r}[(\mathrm{g}_{z'}\delta B_{z'})^2 + (\mathrm{g}_{y'}\delta B_{y'}\cos\psi)^2]}, \tag{6.2}$$

where the basis (x', y', z') corresponds to z' out of plane and x' along the wire (see Figure 5.13). For sample A, $\psi = \Delta\varphi$ and for sample B, $\psi = \pi/2 - \theta$.

This expression can be expressed as a function of several experimental parameters. Because the oscillating magnetic field is dominantly generated by the current passing through the inductance wire, which does not depend on x', the integral simplifies into

$$\int_V d\mathbf{r}[(\mathrm{g}_{z'}\delta B_{z'})^2+(\mathrm{g}_{y'}\delta B_{y'}\cos\psi)^2] = L\iint_{z'<0} dy'dz'[(\mathrm{g}_{z'}\delta B_{z'}(y',z')^2+(\mathrm{g}_{y'}\delta B_{y'}(y',z')\cos\psi)^2], \tag{6.3}$$

where L is the inductance wire length. Moreover, the integral is only for $z' < 0$ because the spins are located below the resonator only. The double integral can be split in two terms,

$$\begin{aligned}&\iint_{z'<0} dy'dz'[(\mathrm{g}_{z'}\delta B_{z'}^2 + (\mathrm{g}_{y'}\delta B_{y'}\cos\psi)^2] = \\ &\frac{\iint_{z'<0} dy'dz'[(\mathrm{g}_{z'}\delta B_{z'})^2 + (\mathrm{g}_{y'}\delta B_{y'}\cos\psi)^2]}{\iint_{z'<0} dy'dz'[\delta B_{z'}^2 + \delta B_{y'}^2]}\iint_{z'<0} dy'dz'[\delta B_{z'}^2 + \delta B_{y'}^2],\end{aligned} \tag{6.4}$$

where the first one is interpreted as an averaged g-factor squared, which we call $\tilde{\mathrm{g}}$,

$$\tilde{\mathrm{g}} = \sqrt{\frac{\iint_{z'<0} dy'dz'[(\mathrm{g}_{z'}\delta B_{z'})^2 + (\mathrm{g}_{y'}\delta B_{y'}\cos\psi)^2]}{\iint_{z'<0} dy'dz'[\delta B_{z'}^2 + \delta B_{y'}^2]}}. \tag{6.5}$$

In order to calculate the second term, we compute the energy of a n-photon Fock state in the resonator using the magnetic field,

$$E_n = \frac{1}{\mu_0}\int d\boldsymbol{r}\,\langle n|\,\hat{\boldsymbol{B}}_{\boldsymbol{1}}(\boldsymbol{r})^2\,|n\rangle = \frac{1}{\mu_0}\int d\boldsymbol{r}\,\langle n|\,\boldsymbol{\delta B}(\boldsymbol{r})^2(\hat{a}+\hat{a}^\dagger)^2\,|n\rangle = \frac{2n+1}{\mu_0}\int d\boldsymbol{r}|\boldsymbol{\delta B}(\boldsymbol{r})|^2. \tag{6.6}$$

The energy of a n-photon Fock state is also given by $E_n = \hbar\omega_0(n + \frac{1}{2})$. Therefore,

$$\int d\boldsymbol{r}|\boldsymbol{\delta B}(\boldsymbol{r})|^2 = \frac{\mu_0\hbar\omega_0}{2}, \tag{6.7}$$

and the second term becomes

$$\iint_{z'<0} dy'dz'[\delta B_{z'}^2 + \delta B_{y'}^2] = \frac{1}{2L}\int d\boldsymbol{r}|\boldsymbol{\delta B}(\boldsymbol{r})|^2 = \frac{\mu_0\hbar\omega_0}{4L}. \tag{6.8}$$

Wrapping everything up, the ensemble coupling at zero temperature can be expressed as

$$g_{\text{ens}} = \frac{\mu_B\tilde{\mathrm{g}}}{4\hbar}\sqrt{c\mu_0\hbar\omega_0}. \tag{6.9}$$

This equation, which has been already derived for similar systems in [Kub+10], links the ensemble coupling constant g_{ens} to the erbium concentration c. We note that the average g-factor $\tilde{\mathrm{g}}$ depends only on the ratio between $\iint_{z'<0} dy'dz'\delta B_{y'}^2$ and $\iint_{z'<0} dy'dz'\delta B_{z'}^2$. Using a COMSOL simulation over a rectangle of 400×200 μm^2 under a 5 μm-wide wire, this ratio is found to be 1.21 ± 0.03 (the simulation result is sampled every 0.1 μm) such that $\tilde{\mathrm{g}} = \sqrt{[\mathrm{g}_{z'}^2 + 1.21(\mathrm{g}_{y'}\cos\psi)^2]/2.21}$.

At finite temperature, this equation must be rescaled by the factor $\sqrt{P(T)}$, where $P(T)$ is the spin polarization, as discussed in Section 3.3.0.1. However, below 50 mK, the $I = 0$ erbium spins are fully polarized in their ground state and $P(T) \sim 1$.

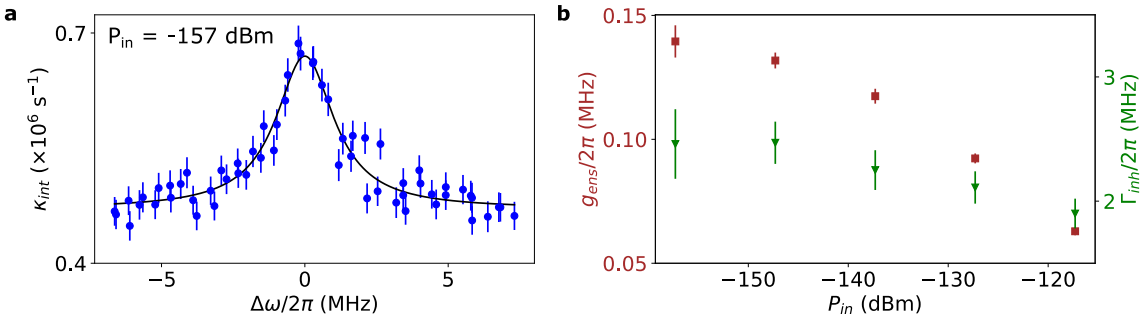

Figure 6.13 – **Continuous-wave spectroscopy of resonator 3 from sample A at 10 mK and $\varphi = 30°$. a.** Internal loss rate κ_{int} as a function of B_0, around 67.2 mT, and converted into a frequency detuning $\Delta\omega$, measured with input power P_{in} at the sample of -157 dBm. φ is set to 30°. The solid black line is a fit to the data with Equation 6.10. **b.** Fitted ensemble coupling g_{ens} and linewidth Γ_{inh} as functions of P_{in}.

6.3.2 Sample A

In order to estimate the erbium concentration, the next step is to measure the ensemble coupling g_{ens}. This can be done using the reflection coefficient S_{11} measured with a VNA. Indeed, Equation 3.57 shows that in the low excitation regime, the spin ensemble broadens the resonance linewidth according to

$$\tilde{\kappa}_{\text{int}} = \kappa_{\text{int}} + \frac{g_{\text{ens}}^2 \Gamma_{\text{inh}}}{(\omega - \omega_s)^2 + (\Gamma_{\text{inh}}/2)^2}, \tag{6.10}$$

which allows us to fit the ensemble coupling g_{ens} and the inhomogeneous linewidth Γ_{inh}.

Figure 6.13a shows a typical measurement of the internal loss rate as the magnetic field is swept over the erbium transition, with resonator 3 of sample A. The data is fitted with Equation 6.10. This measurement should be performed at sufficiently low power to avoid saturation of the spins. The internal loss rate is thus measured for various input powers P_{in}. In the low power regime, the spin ensemble is not saturated and the extracted spin parameters, g_{ens} and Γ_{inh}, are expected to reach a plateau. The fitted ensemble coupling g_{ens} and inhomogeneous linewidth Γ_{inh} are plotted in Figure 6.13b as a function of the input power P_{in}. The inhomogeneous linewidth is almost constant with input power while the ensemble coupling varies by nearly a factor 3 and starts reaching a plateau a low power. The fitted ensemble coupling at lowest power is $g_{\text{ens}}/2\pi = 140 \pm 6$ kHz.

The average g-factor at $\psi = \Delta\varphi = \varphi - \varphi_{\text{w}} = 21°$ is $\tilde{\text{g}} = 5.8$. From Equation 6.9, we estimate the concentration of the zero nuclear-spin isotopes of erbium, $c = (0.7 \pm 0.1) \times 10^{13}\,\text{cm}^{-3}$. This corresponds to a total trivalent erbium concentration (including all isotopes) of $[\text{Er}^{3+}] = c/(0.77 \times 1.3 \times 10^{22}\ \text{cm}^{-3}) = 0.7 \pm 0.1$ ppb (see Section 2.2.1). The value of the ensemble coupling allows us to calculate the cooperativity between the spin ensemble and the resonator at this magnetic field orientation. Equation 3.58 yields $C \sim 0.08$, which shows that these measurements are in the low cooperativity regime.

6.3.3 Sample B

The same study is done on sample B with $\theta = 0°$ and the measurement is shown in Figure 6.14. The ensemble coupling does not yet reach a plateau at low power which makes it difficult to precisely extract the ensemble coupling when the spins are not saturated. Nevertheless, the fitted ensemble coupling at lowest power, $g_{\text{ens}}/2\pi = 280 \pm 20$ kHz, can be used to estimate the erbium concentration. At $\theta = 0°$, $\tilde{\text{g}} = 5.6$ and Equation 6.9

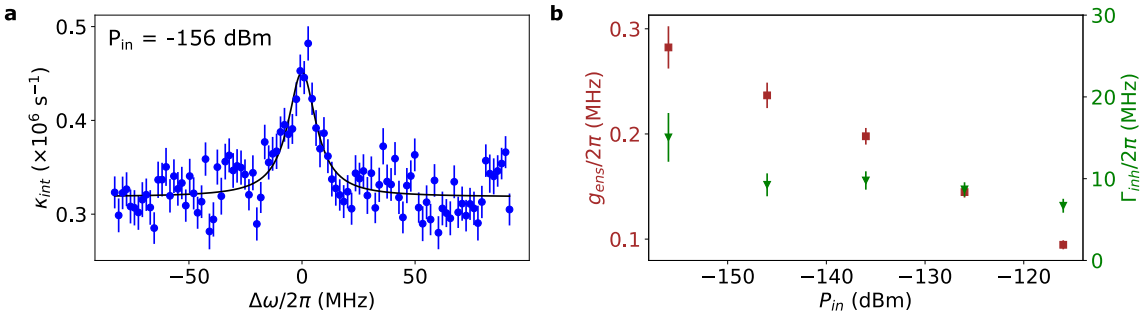

Figure 6.14 – **Continuous-wave spectroscopy of resonator 3 from sample B at 10 mK and $\theta = 0°$. a.** Internal loss rate κ_{int} as a function of B_0, around 451 mT, and converted into a frequency detuning $\Delta\omega$, measured with input power P_{in} at the sample of −156 dBm. θ is set to 0°. The solid black line is a fit to the data. **b.** Fitted ensemble coupling g_{ens} and linewidth Γ_{inh} as functions of P_{in}.

yields $c = 3.1 \pm 0.2 \times 10^{13}$ cm^{-3}. This gives a total concentration of erbium ions of $[\text{Er}^{3+}] = 3.1 \pm 0.2$ ppb, which is of the same order of magnitude as the concentration found in sample A. Also we calculate the cooperativity at this magnetic field orientation. Equation 3.58 yields $C \sim 0.03$, showing as in sample A that these measurements are in the low cooperativity regime.

Chapter 7

Coherence time measurements

This chapter focuses on the coherence properties of erbium ions in samples A and B. The coherence is studied with the Hahn-echo sequence, by varying the interpulse delay τ. All measurements presented in this chapter are performed at high pulse power, thus probing spins in the bulk of the crystal.

7.1 Reaching the nuclear spin limit at 10 mK

We first present measurements performed at the base temperature of the cryostat, which is 10 mK.

7.1.1 Sample A

In sample A, we start by measuring the coherence time with the field oriented at $\varphi = \varphi_c = 47°$, which is close to the resonator wire direction and is the default orientation of our setup. The magnetic field value is set to $B_0 = 67.2$ mT, corresponding to the resonance condition between the erbium $I = 0$ transition and resonator 3 at $\omega_0/2\pi = 7.881$ GHz.

Figure 7.1 presents the coherence time measurement at 10 mK. The echo amplitude is averaged in magnitude over 60 traces and is plotted as a function of 2τ, τ being the interpulse delay of the Hahn-echo sequence. The data are fitted with $A_e = \sqrt{Ae^{-2(2\tau/T_2)^x} + C}$ (see Section 5.3.4). The fit yields a coherence time $T_2 = 23.2 \pm 0.5$ ms, with a stretching exponent $x = 2.4 \pm 0.1$. Compared with the state of the art of Section 4.5, this measured coherence time is nearly three orders of magnitude longer than previous measurements of Er^{3+} electron spin coherence in $CaWO_4$ at 2.5 K [Ber+07]. We attribute this drastic improvement to both the low residual paramagnetic impurity concentration and enhanced thermal spin-polarization at 10 mK, both of which greatly reduce electronic spin-spin interactions in the crystal. Indeed, at $B_0 = 67.2$ mT, most of the paramagnetic impurities are frozen in their ground state at 10 mK so that their contribution to decoherence via spectral diffusion is quenched. This measured coherence time is also more than one order of magnitude longer than previous state-of-the-art measurements of electron spin coherence in a natural abundance material [Li+20], away from a ZEFOZ transition (see Section 4.5). We will detail the dominating decoherence processes in the following sections.

7.1.1.1 Cluster correlation expansion (CCE)

When the spectral diffusion from paramagnetic impurities is quenched, the spectral diffusion caused by nuclear spins may become the dominant decoherence process. The contribution of the tungsten nuclear spins of $CaWO_4$ to spectral diffusion was computed using cluster-correlation expansion (CCE) simulations (see Section 4.2.4) by Sen Lin and Ren Bao Liu from the Chinese university of Hong Kong. In the simulation, the ^{183}W nuclear spins are

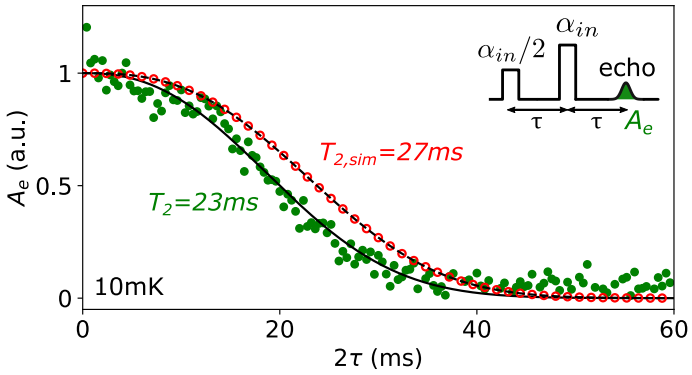

Figure 7.1 – **Erbium Hahn-echo electron spin coherence time T_2 measured with sample A, at 10 mK and $\varphi = 47°$.** The data (green circles) are the echo amplitude averaged in magnitude as a function of the delay 2τ between the first pulse of a Hahn-echo sequence and the echo, measured with resonator 3. Each data point is averaged over 60 measurements with a repetition time of 4 seconds. The solid black line is a fit with $A_e = \sqrt{Ae^{-2(2\tau/T_2)^x} + C}$, yielding $T_2 = 23.2 \pm 0.5$ ms and $x = 2.4 \pm 0.1$. The offset C arising from magnitude averaging is subtracted from the squared data and the squared fit (square roots of negative noise on $A_e^2 - C$ are obviously absent from the plot) and the echo decay is normalized to 1. Open red circles are the result of a cluster-correlation expansion (CCE) simulation for the same field orientation. The dashed black line is a fit to the simulation with $A_e = e^{-(2\tau/T_{2,\mathrm{sim}})^{x_{\mathrm{sim}}}}$, yielding $T_{2,\mathrm{sim}} = 27.2$ ms and $x_{\mathrm{sim}} = 2.74$.

placed randomly on the $CaWO_4$ lattice sites of tungsten atoms and the Er^{3+} ions randomly substitute Ca^{2+}. The simulation has already converged when considering a bath with all nuclear spins within a sphere of radius of 11 nm around the central spin. The result of the simulation is shown in Figure 7.1, for $\varphi = \varphi_c = 47°$ corresponding to the experimental conditions. It can be fitted by the echo decay function $A_e = e^{-(2\tau/T_{2,\mathrm{sim}})^{x_{\mathrm{sim}}}}$, which yields $T_{2,\mathrm{sim}} = 27.2$ ms and $x_{\mathrm{sim}} = 2.74$. Experimental and simulated data are very similar and we can therefore conclude that the experimentally measured coherence time at 10 mK is mostly limited by nuclear spin spectral diffusion.

This CCE simulation can be compared with the simplified model of Kanai *et al.* presented in Section 4.2.4. According to Table 4.1, this model predicts a coherence time of 10 ms for an electron spin g = 8.38 in $CaWO_4$, with stretching exponent $x = 2$. This coherence time value is shorter than our CCE calculations by a factor 2.7. This discrepancy is attributed to the random nuclear spin positions assumed in the simplified model of Kanai *et al.*, whereas in $CaWO_4$, the nuclear spins occupy random sites on a regular lattice which has been taken into account in the simulation of Figure 7.1. To validate this hypothesis, Figure 7.2 shows two CCE simulations. One of them is identical to the one presented in Figure 7.1. The second one is a simulation where the tungsten nuclear spin bath is assumed to be amorphous. This new simulation is fitted with the same functional form, yielding $T_{2,\mathrm{sim}} = 8.1$ ms instead of 27.2 ms and $x_{\mathrm{sim}} = 1.9$ instead of 2.7. We thus conclude that the simplified model of Kanai *et al.* gives a correct order of magnitude but a precise estimate of the nuclear spin limited coherence time requires to take into account the crystal structure. The amorphous limit predicts a shorter coherence time because the lattice structure, which is neglected, sets in fact a lower bound on the distance between nuclear spins, which has a sizeable effect when the spin concentration is not too small.

Because the discrete positions of tungsten atoms need to be taken into account in the simulations, the orientation of the magnetic field also matters because it affects the dipole-dipole interaction between the tungsten atoms according to Equation 2.28. Due to the tetragonal symmetry of $CaWO_4$, the dipole-dipole coupling is necessarily periodic

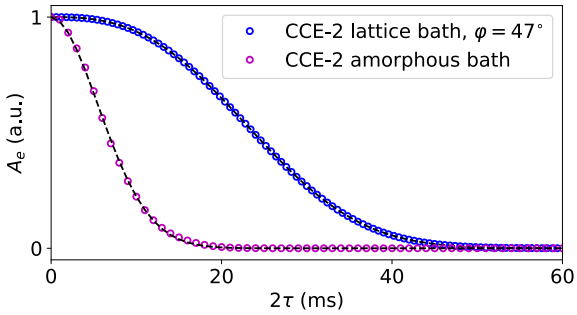

Figure 7.2 – **CCE simulations of the spin decoherence in the amorphous limit and in a lattice at $\varphi = 47°$.** The blue open circles are the simulation already presented in Figure 7.1, at $\varphi = 47°$. The purple open circles are a simulation where the tungsten nuclear spin bath is taken as amorphous, with no crystal structure. The parameters of the simulations are the magnetic field $B_0 = 67$ mT, the temperature $T = 10$ mK and the field orientation $\varphi = \varphi_c = 47°$ for the lattice spin bath only. The simulations are fitted with $A_e = e^{-(2\tau/T_{2,\mathrm{sim}})^{x_{\mathrm{sim}}}}$ (dashed black lines). For the simulation in a lattice spin bath, the fit yields $T_{2,\mathrm{sim}} = 27.2$ ms and $x_{\mathrm{sim}} = 2.7$. For the simulation in an amorphous bath, the fit gives $T_{2,\mathrm{sim}} = 8.1$ ms and $x_{\mathrm{sim}} = 1.9$.

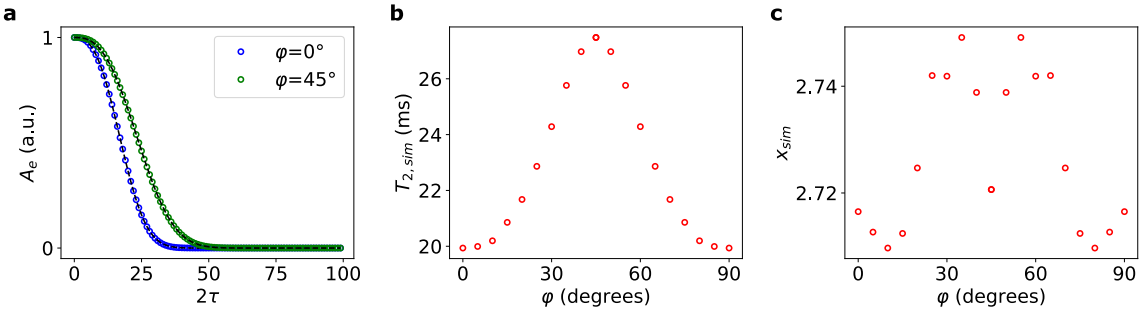

Figure 7.3 – **Angular dependence of the CCE simulations in the (a, b)-plane. a.** Echo decay simulated with CCE for two angles, $\varphi = 0°$ (open blue circles) and $\varphi = 45°$ (open green circles). The black dashed lines are fits with $A_e = e^{-(2\tau/T_{2,\mathrm{sim}})^{x_{\mathrm{sim}}}}$. The fit yields $T_{2,\mathrm{sim}} = 20.0$ ms at $\varphi = 0°$ and $T_{2,\mathrm{sim}} = 27.5$ ms at $\varphi = 45°$. **b.** Fitted coherence time from the CCE simulations, $T_{2,\mathrm{sim}}$, as a function of angle φ. **c.** Fitted stretching exponent from the CCE simulations, x_{sim}, as a function of angle φ.

with a $\pi/2$ period and symmetric around $\pi/4$. The result of the angular dependence of the CCE simulation in the crystal (a, b)-plane is shown in Figure 7.3. The simulated coherence time is minimum at $\varphi = 0°$ with $T_{2,\mathrm{sim}} = 20.0$ ms and maximum at $\varphi = 45°$ with $T_{2,\mathrm{sim}} = 27.5$ ms. The stretching exponent x_{sim} varies very little with angle φ.

7.1.1.2 Electron-spin echo envelope modulation (ESEEM)

The noise of the data shown in Figure 7.1 seems to decay with the inter-pulse delay τ. This apparent noise originates from ESEEM, which modulates the echo decay envelope (see Section 4.4). Indeed, measuring the echo amplitude with a much shorter sampling time $\Delta\tau = 1$ μs for several angles φ shows a clear modulation which is plotted in Figure 7.4 and Figure 7.5. This was measured close to $\varphi = 31°$ because the narrow inhomogeneous linewidth around this angle leads to a stronger signal. These data are averaged in quadrature. The modulation is evidenced by taking the Fourier transform of each curve and the modulation frequencies show some angular variation due to the anisotropy of the dipolar coupling between erbium and tungsten.

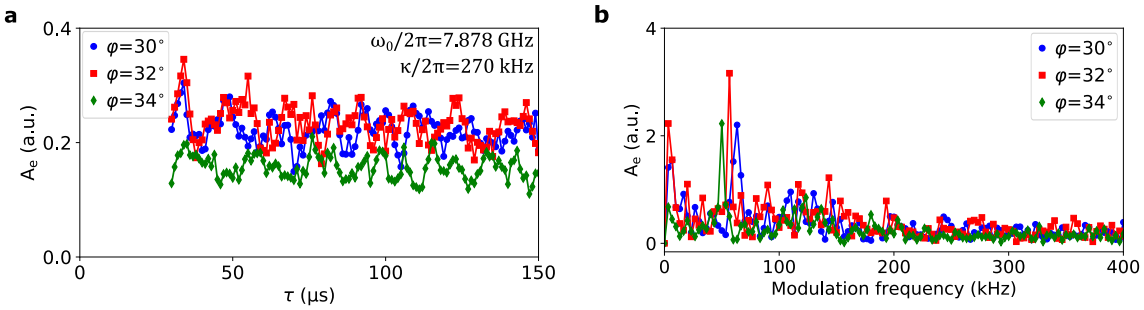

Figure 7.4 – **Electron spin echo envelope modulation measured with resonator 3 of sample A. a.** Echo amplitude averaged in quadrature as a function of short inter-pulse delay τ, measured at 10 mK and with different field orientations φ. The resonance has a frequency $\omega_0/2\pi = 7.878$ GHz and a linewidth $\kappa_t/2\pi = 270$ kHz. 4 μs-long square pulses are used such that the pulse bandwidth is $\Delta\omega_{\text{pulse}}/2\pi \approx 250$ kHz. **b.** Fast Fourier transform of the data of subplot a.

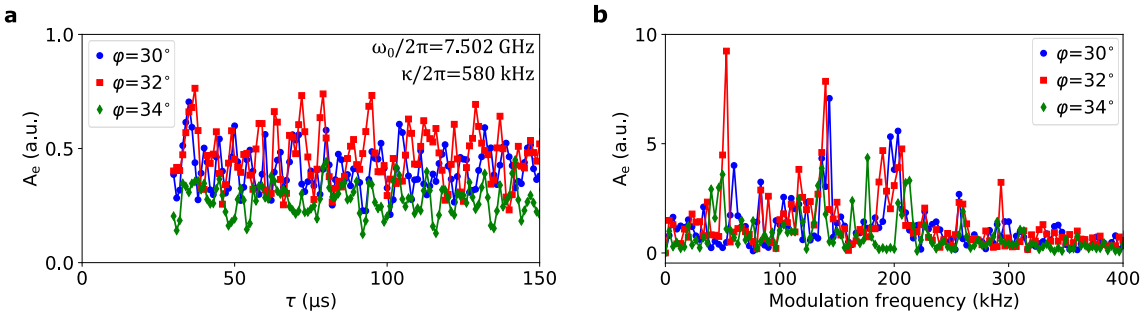

Figure 7.5 – **Electron spin echo envelope modulation measured with resonator 2 of sample A. a.** Echo amplitude averaged in quadrature as a function of short inter-pulse delay τ, measured at 10 mK and with different field orientations φ. The resonance has a frequency $\omega_0/2\pi = 7.502$ GHz and a linewidth $\kappa_t/2\pi = 580$ kHz. 1 μs-long square pulses are used such that the pulse bandwidth is $\Delta\omega_{\text{pulse}}/2\pi \approx 1$ MHz. **b.** Fast Fourier transform of the data of subplot a.

The theoretical ESEEM spectrum is computed in Figure 7.6. Most modulation frequencies are around 200 kHz while a few frequency peaks are strongly angular dependent. This corresponds roughly to the peaks observed in Figure 7.4b and Figure 7.5b, although we did not manage to reach quantitative agreement. However, it is interesting to note that these data are taken with two resonators with different resonance linewidths. The resonance linewidth κ_t combined with the excitation pulse bandwidth $\Delta\omega_{\text{pulse}}$ filters out high frequencies of the theoretical ESEEM (see Section 4.4 and Section 3.3.2). In the data of Figure 7.4, $\kappa_t/2\pi = 270$ kHz and $\Delta\omega_{\text{pulse}}/2\pi \approx 250$ kHz so, very roughly, modulation frequencies larger than about 125 kHz are filtered out. In the data of Figure 7.5, $\kappa_t/2\pi = 580$ kHz and $\Delta\omega_{\text{pulse}}/2\pi \approx 1$ MHz so modulation frequencies larger than about 290 kHz are filtered out. This is compatible with the cutoffs observed experimentally.

Ideally when measuring T_2, the ESEEM pattern should be sampled correctly. However, its typical period is about 15 μs which is three orders of magnitude shorter than the coherence time. To be able to measure T_2 in a reasonable time, the data can be acquired by packets of points with a very short sampling time, typically $\Delta\tau = 2$ μs. This allows us to locally sample the ESEEM correctly. This is especially important for measurements with resonator 2, where the larger spin excitation bandwidth filters less ESEEM frequencies and the ESEEM pattern is more contrasted.

In order to verify that ESEEM is not affecting the coherence time measurement shown

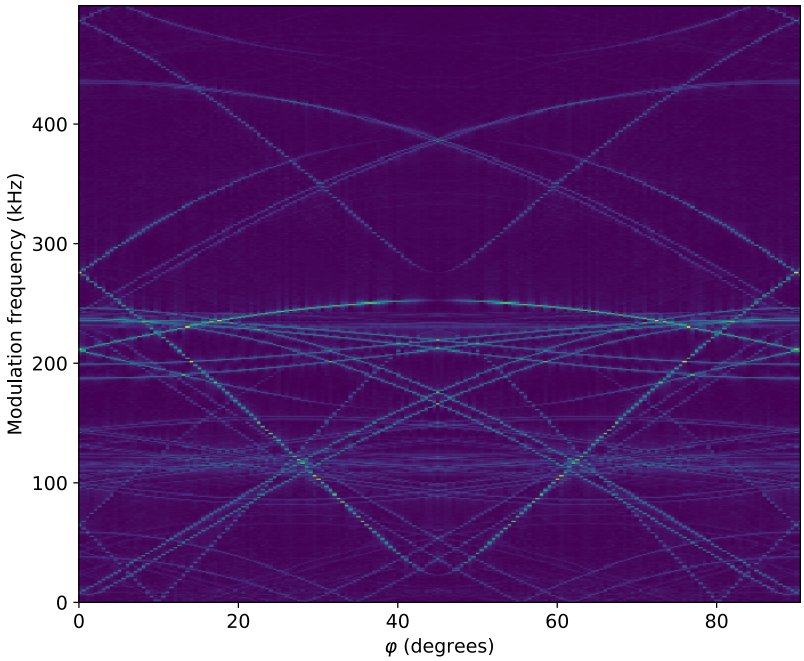

Figure 7.6 – **Theoretical ESEEM spectrum.** Fourier transform of the theoretical ESEEM signal as a function of angle φ. This spectrum is computed at $B_0 = 67.2$ mT and $\theta = 93°$, corresponding to the angle found in the X-Ray diffraction pattern (see Section 5.1.3).

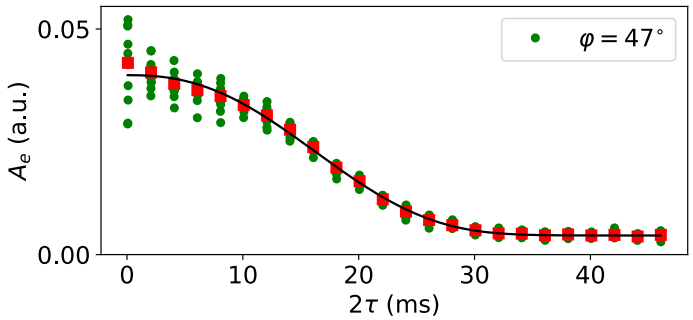

Figure 7.7 – **Erbium electron spin coherence time measurement with resonator 2 of sample A at 10 mK and $\varphi = 47°$.** Echo amplitude averaged in magnitude as a function of the delay 2τ between the first pulse of the Hahn-echo sequence and the echo (green circles). The data are measured in packets of 10 points spaced by $\Delta\tau = 2$ μs to account for ESEEM. The red squares are the average echo amplitude over each packet of 10 points. The solid black line is a fit to the data with $A_e = \sqrt{Ae^{-2(2\tau/T_2)^x} + C}$, yielding $T_2 = 20.5 \pm 0.2$ ms and $x = 2.42 \pm 0.1$.

in Figure 7.1, we have taken another dataset, in which we sample the echo around several values of τ spaced by 1 ms (coarse time step) with a much finer time-step, $\Delta\tau = 2$ μs, enabling to resolve the ESEEM. The echo amplitude as a function of 2τ is shown in Figure 7.7, together with the ESEEM averaged echo decay and a fit to the data which yields $T_2 = 20.5 \pm 0.2$ ms and $x = 2.42 \pm 0.1$ ms. These values are similar as those found in Figure 7.1. The fitted coherence time is slightly shorter, but this is attributed to some change in the setup as the two datasets were taken in different runs (see Section 7.1.1.5).

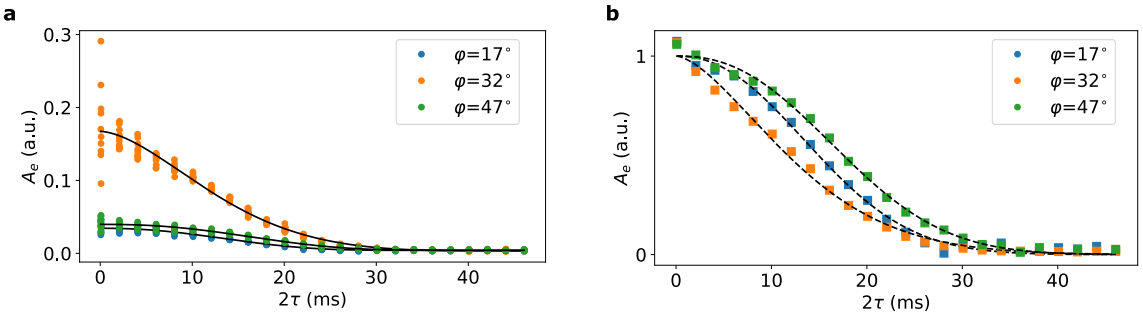

Figure 7.8 – **T_2 measurements at 10 mK for different angles φ with sample A. a.** The echo decay is measured with resonator 2 in packets of 10 points spaced by $\Delta\tau = 2$ μs to account for ESEEM. The data at $\varphi = 47°$ is the same data is in Figure 7.7. The signal is much larger at $\varphi = 32°$ due to the narrow erbium linewidth. The data are averaged in magnitude and solid black lines are fits with $A_e = \sqrt{Ae^{-2(2\tau/T_2)^x} + C}$. **b.** Same data as in subplot a where the packets of 10 points have been averaged out for better visibility. The data have been rescaled such that the fit (dashed black line) consists solely in the decay part as $e^{-(2\tau/T_2)^x}$.

7.1.1.3 T_2 angular dependence in the (a, b)-plane

The CCE simulation predicts a variation of the coherence time T_2 with angle φ when the field is applied in the (a, b)-plane (see Figure 7.3). The measurement of the angular dependence of T_2 is performed with resonator 2 of sample A. Indeed, due to its larger linewidth, $\kappa_t/2\pi = 580$ kHz, resonator 2 allows for a larger spin excitation bandwidth and therefore enhanced signal compared to the other resonators. However the ESEEM is also stronger because it is less filtered by the resonator linewidth and the data is acquired as in Figure 7.7, with packets of 10 points spaced by $\Delta\tau = 2$ μs.

Figure 7.8 shows the coherence time measurements for various angles φ. In particular, the data at $\varphi = 47°$ is the same data as in Figure 7.7. The echo amplitude at small τ values depends on many parameters including the relaxation time T_1, the inhomogeneous broadening of the erbium line and the orientation of the magnetic field $\boldsymbol{B_0}$ with respect to the inductance wire direction. The repetition time of the Hahn-echo sequence is adjusted for each angle φ to match the erbium relaxation time measurements (see Figure 8.1b). In particular, the signal measured at $\varphi = 32°$ is much stronger due to the narrow inhomogeneous linewidth around this specific angle. The data, which is averaged in magnitude, is fitted with $A_e = \sqrt{Ae^{-2(2\tau/T_2)^x} + C}$, yielding the coherence time T_2. Rescaling the data in subplot b shows that the measured coherence time shows a measurable dependence on φ. On this subplot, the ESEEM resolved packets are averaged out for better visibility.

The complete angular dependence of the coherence time is shown in Figure 7.9a and b. The fitted coherence times are compared with the CCE simulation of Figure 7.3. Except for the point at $\varphi = 32°$ which behaves differently (see the next section), the measured $T_2(\varphi)$ follows qualitatively the expected trend predicted by the CCE simulation, with shorter T_2 around $\varphi = 0°$ and longer T_2 around $\varphi = 47°$.

The slightly shorter measured T_2 compared to the CCE is an indication that paramagnetic spectral diffusion is not completely quenched, which is not surprising given the variety of paramagnetic species present in the sample, some of them not being polarized in their ground state at 10 mK. To give a higher bound on this residual paramagnetic contribution, the data, shown partially in Figure 7.8, are fitted with a second model, $A_e = \sqrt{Ae^{-2[(2\tau/T_{2,\mathrm{sim}})^{x_{\mathrm{sim}}} + (2\tau/T_{2,p})^{x_p}]} + C}$, where $T_{2,\mathrm{sim}}$ and x_{sim} are the CCE simulated values and $T_{2,p}$ and x_p are the coherence time and exponent from the paramagnetic spin spectral diffusion. The fitted $T_{2,p}$ and x_p are plotted in Figure 7.9c and d. Apart from

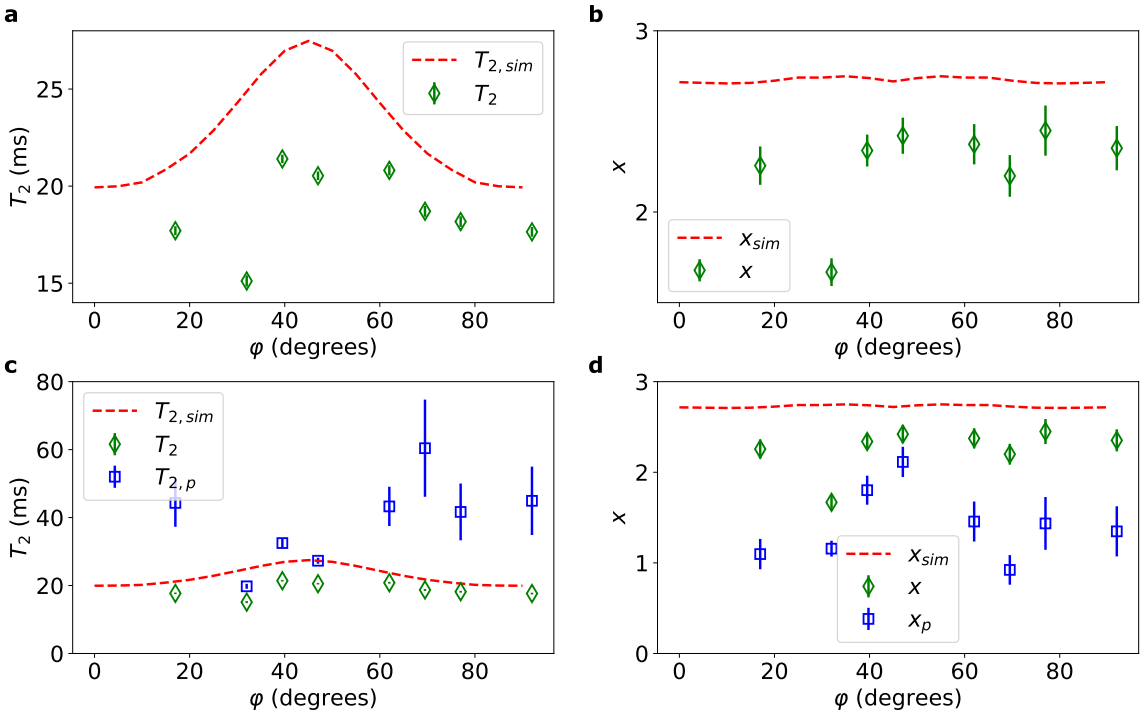

Figure 7.9 – **Angular dependence of the coherence time in the (a, b)-plane, measured with sample A. a.** & **b** Measured coherence time T_2 and stretching exponent x (green diamonds) as a function of the magnetic field angle φ. The red dashed line is the result of the CCE simulation shown in Figure 7.3. **c.** & **d.** Same data as in subplots a and b plus the result of an additional fit of the Hahn-echo decay curves with $A_e = \sqrt{Ae^{-2[(2\tau/T_{2,\mathrm{sim}})^{x_{\mathrm{sim}}}+(2\tau/T_{2,p})^{x_p}]} + C}$, in order to extract the net decoherence effect of spectral diffusion due to paramagnetic impurities.

the data at $\varphi = 32°$, the fitted coherence time is at least of the order of $30 - 50$ ms. This quantity might be slightly angular dependent due to the possible presence of unfrozen impurities whose **g**-factor is anisotropic in the (a, b)-plane.

7.1.1.4 Instantaneous diffusion (ID)

The relatively low coherence time and stretching exponent measured at $\varphi = 32°$ (see Figure 7.9a and b) indicate that instantaneous diffusion may have a non-negligible contribution. Indeed, due to the narrow erbium linewidth around $\varphi_0 = 31°$ (see Section 6.2), the concentration of erbium ions within the pulse excitation bandwidth is maximum and can lead to relatively strong instantaneous diffusion.

As explained in Section 4.3, ID is expected to give an exponential decay $A_{e,\mathrm{ID}}(2\tau) = e^{-2\tau/T_{2,\mathrm{ID}}}$ with

$$\frac{1}{T_{2,\mathrm{ID}}} = \frac{\pi}{9\sqrt{3}}\mu_0 \frac{(\mathrm{g}_{\mathrm{eff}}\mu_B)^2}{\hbar}\frac{\Delta\omega}{\Gamma_{\mathrm{inh}}} c \sin^2\frac{\theta_2}{2}, \tag{7.1}$$

where μ_B is the Bohr magneton, $c = 0.77[\mathrm{Er}^{3+}]$ the concentration of the erbium zero-nuclear-spin isotopes, $\Delta\omega$ the spin excitation bandwidth, as defined in Section 3.3.2, Γ_{inh} the spin inhomogeneous linewidth and θ_2 the refocusing angle. ID is caused by the fraction of erbium ions within the excitation bandwidth which has an effective concentration $\tilde{c} = c\Delta\omega/\Gamma_{\mathrm{inh}}$. Γ_{inh} is known from Section 6.2 and c from Section 6.3. We simply need to evaluate $\Delta\omega$. For the measurement of Figure 7.1, 4 μs-long pulses are used and the resonance linewidth is $\kappa_t/2\pi = 350\,\mathrm{kHz}$. According to Section 3.3.2, the spin excitation bandwidth is $\Delta\omega/2\pi \approx 0.22$ MHz. For the measurement of Figure 7.8, 1 μs-long pulses

are used and the resonance linewidth is $\kappa_t/2\pi = 580\,\text{kHz}$ so the spin excitation bandwidth is $\Delta\omega/2\pi \approx 0.52\,\text{MHz}$.

$\Gamma_{\text{inh}}/2\pi$ is of the order of $1 - 20\,\text{MHz}$ (see Figure 6.9). Therefore, the effective concentration $\tilde{c}$ is typically $1 \times 10^{11} - 3 \times 10^{12}$ cm^{-3} and the distance between two excited erbium ions is of the order of 1 μm. As the excited spins are in the bulk (few tens of μm away from the surface), those within a few μm distance rotate roughly by the same Rabi angles. We also know from Section 3.3.1.2 that spins contributing mostly to the Hahn-echo undergo rotations of first $\theta_1 \sim 0.6\pi/2$ then $\theta_2 \sim 0.6\pi$. Thus we take $\theta_2 = 0.6\pi$ for the neighboring refocused spins, yielding $\sin(\theta_2/2)^2 \sim 0.65$.

Estimation at $\varphi = 47°$

With these values, the expected contribution from ID can be calculated. At $\varphi = 47°$, the inhomogeneous linewidth $\Gamma_{\text{inh}}/2\pi$ was measured to be 11 MHz (see Figure 6.9) and Equation 7.1 gives $T_{2,\text{ID}} \sim 740$ ms. This value is more than one order of magnitude larger than the measured coherence time of Figure 7.1 and confirms that ID is not the dominant source of decoherence at this angle. For the measurement of Figure 7.8, $T_{2,\text{ID}}$ is reduced to 320 ms, due to the larger spin excitation bandwidth.

Estimation at $\varphi = 32°$

The ID contribution increases when the spin linewidth Γ_{inh} gets narrower. At $\varphi = 32°$, $\Gamma_{\text{inh}}/2\pi = 1.8$ MHz and $\Delta\omega/2\pi \approx 0.52\,\text{MHz}$, yielding $T_{2,\text{ID}} \sim 50$ ms. In order to validate this estimation, the data shown in Figure 7.8 at $\varphi = 32°$ is fitted again with

$$A_e(2\tau) = \sqrt{A e^{-2\left[\left(\frac{2\tau}{T_{2,\text{sim}}}\right)^{x_{\text{sim}}} + \left(\frac{2\tau}{T_{2,p}}\right)^{x_p} + \frac{2\tau}{T_{2,\text{ID}}}\right]} + C}, \tag{7.2}$$

where $T_{2,\text{sim}}$ and x_{sim} correspond to spectral diffusion due to the nuclear spin bath, $T_{2,p}$ and x_p to spectral diffusion due to paramagnetic impurities and $T_{2,\text{ID}}$ to instantaneous diffusion. The nuclear spin part is taken from the CCE simulation, with $T_{2,\text{sim}} = 24.7\,\text{ms}$ and $x_{\text{sim}} = 2.74$. To minimize the number of free parameters, the paramagnetic contribution is also fixed and set equal to the one at $\varphi = 47°$, which gives a reasonable order of magnitude (the fit of the paramagnetic contribution at $\varphi = 47°$ shown in Figure 7.9c and d gave $T_{2,p} = 28 \pm 1\,\text{ms}$ and $x_p = 2.1 \pm 0.2$). Fitting only the remaining contribution from ID in Equation 7.2 yields $T_{2,\text{ID}} = 33 \pm 2\,\text{ms}$, which is close to the estimation above and confirms that ID is not negligible at angles where the erbium inhomogeneous linewidth is the narrowest. The result of the fit is shown in Figure 7.10

In order to further study the instantaneous diffusion at $\varphi = 32°$, the data of Figure 7.10 are measured for various pulse lengths dt. The measurement is shown in Figure 7.11. Increasing the pulse length from 1 μs to 8 μs is expected to decrease the excited spin concentration $\tilde{c} = c\Delta\omega/\Gamma_{\text{inh}}$ and thus to increase the spin coherence time (see Equation 7.1). The dependence of the fitted coherence time T_2 as a function of the pulse length dt is plotted in subplot c and does not show a monotonous increase. We have no explanation for this unexpected trend.

7.1.1.5 Magnetic field noise

All Hahn-echo coherence time measurements in this chapter are obtained with magnitude averaging of the echo amplitude. Figure 7.12 shows again the Hahn-echo decay of Figure 7.1, which is averaged in magnitude, and in addition the corresponding Hahn-echo decay with quadrature averaging of the individual echoes. The two averaging methods were defined in

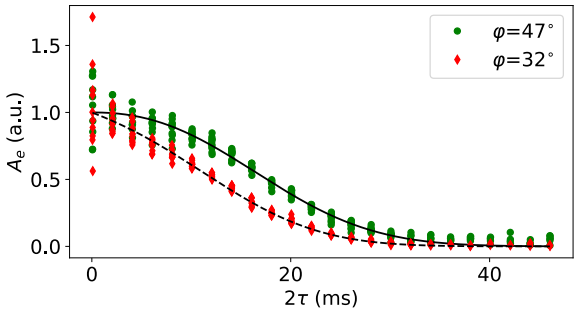

Figure 7.10 – **Hahn-echo coherence time measurements at 10 mK for two magnetic field orientations in sample A.** These data are the same as in Figure 7.8a. Green circles are measurements at $\varphi = 47°$ and red diamonds are measurements at $\varphi = 32°$. The fits are different. The solid black line is a fit of the data at $\varphi = 47°$ with $A_e = \sqrt{Ae^{-2[(2\tau/T_{2,\mathrm{sim}})^{x_{\mathrm{sim}}}+(2\tau/T_{2,p})^{x_p}]} + C}$ where $T_{2,\mathrm{sim}} = 27.2\,\mathrm{ms}$ and $x_{\mathrm{sim}} = 2.74$ are taken from the CCE simulation. The fit yields $T_{2,p} = 28 \pm 1\,\mathrm{ms}$ and $x_p = 2.1 \pm 0.2$. The dashed black line is a fit of the data at $\varphi = 32°$ which includes ID, $A_e = \sqrt{Ae^{-2[(2\tau/T_{2,\mathrm{sim}})^{x_{\mathrm{sim}}}+(2\tau/T_{2,p})^{x_p}+2\tau/T_{2,\mathrm{ID}}]} + C}$. At $\varphi = 32°$, the CCE simulation predicts $T_{2,\mathrm{sim}} = 24.7\,\mathrm{ms}$ and $x_{\mathrm{sim}} = 2.74$. $T_{2,p}$ and x_p are fixed from the fitted values at $\varphi = 47°$. Fitting the remaining ID contribution yields $T_{2,\mathrm{ID}} = 33 \pm 2\,\mathrm{ms}$.

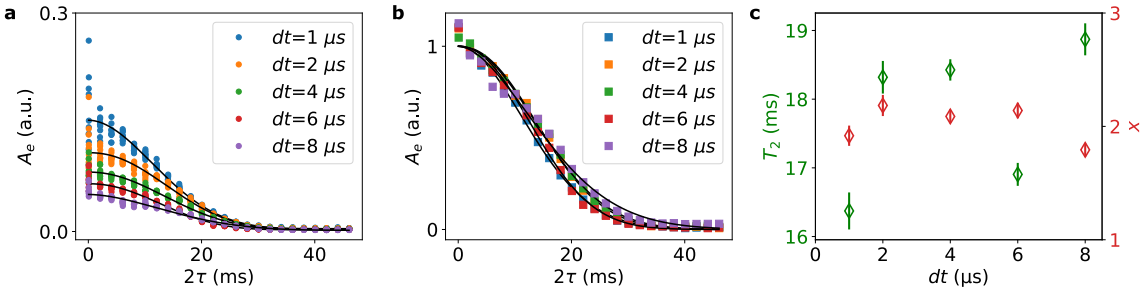

Figure 7.11 – **Hahn-echo coherence time at $\varphi = 32°$, 10 mK, measured with resonator 2 of sample A a.** Echo amplitude averaged in magnitude as a function of 2τ for various pulse lengths dt. The solid black lines are fits with $A_e = \sqrt{Ae^{-2(2\tau/T_2)^x} + C}$. **b.** Same data where the ESEEM-sampling packets have been averaged out. The data have been rescaled such that the fit (dashed black line) consists solely in the decay part in $e^{-(2\tau/T_2)^x}$. **c.** Fitted coherence times (green diamonds) and stretching exponents (red diamonds) as a function of the pulse length dt.

Section 5.3.4. The echo amplitude decays much faster with quadrature averaging. Fitting the quadrature averaged data with $A_e = Ae^{-(2\tau/T_{2,\mathrm{phase}})^{x_{\mathrm{phase}}}}$ yields $T_{2,\mathrm{phase}} = 4.0 \pm 0.2\,\mathrm{ms}$, while the fit of the magnitude averaged data with $A_e = \sqrt{Ae^{-2(2\tau/T_{2,\mathrm{mag}})^{x_{\mathrm{mag}}}} + C}$ gives $T_{2,\mathrm{mag}} = 23.2 \pm 0.5\,\mathrm{ms}$, as already mentioned at the beginning of this chapter.

The discrepancy of the fitted coherence times obtained with these two averaging methods means that the echo phase ϕ_{echo}, which should be well defined in the quadrature IQ-plane, is getting random for $\tau > 2\,\mathrm{ms}$. Therefore, the quadrature averaging, which is sensitive to the echo phase, yields shorter coherence times than the magnitude averaging, which is insensitive to it. We attribute the loss of the echo phase at large τ to noise in the applied magnetic field $\boldsymbol{B_0}$ in the 100 Hz-10 kHz frequency band, which modulates the ensemble transition frequency, thus randomizing ϕ_{echo} for $\tau > 2\,\mathrm{ms}$. Such phase noise has been observed in several pulsed EPR experiments on systems with long coherence times, for instance for donors in ^{28}Si [Tyr+03]. Magnitude averaging is then used to measure T_2. In particular, optical T_2 measurements are always magnitude averaged, since they use

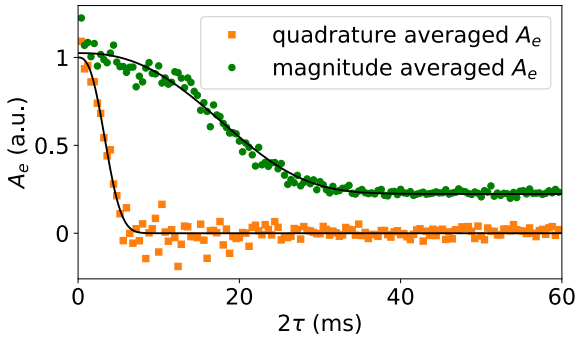

Figure 7.12 – **Electron spin coherence time measurement at 10 mK and $\varphi = 47°$ for sample A and resonator 3, with magnitude and quadrature averaging.** The magnitude averaged data (green circles) are the same data as in Figure 7.1. The quadrature averaged data (orange squares) are obtained from the same measurement by changing the data analysis. Solid black lines are fits with $A_e = Ae^{-(2\tau/T_{2,\text{phase}})^{x_\text{phase}}}$ for the quadrature averaged data, and with $A_e = \sqrt{Ae^{-2(2\tau/T_{2,\text{mag}})^{x_\text{mag}}} + C}$ for the magnitude averaged data. The fits yield $T_{2,\text{phase}} = 4.0 \pm 0.1\,\text{ms}$, $x_\text{phase} = 2.6 \pm 0.2$, $T_{2,\text{mag}} = 23.2 \pm 0.5\,\text{ms}$ and $x_\text{mag} = 2.4 \pm 0.1$.

photodiodes to detect the echo [Böt+09]. One drawback of this echo phase instability is that it prevented us from using dynamical decoupling (DD) sequences to enhance the coherence time [Ma+14]. Indeed, DD sequences require good-quality π pulses, which is not available in our setup due to the spread of Rabi frequencies, or phase-cycled averages in order to suppress spurious stimulated echoes, which rely on a stable echo phase.

We now briefly compare T_2 measurements performed in different setups. The measurement presented in Figure 7.1 was performed in a first setup, where the sample is placed at the center of two orthogonal Helmholtz coils, as described in Chapter 5 (setup 1). Then, the sample was moved to another cryostat, with a 3D-magnet which can run in persistent mode (setup 2). The sample was later moved back to the first setup (setup 3). Finally, the sample was put again in the cryostat with the 3D magnet, where all gold-plated copper pieces inside the magnet were re-fabricated without gold-plating (setup 4). Figure 7.13 shows the Hahn-echo decay measured at $\varphi = 47°$ in these four setups, where the data is analyzed with both magnitude and quadrature averaging methods. In setup 1, $T_{2,\text{mag}} = 23$ ms and $T_{2,\text{phase}} = 4$ ms (green dots, same data as in Figure 7.12). In setup 2, $T_{2,\text{mag}} = 16$ ms and $T_{2,\text{phase}} = 1.4$ ms (blue dots). In setup 3, $T_{2,\text{mag}} = 20$ ms and $T_{2,\text{phase}} = 4$ ms (red dots). In setup 4, $T_{2,\text{mag}} = 22$ ms and $T_{2,\text{phase}} = 1.9$ ms (black dots). We measure significantly different values in the different setups. In particular, the magnitude averaged $T_{2,\text{mag}}$ changes from setup 1 to 2 from 23 to 16 ms. We then recover values around 20-22 ms in setups 3 and 4, close to the value of setup 1. The quadrature averaged $T_{2,\text{phase}}$ is similar in setups 1 and 3, with $T_{2,\text{phase}} = 4$ ms and reduced in setups 2 and 4, with $T_{2,\text{phase}} \sim 1 - 2$ ms. One hypothesis for the variation of $T_{2,\text{mag}}$ is the presence of eddy currents in the gold-plated copper pieces which were designed to hold the sample in the 3D magnet. These eddy currents may perturb dynamically the applied magnetic field and reduce the spin coherence properties. After re-fabricating these copper pieces without gold-plating, we recover a similar $T_{2,\text{mag}}$ compared to setup 1. We have no explanation for the slightly smaller T_2 measured in setup 3 compared to setup 1 (20 vs 23 ms), as both setups are the same. We note that $T_{2,\text{phase}}$ is shorter in setup 4 compared to setups 1 and 3, indicating that there is more magnetic field noise in the kHz range, which randomizes the echo phase.

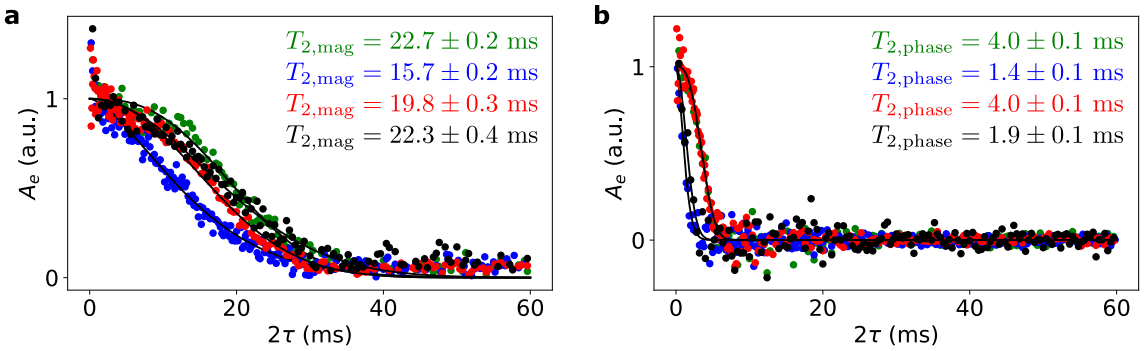

Figure 7.13 – **Hahn-echo coherence time measured at $\varphi = 47°$ and 10 mK, with resonator 3 of sample A, in different experimental setups. a.** Magnitude averaged echo amplitude as a function of 2τ. **b.** Quadrature averaged echo amplitude as a function of 2τ. All data (colored circles) are measured with 4 μs long pulses and the Hahn-echo sequence is repeated every 4 s. The echo amplitude is averaged over 20 to 60 measurements. The magnitude averaged data are fitted with $A_e = \sqrt{Ae^{-2(2\tau/T_{2,\mathrm{mag}})^{x\mathrm{mag}}} + C}$ and the quadrature averaged data are fitted with $A_e = Ae^{-2(2\tau/T_{2,\mathrm{phase}})^{x\mathrm{phase}}}$ (solid black lines). The fitted coherence times are indicated on the plots. Both data and fits are rescaled for a better comparison. The data are taken in different experimental setups which are described in chronological order: 1. The green dots are the data of Figure 7.1, measured in a first cryostat with the two Helmholtz coils. 2. The blue dots are obtained in another cryostat with gold-plated parts inside a 3D magnet in persistent mode. 3. The red points are obtained after moving the experiment back to the first cryostat. 4. The black points are measured in the second cryostat where all the parts inside the magnet have been replaced by copper pieces without gold-plating.

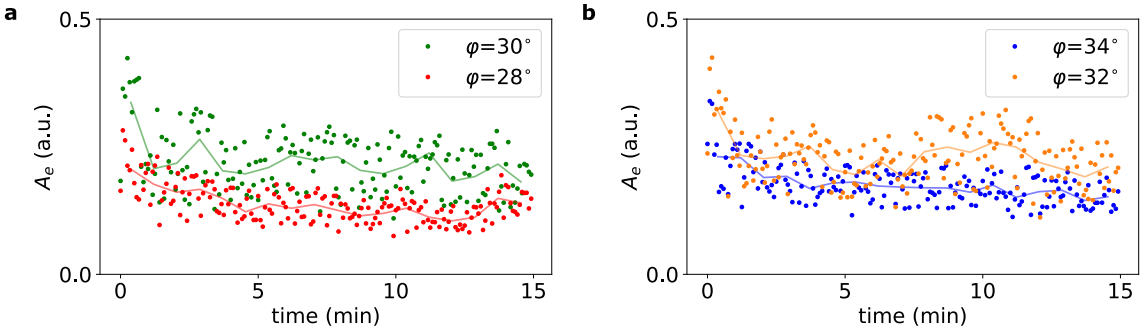

Figure 7.14 – **Echo amplitude measured as a function of time with resonator 3 of sample A at 10 mK.** A Hahn-echo sequence with $\tau = 40$ μs and 4 μs long pulses is repeated every 5 s during 15 minutes. The single-shot echo amplitudes (colored dots) are plotted as a function of the time when they are measured. These data are measured for various angles φ. The solid lines are averages over 10 data points. Before each measurement, the echo is measured as a function of the magnetic field amplitude B_0 for the given angle φ. Then the magnetic field is set at the center of the erbium line and the measurement starts.

7.1.1.6 Possible phonon bottleneck

In these echo measurements, we sometimes encounter an unexpected echo decay as we repeat the Hahn-echo sequence. Figure 7.14 shows single shot echoes, taken at various angles φ close to $\varphi_0 = 31°$, as a function of time. The Hahn-echo is repeated every 5 seconds, corresponding to the measured spin relaxation time T_1. Before each measurement, the magnetic field is swept across the erbium line with the chosen angle φ and is then fixed at the center of the erbium line. Although the relaxation time is about 5 seconds, the

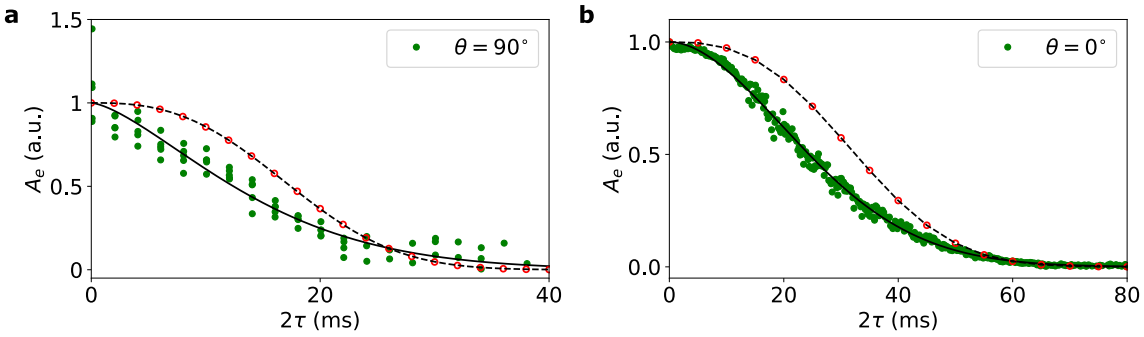

Figure 7.15 – **Erbium electron spin coherence time T_2 measured with resonator 3 of sample B at 10 mK. a.** Measured Hahn-echo amplitude, averaged in magnitude, as a function of 2τ, at $\theta = 90°$ (field aligned with the crystal b-axis). This measurement is done in packets of 5 points separated by $\Delta\tau = 2$ μs to take ESEEM into account. The solid black line is a fit with $A_e = \sqrt{Ae^{-2(2\tau/T_2)^x} + C}$, yielding $T_2 = 16.0 \pm 0.5$ ms and $x = 1.5 \pm 0.1$. The data is compared with the corresponding CCE simulation (red open circles). The simulation is fitted with $A_e = e^{(2\tau/T_{2,\mathrm{sim}})^{x_{\mathrm{sim}}}}$ (dashed black line), giving $T_{2,\mathrm{sim}} = 20.0$ ms and $x_{\mathrm{sim}} = 2.72$. **b.** Measured Hahn-echo amplitude, averaged in magnitude, as a function of 2τ, at $\theta = 0°$ (field aligned with the crystal c-axis). This measurement is sampled linearly as ESEEM can be neglected at $B_0 = 451$ mT. The corresponding CCE simulation is shown with open red circles. The data and simulation are fitted with the same functions as in subplot a. The solid black line is a fit to the data, yielding $T_2 = 30.0 \pm 0.1$ ms and $x = 1.85 \pm 0.02$. The dashed black line is a fit to the simulation, giving $T_{2,\mathrm{sim}} = 37.2$ ms and $x_{\mathrm{sim}} = 2.74$.

echo amplitude decreases slightly with a much slower rate before reaching its steady-state, over typical timescales of a few minutes. This may originate from phonon-bottleneck (see Section 2.4). We did not investigate further to demonstrate this hypothesis. However, to prevent this additional echo decay from affecting the very first points of the Hahn-echo decay curves, the latest acquired data were taken starting from the largest τ values and then decreasing τ. For instance, in Figure 7.13, the data of the first three runs (in green, blue and red) are measured with increasing τ values and the data of the last run (in black) are measured with decreasing τ values. We thus check in this way that it does not affect the fitted coherence time of $T_2 \sim 20$ ms.

7.1.2 Sample B

The Hahn-echo coherence time of erbium is also measured with sample B at 10 mK. Figure 7.15 shows the erbium electron spin coherence time measured with the field along the b-axis ($\theta = 90°$), which is equivalent to the data of sample A at $\varphi = 0°$, and along the c-axis ($\theta = 0°$). The data acquired at $\theta = 90°$ is sampled around several values of τ with a finer step of $\Delta\tau = 2$ μs to sample the ESEEM correctly. This is not needed for the data acquired at $\theta = 90°$ as the erbium resonance magnetic field, $B_0 = 451$ mT instead of $B_0 = 67.2$ mT, is sufficiently high to suppress ESEEM. The magnitude averaged data are fitted with $A_e = \sqrt{Ae^{-2(2\tau/T_2)^x} + C}$. The fit of the $\theta = 90°$ data yields $T_2 = 16.0 \pm 0.5$ ms, whereas $T_2(\theta = 0°) = 30.0 \pm 0.1$ ms. The data are compared with the CCE simulations performed with the corresponding magnetic field orientation. These simulations are fitted with $A_e = e^{(2\tau/T_{2,\mathrm{sim}})^{x_{\mathrm{sim}}}}$, where $T_{2,\mathrm{sim}} = 20.0$ ms at $\theta = 90°$ and $T_{2,\mathrm{sim}} = 37.2$ ms at $\theta = 0°$. The similarity between the measured and simulated echo decays indicates that in sample B the decoherence is also mainly limited by spectral diffusion caused by the nuclear spin bath. The longer T_2 on the c-axis is due to the reduced erbium magnetic moment compared to the (a, b)-plane.

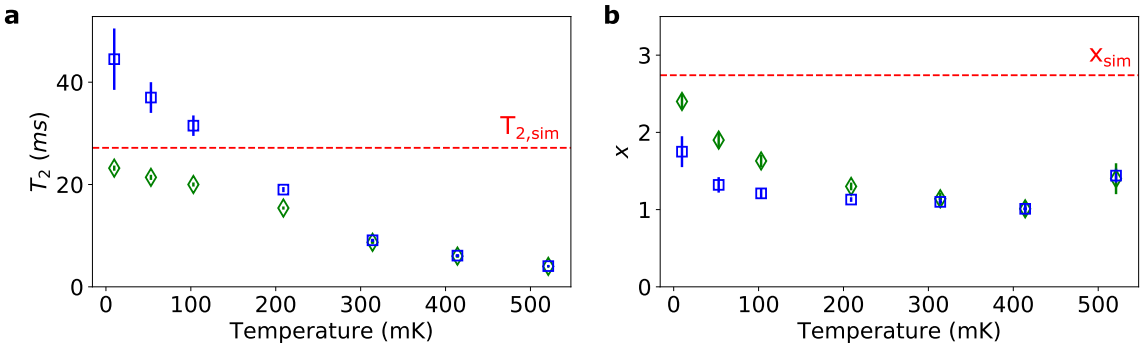

Figure 7.16 – **Temperature dependence of the Hahn-echo coherence time in sample A at $\varphi = 47°$.** Measured coherence time T_2 (**a**) and stretching exponent x (**b**) (green diamonds) as a function of the cryostat temperature. The red dashed line is the result of the CCE simulation which is temperature independent in our experimental range. The blue squares result from a second fit of the data with $A_e = \sqrt{Ae^{-2[(2\tau/T_{2,\mathrm{sim}})^{x_{\mathrm{sim}}}+(2\tau/T_{2,p})^{x_p}]} + C}$ in order to extract the net decoherence effect of spectral diffusion due to paramagnetic impurities.

7.2 Temperature dependence of the electron spin coherence time

7.2.1 Sample A

We measure the Hahn-echo decay as a function of temperature at $\varphi = \varphi_c = 47°$. The measurement shown in Figure 7.1 is repeated for several cryostat temperatures and the magnitude averaged echo amplitude is fitted with $A_e = \sqrt{Ae^{-2(2\tau/T_2)^x} + C}$. The resulting fitted coherence time T_2 and stretching exponent x are plotted as a function of temperature in Figure 7.16 (green diamonds). We observe that both T_2 and x strongly depend on temperature. In particular, the Hahn echo coherence time decreases by about a factor 6 at 500 mK, with $T_2 = 4.0$ ms instead of $T_2 = 23$ ms at 10 mK.

Since nuclear-spin spectral diffusion is expected to be temperature-independent as the nuclear spin bath is completely unpolarized, we attribute the decrease of T_2 and the change in x to spectral diffusion by paramagnetic impurities, which is suppressed at low temperature because of their polarization in the ground state (see Chapter 4). To make this effect more evident, we extract the paramagnetic spectral diffusion contribution, by fitting $T_{2,p}$ and x_p using the procedure explained in Section 7.1.1.3. The result is plotted in Figure 7.16 (blue squares). We observe that $T_{2,p}$ decreases by as much as one order of magnitude between 10 mK and 500 mK. Therefore, this confirms that there is a cross-over from spectral diffusion by nuclear spins to paramagnetic impurities at higher temperature.

As explained in Chapter 5 and Chapter 6, sample A contains several different paramagnetic impurities, in concentrations similar or larger than erbium that are difficult to evaluate precisely, and with g-factors that are not known. It is therefore difficult to model their impact, and thus we are not able to understand quantitatively the decrease of T_2. Along the same line of thought, we believe that the stretching exponent (decreasing from approximately 2.5 at 10 mK to a value closer to 1 at higher temperatures) results from the contribution of several uncorrelated baths, but we are not able to understand it quantitatively.

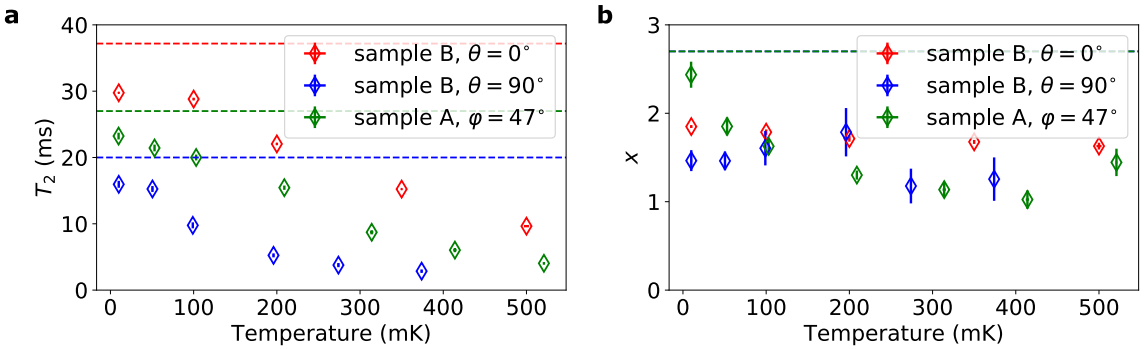

Figure 7.17 – **Temperature dependence of the Hahn-echo coherence time in samples A and B.** Temperature dependence of the fitted coherence time T_2 (**a**) and fitted stretching exponent x (**b**) for sample A at $\varphi = 47°$ (green diamonds, same data as in Figure 7.16), and sample B at $\theta = 90°$ (blue diamonds) and at $\theta = 0°$ (red diamonds). The dashed lines are the corresponding CCE simulated $T_{2,\mathrm{sim}}$ and x_{sim}.

7.2.2 Sample B

The temperature dependence of T_2 is also measured in sample B for two field orientations, $\theta = 90°$ and $\theta = 0°$, starting at 10 mK with the data shown in Figure 7.15. The temperature dependence of the fitted coherence time T_2 and stretching exponent x as a function of the cryostat temperature is plotted in Figure 7.17, overlaid with the data of sample A already shown in Figure 7.16. All fitted coherence times T_2 decrease significantly when the cryostat temperature increases, while it saturates near the nuclear spin limit (indicated with a dashed line) at base temperature.

The data measured at $\theta = 90°$ can be compared with the data of sample A as this was measured with approximately the same magnetic field amplitude, around 70 mT, although the angle φ is different. The decrease of T_2 in sample B is already significant at 100 mK, where T_2 is reduced by about a factor 2 compared to its value at 10 mK. In sample A, the equivalent temperature is rather 200 mK. This seems to indicate that sample B contains overall a larger concentration of paramagnetic impurities, although the concentrations of Kramers ions were estimated to be smaller in sample B (see Table 5.1).

Chapter 8

Relaxation time measurements

To complete the study of the dynamics of erbium in samples A and B, we now turn to measurements of the longitudinal spin relaxation time T_1. We first present spin relaxation measurements performed at high power, thus probing spins weakly coupled to the resonator; they relax via the direct-phonon process. We then present measurements performed at lower power, thus probing spins more coupled to the resonator, which enables us to observe a cross-over to radiative relaxation via the Purcell effect.

8.1 Spin-lattice relaxation

Throughout this section, we describe relaxation time measurements performed at high microwave pulse powers, thus exciting spins weakly coupled to the resonator so that their relaxation is dominantly non-radiative.

The relaxation time of Kramers ions has rarely been studied in the sub-Kelvin temperature range. The spin-lattice relaxation of Er^{3+}:$CaWO_4$, down to 1 K and with the magnetic field applied perpendicular to the c-axis, was already measured by Antipin *et al.* [Ant+68] and the corresponding data was presented in Figure 2.9. Below 1 K, we expect T_1 to originate only from the direct phonon process, which relaxation time given in Equation 2.41 rewrites

$$T_1 = \frac{1}{\alpha_D g_{\text{eff}}^3 B_0^5} \tanh \frac{\hbar\omega_0}{2k_0 T} = T_{1,0\text{K}} \tanh \frac{\hbar\omega_0}{2k_0 T}, \tag{8.1}$$

where $T_{1,0\text{K}}$ is the relaxation time at zero temperature. At 10 mK and $\omega_0/2\pi \sim 7-8$ GHz, the hyberbolic tangent term is about 1.

This equation can be used to extrapolate the fitted temperature dependence of Figure 2.9 down to 10 mK. Indeed, the direct phonon process at high temperature is fitted with $T_1^{-1} = AT$, where $A = 2k_B/(\hbar\omega_0) \times 1/T_{1,0\text{K}}$. Additionally, for a given magnetic field orientation, $T_{1,0\text{K}}$ varies as ω_0^{-5}. Thus, extrapolating Antipin's fit at $\omega_0/2\pi \sim 7-8$ GHz, we expect a typical spin-lattice relaxation time at zero temperature, $T_{1,0\text{K}}$, of a few seconds.

Moreover, due to the anisotropy of the spin-lattice coupling included in the α_D-parameter, the direct phonon relaxation rate in Kramers ions is expected to be anisotropic in the (a, b)-plane. The anisotropy of both one- and two-phonon processes was demonstrated experimentally for erbium ions in $LiYF_4$ in another work of Antipin [Ant+81].

8.1.1 Sample A: rotation pattern in the (a, b)-plane

We measure the relaxation time using an inversion recovery sequence. It consists in a first inversion pulse of amplitude α_{in} and duration dt. After a delay T, during which the spins start relaxing towards equilibrium, a Hahn-echo sequence, with two pulses of

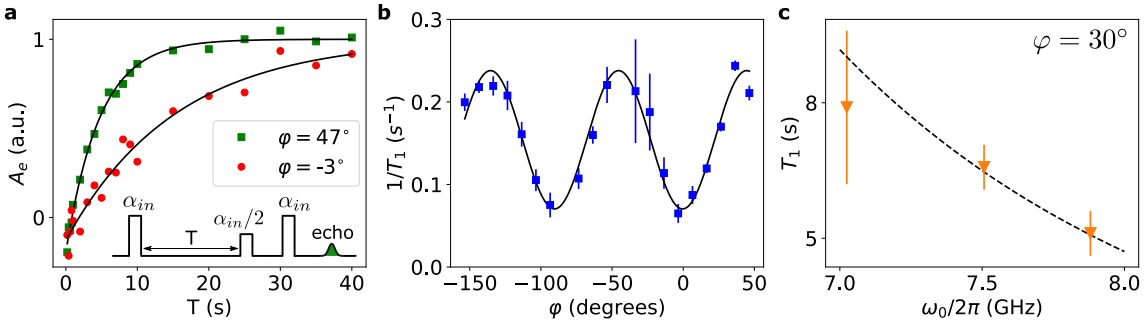

Figure 8.1 – **Measured erbium relaxation time in sample A at 10 mK.** The inversion recovery sequence includes a first pulse of amplitude α_{in}, followed after a delay T by a Hahn-echo detection sequence of same amplitude α_{in}. **a.** Measured echo amplitude recovery as a function of the delay T, at $\varphi = 47°$ (green squares) and $\varphi = -3°$ (red circles), with high input pulse power. This is measured with resonator 3 at $\omega_0/2\pi = 7.881$ GHz. Solid black lines are exponential fits with $T_1 = 4.7 \pm 0.2$ s at $\varphi = 47°$ and $T_1 = 15 \pm 3$ s at $\varphi = -3°$. **b.** Fitted relaxation rate $1/T_1$ (blue squares) as a function of φ for resonator 3. The solid black line is a fit with $T_1^{-1} = A + B \sin(4\varphi + \varphi_1)$, as described in [Ant+81], where φ_1 is found to be $92 \pm 3°$. **c.** Relaxation time at $\varphi = 30°$ as a function of the resonator frequency ω_0. Each data point is an average over several relaxation measurements in the high pulse power regime, from the data of Figure 8.5. The black dashed line indicates that the data is compatible with a dependence of T_1 as ω_0^{-5}.

amplitudes $\alpha_{in}/2$ and α_{in} and duration dt, is applied to the spins. When the delay T is much longer than T_1, the spins have completely relaxed to their equilibrium polarization and the Hahn-echo sequence triggers the steady-state spin echo. On the contrary, when the delay T is much shorter than T_1 and if the spins were completely reverted by the inversion pulse, the spin echo would be inverted in sign. As explained in Section 3.3.1.2, the spin echo approximately originates from spins rotating by $0.6\pi/2$ during the first pulse of the Hahn-echo sequence. These spins rotate by 0.6π during the inversion pulse and refocusing pulse. With this simple model, the Hahn-echo at short T is thus not expected to be fully inverted compared to the steady-state echo.

In Figure 8.1a, we plot the echo integral as a function of the delay T between the first pulse and the detection echo sequence, measured for two angles φ. The cryostat temperature is set to 10 mK and the measurement is performed with resonator 3, at $\omega_0/2\pi = 7.881$ GHz. The data are well fitted by an exponential function, yielding the spin relaxation time T_1; for $\varphi = 47°$, we find $T_1 = 4.7 \pm 0.2$ s, and for $\varphi = -3°$, we find $T_1 = 15 \pm 3$ s, indicating a strong relaxation time anisotropy. Repeating this measurement for more values of φ enables to plot T_1 as a function of φ (see Figure 8.1b). The relaxation rate is well fitted by a sinusoidal curve, as expected from the previous work of Antipin *et al.* [Ant+81]. Finally the spin-lattice relaxation measurement is repeated for the three resonators of sample A at $\varphi = 30°$. Figure 8.1c shows the relaxation time as a function of the resonator frequency. The data is fitted with a function proportional to ω_0^{-5} which is the expected frequency dependence of T_1 according to Equation 8.1.

We also measure the relaxation time T_1 as a function of the cryostat temperature for resonator 3, with the same pulse power and at $\varphi = \varphi_c = 47°$. The data is shown in Figure 8.2 and is fitted with Equation 8.1. The fit yields the relaxation time at zero temperature for this magnetic field orientation, $T_{1,0\mathrm{K}} = 4.8 \pm 0.1$ s. The good agreement between data and fit confirms that multi-phonon processes are not relevant at sub-Kelvin temperatures.

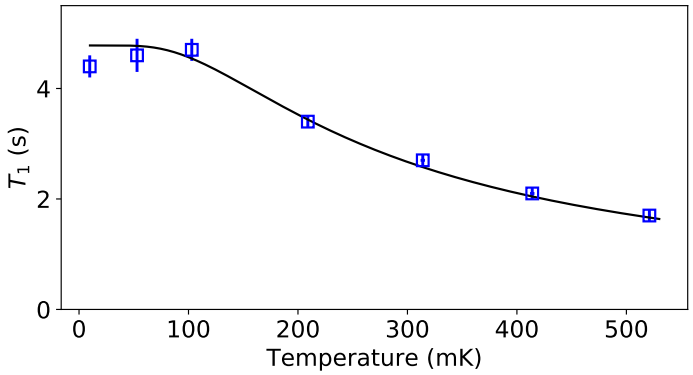

Figure 8.2 – **Spin-lattice relaxation time as a function of temperature, for erbium ions in sample A at $\varphi = \varphi_c = 47°$.** Relaxation time at high input pulse power as a function of the cryostat temperature (squares). The solid line is a fit with $T_1 = T_{1,0K} \tanh[\hbar\omega_0/(2k_BT)]$ as predicted for the direct-phonon process. The fit yields $T_{1,0K} = 4.8 \pm 0.1$ s.

8.1.2 Sample B

Similar measurements are performed with sample B. Figure 8.3a and b show relaxation time measurements at high pulse power for two magnetic field orientations, $\theta = 0°$ and $\theta = 90°$, which are fitted with exponential functions.

The measured relaxation time at $\theta = 90°$, $T_1 = 17 \pm 2$ s, can be compared with the relaxation time measured with sample A around $\varphi = 0°$, displayed in Figure 8.1a and b. Indeed this corresponds to the same magnetic field orientation and both resonators have similar frequencies, with $\omega_0/2\pi \sim 7.9$ GHz. The sinusoidal fit of the data of sample A in Figure 8.1b yields $T_1(\varphi = 0°) = 14$ s, which is in agreement with the relaxation time measured with sample B.

At $\theta = 0°$, the fitted relaxation time is shorter by more than one order of magnitude, with $T_1 = 0.2$ s. This can be understood from the angular dependence of Equation 8.1. In fact, at constant frequency, the direct phonon relaxation time is expected to vary as $T_1 \propto g_{\text{eff}}^2/\alpha_D$, where both g_{eff} and α_D depend on θ. The angular dependence of g_{eff} predicts already a decrease by a factor $8.38^2/1.247^2 \sim 45$ from $\theta = 90°$ to $\theta = 0°$, which is not too far from the ratio of about 80 which is measured. Its temperature dependence at this magnetic field orientation is shown in Figure 8.3c. The data is fitted with Equation 8.1 yielding a zero temperature relaxation time of $T_{1,0K} = 0.2$ s.

8.2 Radiative relaxation

We now turn to relaxation time measurements performed at low power with sample A. They probe spins that are more strongly coupled to the resonator, and thus are expected to relax radiatively.

8.2.1 CPMG signal enhancement

Lowering the power reduces the signal-to-noise (SNR). To improve it, we make use of the Carr-Purcell-Meiboom-Gill (CPMG) sequence, where the usual Hahn-echo sequence $(\pi/2 - \tau - \pi - \tau - \text{echo})$ is followed by a CPMG sequence consisting in a chosen number N of refocusing pulses $(\tau - \pi - \tau - \text{echo}) \times N$ [Alb+20]. This sequence is shown in Figure 8.4a. The Hahn-echo sequence plus the N refocusing pulses produce a series of $N + 1$ spin-echoes which can be averaged out to increase the SNR of the echo. Figure 8.4a shows a few echoes obtained with such a sequence, at high pulse power. The first echo is the usual Hahn-echo

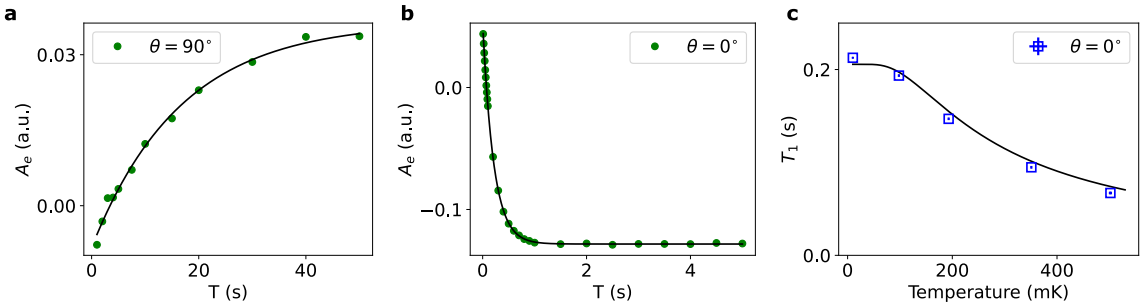

Figure 8.3 – **Measured relaxation time of erbium ions in sample B. a.** Measured echo amplitude recovery as a function of the delay T of an inversion recovery sequence, for $\theta = 90°$. This is measured with resonator 3 at $\omega_0/2\pi = 7.853$ GHz and at high input pulse power. The solid black line is an exponential fit yielding $T_1 = 17 \pm 2$ s. **b.** Same measurement performed at $\theta = 0°$. The exponential fit (solid black line) gives $T_1 = 0.213 \pm 0.001$ s. **c.** Fitted T_1 as a function of the cryostat temperature at $\theta = 0°$. The solid black line is a fit with Equation 8.1, yielding $T_{1,0\mathrm{K}} = 0.206 \pm 0.001$ s.

which is then refocused by each CPMG π pulse. Because we are probing a spin ensemble, the CPMG pulses are imperfect π-pulses. As a consequence, they do not only refocus the echo but also trigger stimulated echoes which may add up to the refocused echo. This is not a problem when the CPMG sequence is kept identical during the whole measurement. Indeed, we checked in the high power regime that the fitted spin relaxation time from the recoveries of the Hahn-echo and the CPMG-averaged echo are identical within their errorbars. We thus assume that there is a linear relation between the CPMG-averaged echo and the Hahn-echo such that fitting the echo recovery of the CPMG-averaged data yields the correct relaxation time.

The CPMG parameters, which are used throughout this section, are the following: the Hahn-echo delay τ is chosen to be 30 μs, the spacing between the CPMG pulses is $2\tau = 60$ μs and $N = 332$. Note that the spacing between CPMG pulses can be set independently of the Hahn-echo delay τ but should stay the same over the whole measurement.

The echo amplitude decreases with the CPMG pulse index due to pulse imperfections and decoherence effects. The decay is more visible in Figure 8.4c, where the normalized integrated echoes as a function of the CPMG pulse index are plotted for all three resonators of sample A. Note that the typical CPMG echo decay time is not linked to the measured coherence time of 23 ms. The CPMG sequence is expected to give a much longer decay which is not the case here as these echoes are averaged in quadrature. The normalized integrated echoes measured at high power are used as weights for averaging out the $N + 1$ spin-echoes in all the following measurements. Figure 8.4b compares the Hahn-echo of subplot a with the CPMG averaged echo, their shapes are similar. In this measurement, as the pulse power is high, the Hahn-echo SNR is sufficient and CPMG averaging is not needed. When the pulse power is reduced, the Hahn-echo SNR decreases and CPMG averaging becomes a powerful tool for SNR improvement.

We note here that the CPMG sequence can also be used as a dynamical decoupling sequence to enhance the coherence time T_2. In this case however, suppressing stimulated echoes which arise from pulse imperfections is critical and this requires phase-cycling sequences [Ma+14].

8.2.2 Power dependence of the spin relaxation time

To measure the relaxation time with CPMG signal enhancement, we use the inversion recovery sequence described in Section 8.1.1, followed by the CPMG sequence introduced

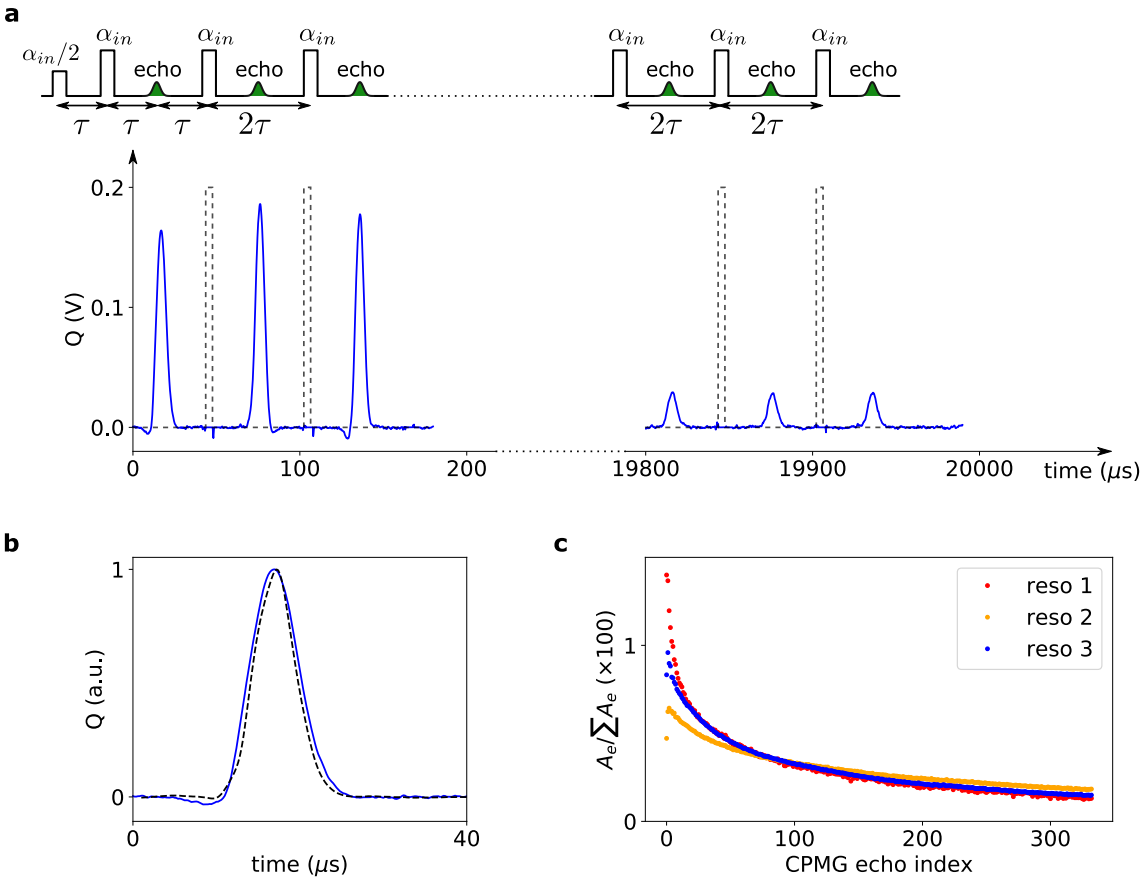

Figure 8.4 – **CPMG echoes. a.** *Top.* Sketch of a Hahn-echo sequence followed after a delay τ by a CPMG sequence consisting in a series of N pulses of same amplitude and duration as the refocusing pulse of the Hahn-echo sequence. The CPMG pulses are spaced by 2τ and an echo forms at time τ after each CPMG pulse. *Bottom.* Hahn-echo followed by $N = 332$ CPMG echoes recorded at high pulse power on the Q quadrature with resonator 3 of sample A, at $\varphi = 30°$ (solid blue line). The CPMG control pulses sent by the AWG, of duration $dt = 4$ μs and separation $2\tau = 60$ μs, are shown in a dashed grey line. The sequence is repeated every 4 s and averaged 300 times. The x-axis is cut to show only the three first and last echoes. The total sequence lasts about 20 ms. **b.** Hahn-echo (blue, same data as the first echo of subplot a) superposed with the CPMG averaged echo (black dashed line). The latter is computed as the weighted average of all $N + 1$ echoes where the weights are the normalized integral of each echo. **c.** Normalized integrated echo $A_e / \sum A_e$ as a function of its index in the CPMG sequence for all three resonators. These data, measured at high pulse power, are used as the weights for the CPMG averaging in all further experiments with CPMG signal enhancement.

above. The total sequence is sketched in Figure 8.5a and is used to measure relaxation with various pulse amplitudes α_{in} for all three resonators of sample A. In order to maximize the SNR, this measurement is also performed at $\varphi = 30°$, where the erbium inhomogeneous line is close to its minimum (see Section 6.2.1).

Figure 8.5a shows the CPMG-averaged echo amplitude as a function of T, for various pulse amplitudes α_{in}, measured with resonator 1. The data are well fitted by exponential curves, where the extracted spin relaxation time T_1 is strongly dependent on α_{in}.

We plot the fitted relaxation times T_1 for all three resonators as a function of the pulse amplitude α_{in} in Figure 8.5b and c. An approximately quadratic increase of T_1 with α_{in} is observed for small α_{in}, followed by a saturation at a maximum value for larger

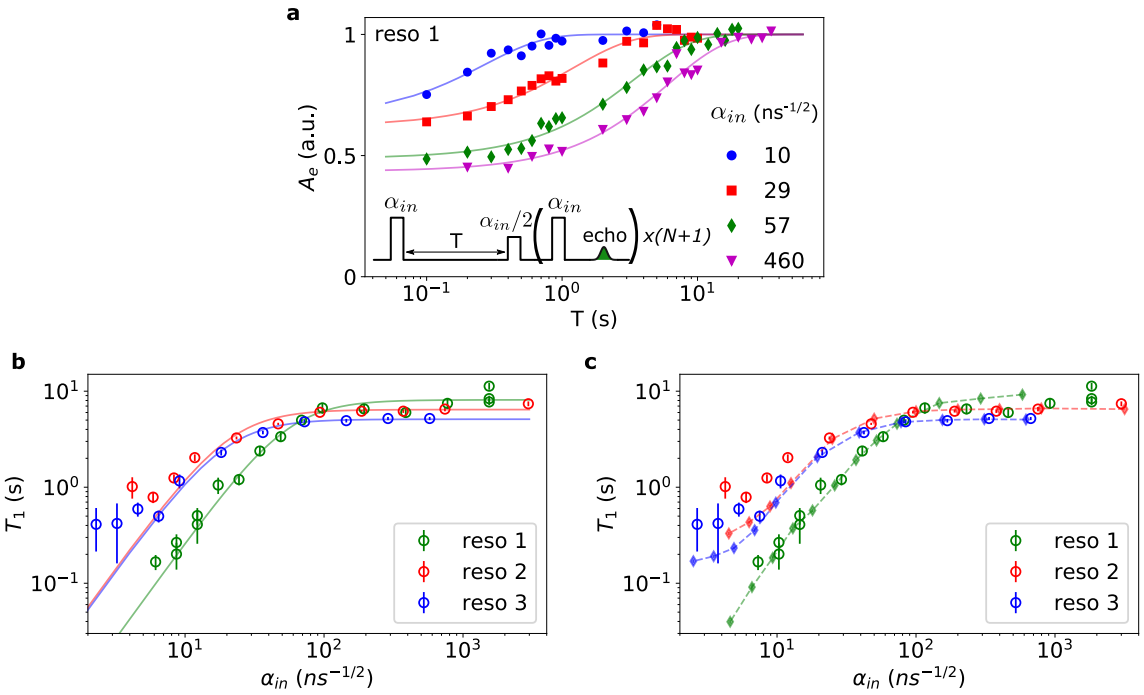

Figure 8.5 – **Power dependence of the erbium relaxation time in sample A at 10 mK. a.** Relaxation time measurements for various pulse amplitude α_{in} with resonator 1 of sample A. The inversion recovery sequence is followed by N pulses of amplitude α_{in} for CPMG signal enhancement. Full symbols are the measured echo amplitude A_e, resulting from CPMG averaging of the $N+1$ echoes, as a function of T. Solid lines are exponential fits, yielding the spin relaxation time T_1. The data are measured with resonator 1. φ is set to 30° in order to maximize the signal. **b.** Fitted values of T_1 as a function of α_{in} for the three resonators (open circles). They are fitted with Equation 8.2 (solid lines), with two adjustable parameters: the input line attenuation and the spin-lattice relaxation time. **c.** Fitted values of T_1 as a function of α_{in} for the three resonators (open circles). The colored diamonds (linked with a dashed line) result from simulations where the only adjustable parameters are the input line attenuation and the spin-lattice relaxation time.

α_{in}. This dependence of T_1 on α_{in} can be understood qualitatively by the cross-over between two relaxation channels: the Purcell relaxation rate, which at resonance expresses as $\Gamma_P = 1/T_{1,\text{Purcell}} = 4g_0^2/\kappa_t$ according to Equation 3.34, and the spin-lattice relaxation rate $\Gamma_{sl} = 1/T_{1,\text{phonon}}$. Low-$\alpha_{in}$ measurements probe spins with a large g_0, close to the inductive wire, where Purcell relaxation dominates, whereas spin-lattice relaxation becomes the limiting rate for weakly coupled spins, far from the resonator, measured with large α_{in}.

The quadratic dependence of the Purcell-limited T_1 can be understood from the simple model introduced in Section 3.3.1.2. In the narrow-line case, the Hahn-echo detection sequence is mostly sensitive to spins which rotate by 0.6π during the refocusing pulse of duration dt. The coupling constant g_0 of these spins, given by Equation 3.59, is inversely proportional to the pulse amplitude α_{in}. Therefore, the Purcell relaxation time, $T_{1,\text{Purcell}} = \kappa_t/(4g_0^2)$ at resonance, is expected to vary as α_{in}^2. This is roughly what is observed in the data plotted in logarithmic scale in Figure 8.5b and c.

With this simple picture, the power dependence of T_1 can be fitted with

$$\frac{1}{T_1} = \frac{1}{T_{1,\text{phonon}}} + \frac{4g_0^2}{\kappa_t} \sim \frac{1}{T_{1,\text{phonon}}} + \frac{\kappa_t}{\kappa_c} \times \left(\frac{0.6\pi}{2\alpha_{in} dt}\right)^2, \tag{8.2}$$

where the only free parameters are $T_{1,\text{phonon}}$ and the input line attenuation which enables us to calibrate α_{in}, the absolute pulse amplitude used for measuring the data. The result of

the fit is shown in Figure 8.5b. The fits reproduce well the data, with a quadratic increase at low power and a plateau at high power. The fits yield spin-lattice relaxation times of $T_{1,\text{phonon}} = 8.1 \pm 0.4$ s, 6.4 ± 0.3 s and 5.1 ± 0.1 s for resonators 1, 2 and 3 respectively. These values are in agreement with the data of Figure 8.1c which is expected as they were extracted from the same dataset. The fits also correct our estimation of the input line attenuation by -8 ± 1 dB for resonator 1 and -5 ± 1 dB for resonators 2 and 3.

8.2.3 Simulations of spin-relaxation power dependence

Figure 8.5c compares the data with numerical simulations which take into account the full distribution of spin-resonator coupling constants g_0 and the distribution of Larmor frequencies Δ with respect to the resonator frequency ω_0, the two distributions being independent [Ran+20c]. The parameters of the simulations are the following:

- for resonator 1 (with a 2 μm wide inductance wire), there are 420 discrete frequency bins taken with uniform spacing between $-4\kappa_t$ and $4\kappa_t$, where $\kappa_t/2\pi = 185$ kHz, and 120 values of coupling strength $g_0/2\pi$, equally spaced between 1 and 1000 Hz,
- for resonator 2 (with a 5 μm wide inductance wire), there are 800 discrete frequency bins taken with uniform spacing between $-3\kappa_t$ and $3\kappa_t$, where $\kappa_t/2\pi = 620$ kHz, and 120 values of coupling strength $g_0/2\pi$, equally spaced between 0.5 and 500 Hz,
- for resonator 3 (with a 5 μm wide inductance wire), there are 480 discrete frequency bins taken with uniform spacing between $-3.5\kappa_t$ and $3.5\kappa_t$, where $\kappa_t/2\pi = 350$ kHz, and 120 values of coupling strength $g_0/2\pi$, equally spaced between 0.5 and 500 Hz.

Each spin with frequency detuning Δ and coupling constant g_0 relaxes with rate $\Gamma = \Gamma_P + \Gamma_{sl}$, where Γ_{sl} is the spin-lattice relaxation rate and $\Gamma_P = \kappa_t g_0^2/(\kappa_t^2/4 + \Delta^2)$ is the Purcell relaxation rate of Equation 3.34. Γ_{sl} is chosen according to the fit of Figure 8.1c, with $\Gamma_{sl}^{-1} = 9.1$ s for resonator 1, $\Gamma_{sl}^{-1} = 6.5$ s for resonator 2 and $\Gamma_{sl}^{-1} = 5.1$ s for resonator 3. For spins at a distance greater than approximately 15 μm from the inductance wire, the relaxation is dominated by Γ_{sl}, whereas for spins located closer to the inductance wire, it is dominated by Γ_P.

The inhomogeneous absorption linewidth at $\varphi = 30°$ is $\Gamma_{\text{inh}}/2\pi = 2$ MHz, which is more than three times wider than the broadest resonance linewidth. Thus the spin frequency distribution ρ_Δ is approximated with a constant. The coupling constant distribution ρ_{g_0} is plotted in Figure 8.6 for the three resonators of sample A. It is calculated by making a histogram out of the coupling constant map, which is computed from the COMSOL simulation of the magnetic field around the inductance wire. This map is similar to the one shown in Figure 5.13, where the angle $\varphi = 30°$, the inductance wire width and the resonator frequency have been modified. The coupling constant distribution behaves approximately as $1/g_0^3$ at low g_0 and shows a peak at high g_0 due to the spins located close to the wire. This peak occurs at higher coupling constant for resonator 1 due to its narrower inductance wire width, of 2 μm instead of 5 μm for the two other resonators. Indeed, narrowing the inductance wire width increases the magnetic field generated around the inductance wire and thus the coupling to nearby spins. The slight difference between the distributions of resonators 2 and 3 comes from their different resonator frequency ω_0.

For simplicity, the simulated pulse sequence for T_1 is the inversion recovery sequence ($\alpha_{in} - T - \alpha_{in}/2 - \tau - \alpha_{in} - \tau -$ echo), even though we used CPMG averaging to increase the SNR. After the simulation, the attenuation of the input line is adjusted to fit the data. Compared to an initial rough estimate, we find that the input attenuation has to be corrected by about 5 to 10 dB depending on the resonator, with -10 dB for resonator 1, -6 dB for resonator 2 and -7 dB for resonator 3. These values are close to the ones found

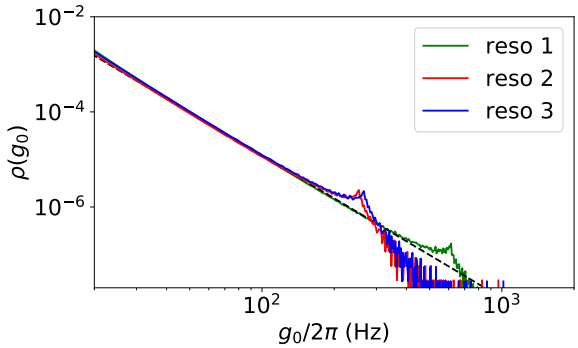

Figure 8.6 – **Spin-resonator coupling distribution**. The coupling distribution is shown in logarithmic scale for the three resonators of sample A, simulated at $\varphi = 30°$. The COMSOL simulation takes into account spins located in a surface $L_{y'} \times L_{z'} = 400 \times 200$ μm^2 below the inductance wire. The dashed black line is a fit with $\rho(g_0) \propto g_0^{-3}$. The peak at high coupling strength corresponds to spins located close to the wire.

earlier with the fit of the data to Equation 8.2. The simulations are overlaid with the data in Figure 8.5c.

Contrarily to the simplistic T_1 model of Equation 8.2, the numerical simulations confirm that the data taken with resonators 2 and 3 (of wire width 5 μm) start to saturate at low power while the relaxation time of resonator 1 (of wire width 2 μm) keeps decreasing. This can be attributed to the fact that for resonators 2 and 3, the lowest pulse amplitudes α_{in} probe the nearest spins from the inductance wire, corresponding to the peak in the coupling distribution at $g_0/2\pi \sim 260$ Hz (see Figure 8.6). For resonator 1, the nearest spins are more coupled, with $g_0/2\pi \sim 600$ Hz, and are not yet being probed by the lowest pulse amplitudes used in our measurements.

Part III

Experiment 2: spin dynamics of erbium ions in a highly doped $CaWO_4$ crystal

Chapter 9

Device and experimental setup

Several quantum applications of erbium spin ensembles, for instance quantum memories, require a high concentration of erbium ions in order to target large efficiencies. In this context, it is also interesting to investigate the erbium dynamics in $CaWO_4$ with a much larger concentration compared to the residual ppb concentration of erbium in the previous undoped crystals. This is the subject of this third part.

The measurements presented here are performed with a sample extracted from a $CaWO_4$ boule purchased commercially at Scientific Materials, with a nominal concentration of 50 ppm erbium. The sample used in these experiments was cut and polished by the team of Philippe Goldner at ChimieParisTech. All measurements presented in this third part are performed at high power, probing spins in the bulk of the crystal.

9.1 Superconducting resonator design

The design chosen for this experiment is different from the one of Chapter 5 on two main aspects. First, the resonator is probed with a hanger instead of reflection geometry (see Chapter 3). Second, instead of putting the superconducting LC-resonator in a 3D copper box, it is surrounded by a superconducting ground plane sputtered on the surface of the $CaWO_4$ sample. The latter has a surface of dimensions 3×5 mm^2 in the (b, c)-plane, where the c-axis is along the long edge, and 0.5 mm thickness along the a-axis. Note that this orientation with respect to the crystal axes is the same as for sample B of part 2 (see Figure 5.5).

The resonator itself is designed with a capacitor made of 30 inter-digitated fingers of 20 μm width and an inductance wire of length 725 μm and width 5 μm as depicted in Figure 9.1. The resonator is grounded on one side and on the other side, it is capacitively coupled with gap $g = 100$ μm to a feedline designed to have an impedance of 50 Ω. The wire length l is adjusted to match the desired frequency. Changing the gap g between the resonator pad and the 50 Ω impedance feedline in the simulation enables us to tune the resonator coupling rate κ_c.

9.1.1 Electromagnetic simulations

The design of Figure 9.1 is simulated with Ansys HFSS. The resonator is patterned on the $CaWO_4$ sample such that its inductance wire is parallel to the sample short edge and so perpendicular to the c-axis. The simulation gives $\omega_0/2\pi = 4.73$ GHz and $\kappa_c = 1.9 \times 10^6$ s^{-1}. The simulated electric field and surfacic current with 1 Joule in the resonator mode are shown in Figure 9.2. Adding a series lumped inductance of 50 pH to the inductance wire enables us to estimate the impedance of the resonator, $Z_0 \sim 19$ Ω.

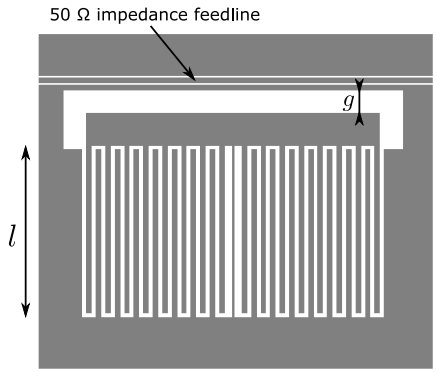

Figure 9.1 – **Sketch of the resonator with key tunable parameters.** l is the wire length and g is the gap between one pad of the resonator and the 50 Ω impedance feedline. The other pad of the resonator is grounded to the metallic ground plane which extends on the whole sample surface.

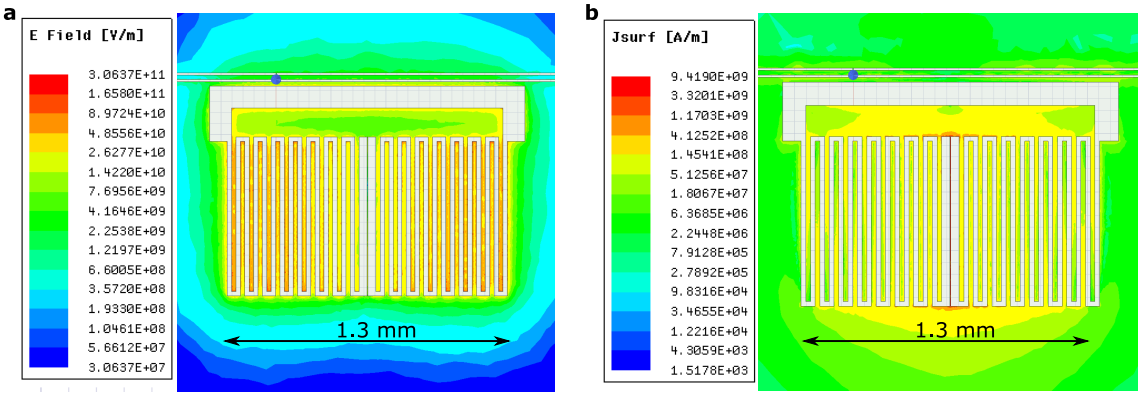

Figure 9.2 – **HFSS simulations. a.** Electric field in logarithmic scale with 1 Joule applied in the resonator mode. **b.** Surfacic current in logarithmic scale with 1 Joule applied in the resonator mode. The blue dot on the feedline is simply the z- axis of the simulation pointing out of plane.

9.1.2 Fabrication recipe

As in the previous experiment, the resonator is fabricated in niobium. A thin layer of 100 nm of niobium is sputtered on the $CaWO_4$ sample before dry etching with CF_4. The etching rate of $CaWO_4$ with CF_4 is measured to be negligible (of the order of 2 ± 1 nm/min). The step-by-step process is the following:

- **Substrate cleaning:** cleaning in acetone and ultrasounds for a few minutes, followed by a rinse in isopropanol (IPA).
- **Metal deposition:** deposit 100 ± 5 nm of niobium by sputtering at a rate of 2 nm/s.
- **Resist coating:** bake the sample for 1' at 110°C in order to evaporate any solvant. Spin coat the sample with UV3 resist: 60" at 6000 rpm (revolutions per minute) with acceleration 4000 rpm. The final resist thickness is approximately 500 nm. Soft bake 1' at 130°C.
- **Electron beam lithography:** write the circuit with a Raith electron beam lithography system (with dose 7 $\mu C/cm^2$, dose scaling 1.2, voltage 10 kV and aperture 30 μm). The UV3 resist is positive such that only parts of the sample where the metal needs to be removed are exposed.

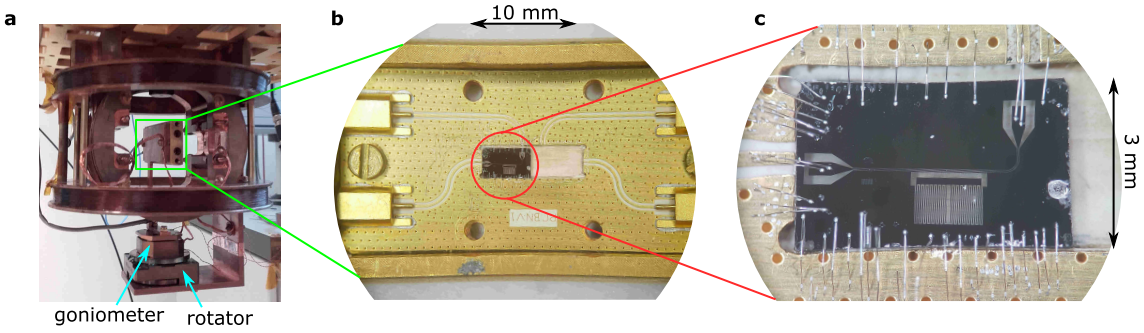

Figure 9.3 – **Setup inside the Helmholtz coils of the dilution fridge. a.** A rectangular box is placed at the center of pairs of Helmholtz coils mounted on the mixing chamber plate. The lid of the box includes a rod which is screwed on a stack of piezo-electric actuators, including a rotator at the bottom and a goniometer on top. **b.** Inside the rectangular gold-plated copper box. Printed circuit board (PCB) where the two left ports are used to measure the resonator in transmission. **c.** $CaWO_4$ sample covered with a niobium film where the resonator has been patterned. The sample is connected to the core and ground plane of the PCB with aluminium wirebonds.

- **Resist development:** post exposition bake at 140°C for 1', cooldown for 1', followed by 20" in MF CD-26.

- **Dry etching:** reactive ion etching at a base pressure of 50 μbar, with 10 sccm (standard cubic centimeters per minute) of Ar and 20 sccm of CF_4, at a power of 50 W. A silicon piece sputtered with niobium at the same time as the $CaWO_4$ sample is put under the laser. Etching takes approximately 4', including an overetch time of 10 %.

- **Resist removal:** 5' in a bath of hot remover (Technistrip P1331) at 70°C. Rinse with water.

9.1.3 Resonator microwave characterization at 10 mK

After fabrication, the sample is glued using PMMA resist on a printed circuit board (PCB) with SMP ports. The sample is then bonded to the PCB with thin aluminium wirebonds as shown in Figure 9.3b and c. The PCB is screwed in a rectangular gold-plated copper box and is put inside a couple of orthogonal Helmholtz coils which are fixed on the mixing chamber plate of the dilution fridge. The box fundamental mode is at high frequency such that it does not interfere with the resonator frequency.

Once cooled down to 10 mK, the resonator transmission coefficient S_{21} is measured with a VNA. Figure 9.4 shows S_{21} measured with about 1000 photons in the resonator. The resonance frequency is $\omega_0/2\pi = 4.37$ GHz, the coupling rate is $\kappa_c = 3.0 \times 10^6$ s^{-1} and the internal loss rate varies with input power, or equivalently with the number of photons in the resonator according to Equation 3.21. The dependence of the internal loss rate as a function of the number of photons in the resonator n is shown in Figure 9.4c. The internal loss rate at lowest photon number is $\kappa_{\text{int}} = 0.65 \times 10^6$ s^{-1}. As already observed with the resonators of the previous experiment, the internal loss rate decreases with n, due to saturation of two level systems [Wan+09]. The resonator parameters were observed to change slightly from one run to another.

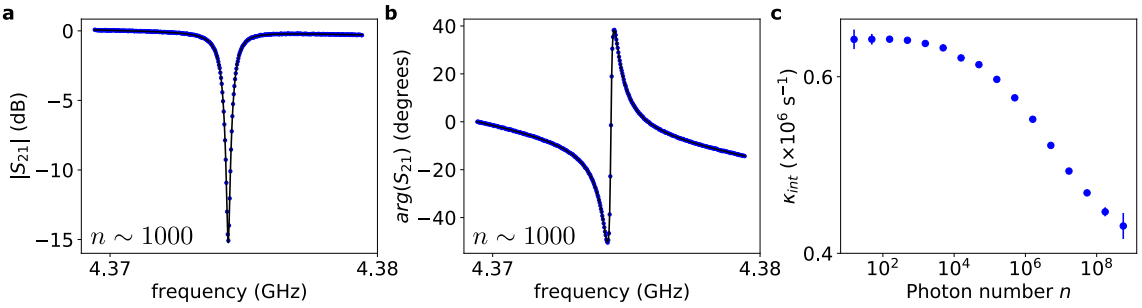

Figure 9.4 – **Measured transmission coefficient of the resonator at 10 mK. a. & b.** The transmission coefficient S_{21} is measured as a function of frequency with about 1000 photons in the resonator (blue dots). The black line shows a fit with Equation 3.7 multiplied by a linear background. **c.** Internal loss rate as a function of the number of photons in the resonator. The resonator parameters (frequency, coupling and internal loss rates) were found to slightly vary from one run to another.

9.2 Experimental setup for electron spin resonance at 10 mK

9.2.1 Low temperature setup

The experimental setup used to study this sample is very similar to the one presented in Chapter 5. The major difference is that the resonator is designed with a hanger instead of reflection geometry. The TWPA is different but behaves similarly. Inner DC blocks, preventing spurious currents from perturbing the TWPA in the previous experiment, are not needed. The updated wiring scheme of Figure 5.14 is shown in Figure 9.5. The echo setup is identical to the one of Chapter 5 (see Figure 5.17).

9.2.2 Magnetic field alignment with Attocube piezo-electric actuators

In this experiment, the magnetic field alignment within the niobium film is critical because of the large superconducting area of the ground plane. The couple of orthogonal Helmholtz coils applies a magnetic field within a plane which is roughly aligned with the sample surface. To be able to correct for a small out-of-plane field component, we purchased a set of cryogenic nanopositioners (from the company Attocube), which includes a piezo rotator (ANR240) and a piezo goniometer (ANGp101/RES). The positioner body is made out of beryllium copper and titanium and the actuator material is PZT ceramics. The piezo stack, with the goniometer screwed on top of the rotator, is sketched in Figure 9.6 and visible in Figure 9.3a. In particular, it was designed to withstand the weight of the sample box. The rotator allows us to correct the magnetic field alignment when the field is applied with one of the Helmholtz coil pairs, while the goniometer placed on the rotator allows us to do so in the other direction of the magnetic field. Both piezo devices are either manually or computer controlled via an Attocube piezo step controller (ANC150/3), which drives them with a typical voltage and frequency of 70 V and 100 Hz respectively.

This setup is tested with a niobium resonator patterned on a silicon sample with a very similar design to the one presented in Section 9.1. At 10 mK, its resonance frequency is $\omega_0/2\pi = 5.81$ GHz and its coupling rate is $\kappa_c = 0.5 \times 10^6$ s^{-1}. Its internal loss rate is strongly power dependent as shown in Figure 9.7a, varying between 6×10^6 s^{-1} at low power and 0.4×10^6 s^{-1} at high power. A magnetic field misalignment is expected to increase the loss rate as the magnetic field increases, due to vortices appearing in the niobium film. Since vortex-added losses are expected to be independent of power, we use a

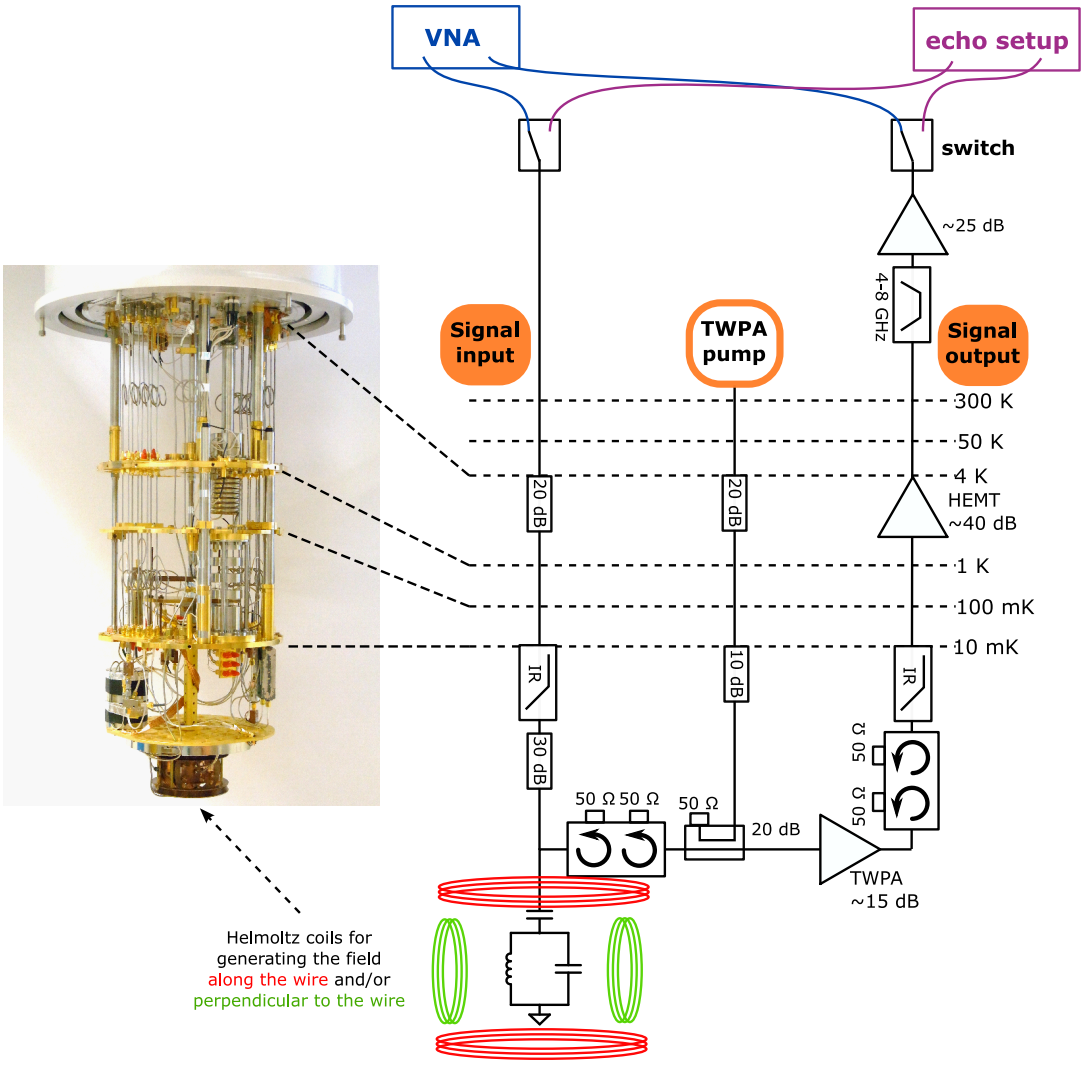

Figure 9.5 – **Microwave setup inside the Bluefors dilution refrigerator.** This setup is almost identical to the one of Figure 5.14 except that the resonator is probed in a hanger geometry. Moreover, inner DC blocks at the TWPA input and output ports are not needed in this experiment.

high microwave power to adjust the alignment, in order to start from the minimum initial loss rate of $\kappa_{\text{int}} = 0.4 \times 10^6$ s^{-1}. The effect of tuning the rotator on the resonator frequency and internal loss rate is shown in Figure 9.7b and c. In this case, tuning the rotator halves the resonance frequency shift and the internal loss rate is preserved below 0.5×10^6 s^{-1} up to 150 mT. Vortex penetration is still observed, with small sudden jumps of the resonance frequency, but at higher field, and has lower impact on the internal losses. A slight increase of the internal loss rate is observed at $B_0 \sim 10$ mT which is attributed to the aluminium wirebonds switching from superconducting to normal state.

In practice, the field alignment is performed in the following steps. The sample is roughly aligned by eye during sample mounting by tuning the goniometer and rotator at room temperature. Once the fridge is cold, an in-plane magnetic field of typically 100 mT is applied, either perpendicular or parallel to the wire axis. The corresponding piezo is tuned step by step until the resonator frequency is maximized. Then the field is decreased back to zero and applied in the other direction to tune the second piezo actuator. Such tuning with the test resonator is shown in Figure 9.8. This tuning protocol causes vortices

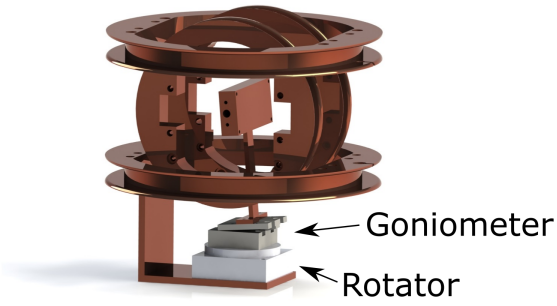

Figure 9.6 – **Schematics of the stack of Attocube piezo-electric actuators.** The sample box is fixed on the goniometer which is itself screwed on the rotator. Both nanopositioners are tuned to align the magnetic field generated by the two pairs of Helmholtz coils within the superconducting film sputtered on the sample.

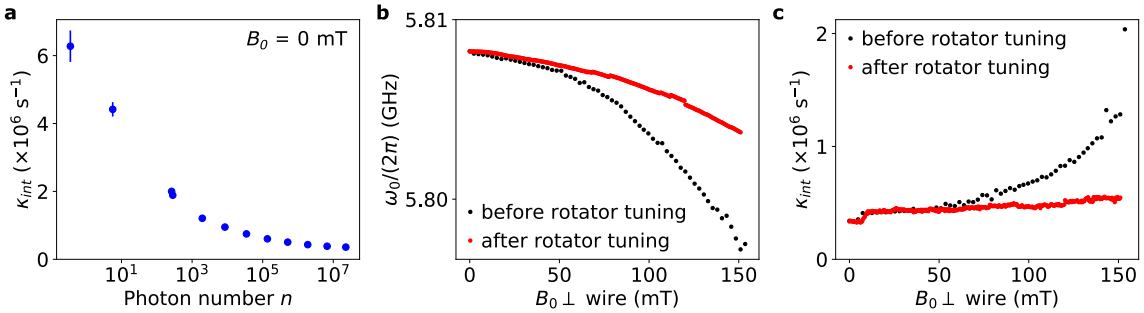

Figure 9.7 – **Testing the piezo-electric nanopositioners.** The field alignment setup is tested with a niobium resonator on a silicon sample, with frequency $\omega_0/2\pi = 5.81$ GHz and coupling rate $\kappa_c = 0.5 \times 10^6$ s^{-1}. **a.** Power dependence of the internal loss rate κ_{int}. All the measurements are then performed at highest power, where $\kappa_{\text{int}} = 0.4 \times 10^6$ s^{-1}. **b. & c.** Frequency and internal loss rate as a function of the magnetic field strength B_0, applied in-plane and perpendicular to the wire axis, before (black) and after (red) tuning the rotator. The superconducting film needs to be thermically cycled to above its critical tempeperature between the two measurements to recover its properties. The reproducible increase of internal losses at $B_0 \sim 10$ mT is attributed to the aluminium wirebonds which change from superconducting to normal state.

to penetrate the niobium film, which lead to sudden jumps of the resonance frequency and internal loss rate. After the tuning, we therefore operate a thermal cycling up to 10 K, and we then cool the sample again (in zero applied field).

During the tuning of the piezo stack, the mixing chamber temperature increases, to a maximum temperature depending on the stepping rate, typically from a few tens of milliKelvin up to 100 mK. In general, the resonator frequency does not vary significantly in this temperature range and the piezo stack tuning is performed at base temperature. However, the resonance frequency of the test resonator varies noticeably between 10 mK and 200 mK. Therefore the tuning shown in Figure 9.8 is performed at 400 mK, where the resonator frequency is less sensitive to a temperature increase. We also note that the behaviour of these piezo devices is strongly hysteretic such that the optimum position of each device cannot be determined by just counting the excess steps since the frequency reached its maximum. The resonance frequency has to be constantly measured as the piezo device is tuned and the tuning stops when the resonance frequency reaches its maximum value. Moreover, we did not manage to determine the correspondence between a piezo step and a rotation angle.

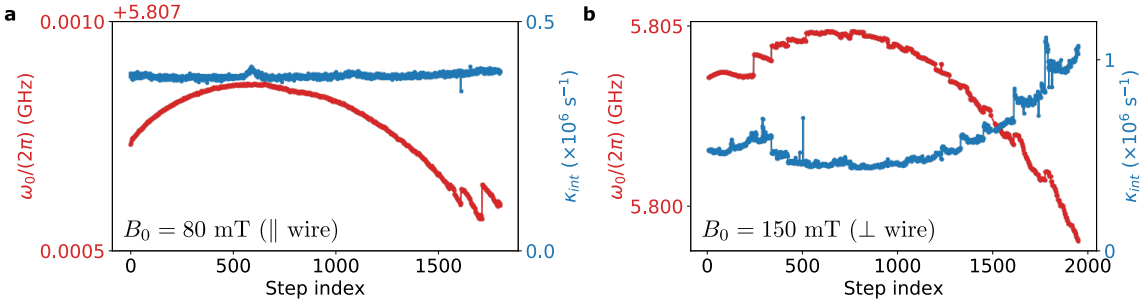

Figure 9.8 – **Piezo rotator and goniometer tuning. a.** Goniometer tuning. An in-plane magnetic field of $B_0 = 80$ mT is applied parallel to the wire axis. The resonator frequency and internal loss rate are recorded as a function of the step index of the goniometer, where each step changes slightly the angle of the sample with respect to the applied magnetic field. The discontinuities visible after index 1500 correspond to the range limit of the goniometer. The goniometer's position is adjusted until the resonance frequency is maximum. **b.** Rotator tuning. This measurement is performed right after the measurement of subplot a. The magnetic field is decreased to 0 and ramped again to $B_0 = 150$ mT in the in-plane direction perpendicular to the wire axis. The discontinuities are attributed to vortices which entered the niobium film while the goniometer was tuned. The rotator's position is adjusted until the resonance frequency is maximum. Both measurements shown in this figure are performed at 400 mK corresponding to a temperature where the resonance frequency was less sensitive to the heating of the mixing chamber. This was however specific to this test resonator. Tuning the resonator on $CaWO_4$ did not require to heat up the mixing chamber. After tuning, the mixing chamber is heated up to above the niobium critical temperature and cooled down in zero magnetic field to get rid of the vortices.

Chapter 10

Continuous-wave electron spin resonance spectroscopy

In this chapter, we report continuous-wave spectroscopy measurements of the $CaWO_4$ sample with nominal erbium concentration of 50 ppm. These measurements enable us to extract information about the various dopants present in the sample, such as their concentration and their ensemble coupling to the resonator.

10.1 Characterizing the paramagnetic impurities

10.1.1 Spectroscopy with the magnetic field along the resonator wire axis

We start by characterizing the paramagnetic centers in the sample with continuous-wave ESR spectroscopy. To do so, we measure the transmission coefficient S_{21} as a function of frequency and sweep the magnetic field $\boldsymbol{B_0}$ applied parallel to the wire axis (i.e. perpendicular to the c-axis). The results are shown in Figure 10.1. The measurement of $|S_{21}|$ displays several avoided crossings, each of them corresponding to the resonance condition between the resonator and one electron spin transition, in a regime where the cooperativity is larger than unity, as explained in Section 3.3.0.1.

To identify each avoided crossing, the data are compared with the energy level spectrum of Er^{3+}:$CaWO_4$, computed in Figure 2.5, with $\boldsymbol{B_0} \perp c$. The main ESR allowed spin transitions at the resonator frequency $\omega_0/2\pi = 4.38$ GHz are marked in red. The electron spin transition of the $I = 0$ erbium ions occurs at $B_0 = 37$ mT, while for the ^{167}Er isotope, the eight ($\Delta m_S = \pm 1,\ \Delta m_I = 0$) hyperfine transitions are marked. They are the only allowed transitions in the high magnetic field limit, where the labels m_S and m_I are well-defined. In the low field regime, spin-state mixing due to the hyperfine coupling can induce other electron spin transitions, in particular with $\Delta m_I = \pm 1$. These transitions are partially allowed in our magnetic field range and correspond to the small bumps of the internal loss rate between two successive identified hyperfine transitions.

We note that reaching the high cooperativity regime for the erbium $I = 0$ spins is expected in this sample. Indeed, the nominal 50 ppm erbium concentration of this $CaWO_4$ sample is more than four orders of magnitude larger than in the samples studied in part II. The cooperativity, which was of the order of $0.01 - 0.1$ in the previous samples (see Section 6.3), is supposed to increase by roughly the same amount, depending on the inhomogeneous linewidth, via the square of the ensemble coupling constant, g_{ens}^2, which is proportional to the erbium concentration.

In addition to erbium, other EPR lines are visible. There is a strong avoided crossing at $B_0 = 80$ mT, as well as weaker signals from $B_0 = 40$ mT to 70 mT. They are attributed

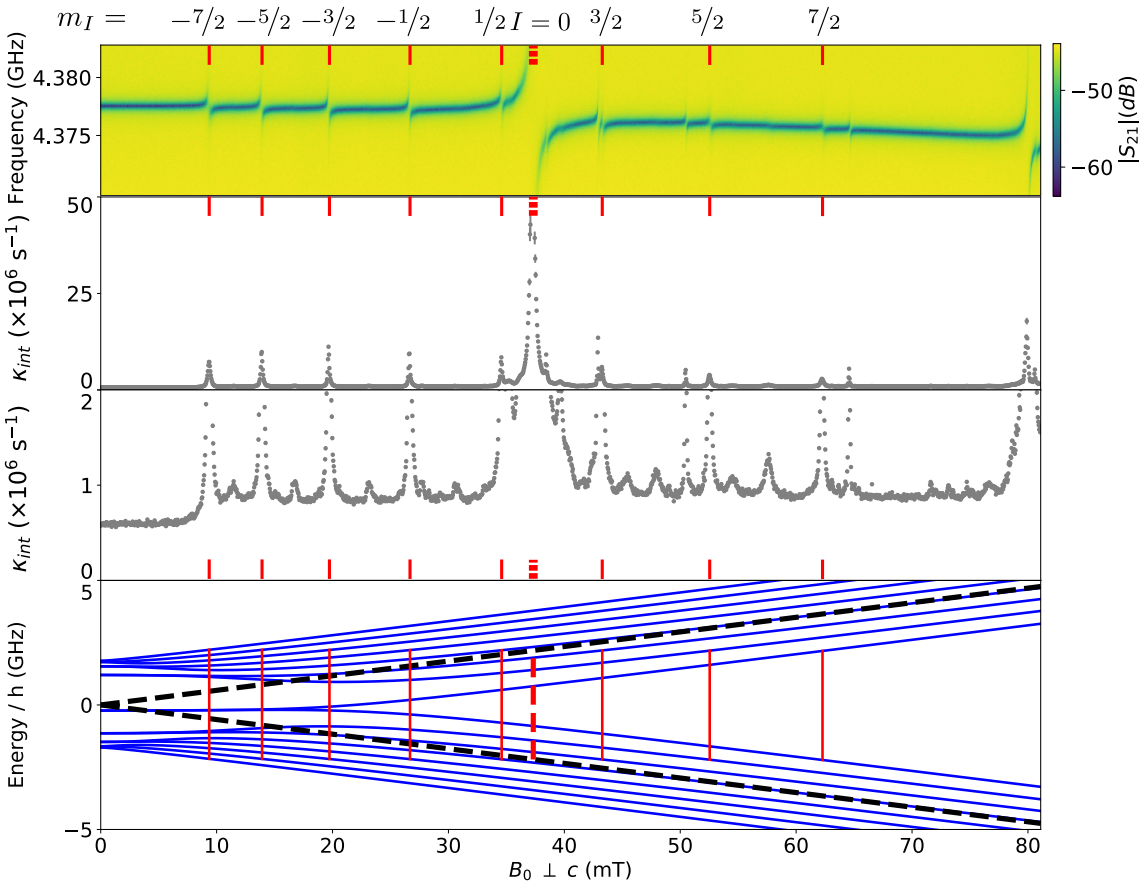

Figure 10.1 – **Continuous-wave spectroscopy with the magnetic field applied along the wire ($\boldsymbol{B_0} \perp \boldsymbol{c}$).** *Top.* Magnitude in dB of the transmission coefficient S_{21} measured around the resonator frequency $\omega_0/2\pi \sim 4.38$ GHz. This measurement is repeated as the magnetic field B_0, which is applied along the resonator wire and thus perpendicular to the crystal c-axis, is increased from 0 to 80 mT. The power at the resonator input corresponds to approximately 1000 photons in the resonator at zero field. The temperature is set to 100 mK. *Middle.* Fitted internal loss rate κ_{int} from the S_{21} data, using Equation 3.7, as a function of the magnetic field B_0. Each crossing of a spin transition corresponds to an increase of the internal losses as explained in Section 3.3.0.1. These data are shown with two different y-scales in order to observe the weaker signals. *Bottom.* Theoretical energy level spectrum of Er^{3+}:$CaWO_4$ at $\theta = 90°$ ($\boldsymbol{B_0} \perp c$), copied from Figure 2.5a. The red lines correspond to ESR allowed transitions (where $|\langle e|\hat{S}'_x|g\rangle| \sim |\langle e|\hat{S}'_y|g\rangle| \sim 0.5$) at the resonator frequency $\omega_0/2\pi = 4.38$ GHz. The erbium $I = 0$ transition (dashed red line) matches the strongest anticrossing of the S_{21} data, while the hyperfine transitions of ^{167}Er (solid red lines), labelled with their projection on I'_z, match weaker avoided crossings. Other ESR transitions are visible (for instance at 80 mT) and are attributed to Yb^{3+}.

to ytterbium ions as will be discussed in the next section.

10.1.2 Magnetic rotation spectrum

To confirm that the main observed transitions are erbium electron spins, the spectroscopy shown in Figure 10.1 is repeated for different magnetic field angles θ from the c-axis. This is possible because the sample surface lies in the (b, c)-plane. The internal loss rate κ_{int}, extracted from the measured transmission coefficient S_{21} with respect to frequency, is plotted as a function of the magnetic field value B_0 and the angle θ in Figure 10.2. The data presented in Figure 10.1 corresponds to $\theta = 90°$. This set of data is taken at a cryostat temperature of about 20 mK instead of 100 mK for the data of Figure 10.1. The internal loss rate shows narrow peaks which are strongly angular dependent. As already observed in Figure 9.7c, the internal losses increase slightly around $B_0 \sim 10$ mT for all angles θ, due to the aluminium wirebonds switching from superconducting to normal state.

To understand the resonances observed in Figure 10.2, the expected transition frequencies of known impurities in $CaWO_4$ are overlaid with the data. As expected, most of the lines appear to match erbium, either the $I = 0$ or the ^{167}Er $I = 7/2$ isotope. Less expected are the lines matching the spectrum of ytterbium. Ytterbium absorption appears to be of the same order of magnitude as erbium, implying (somewhat unexpectedly) that the two species have similar concentrations. After discussion with the company, it appears that indeed ytterbium was used for doping a crystal grown just before ours, which probably explains its high abundance. Finally, another packet of six lines match roughly with manganese.

The theoretical spin transitions are computed with the following models.

Erbium and ytterbium, which are both Kramers ions, are modelled with their effective spin $S = 1/2$ (see Section 2.2) and their spin Hamiltonian is

$$\mathcal{H}_{\text{Er, Yb}} = \mu_B \boldsymbol{B_0} \cdot \mathbf{g} \cdot \hat{\boldsymbol{S}} + \hat{\boldsymbol{S}} \cdot \boldsymbol{A} \cdot \hat{\boldsymbol{I}}, \tag{10.1}$$

where the $\mathbf{g}$- and $\boldsymbol{A}$-tensors are given in Table 2.4. The theoretical electron spin transitions at $\omega_0/2\pi = 4.38$ GHz match the data and enable us to correct for a small angular offset of $\Delta\theta = 2°$.

The third electron spin identified in Figure 10.2 is manganese, whose isotope ^{55}Mn, present in 100% abundance, has an electron spin $S = 5/2$ and a nuclear spin $I = 5/2$. The spin Hamiltonian of manganese has a different shape compared to erbium and ytterbium because it is not a rare-earth ion. Its spin Hamiltonian in $CaWO_4$ can be found in the literature [HB60] and has the following shape,

$$\begin{aligned}\mathcal{H}_{\text{Mn}} =& \mathrm{g}_{\parallel}\mu_B B_{0,z} S_z + \mathrm{g}_{\perp}\mu_B (B_{0,x} S_x + B_{0,y} S_y) + A_{\parallel} S_z I_z + A_{\perp}(S_x I_x + S_y I_y) \\ &+ \frac{a}{6}\left[S_z^4 + S_x^4 + S_y^4 - \frac{707}{16}\right] + D\left[S_z^4 - \frac{35}{12}\right] + \frac{7}{36}F\left[S_z^4 - \frac{95}{14}S_z^2 + \frac{81}{16}\right],\end{aligned} \tag{10.2}$$

where $g_{\parallel} \sim g_{\perp} \sim 2$, $A_{\parallel}/h \sim A_{\perp}/h \sim -267$ MHz, $D/h = -413$ MHz, $a/h = (-)14$ MHz and $(a/2 + F/3)/h = -3.6$ MHz. The sign of a is ambiguous although this does not affect the spectrum in our case.

The electron spin transitions plotted in red in Figure 10.2 are the six hyperfine transitions corresponding to the electron spin switching from $m_S = -5/2$ to $m_S = -3/2$ while m_I is constant. Indeed, the electron spin states $m_S = -5/2$ are the only populated levels at 20 mK. The theoretical spectrum qualitatively fits the data although the agreement is not as good as for erbium and ytterbium. This could be explained by the fact that Hempstead and Bowers measured the manganese spectrum at 23 GHz [HB60]. Our measurement at 4 GHz suggests that the parameters of the spin Hamiltonian should be revisited but this was not attempted here.

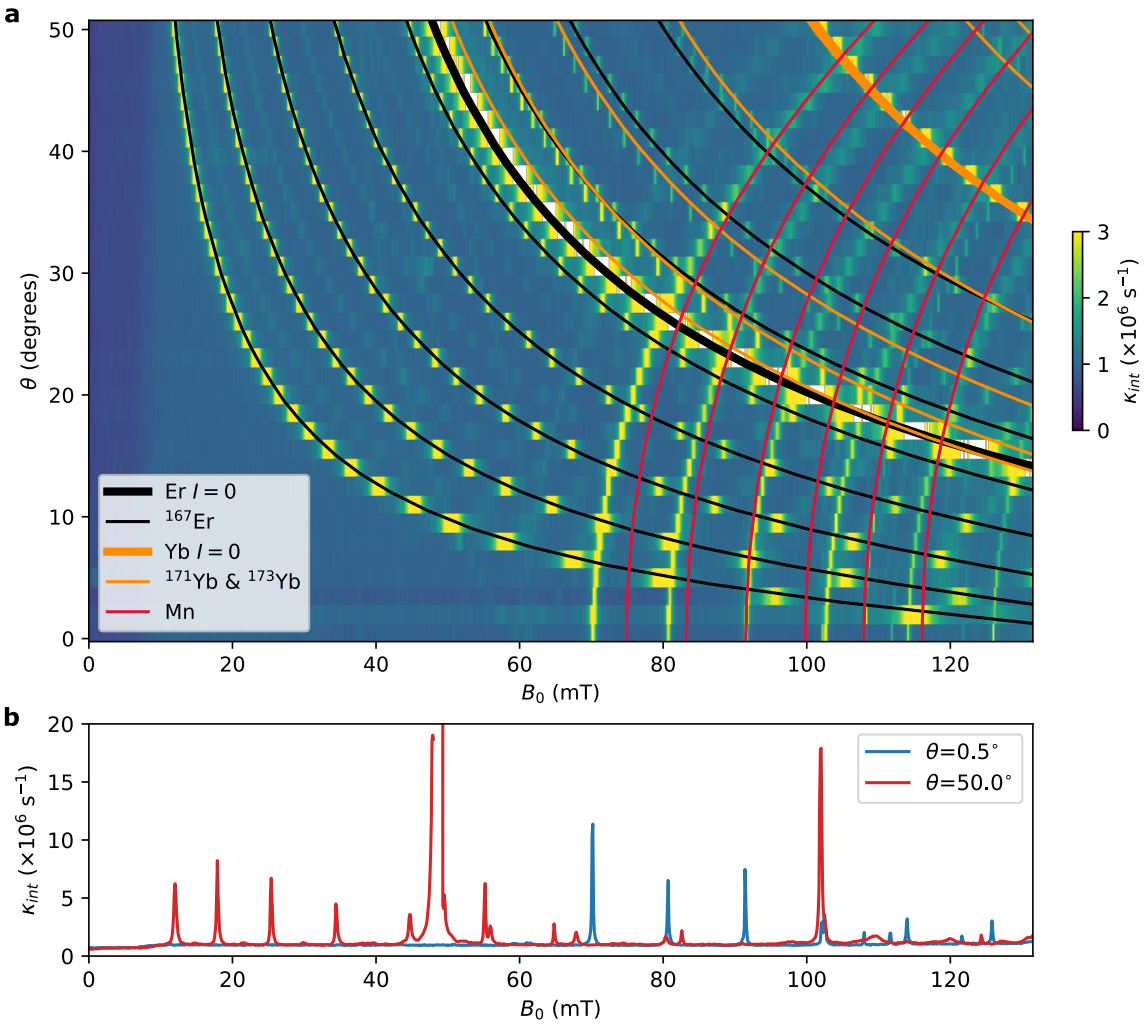

Figure 10.2 – **Magnetic rotation spectrum.** The continuous-wave spectroscopy of Figure 10.1 is repeated at 20 mK for several magnetic field orientations, corresponding to an angle θ from the c-axis. **a.** The fitted internal loss rate κ_{int} is plotted as a function of B_0 and θ. Each peak is a signature of some electron spin transition crossing the resonator frequency $\omega_0/2\pi \sim 4.38$ GHz. The data is overlaid by the theoretical spectra of Er^{3+}, Yb^{3+} and Mn^{2+}. The theoretical curves of erbium and ytterbium are used to adjust the angle θ of the experiment, which is found to be off by 2°. The spin Hamiltonians used to compute the spectra are given in the main text. We note that the theoretical transitions for manganese do not exactly match the observed resonances. For rare-earth isotopes with a non-zero nuclear spin, ^{167}Er, ^{171}Yb and ^{173}Yb, only the nuclear-spin preserving $\Delta m_I = 0$ transitions are shown. Due to spin-state mixing, however, some weak $\Delta m_I = \pm 1$ transitions can be identified. Moreover, the slight increase of κ_{int} at $B_0 \sim 10$ mT is attributed to the aluminium wirebonds which change from superconducting to normal state. Note that the color scale stops at $\kappa_{\text{int}} = 3 \times 10^6$ s^{-1} which cuts off the added losses of the most strongly coupled transitions like the erbium or the ytterbium $I = 0$. **b.** Fitted internal loss rate κ_{int} as a function of B_0 at $\theta = 0.5°$ and $\theta = 50°$.

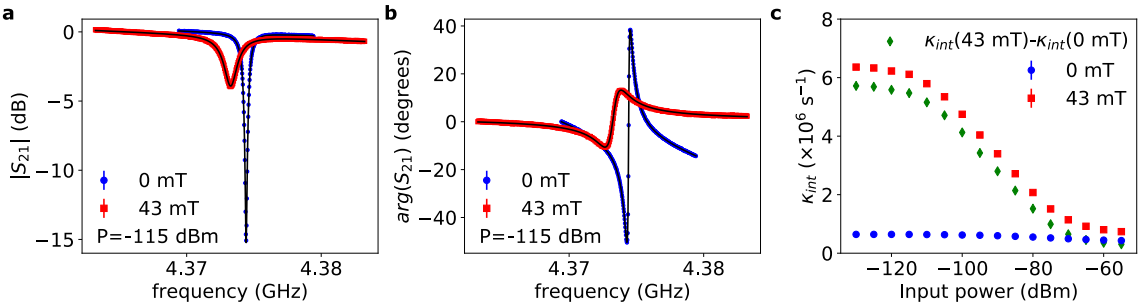

Figure 10.3 – **Power dependence of the internal loss rate on the $m_I = 3/2$ electron spin transition at 100 mK. a. & b.** The transmission coefficient S_{21} is measured as a function of frequency with input power at the sample $P = -115$ dBm, at 10 mK and zero field (blue circles, same data as in Figure 9.4) and at 100 mK and $B_0 = 43$ mT which matches the hyperfine transition $m_I = 3/2$ of erbium (red squares). At zero field, when there is no spin, the transmission coefficient S_{21} does not vary significantly below 100 mK and the two data sets can be compared. **a.** $|S_{21}|$. **b.** Angle of S_{21}. **c.** Power dependence of the internal loss rate, where there is no spin (blue, $B_0 = 0$ mT) and where there is a spin transition (red, $B_0 = 43$ mT). The additional losses due to the presence of the spins are computed as the subtraction of these two quantities and are plotted with green diamonds.

10.2 Ensemble coupling and spin concentration

10.2.1 Fitting the transmission spectra to extract the ensemble coupling

The spectrum of Figure 10.1 can be fitted using Equation 3.54 in order to extract the ensemble coupling g_{ens} and the inhomogeneous linewidth Γ_{inh} of each electron spin transition.

Before doing so, we check that the resonator input power used to measure S_{21} is not saturating the spins. This is done in Figure 10.3, where the transmission coefficient is measured at zero field, where there is no spin, and at $B_0 = 43$ mT, where the resonator is resonant with the hyperfine transition $m_I = 3/2$ of erbium. At 43 mT, the cryostat temperature is set to 100 mK in order to increase the erbium population in this hyperfine level (see Section 2.2.4). The power dependence of the internal loss rate on the hyperfine transition is compared with the power dependence at zero field. In particular, the added losses due to the spins are computed as the subtraction between these two quantities and vary by more than one order of magnitude between -130 dBm and -60 dBm. The data of Figure 10.1 was measured with input power is $P = -115$ dBm where the internal loss rate is not decreasing due to saturation. The data of Figure 10.2, which purpose was to identify paramagnetic centers, was taken at $P = -95$ dBm in order to fasten the measurement. We assume that the input power of $P = -115$ dBm does not saturate the spins even at the lowest temperatures, where the $m_I = 3/2$ concentration is reduced by about a factor 10.

With the input power $P = -115$ dBm at the sample, the spectrum of Figure 10.1 is measured again around the $I = 0$ erbium spin transition for various cryostat temperatures, ranging from 10 mK to 500 mK. The data taken at the two extreme temperatures are shown in Figure 10.4a. The magnetic field range contains five identified electron spin transitions: $I = 0$ erbium spins at $B_0 = 37$ mT, two hyperfine transitions of ^{167}Er, the $m_I = 1/2$ at $B_0 = 34$ mT and the $m_I = 3/2$ at $B_0 = 43.5$ mT, one hyperfine transition of ^{171}Yb ($m_I = 1/2$) at $B_0 = 43.0$ mT and one hyperfine transition of ^{173}Yb ($m_I = -5/2$) at $B_0 = 38$ mT.

Model

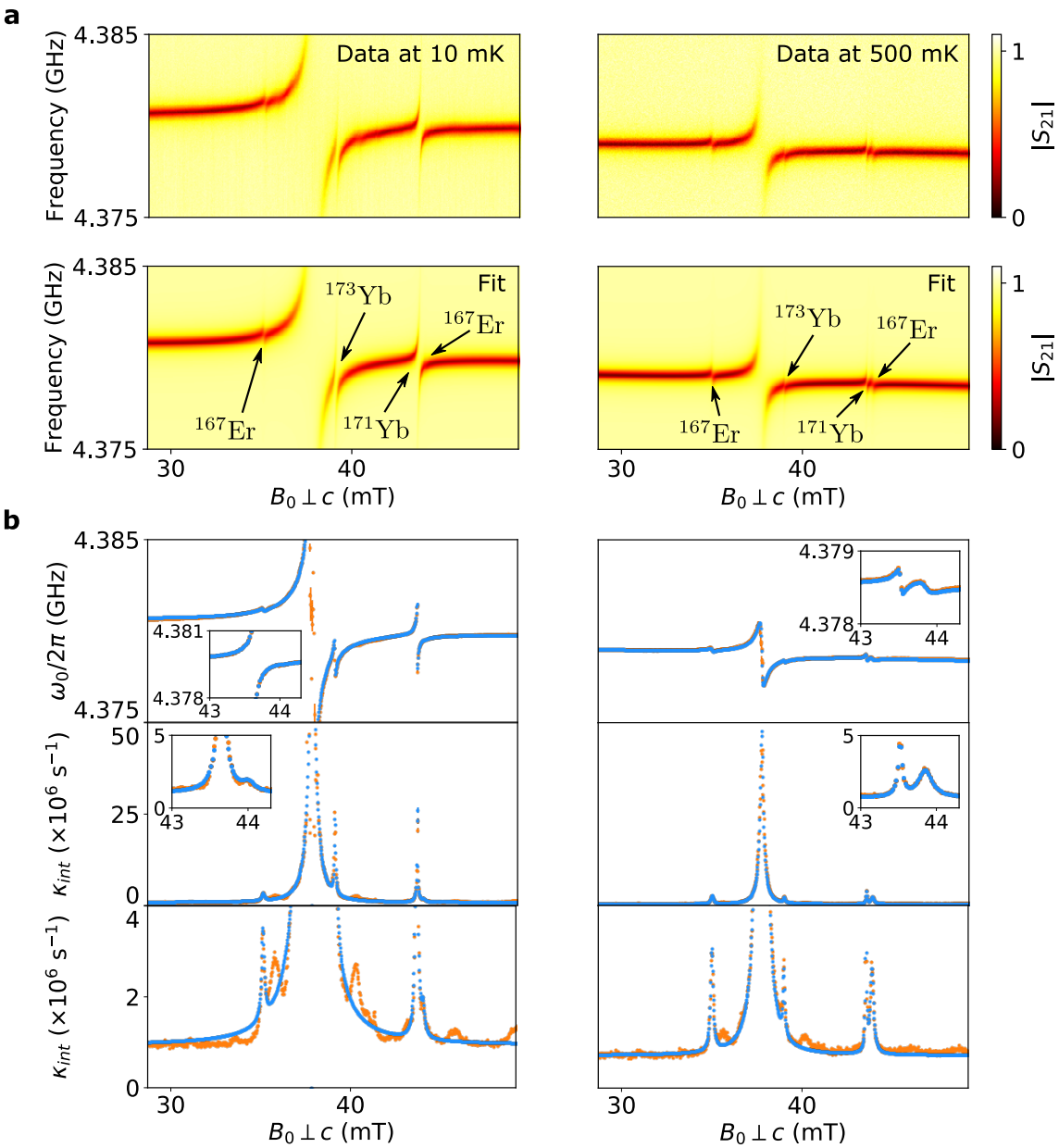

Figure 10.4 – **Continuous-wave spectroscopy around the $I = 0$ erbium avoided crossing, measured at 10 mK and 500 mK. a.** *Top.* Magnitude of the transmission coefficient S_{21} as a function of frequency and magnetic field amplitude B_0, where the background in frequency has been subtracted, measured at two cryostat temperatures, 10 and 500 mK (left and right respectively). Five electron spin transitions are identified: the $I = 0$ erbium at $B_0 = 37$ mT, two transitions of the ^{167}Er isotope, the $m_I = 1/2$ transition at $B_0 = 35$ mT and the $m_I = 3/2$ transition at $B_0 = 43.5$ mT, the $m_I = -5/2$ transition of ^{173}Yb at $B_0 = 38$ mT and the $m_I = 1/2$ transition of ^{171}Yb at $B_0 = 43.0$ mT (these B_0 values are the theoretical values computed at $\omega_0/2\pi = 4.38$ GHz, the difference by ± 0.5 mT compared to the data is attributed to both the precision of the coil calibration constant and a small hysteresis in the applied magnetic field). *Bottom.* Fitted transmission coefficient S_{21} with three free parameters for each identified transition k: its ensemble coupling $g_{\mathrm{ens},k}$, its inhomogeneous linewidth $\Gamma_{\mathrm{inh},k}$ and its resonance magnetic field $B_{0,k}$. **b.** Extracted resonator frequency ω_0 and internal loss rate κ_{int} from the S_{21} data (orange) and the S_{21} fit (blue), using Equation 3.7, as a function of B_0. The insets show a zoom on the two hyperfine transitions at $B_0 = 43 - 44.5$ mT. The ^{167}Er transition within this range is almost absent at 10 mK due to the very small population of this hyperfine level at low temperature (see Section 2.2.4).

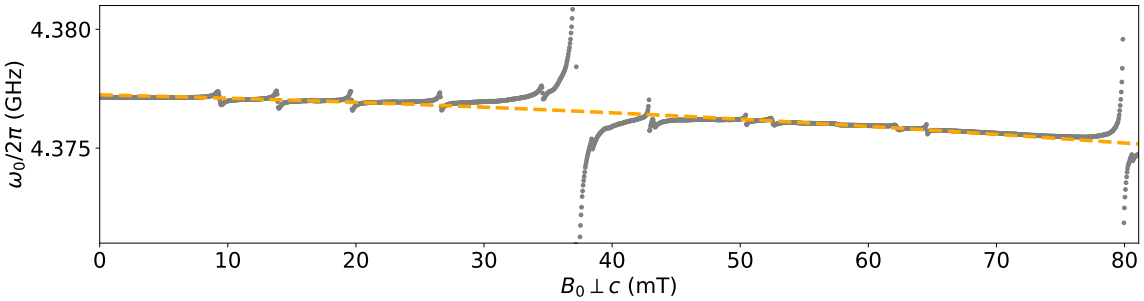

Figure 10.5 – **Parabolic fit of the resonator frequency as a function of magnetic field.** The resonator frequency is extracted from the data of Figure 10.1. The orange dashed line is a parabolic fit which is used to approximate the dependence of the resonator frequency on the magnetic field in the absence of electron spins.

The model which reproduces the data in Figure 10.4 uses Equation 3.54,

$$S_{21} = 1 - \frac{i\kappa_c/2}{(\omega - \omega_0(B_0)) + i\kappa_t/2 - \sum_k W_k(\omega)}, \tag{10.3}$$

where the index k labels each of the five transitions present in the data. It can be seen from Figure 10.1 that the resonator frequency $\omega_0(B_0)$ slightly decreases with the magnetic field, due to the resonator kinetic inductance [Hea+08]. We include this in the model by fitting the measured $\omega_0(B_0)$ with a parabola (see Figure 10.5). The resonator coupling and total damping rates κ_c and κ_t are determined away from spin transitions.

For simplicity, we model the inhomogeneous lineshapes as being Lorentzians of width $\Gamma_{\text{inh},k}$ (we compared Gaussian and Lorentizan and found that the latter gave a more satisfactory agreement). Thus, the W_k functions are given by

$$W_k(\omega) = \frac{g_{\text{ens},k}^2}{(\omega - \omega_{s,k}(B_0)) + i\Gamma_{\text{inh},k}/2}. \tag{10.4}$$

The spin frequency $\omega_{s,k}(B_0)$ is linearized in the vicinity of the resonance field $B_{0,k}$: $\omega_{s,k}(B_0) = \omega_0(B_{0,k}) + \alpha_k \mu_B (B_0 - B_{0,k})/\hbar$, where $\alpha_k = (\hbar/\mu_B)\partial\omega/\partial B_0(B_{0,k})$. This description is useful to treat the hyperfine transitions because the hyperfine coupling changes slightly the sensitivity of the spin frequency to magnetic field. In case of an $I = 0$ spin transition, $\alpha_k = \text{g}_{\text{eff},k}$. The resonance field $B_{0,k}$ was seen to vary by ± 0.5 mT due to a small field hysteresis.

Fitting process

Due to the large number of free parameters, the data are not fitted with all five electron spin transitions simultaneously. Instead the fit is done with the following steps:

1. The field dependence of the resonator frequency in the absence of spins, $\omega_0(B_0)$, is computed with a parabolic fit of the extracted resonator frequency as a function of B_0, as shown in Figure 10.5. The dataset should be taken within the same run as this function depends slightly on the tuning of the Attocube nanopositioners.

2. Only the $I = 0$ erbium avoided crossing is fitted as it is by far the strongest signal present in the data of Figure 10.4a. All the magnetic field regions containing some signal from other spin transitions are removed from the fit. The function $\omega_0(B_0)$ can be locally adjusted with a linear background if necessary. The fit yields the parameters of the $I = 0$ erbium transition, $g_{\text{ens,Er } I=0}$, $\Gamma_{\text{inh,Er } I=0}$ and $B_{0,\text{Er } I=0}$.

3. Each hyperfine transitions is fitted separately, except for the $m_I = 3/2$ transition of ^{167}Er and the $m_I = 1/2$ transition of ^{171}Yb which are so close that they are fitted together. The resonator frequency $\omega_0(B_0)$ is locally adjusted with a linear background. The fitting function S_{21} of Equation 10.3 includes the $I = 0$ transition which parameters are fixed from step 2 plus the relevant hyperfine transitions, yielding $g_{\mathrm{ens},k}$, $\Gamma_{\mathrm{inh},k}$ and $B_{0,k}$. This is repeated for all hyperfine transitions.

The fit presented in Figure 10.4a combines all the fitted parameters, $g_{\mathrm{ens},k}$, $\Gamma_{\mathrm{inh},k}$ and $B_{0,k}$, of the five electron spin transitions in Equation 10.3, which makes 15 parameters in total. The fit reproduces well the data.

To better estimate the quality of the fit, Figure 10.4b shows the extracted resonator frequency ω_0 and internal loss rate κ_{int} of both the S_{21} data (in orange) and the S_{21} fit (in blue). These values are extracted using Equation 3.7. The fit shows satisfactory agreement with the data. We note that two symmetric bumps on the sides of the $I = 0$ peak are visible, whose physical origin is not understood.

The zoom in the insets on the two hyperfine transitions of ^{167}Er and ^{171}Yb between 43 and 44.5 mT show that these two lines, despite their closeness, are well separated from each other. This erbium hyperfine transition, which is also well separated from the erbium $I = 0$ broad avoided crossing, will be studied extensively in the following chapter. Interestingly, the signal of the erbium hyperfine transition nearly vanishes at 10 mK, making just a small shoulder close to the internal loss peak caused by the ytterbium hyperfine transition. This comes from the temperature dependence of the hyperfine level population and will be made more explicit in the next section.

10.2.2 Temperature dependence of the coupling constant and spin temperature

The fitted ensemble coupling and inhomogeneous linewidth of the three erbium transitions present in Figure 10.4 are plotted as a function of the cryostat temperature in Figure 10.6. We observe that Γ_{inh} is independent of temperature. This is expected, since it is governed by the distribution of electric fields inside the crystal (see Section 2.5). However, the fact that the inhomogeneous linewidths are different for the three erbium transitions, by up to a factor 2, is not understood. The $I = 0$ erbium transition has the largest linewidth with $\Gamma_{\mathrm{inh}}/2\pi = 36$ MHz. The ensemble coupling g_{ens} is observed to depend strongly on temperature. As explained in Section 3.3.0.1, this is due to the fact that the ensemble coupling g_{ens}, derived in Section 6.3, is rescaled with the polarization $P(T)$ of the relevant level population as

$$g_{\mathrm{ens}}(T) = \frac{\mu_B \tilde{\mathrm{g}}}{4\hbar}\sqrt{P(T) c \mu_0 \hbar \omega_0}. \tag{10.5}$$

We observe that the $I = 0$ curve reaches a value close to 16 MHz at the lowest temperatures, and decreases at temperatures larger than 50 mK. The hyperfine curves have a qualitatively different behavior. g_{ens} rapidly increases with temperature, reaches a maximum, and then decreases. This behavior is explained by the temperature dependence of the polarization $P(T)$ (see Section 2.2.4). In fact, at zero temperature, all the ^{167}Er spins are in the hyperfine ground state level, $|m_S = -1/2, m_I = -7/2\rangle$, and the polarization of the $m_I = 3/2$ transition is therefore zero.

To fit the $g_{\mathrm{ens}}(T)$ data with the model, we proceed as follows. First, we note that the ratio between the three curves is fully predicted by the model, and cannot be considered as an adjustable parameter. Indeed, the relative abundance of ^{167}Er is known (see Table 2.4). Thus, according to Equation 10.5, the ratios between the ensemble couplings of the three

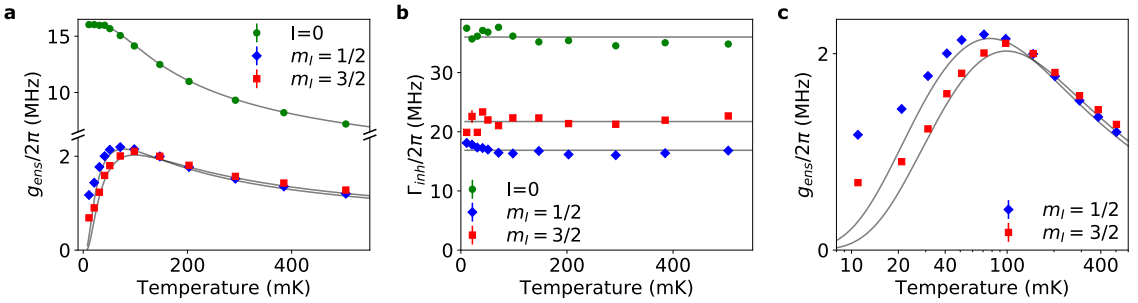

Figure 10.6 – **Temperature dependence of the ensemble coupling constant and the inhomogeneous linewidth. a.** Ensemble coupling of all erbium spin transitions present in Figure 10.4 as a function of the cryostat temperature (colored symbols). These values are extracted from the fit of the transmission coefficient $S_{21}(\omega, B_0)$ at each temperature, as in Figure 10.4. The ensemble coupling data are fitted simultaneously using Equation 10.5 (solid lines). The fit yields a coupling constant of the $I = 0$ erbium ions of $g_{\text{ens}}/2\pi = 16.0 \pm 0.1$ MHz at zero temperature. Note that the y-axis is cut between 2 and 10 MHz for better visibility. **b.** Inhomogeneous linewidth of the same spin transitions extracted from the fit of $S_{21}(\omega, B_0)$ as a function of the cryostat temperature (colored symbols). The inhomogeneous linewidths are expected to be constant with temperature. Taking their mean value yields $\Gamma_{\text{inh}}/2\pi = 36 \pm 1$ MHz for the $I = 0$ erbium ions, $\Gamma_{\text{inh}}/2\pi = 17 \pm 1$ MHz for the $m_I = 1/2$ erbium ions and $\Gamma_{\text{inh}}/2\pi = 22 \pm 1$ MHz for the $m_I = 3/2$ erbium ions (solid lines). **c.** Same data (colored symbols) and fit (solid lines) as in subplot a. The temperature is in logarithmic scale to emphasize how much the hyperfine couplings deviate from their fits at low temperature. This enables us to extract the spin temperature at 20 mK and 10 mK as 27 ± 2 mK and 23 ± 2 mK respectively.

erbium transitions are

$$\begin{aligned}
\frac{g_{\text{ens,Er } m_I=1/2}(T)}{g_{\text{ens,Er } I=0}(T)} &= \frac{\tilde{\text{g}}_{\text{Er } m_I=1/2}}{\tilde{\text{g}}_{\text{Er } I=0}} \sqrt{\frac{0.23 P_{\text{Er } m_I=1/2}(T)}{0.77 P_{\text{Er } I=0}(T)}}, \\
\frac{g_{\text{ens,Er } m_I=3/2}(T)}{g_{\text{ens,Er } I=0}(T)} &= \frac{\tilde{\text{g}}_{\text{Er } m_I=3/2}}{\tilde{\text{g}}_{\text{Er } I=0}} \sqrt{\frac{0.23 P_{\text{Er } m_I=3/2}(T)}{0.77 P_{\text{Er } I=0}(T)}}.
\end{aligned} \tag{10.6}$$

The polarization function $P(T)$ is calculated from the energy level spectra at the magnetic field $B_{0,k}$ of each transition k.

We point out here that the averaged g-factor $\tilde{\text{g}}$ of Equation 6.5 was derived for a zero-nuclear spin transition and has to be generalized to hyperfine transitions. The spin matrix elements are modified in the presence of hyperfine coupling and need to be included as such in the derivation. Starting from the single-spin coupling g_0 of Equation 5.2, the averaged g-factor is calculated for the magnetic field orientation used in this experiment, i.e. with $\boldsymbol{B_0}$ parallel to the inductance wire (corresponding to $\cos\psi = 1$ in Equation 6.5),

$$\tilde{\text{g}} = 2\sqrt{\frac{\iint_{z'<0} dy'dz' [(\text{g}_{z'} |\langle e| \hat{S}_{z'} |g\rangle| \delta B_{z'})^2 + (\text{g}_{y'} |\langle e| \hat{S}_{y'} |g\rangle| \delta B_{y'})^2]}{\iint_{z'<0} dy'dz' [\delta B_{z'}^2 + \delta B_{y'}^2]}}, \tag{10.7}$$

where (x', y', z') are the axes defined in Figure 5.13, x' is the direction of the inductance wire and z' is pointing out-of-plane. We note that this equation is only valid for this specific magnetic field orientation. Any other orientation would involve the third matrix element $\langle e| \hat{S}_{x'} |g\rangle$.

As in Section 6.3, the magnetic field $\boldsymbol{\delta B}$ is obtained with a COMSOL simulation over a rectangle of 400×200 μm^2 under a 5 μm-wide wire and the simulation result is sampled

every 0.1 μm. The spin matrix elements, $\langle e|\,\hat{S}_{z'}\,|g\rangle$ and $\langle e|\,\hat{S}_{y'}\,|g\rangle$, are calculated with the spin Hamiltonian at the resonance magnetic field $B_{0,k}$ of each transition k. This gives $\tilde{g}_{\mathrm{Er}\ I=0} = 5.71$, $\tilde{g}_{\mathrm{Er}\ m_I=1/2} = 4.75$ and $\tilde{g}_{\mathrm{Er}\ m_I=3/2} = 4.98$.

From the polarization $P(T)$ and the averaged g-factor $\tilde{g}$, the ratios of Equation 10.6 are fully determined. Thus, the data of Figure 10.6c are fitted simultaneously with the ensemble coupling of the $I = 0$ erbium transition at zero temperature, $g_{\mathrm{ens,Er}\ I=0}(0\ K)$, as only fitted parameter. The fit yields $g_{\mathrm{ens,Er}\ I=0}(0\ K)/2\pi = 16.0 \pm 0.1$ MHz.

We obtain a quantitative agreement with the model for the simultaneous fitting of all three curves, for temperatures higher than 30 mK. At temperatures lower than 30 mK, we observe a discrepancy between the hyperfine data and the fit (see Figure 10.6c where the data and the fit of subplot a are reproduced with a logarithmic scale emphasizing the low temperature regime). This deviation enables to estimate the spin temperature T_s below 30 mK, with $T_s = 27 \pm 2$ mK at cryostat temperature $T = 21$ mK and $T_s = 23 \pm 2$ mK at cryostat temperature $T = 11$ mK. We attribute this phenomenon to an imperfect thermalization of the rare-earth spin population with the cryostat base temperature. This could be due either to an imperfect thermalization of the sample itself, or to an imperfect thermalization of the rare-earth ion population with the lattice.

Similar results were obtained in [Pro16], showing good thermalization of the erbium hyperfine manifold down to approximately 50 mK. On the other hand, the situation is very different for donors in silicon, whose hyperfine manifold population was shown to be de-coupled from the silicon lattice below about 200mK [Alb+20].

From these fits, one can also calculate the cooperativity of these spin transitions at a given temperature. The resonator total damping rate away from a spin transition is $\kappa_t \sim 3.7 \times 10^6$ s^{-1}. The $I = 0$ erbium inhomogeneous linewidth is $\Gamma_{\mathrm{inh}}/2\pi = 36$ MHz and its ensemble coupling constant at 10 mK is $g_{\mathrm{ens}}/2\pi = 16$ MHz. This yields a cooperativity at 10 mK of $C \sim 50$. For the two erbium hyperfine transitions, $m_I = 1/2$ and $m_I = 3/2$, their inhomogeneous linewidth is $\Gamma_{\mathrm{inh}}/2\pi \sim 20$ MHz and their maximum ensemble coupling is reached at about 100 mK with $g_{\mathrm{ens}}/2\pi \sim 2$ MHz (see Figure 10.6). This gives a cooperativity $C \sim 1$. Therefore, the $I = 0$ erbium spins are in the high-cooperativity regime with the resonator and the hyperfine transitions have a cooperativity near unity.

10.2.3 Estimating the concentration of erbium and ytterbium

The fit of Figure 10.6a, yielding the erbium $I = 0$ coupling constant at zero temperature, $g_{\mathrm{ens,Er}\ I=0}(0\ K)/2\pi = 16.0 \pm 0.1$ MHz, also allows us to calculate the absolute erbium spin concentration using Equation 10.5. With $\tilde{g}_{\mathrm{Er},\ I=0} = 5.71$ and $P(0\ K) = 1$, the fitted ensemble coupling gives $c = 1.74 \times 10^{17}$ cm^{-3}. This includes only the $I = 0$ erbium isotopes which represent 77 % of all erbium ions. The corresponding total erbium concentration is $[\mathrm{Er}^{3+}] = c/(0.77 \times 1.3 \times 10^{22}\ \mathrm{cm}^{-3}) = 18 \pm 0.1$ ppm (see Section 2.2.1). The difference with the nominal value of 50 ppm is likely due to spatial inhomogeneity of the growth process.

Finally, as the sample is accidentally co-doped with ytterbium, we now want to estimate its concentration as well. Using the data of Figure 10.1, the zero-nuclear spin transitions of both erbium and ytterbium are fitted using the process explained in Section 10.2.1. The fits are performed in magnetic field ranges where these avoided crossings are visible, i.e. from 29 to 49 mT for erbium $I = 0$ and from 74 to 80 mT for ytterbium $I = 0$. Within these ranges, magnetic field regions where other hyperfine avoided crossings are visible are removed from the fit.

The fit of the erbium $I = 0$ transition (at $B_0 = 37$ mT) yields $g_{\text{ens, Er}}/2\pi = 13.760 \pm 0.005$ MHz and $\Gamma_{\text{inh, Er}}/2\pi = 33.5 \pm 0.2$ MHz. The fit of the ytterbium $I = 0$ transition (at $B_0 = 80$ mT) yields $g_{\text{ens, Yb}}/2\pi = 14.75 \pm 0.02$ MHz and $\Gamma_{\text{inh, Yb}}/2\pi = 5.6 \pm 0.1$ MHz. This spectrum was recorded at $T = 100$ mK and the fitted ensemble coupling and inhomogeneous linewidth of erbium are compatible with the data shown in Figure 10.6 at 100 mK.

This enables us to compare the concentrations of both species using the relation

$$\frac{g_{\text{ens, Yb}}}{g_{\text{ens, Er}}} = \frac{\tilde{g}_{\text{Yb } I=0}}{\tilde{g}_{\text{Er } I=0}} \sqrt{\frac{0.7[\text{Yb}^{3+}]P_{\text{Yb } I=0}(T)}{0.77[\text{Er}^{3+}]P_{\text{Er } I=0}(T)}}, \tag{10.8}$$

where the polarization functions are $P_{I=0}(T) = \tanh\left[\hbar\omega_0/(2k_BT)\right]$ and are thus identical for the two spins. The averaged g-factors are $\tilde{g}_{\text{Er } I=0} = 5.71$ and $\tilde{g}_{\text{Yb } I=0} = 2.75$, yielding a ratio between the concentrations of

$$\frac{[\text{Yb}^{3+}]}{[\text{Er}^{3+}]} = \left(\frac{g_{\text{ens, Yb}}}{g_{\text{ens, Er}}} \frac{\tilde{g}_{\text{Er } I=0}}{\tilde{g}_{\text{Yb } I=0}}\right)^2 \frac{0.77}{0.7} = 0.57. \tag{10.9}$$

Thus the concentration of ytterbium (all isotopes included) is $[\text{Yb}^{3+}] = 10 \pm 0.1$ ppm, about twice smaller than the erbium concentration.

These continuous-wave spectroscopy measurements therefore allow us to identify several paramagnetic spins present in our sample, not only erbium, but also ytterbium and manganese. Quantifying the concentration and measuring the inhomogeneous broadening of erbium and ytterbium will be useful in the next chapter to model how these two dominant spin species affect the electron spin coherence in this crystal. We did not attempt to quantify the concentration of manganese but assume that its concentration is smaller than those of erbium and ytterbium.

Chapter 11

Pulsed electron spin resonance and spectral diffusion analysis

In this chapter we present pulse EPR measurements of erbium ions in the high-doped sample. We first provide a detailed analysis of the ESEEM oscillations. We then turn to a study of the coherence time as a function of temperature, focusing on one hyperfine transition. Despite the high paramagnetic concentration, we report coherence times above 1 ms at 10 mK. A strong temperature dependence is observed, and is modelled as being caused by spectral diffusion due to the erbium and ytterbium ions. For all the measurements presented in this chapter, the magnetic field is applied along the wire axis which is perpendicular to the c-axis, such that $\theta = 90°$.

11.1 Electron spin echo envelope modulation (ESEEM)

In a first step, we perform two-pulse ESEEM measurements on several erbium spin transitions. We choose to work on the transitions $|m_I = -3/2\rangle$, $|m_I = -1/2\rangle$, $I = 0$ and $|m_I = 3/2\rangle$, corresponding to $B_0 = 20,\ 26,\ 36\ , 43$ mT respectively. Strong modulations of the echo amplitude are observed, as seen in Figure 11.1. They are due the erbium coupling to nearby tungsten nuclei, as explained in Section 4.4.

The data, which represent the quadrature-averaged echo amplitude as a function of the interpulse delay τ of a Hahn-echo sequence, are fitted with Equation 4.16 using six free parameters. The first three parameters characterize the magnetic field with its amplitude B_0, its angle θ from the c-axis and its angle φ of its projection on the (a, b)-plane from the crystal a-axis. The last three parameters, A, T_2 and x, characterize the echo decay as $A_e(2\tau) = Ae^{-(2\tau/T_2)^x}$. The number of neighboring tungsten atoms taken into account in the fit is about 1000 and we observe that the fit quality starts to degrade below 100 tungsten atoms.

Due to the large number of parameters and the presence of several local minima, the fit is repeated 200 times with random initial guesses, giving a distribution of results for each parameter. The maximum of each distribution corresponds to the global minimum of the fitting function and their variance defines the errorbar of each parameter.

The magnetic field orientation is the same for all data. θ and φ are therefore fitted once, with the erbium $I = 0$ data which displays more ESEEM oscillations due to its longer coherence time. Note that this dataset is measured at different cryostat temperatures, between 10 mK and 100 mK, and the temperature affects strongly the coherence time as will be demonstrated in the following sections. This explains why the $I = 0$ data, measured at 10 mK, has a longer coherence time than the $m_I = 3/2$ data, measured at 80 mK. The fit yields $\theta = 91.47 \pm 0.01°$ and $\varphi = 90.50 \pm 0.01°$ (modulo 90°). From this fit, we conclude

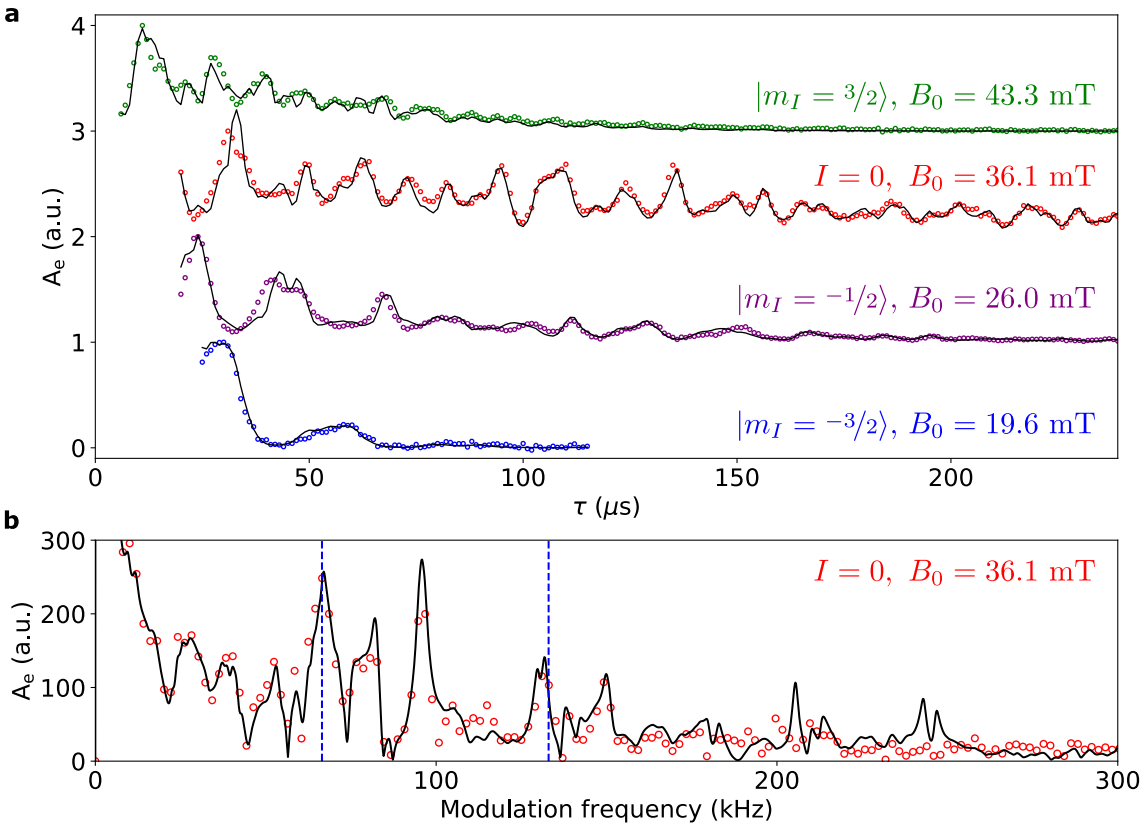

Figure 11.1 – **Modulation of the Hahn-echo decay of several erbium electron spin transitions. a.** Two-pulse ESEEM measurement using a Hahn-echo sequence with inter-pulse delay τ for four erbium spin transitions. The colored dots are the echo amplitude as a function of τ. These data are taken at different cryostat temperatures, from 10 to 100 mK, and the pulse length is either 1 or 2 μs. The data are fitted with a model (solid black line) including the ESEEM modulation and the echo decay due to decoherence. The labelling magnetic field value results from the fit and matches the expected resonance magnetic field within ± 0.5 mT. **b.** Fourier transform of the $I = 0$ erbium data and fit shown in subplot a. The blue dashed lines indicate ω_W and $2\omega_W$, where ω_W is the Larmor frequency of the ^{183}W nuclear spins in free space at $B_0 = 36.1$ mT.

that the sample surface is close to the crystalline plane (b, c) (or equivalently (a, c)), as expected.

The rest of the data are fitted with the four remaining parameters. In particular, the magnetic field amplitude shown in Figure 11.1 is given with an uncertainty of ± 0.1 mT and matches its expected value within ± 0.5 mT (the data for the $I = 0$ transition are measured 1 mT away from its resonance magnetic field due to the strong avoided level crossing). The coherence time varies between 40 and 400 μs and will be studied in more detail in the following sections.

The $I = 0$ erbium data is Fourier-transformed in Figure 11.1b. The Fourier transform of the fit matches well the data at low modulation frequency. We note however that the high frequency peaks, above 200 kHz, are absent from the data. As discussed in Section 4.4, the narrow bandwidth of the superconducting resonator filters the ESEEM both during excitation and detection. This complex filtering is not included in the model. Roughly, ESEEM frequencies larger than the HWHM of the resonator bandwidth, around 300 kHz, are filtered out. Moreover, looking back to Equation 4.17, weakly-coupled tungsten spins $(A, B, C \ll \omega_W)$ are split by their Larmor frequency such that $\omega_\downarrow = \omega_\uparrow = \omega_W = \gamma_W B_0$. In

this limit, the two frequencies appearing in the ESEEM are ω_W and $2\omega_W$ and their relative amplitude is 4:1. These two frequencies computed at $B_0 = 36$ mT are indicated and match two of the main frequencies of the ESEEM signal.

11.2 Spin dynamics on the I=0 transition

The spin dynamics are first investigated for the $I = 0$ erbium spin transition. The magnetic field cannot be set exactly at the resonance magnetic field of the $I = 0$ transition. Indeed, due to the strong avoided crossing of Figure 10.4, the resonator signal vanishes at the resonance magnetic field due to spin absorption. Instead, the magnetic field is set on either side of the avoided crossing, where the observed echo at the resonator frequency is maximum. This occurs typically between 0.5 and 1 mT away from the resonance magnetic field.

11.2.1 Relaxation time

The relaxation time T_1 is measured using an inversion recovery sequence at 10 mK with 2 μs long pulses and is shown in Figure 11.2a. The echo recovery as a function of the delay T is double-exponential with two time constants of the order of seconds. Spin-lattice relaxation is expected to give a single exponential decay. From the experiment on the pure $CaWO_4$ crystal, presented in Chapter 8, the spin-lattice relaxation time can be extrapolated at the actual resonator frequency $\omega_0/2\pi = 4.34$ GHz. Indeed Equation 2.41 shows that when the magnetic field is applied along a given crystal orientation, the spin-lattice relaxation time is inversely proportional to ω_0^5. According to Figure 8.1, the spin-lattice relaxation time when $\boldsymbol{B_0}$ is applied along the crystal a or b-axis is $T_1 = 15 \pm 3$ s at $\omega_0/2\pi = 7.88$ GHz. Therefore, the expected spin-lattice relaxation time at $\omega_0/2\pi = 4.34$ GHz is 20 times larger, $T_{1,\text{phonon}} \sim 5$ minutes. As a consequence, the measured relaxation time constants do not match spin-lattice relaxation. We attribute them rather to spectral or spatial diffusion. Indeed, the $I = 0$ erbium-erbium flip-flop rate is high in this sample, as will be discussed in greater detail in the following sections. The inversion pulse is exciting a small fraction of all erbium ions present in the sample, because of spectral and spatial filtering by the resonator. Due to flip-flops, the generated longitudinal magnetization may diffuse both spatially and spectrally towards erbium ions that escape detection by the echo sequence, leading to an apparent decay that can be faster than the spin-lattice rate. This is likely the origin of the decay observed in Figure 11.2a. Further evidence will be brought in Section 11.3.3 below.

11.2.2 Coherence time

We now turn to the coherence time of the $I = 0$ transition. We measure the echo amplitude as a function of the delay τ of a Hahn echo sequence with quadrature averaging. The data are shown in Figure 11.2b. They show a strong ESEEM, with a decaying envelope. Using the analysis already described in Section 11.1, we fit the coherence time $T_2 = 425 \pm 13$ μs.

To understand the coherence limiting processes, the instantaneous diffusion contribution is computed using Equation 4.14. The pulse length used for this measurement is $dt = 2$ μs and the resonator bandwidth is broadened by the erbium spin line with $\kappa_t/2\pi \sim 2.6$ MHz. Thus the spin excitation bandwidth is limited by the pulse length and $\Delta\omega/2\pi \sim 0.6$ MHz (see Section 3.3.2). The angular factor $\sin^2(\theta_2/2)$ is taken as 0.65 following the discussion of Section 7.1.1.4. Finally, from the previous section, we know that the $I = 0$ erbium spins have an inhomogeneous linewidth of $\Gamma_{\text{inh}}/2\pi = 36$ MHz and a concentration of 0.77×18 ppm. With all these parameters, Equation 4.14 yields $T_{2,\text{ID}} = 35$ μs. This is shorter than the measured T_2 by more than an order of magnitude.

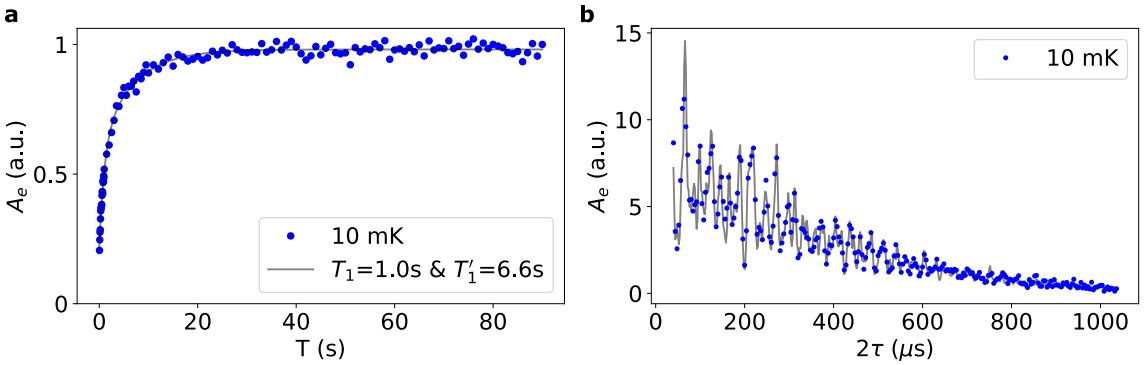

Figure 11.2 – **Electron spin dynamics of the $I = 0$ erbium spins at the cryostat base temperature. a.** Relaxation time measured with an inversion recovery sequence at 10 mK, cryostat temperature. Echo amplitude as a function of the delay T between the inversion pulse of amplitude α_{in} and the Hahn-echo sequence of same amplitude. The data (blue circles) are fitted by a double exponential curve (solid grey line), yielding $T_1 = 1.0 \pm 0.1$ s and $T_1' = 6.6 \pm 0.6$ s. **b.** Coherence time measurement at the same cryostat temperature. The Hahn echo amplitude as a function of 2τ is averaged in quadrature and fitted with $A_e = AV_{2p}(2\tau)e^{-(2\tau/T_2)^x}$, where $V_{2p}(2\tau)$ is the ESEEM modulation envelope fitted in Section 11.1. The fit yields $T_2 = 425 \pm 13$ μs and $x = 1.3 \pm 0.1$.

However, this calculation was performed as if the resonator was exciting the center of the spin line. In fact, this measurement is taken about 0.7 mT away from the resonance magnetic field of the erbium $I = 0$ transition. This corresponds to a frequency detuning of 82 MHz between the resonator at $\omega_0/2\pi$ and the erbium spin frequency at $\omega_s/2\pi$. Additionally we note that the shifted resonator frequency due to the presence of the spin line, $\tilde{\omega}_0/2\pi$, is 3 MHz higher than the resonator frequency without spins, $\omega_0/2\pi$. In total, the excitation frequency at $\tilde{\omega}_0/2\pi$ is about 85 MHz away from the center of the erbium spin transition. As the $I = 0$ inhomogeneous line is nearly Lorentzian with FWHM $\Gamma_{\text{inh}}/2\pi = 36$ MHz, a detuning of 85 MHz reduces the effective excited erbium concentration by a factor $18^2/(85^2 + 18^2) = 0.043$. Therefore, the estimated $T_{2,\text{ID}}$ increases by $1/0.043 = 23$, such that $T_{2,\text{ID}} \sim 800$ μs. This is much closer to our measured coherence time, with a difference by a factor 2, and confirms that instantaneous diffusion is certainly contributing to the measured decoherence.

Moreover, it is likely that the measured coherence time is slightly impacted by echo phase noise occurring for $\tau \gtrsim 600$ μs as will be shown in the next section. This measurement was only performed with quadrature averaging, thus preventing the comparison with magnitude averaging.

11.3 Spin dynamics on the $m_I = 3/2$ hyperfine transition

We now turn to a study of spin dynamics on the $m_I = 3/2$ transition. One specific interest of the hyperfine transitions is that, as explained earlier in Section 10.2.2, their population strongly depends on temperature, so that the instantaneous diffusion contribution can be made negligible by working at low temperatures. Due to the smaller cooperativity compared to the $I = 0$ avoided crossing, the measurement is done at the center of the spin line.

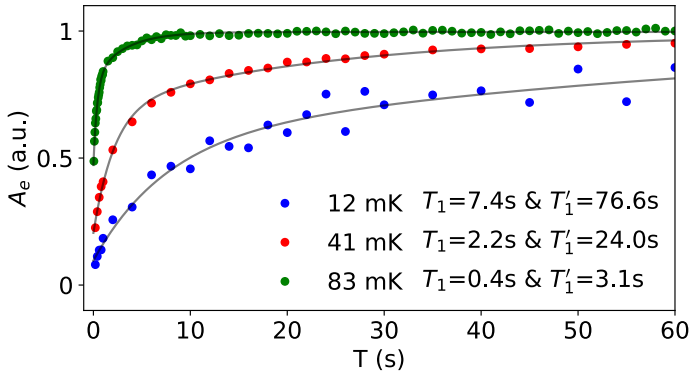

Figure 11.3 – **Electron spin relaxation time measurement of the $m_I = 3/2$ erbium spins at several temperatures.** Echo amplitude as a function of the delay T of an inversion recovery sequence, measured at cryostat temperatures 12 mK (blue dots), 41 mK (red dots) and 83 mK (green dots). The data are fitted with double exponential curves (solid lines) yielding at 12 mK, $T_1 = 7 \pm 2$ s and $T_1' = 77 \pm 22$ s, at 41 mK, $T_1 = 2.2 \pm 0.1$s and $T_1' = 24 \pm 2$s, and at 83 mK, $T_1 = 0.39 \pm 0.03$ s and $T_1' = 3.1 \pm 0.2$ s.

11.3.1 Relaxation times

We start by measuring the spin relaxation time using an inversion recovery sequence with 2 μs long pulses. The echo amplitude A_e as a function of the delay T between the first pulse and the echo detection sequence is shown in Figure 11.3 for three different temperatures. None of the curves are well fitted by a single exponential, and we therefore use a phenomenological double exponential fit, as already discussed for the $I = 0$ transition. The two time constants used for the fit are highly temperature dependent.

Interesting insight is gained by comparing the decay observed at 10 mK on both the $I = 0$ and the $m_I = 3/2$ transitions. They occur on vastly different timescales, on the order of seconds for $I = 0$ (Figure 11.2a) and minutes for $m_I = 3/2$. On the other hand, we recover a decay of order a few seconds at 80 mK on the $m_I = 3/2$ transition, comparable to the $I = 0$ data at 10 mK.

We believe this is evidence that the observed decay is due to spatial or spectral diffusion of the spin polarization. In fact, the small fraction of excited erbium spins after the inversion pulse can flip-flop with a probability that is proportional to the number of resonant spins. This number is proportional to c/Γ_{inh}, the spin concentration per frequency. In the previous experiment on the erbium $I = 0$ transition, we had $c \times 2\pi/\Gamma_{\text{inh}} \sim 0.043 \times 0.77[\text{Er}^{3+}] \times 2\pi/\Gamma_{\text{inh}} \sim 2.1 \times 10^8$ cm^{-3}/Hz (with $\Gamma_{\text{inh}}/2\pi = 36$ MHz, see Section 10.2.2). At 10 mK cryostat temperature, the spin temperature is about 23 mK (see Section 10.2.2) and at 23 mK, the erbium concentration in the $m_I = 3/2$ levels is $c_{m_I=3/2} = 0.01 \times 0.23[\text{Er}^{3+}]$ (see Section 2.2.4). Therefore, as $\Gamma_{\text{inh}}/2\pi = 22$ MHz, $c \times 2\pi/\Gamma_{\text{inh}} \sim 2.4 \times 10^7$ cm^{-3}/Hz. This is one order of magnitude smaller compared to the $I = 0$ erbium spins and spatial or spectral diffusion of spin polarization should be correspondingly slower. At 80 mK, the $m_I = 3/2$ concentration is 8 times higher, thus erbium-erbium flip-flops are more likely, explaining the shorter decay. In fact, this gives $c \times 2\pi/\Gamma_{\text{inh}} \sim 1.9 \times 10^8$ cm^{-3}/Hz which is now comparable to the measurement on the $I = 0$ erbium spins and explains the similarity between both relaxation measurements. We have not attempted to model more quantitatively these data, but nevertheless we can safely conclude that the measured spin relaxation is dominated by spin polarization diffusion processes and not by spin-lattice relaxation (which is expected to be of order 5 minutes for our experimental parameters), both on the $I = 0$ and $m_I = 3/2$ transitions.

11.3.2 Electron spin coherence time

We now study the electron spin coherence time of the $m_I = 3/2$ transition. Figure 11.4a and b show the Hahn-echo amplitude A_e as a function of the delay 2τ between the first pulse and the echo, measured at various cryostat temperatures. The pulse duration for this measurement is $dt = 1$ μs. We first note that the Hahn-echo decay is strongly temperature dependent. Moreover, the data at lowest temperature (10 mK cryostat temperature, corresponding to 23 mK spin temperature) is plotted with both quadrature and amplitude averaged echo amplitudes. The decay of the quadrature averaged data is about twice shorter than the magnitude averaged data. As already observed in Chapter 7, this originates from a randomization of the echo phase for $\tau \gtrsim 0.3$ ms, which is attributed to noise in the applied magnetic field at kHz frequencies. We note that this threshold of 0.3 ms, above which the echo phase becomes random, is shorter than the one of 1-2 ms found in the measurements of Chapter 7. Due to this phase noise, the data measured below 50 mK included are averaged in magnitude. Above 50 mK, the Hahn-echo decay is fast enough so that magnitude averaging is not needed and the data are averaged in quadrature.

The data are fitted with the ESEEM signal $V_{2p}(2\tau)$ multiplied by the echo decay $Ae^{-(2\tau/T_2)^x}$. For the magnitude averaged data, the fit also includes a noise offset C, $A_e = \sqrt{(AV_{2p}(2\tau)e^{-(2\tau/T_2)^x})^2 + C}$. The ESEEM envelope is fitted once with the data at 50 mK. In fact, the larger spin population in the $m_I = 3/2$ levels at 50 mK compared to 10 mK gives a better SNR and at the same time, the coherence time is sufficiently long to probe many successive ESEEM oscillations. The data at 50 mK is measured with a sampling time of 2 μs which is sufficient to fit the ESEEM.

The fits yield the coherence time T_2 and the stretching exponent x which are plotted in Figure 11.4c as a function of spin temperature. We observe a strong decay by one order of magnitude of the coherence time T_2 between 20 mK and 100 mK. The longest coherence time is measured at the lowest spin temperature of 23 mK, with $T_2 = 1.25 \pm 0.05$ ms. The fitted coherence time at 100 mK is $T_2 = 112 \pm 4$ μs. At higher temperature, the coherence time reaches a plateau around 40 μs. The stretching exponent x varies slightly between 1 and 2.

As explained in Chapter 4, spin decoherence can be due to instantaneous diffusion (ID) or spectral diffusion (SD). In particular, we showed that SD is strongly affected by the polarization of the electron spin bath. Here we are interested in understanding quantitatively the temperature dependence of the coherence time. Thus, as the polarization depends on the spin temperature only, we plot all quantities as a function of the spin temperature T_s rather than the cryostat temperature in the rest of this chapter. T_s equals the cryostat temperature down to 30 mK and deviates slightly below this threshold (see Section 10.2.2).

To identify the dominant decoherence process, we first evaluate the ID contribution. The ID-limited coherence time is inversely proportional to the spin concentration within the excitation bandwidth $c\Delta\omega/\Gamma_{\text{inh}}$ (see Equation 4.14). Contrarily to the $I = 0$ erbium transition, the concentration c of erbium spins in the $m_I = 3/2$ levels is temperature dependent (see Section 2.2.4). This concentration goes to 0 at zero temperature and saturates at $0.23[Er^{3+}]/8$ at high temperature (typically larger than 300 mK). The inhomogeneous linewidth is $\Gamma_{\text{inh}}/2\pi = 22$ MHz (see Section 10.2.2). The cavity bandwidth $\kappa_t/2\pi$ is slightly temperature dependent and varies between 0.75 and 1.6 MHz. Combined with the pulse duration of $dt = 1$ μs, the excitation bandwidth $\Delta\omega/2\pi$, calculated with Equation 3.64, varies between 0.63 and 0.94 MHz. We keep its mean value for the ID calculation, $\Delta\omega/2\pi = 0.7 \pm 0.1$ MHz.

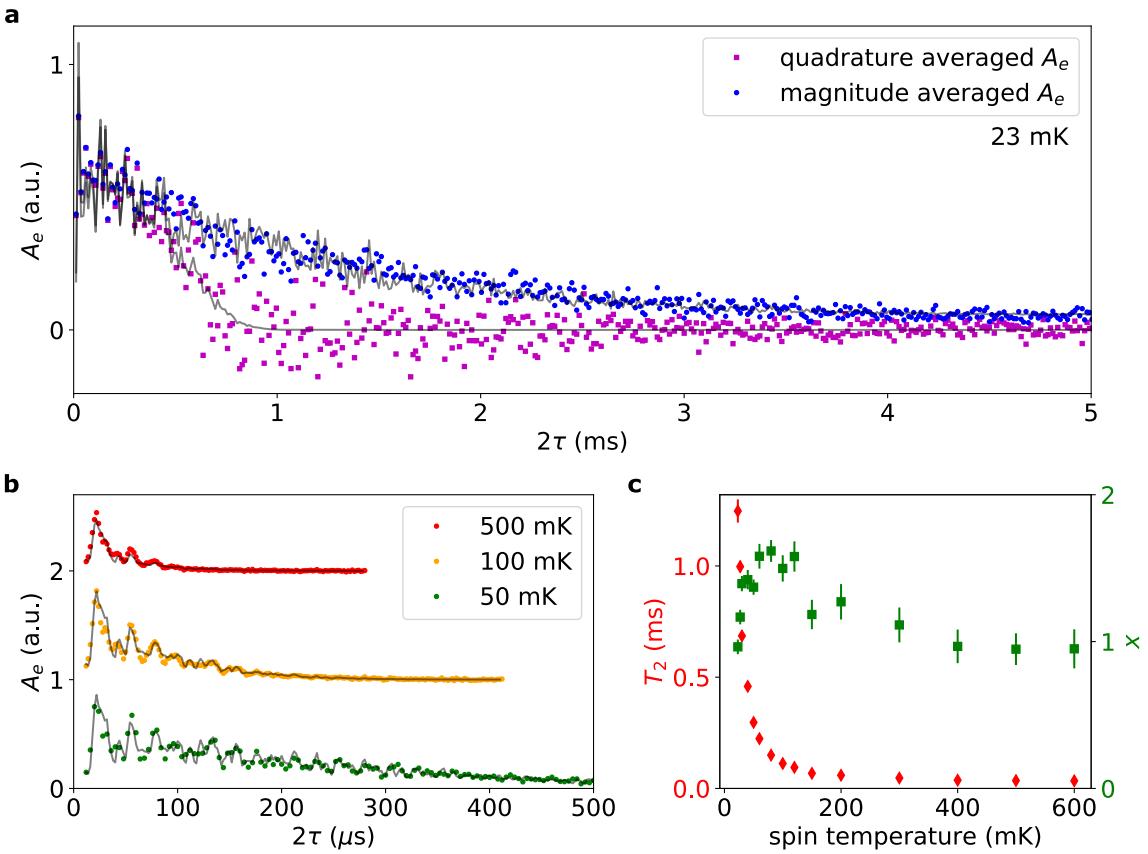

Figure 11.4 – **Electron spin coherence measurement of the $m_I = 3/2$ erbium spins as a function of the spin temperature T_s. a.** & **b.** Hahn-echo amplitude A_e as a function of the delay 2τ between the first pulse and the echo, measured at several temperatures. The temperatures indicated here are the estimated spin temperatures from Section 10.2.2. **a.** Coherence time measurement at $T_s = 23$ mK. The echo amplitude is either averaged in quadrature (purple squares) or in magnitude (blue circles). The data are fitted with functions including the ESEEM and the echo decay (solid lines). The quadrature averaged data are fitted with $A_e = AV_{2p}(2\tau)e^{-(2\tau/T_2)^x}$, where $V_{2p}(2\tau)$ is the ESEEM modulation, yielding $T_2 = 0.60 \pm 0.01$ ms and $x = 3.6 \pm 0.4$. The magnitude averaged data are fitted with $A_e = \sqrt{(AV_{2p}(2\tau)e^{-(2\tau/T_2)^x})^2 + C}$, yielding $T_2 = 1.25 \pm 0.05$ ms and $x = 0.94 \pm 0.05$. The ESEEM is largely undersampled in these data and the function V_{2p} is thus fitted beforehand with other finer sampled data measured at 50 mK. **b.** Coherence time measurements at $T_s = 50$ mK (green dots), 100 mK (orange dots) and 500 mK (red dots). The echo amplitude is averaged in quadrature. The solid lines are fits with $A_e = AV_{2p}(2\tau)e^{-(2\tau/T_2)^x}$. They give $T_2 = 297 \pm 6$ μs and $x = 1.37 \pm 0.05$ at 50 mK, $T_2 = 112 \pm 4$ μs and $x = 1.5 \pm 0.1$ at 100 mK and $T_2 = 35 \pm 6$ μs, $x = 0.9 \pm 0.1$ at 500 mK. **c.** Fitted coherence time T_2 and stretching exponent x as a function of spin temperature.

Using Equation 4.14, we thus estimate that $T_{2,\mathrm{ID}} = 6$ ms at 23 mK and $T_{2,\mathrm{ID}} = 500$ μs at 600 mK, due to the concentration increasing by a factor 13. At high temperature, $T_{2,\mathrm{ID}}$ is one order of magnitude larger than the fitted coherence time and is therefore not the dominant contribution. At low temperature, ID is not completely negligible (which may explain why the stretching exponent x is close to 1 at 23 mK).

ID contribution being negligible at high temperature suggests that SD is the dominant mechanism. The rest of the section is dedicated to an in-depth analysis of the SD process, using three pulse echoes and the uncorrelated sudden-jump model (see Section 4.2.1).

11.3.3 Spectral diffusion study using stimulated echoes

As seen in Chapter 4, spectral diffusion can be characterized by 3 parameters: the homogeneous linewidth Γ_0, the spin-flip rate R and the spin linewidth Γ_{SD}. The Hahn-echo T_2 measurements are not sufficient to independently extract each of these quantities; however the stimulated echo method introduced in Section 4.2.1 can do it. Therefore, we now measure stimulated echo decays for varying parameters.

The three-pulse echo sequence, consisting in three identical pulses spaced by τ and then T_w, triggers a stimulated echo at time $2\tau + T_w$ after the first pulse. Due to pulse imperfections (our pulse are far from perfect $\pi/2$ pulses), the stimulated echo sequence does not only trigger the stimulated echo, but also four spurious echoes. Three spurious echoes come from the two pulse echo generated by each combination of two pulses and the fourth one is the refocused echo of one of them by the last pulse [SJ01]. To prevent overlapping of these spurious echoes with the stimulated echo, phase-cycling has to be used in the experiment, where the sign of each pulse is changed from one sequence to another. These signs are wisely chosen such that averaging all traces together suppresses the contribution of spurious echoes and keeps only the stimulated echo.

Figure 11.5 shows stimulated echo amplitudes as a function of T_w, measured for various delays τ and various spin temperatures T_s. The echo amplitudes are obtained with phase-cycling and are therefore averaged in quadrature. Here, quadrature averaging is justified, because the phase of the echo depends only on the phase stability during the last τ interval. The chosen delays τ are below 100 μs which is less than the time above which the echo phase gets randomized.

We observe that the stimulated echo decay with T_w happens with very different timescales depending on the spin temperature, on the order of seconds at 27 mK and less than a millisecond at 530 mK. These timescales are overall much shorter than the measured relaxation times presented in Figure 11.3. We also note that at each temperature, the decay depends on τ and gets faster when τ increases. As explained in Section 4.2.1, this is a signature of spectral diffusion. The main contribution to spectral diffusion at high temperature comes from the erbium $I = 0$ spin bath due to its large concentration. Moreover, we observe that the data at 100 mK decays typically in 1 ms, which should roughly match the typical spin-flip time R^{-1}. If spectral diffusion was due to T_1-spin flips, we would expect erbium spins to flip with their spin-lattice relaxation time of a few minutes as estimated in Section 11.2.1 (at 100 mK and 43 mT, the spin-lattice relaxation time is reduced by a factor 0.8 compared to 10 mK and it would be 4 minutes instead of 5). This is clearly incompatible with the measured decay and rules out T_1-spin flips. The spectral diffusion is thus due to electron spin flip-flops.

To fit our data, we use the sudden-jump model of Section 4.2. At this point it is useful to comment on its validity. As explained in Section 4.2, the model is derived by assuming that the bath spins undergo random and independent spin-flips. This describes well the situation where the dominant relaxation mechanism is spin-lattice relaxation, and

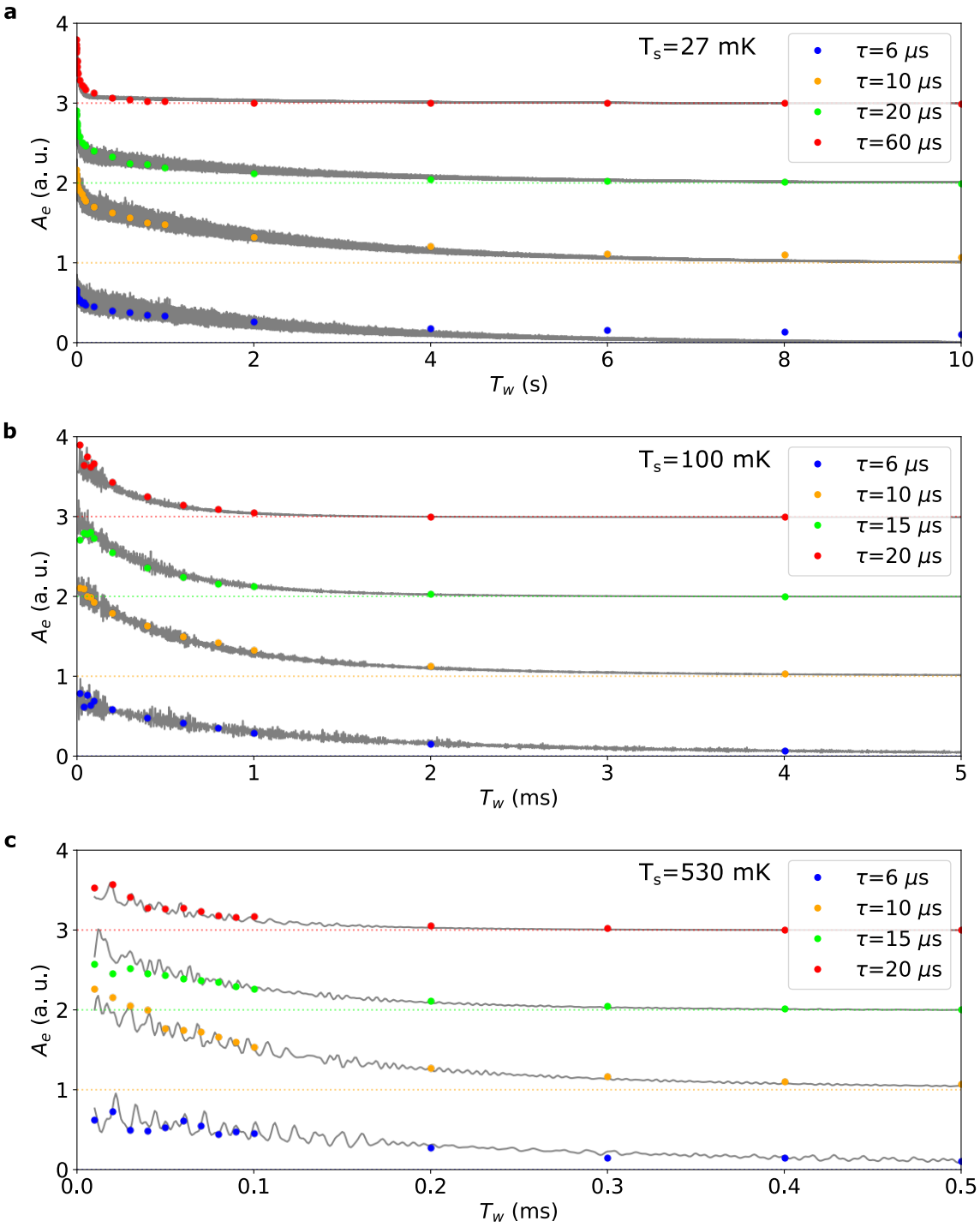

Figure 11.5 – **Stimulated echo decay for various spin temperatures.** The echo is triggered by a series of three identical pulses, spaced by first τ and then T_w, at time $2\tau + T_w$. The stimulated echo amplitude is plotted as a function of the waiting time T_w for different values of the delay τ. Data points are shown as color circles, each color corresponding to a given τ value. For these measurements, $\tau \leq 100$ μs, below the echo phase randomization threshold, and the data are averaged in quadrature. Fits are shown as solid grey lines, they use Equation 4.3 with the amplitude V_0 being modulated by three-pulse ESEEM. The ESEEM parameters are fitted separately using a Hahn-echo decay measurement. All data within one subplot are fitted simultaneously with four free parameters, the global amplitude A, the homogeneous linewidth Γ_0, the erbium spectral diffusion linewidth $\Gamma_{SD,\mathrm{Er}}$ and the erbium spin flip rate R_{Er}. **a.** Stimulated echo decay at $T_s = 27$ mK. This fit includes one extra free parameter which is the spin relaxation time T_1. **b.** Stimulated echo decay at $T_s = 100$ mK. **c.** Stimulated echo decay at $T_s = 530$ mK.

indeed quantitative agreement has been reached in a detailed study on optical coherence in Er:Y_2SiO_5 [Böt+06], based on this model in a limit where relaxation in the bath is dominantly spin-lattice. As explained earlier, we are in a slightly different situation, where flip-flops within the bath occur much faster than spin-lattice relaxation. Therefore, the validity of the model can be questioned. We will come back to this point in the end of the discussion. For the time being, we will apply this model, using Equation 4.3 applied to the two highest-concentrated paramagnetic spin species in this sample, erbium $I = 0$ and ytterbium $I = 0$ spins. The echo amplitude is thus fitted with

$$V(2\tau + T_w) = A \times V_{3p}(2\tau + T_w) \times \exp\left\{-\frac{T_w}{T_1}\right\} \times \exp\left\{-\tau\left[\Gamma_0 + \frac{\Gamma_{\text{SD, Er}}}{2}\left(R_{\text{Er}}\tau + 1 - e^{-R_{\text{Er}}T_w}\right) + \frac{\Gamma_{\text{SD, Yb}}}{2}\left(R_{\text{Yb}}\tau + 1 - e^{-R_{\text{Yb}}T_w}\right)\right]\right\}. \tag{11.1}$$

The ESEEM envelope which is visible in the fits of Figure 11.5 is fitted separately using a Hahn-echo decay measurement. From Equation 2.46 and Equation 4.2, we get that

$$\frac{\Gamma_{\text{SD, Yb}}}{\Gamma_{\text{SD, Er}}} = \frac{g_{\text{eff, Yb}} c_{\text{Yb}}}{g_{\text{eff, Er}} c_{\text{Er}}} \times \frac{\text{sech}^2\left(g_{\text{eff, Yb}}\mu_B B_0/(2k_B T)\right)}{\text{sech}^2\left(g_{\text{eff, Er}}\mu_B B_0/(2k_B T)\right)}, \tag{11.2}$$

which is known without adjustable parameters from the independent determination of c_{Er} and c_{Yb}.

From Equation 4.11, using the fact that $\Xi(\mathbf{g}, \boldsymbol{B_0} \perp c) \sim g_\perp^4/20$ for both erbium and ytterbium, we moreover get that

$$\frac{R_{\text{Yb}}}{R_{\text{Er}}} = \frac{g_{\perp,\text{ Yb}}^4 c_{\text{Yb}}^2}{\Gamma_{\text{inh, Yb}}} \times \frac{\Gamma_{\text{inh, Er}}}{g_{\perp,\text{ Er}}^4 c_{\text{Er}}^2} \times \frac{\text{sech}^2\left(g_{\text{eff, Yb}}\mu_B B_0/(2k_B T)\right)}{\text{sech}^2\left(g_{\text{eff, Er}}\mu_B B_0/(2k_B T)\right)}, \tag{11.3}$$

where all the parameters were determined spectroscopically in Chapter 10.

From these considerations, the only remaining free parameters of Equation 11.1 are the amplitude A, the erbium spectral diffusion linewidth $\Gamma_{\text{SD, Er}}$, the spin flip-flop rate R_{Er} and the relaxation time T_1. Except for the lowest temperature data at $T_s = 27$ mK, spectral diffusion takes place at a rate faster than T_1^{-1} and we thus take $e^{-T_w/T_1} = 1$.

For each temperature, all data $A_e(\tau, T_w)$ are simultaneously fitted and the result is shown in Figure 11.5. The fits match well the data. The ESEEM modulation is clearly undersampled in the data but reproduces well the relative amplitude of data measured at different τ values. The agreement between the data and fit is clearly better in the high temperature regime. At $T_s = 27$ mK, the fit yields a spin relaxation time of $T_1 = 2.5 \pm 0.3$ s which is rather in agreement with the short time constant of the relaxation measurement shown in Figure 11.3. Nevertheless, the T_w decay of the data deviates significantly from the fit, with a slower decay at $\tau = 6$ μs and $\tau = 10$ μs and a faster decay at $\tau = 20$ μs and $\tau = 60$ μs. The fact that the model does not match perfectly the low temperature data is expected. Indeed, spectral diffusion from erbium and ytterbium is almost quenched and other decoherence processes, such as spectral diffusion from other non-frozen paramagnetic spins, may affect the data but are not included in our model.

The fitted parameters, Γ_0, R and Γ_{SD}, are shown in Figure 11.6 as a function of the spin temperature. The spectral diffusion parameters, R and Γ_{SD}, show a strong temperature dependence over several orders of magnitude while the homogeneous linewidth Γ_0 seems constant. The temperature dependence of the erbium parameters, $\Gamma_{\text{SD, Er}}$ and R_{Er}, are fitted with functions proportional to $\text{sech}^2[g_{\text{eff, Er}}\mu_B B_0/(2k_B T)]$. The agreement is rather good and the fits yield $\Gamma_{\text{max, Er}}/2\pi = 400 \pm 20$ kHz and $R_{\text{max, Er}} = 1.4 \pm 0.1$ ms^{-1}. The

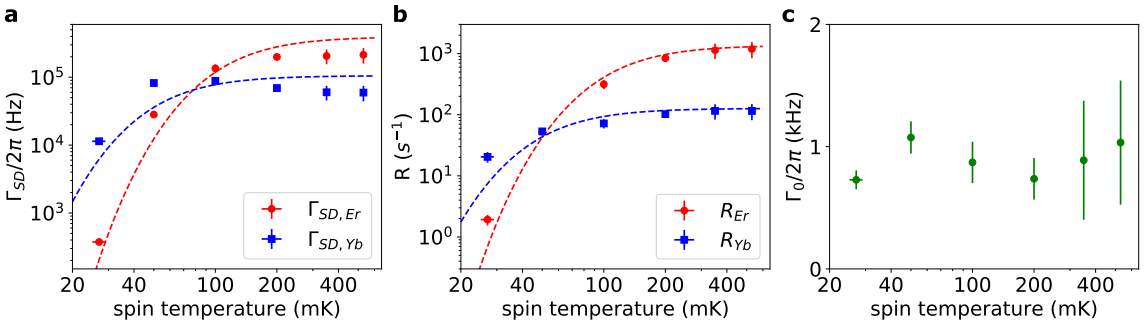

Figure 11.6 – **Fitted spectral diffusion parameters from the stimulated echo decay as a function of spin temperature. a.** Spectral diffusion linewidth Γ_{SD} as a function of temperature for erbium $I = 0$ spins (red circles) and ytterbium $I = 0$ spins (blue squares). The fit of the erbium data (red dashed line) with $\Gamma_{\mathrm{SD,\,Er}} = \Gamma_{\mathrm{max,\,Er}}\,\mathrm{sech}^2\left[g_{\mathrm{eff,\,Er}}\mu_B B_0/(2k_B T)\right]$ yields $\Gamma_{\mathrm{max,\,Er}}/2\pi = 400 \pm 20$ kHz. **b.** Spin flip rate R as a function of temperature for erbium $I = 0$ spins (red circles) and ytterbium $I = 0$ spins (blue squares). The fit of the erbium data (red dashed line) with $R_{\mathrm{Er}} = R_{\mathrm{max,\,Er}}\,\mathrm{sech}^2\left[g_{\mathrm{eff,\,Er}}\mu_B B_0/(2k_B T)\right]$ yields $R_{\mathrm{max,Er}} = 1.4 \pm 0.1$ ms^{-1}. **c.** Homogeneous linewidth Γ_0 as a function of temperature.

data and model for the ytterbium parameters are fully determined from Equation 11.2 and Equation 11.3.

These fits can be compared with the theoretical values of $\Gamma_{\mathrm{max,\,Er}}$ and $R_{\mathrm{max,\,Er}}$. For the estimated $I = 0$ erbium concentration of 0.77×18 ppm, $\Gamma_{\mathrm{max,\,Er}}/2\pi$ is calculated using Equation 2.46, yielding 831 kHz, which is larger by a factor two compared to our fit.

The flip-flop rate can be roughly estimated using Equation 4.10,

$$R_{\mathrm{max,\,Er}} = \frac{1}{12\hbar^2}\mu_0^2\mu_B^4\Xi(\mathbf{g}_{\mathrm{Er}}, \boldsymbol{B_0})c_{\mathrm{Er}}^2\frac{1}{\alpha_0\Gamma_{\mathrm{inh,\,Er}}}, \tag{11.4}$$

where $\Xi(\mathbf{g}_{\mathrm{Er}}, \boldsymbol{B_0}) \sim g_{\perp,\,\mathrm{Er}}^4/20$ with our field orientation and α_0 is a free parameter of the order unity. Taking $\alpha_0 = 1$ gives $R_{\mathrm{Er}} \sim 3$ ms^{-1}, which is roughly of the right order of magnitude.

The semi-quantitative agreement of the parameters extracted from the model with physical quantities is an indication that the sudden-jump model remains valid also when applied to flip-flop-induced spectral diffusion.

11.3.4 Coherence time model from the spectral diffusion analysis

Finally the analysis of spectral diffusion can be used to model the coherence time measured in Section 11.3.2. In fact, as explained in Section 4.2, the sudden-jump model provides a formula for the Hahn-echo coherence time T_2, based on Γ_0, Γ_{SD} and R. With the $I = 0$ erbium and ytterbium contributions, Equation 4.5 becomes

$$T_2 = \frac{2}{\Gamma_{\mathrm{SD,\,Er}}R_{\mathrm{Er}} + \Gamma_{\mathrm{SD,\,Yb}}R_{\mathrm{Yb}}}\left[-\Gamma_0 + \sqrt{\Gamma_0^2 + 2(\Gamma_{\mathrm{SD,\,Er}}R_{\mathrm{Er}} + \Gamma_{\mathrm{SD,\,Yb}}R_{\mathrm{Yb}})}\right]. \tag{11.5}$$

In a first step, this formula is applied to the fitted Γ_0, $\Gamma_{\mathrm{SD,\,Er}}$ and R_{Er} from the measured stimulated echo data at each spin temperature. The result is plotted with green squares in Figure 11.7b and is compared with the Hahn-echo T_2 of Figure 11.4c (red diamonds). Both data are in agreement in the high temperature regime but deviate from

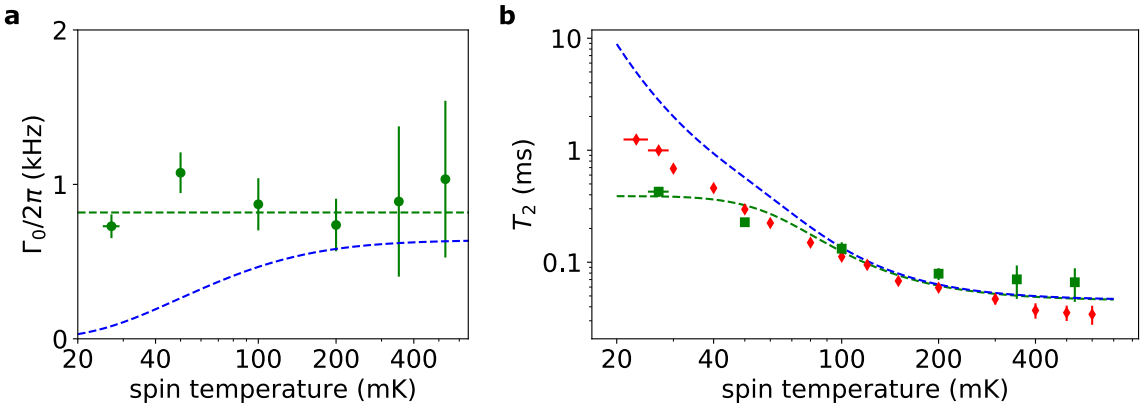

Figure 11.7 – **Model of the coherence time temperature dependence using spectral diffusion. a.** Same data as in Figure 11.6c overlaid with two models for the homogeneous linewidth, either the data is fitted with a constant (green dashed line) or the homogeneous linewidth is taken as the instantaneous diffusion linewidth $\Gamma_0 = 2/T_{2,\mathrm{ID}}$ (blue dashed line). **b.** Coherence time as a function of spin temperature, measured with the Hahn-echo sequence (red diamonds, same data as in Figure 11.4c) and extrapolated from the stimulated echo sequence (green circles) using Equation 11.5. The data is compared with two models where spectral diffusion is computed using the fitted $\Gamma_{\mathrm{max,\ Er}}$ and $R_{\mathrm{max,\ Er}}$ and the homogeneous linewidth Γ_0 is one of the two model functions presented in subplot a.

each other below 50 mK. This can be explained by the fact that the stimulated echo data at lowest temperature was not perfectly reproduced by the fit (see Figure 11.5). Our model is certainly incomplete to describe the decoherence processes occurring at low temperature.

To make a model of the coherence time as a function of temperature, we now use the fitted values of $\Gamma_{\mathrm{max,\ Er}}$ and $R_{\mathrm{max,\ Er}}$ to calculate the spectral diffusion part ($\Gamma_{\mathrm{SD,\ Er}} R_{\mathrm{Er}} + \Gamma_{\mathrm{SD,\ Yb}} R_{\mathrm{Yb}}$). To compute T_2 from Equation 11.5, we also need a model for the homogeneous linewidth Γ_0. On the one hand, the fitted values of Γ_0 as a function of temperature seem constant and we may choose to fit these values with a constant, yielding $\Gamma_0/2\pi = 820 \pm 60$ Hz (see the dashed green line in Figure 11.7a). On the other hand, we know that the fit at low temperature does not exactly reproduce the stimulated echo data and we may want to model Γ_0 with physical quantities. In fact, Γ_0 is expected to be dominated by instantaneous diffusion and we propose a second model where $\Gamma_0 = 2/T_{2,\mathrm{ID}}$ (see the dashed blue line in Figure 11.7a). ID is computed from the values estimated in Section 11.3.2.

This results in the two models shown in Figure 11.7b. In the first case, the T_2 model follows the coherence time extrapolated from the stimulated echo data. This is not surprising as every parameter of Equation 11.5 is directly fitted from the stimulated echo data. However, this model predicts a coherence time of 400 μs at low temperature which is smaller by a factor 3 from the measured coherence time at 23 mK. In the second case, the model fits well the coherence time at high temperature, above 100 mK, where spectral diffusion of erbium and ytterbium $I = 0$ spins is clearly the dominant decoherence process. At low temperature, the model deviates from the measured coherence time, predicting about 5 ms coherence time at 23 mK ($T_{2,\mathrm{ID}} \sim 6$ ms and the erbium and ytterbium spectral diffusion alone would lead to $T_2 \sim 11$ ms), while the measured value is 1.2 ms. This difference is attributed to residual spectral diffusion at low temperature from other paramagnetic species, like manganese for instance, which are not completely polarized at the lowest temperatures. We note that the nuclear spin spectral diffusion plays no role here as it predicts a coherence of about 20 ms according to Chapter 7.

This spectral diffusion analysis shows that coherence time measured on a low populated hyperfine transition can reach millisecond timescales in a nevertheless highly doped crystal. This happens thanks to two main reasons: instantaneous diffusion is reduced due to the small resonant erbium concentration at low temperatures and spectral diffusion from paramagnetic species in the environment is quenched at low temperature, where most electron spins are frozen in their ground state.

Chapter 12

Conclusion

Millikelvin spectroscopy of erbium electron spins in scheelite crystals

This thesis describes electron spin resonance experiments performed on $CaWO_4$ crystals at temperatures ranging from 10 mK to 600 mK, using planar superconducting microwave resonators for detecting the spin signal. The goal of these measurements was to study the dynamics of erbium ions in these crystals, in both high and low concentration regimes. State-of-the-art Hahn-echo coherence time of erbium electron spins on a magnetically-sensitive transition was until now about 50 μs, measured at 2.5 K and certainly limited by spectral diffusion caused by paramagnetic impurities in the erbium environment.

We first measured nominally pure $CaWO_4$ crystals, which were shown to contain rare-earth-ions at the ppb concentration level. At 10 mK and for a moderate magnetic field of typically 50-100 mT, most of the electron spins are frozen in their ground state and therefore do not contribute to decoherence. Hahn-echo coherence times of 23 ms (in the (a, b)-plane) and 30 ms (along the c-axis) were measured. They reach the limit imposed by nuclear spin spectral diffusion. We also showed that the relaxation of spins located close to the resonator, typically distant from the inductive wire by less than 15 μm, is dominated by the spontaneous emission of microwave photons in the detection resonator, via the Purcell effect.

We performed related measurements on a sample with a much higher erbium concentration (18 ppm). The Hahn-echo coherence time of erbium ions reached up to 1.3 ms on a hyperfine transition. Using stimulated echo sequences, we provided a detailed study of the spectral diffusion process, occurring through flip-flops of erbium and ytterbium spins in the environment. These flip-flops were shown to be quenched at base temperature by several orders of magnitude, explaining the increase of coherence time from 40 μs at 600 mK to 1.3 ms at 23 mK.

Perspectives on future experiments

These measurements pave the path towards new experiments of hybrid quantum systems based on erbium ions in $CaWO_4$. Indeed, our work demonstrates that erbium electron spins in scheelite combine long coherence times with a large gyromagnetic ratio, up to 117 GHz/T. This is key for coupling efficiently to other quantum devices such as superconducting circuits.

The perspectives are twofold, either with new experiments on erbium spin ensembles or on single erbium ions. With their long electron spin coherence time and narrow inhomogeneous linewidth, erbium spin ensembles are interesting for multimode quantum memories [Afz+13] and microwave to optical transduction schemes [WCL14]. Another thrilling challenge is to improve our setup sensitivity in order to isolate and manipulate

single ions. Optical detection of individual rare-earth-ions was pioneered a few years ago [Kol+12; Yin+13]. More recently, single rare-earth ions have been detected and manipulated in the optical domain using cavities to enhance the radiative relaxation rate on the optical transition [Che+20; Kin+20].

Our goal within Quantronics group is to transpose these experiments to microwave frequencies, using the superconducting resonator to enhance the microwave radiative rate sufficiently for single erbium detection by its fluorescence. This microwave fluorescence is detected by a single microwave photon detector, developed in our group, which has already proven successful to detect spin ensembles of bismuth donors in silicon [Alb+21]. Once an erbium electron spin is isolated and controlled, its neighboring tungsten nuclear spins, which are magnetically coupled to the erbium spin, become a rich resource for a dense multi-qubit register, with potentially hour-long storage time, as already demonstrated with nitrogen-vacancy centers in diamond [Tam+14] or more recently with ytterbium ions in yttrium orthovanadate [Rus+21]. Such hybrid quantum systems, coupling superconducting circuits to rare-earth-ions, thus may open the way to a new quantum computing architecture, which will be pursued in the future in the group.

Appendix A

Scattering matrix coefficients

In this appendix, the expression for the scattering matrix coefficients of Equation 3.6 and Equation 3.7 are derived. The RLC-resonator in series with the coupling capacitance C_c are associated to an element of impedance Z_L (see Figure 1.1).

Reflection case

In the reflection case, when the switch of Figure 1.1 is open, it can be shown that the reflection coefficient S_{11} is given by [Poz11]

$$S_{11} = \frac{Z_L - Z_c}{Z_L + Z_c}. \tag{A.1}$$

The load impedance Z_L can be calculated as

$$\begin{aligned} Z_L &= \frac{1}{jC_c\omega} + \frac{1}{\frac{1}{jL\omega} + jC\omega + \frac{1}{R}} \\ &= \frac{1}{jC_c\omega} + \frac{jL\omega}{1 - LC\omega^2 + j\frac{L\omega}{R}} \\ &= -jZ_{cpl} + \frac{jZ_R}{1 - \left(\frac{\omega}{\omega_0}\right)^2 + j\frac{Z_R}{R}}, \end{aligned} \tag{A.2}$$

where $Z_{cpl} = 1/(C_c\omega)$, $Z_R = L\omega$ and $\omega_0 = 1/\sqrt{LC}$.

Using this formula in the reflection coefficient gives

$$\begin{aligned} S_{11} &= \frac{(-jZ_{cpl} - Z_c)(1 - (\omega/\omega_0)^2 + jZ_R/R) + jZ_R}{(-jZ_{cpl} + Z_c)(1 - (\omega/\omega_0)^2 + jZ_R/R) + jZ_R} \\ &= \frac{1 - (\omega/\omega_0)^2 + jZ_R/R + jZ_R/(-jZ_{cpl} - Z_c)}{1 - (\omega/\omega_0)^2 + jZ_R/R + jZ_R/(-jZ_{cpl} + Z_c)}. \end{aligned} \tag{A.3}$$

The last term of the numerator and denominator can be simplified in the limit of high quality factors, where $Z_c \ll Z_{cpl}$,

$$\begin{aligned} \frac{jZ_R}{-jZ_{cpl} - Z_c} &= \frac{jZ_R(jZ_{cpl} - Z_c)}{Z_c^2 + Z_{cpl}^2} =_{Z_c \ll Z_{cpl}} \frac{jZ_R(jZ_{cpl} - Z_c)}{Z_{cpl}^2}, \\ \frac{jZ_R}{-jZ_c + Z_0} &=_{Z_0 \ll Z_c} \frac{jZ_R(jZ_c + Z_0)}{Z_c^2}. \end{aligned} \tag{A.4}$$

This results into

$$S_{11} = \frac{1 - (\omega/\omega_0)^2 - Z_R/Z_{cpl} + j(Z_R/R - Z_cZ_R/Z_{cpl}^2)}{1 - (\omega/\omega_0)^2 - Z_R/Z_{cpl} + j(Z_R/R + Z_cZ_R/Z_{cpl}^2)}. \tag{A.5}$$

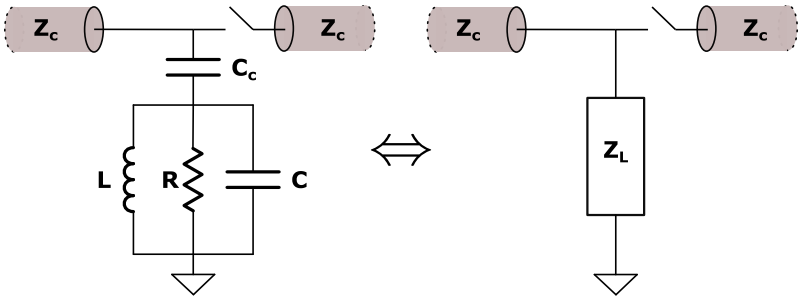

Figure 1.1 – **Equivalent impedance for the resonator and the coupling capacitor**

The real part of the numerator and denominator is found to be

$$1 - (\omega/\omega_0)^2 - Z_R/Z_{cpl} = 1 - \omega^2 L(C + C_c), \tag{A.6}$$

which defines the new resonance frequency as $\omega_0' = 1/\sqrt{L(C + C_c)}$.

By Taylor-expanding the expression of S_{11} around ω_0', we get

$$S_{11} \approx 1 - \frac{2Q/Q_c}{1 + 2jQ(\omega - \omega_0')/\omega_0'}, \tag{A.7}$$

where

$$\begin{aligned} Q_{\text{int}} &\approx \frac{R}{Z_R} \approx R\sqrt{\frac{C + C_c}{L}}, \\ Q_c &\approx \frac{Z_{cpl}^2}{Z_c Z_R} \approx \frac{Z_c}{(Z_c C_c \omega_0')^2}\sqrt{\frac{C + C_c}{L}} \\ Q^{-1} &= Q_{\text{int}}^{-1} + Q_c^{-1}. \end{aligned} \tag{A.8}$$

Hanger case

In the hanger-type measurement, when the switch of Figure 1.1 is closed, it can be shown that [Poz11]

$$S_{21} = \frac{Z_L}{Z_c/2 + Z_L} = \frac{1}{2}\left[1 + \frac{Z_L - Z_c/2}{Z_L + Z_c/2}\right]. \tag{A.9}$$

The last term can be identified as the reflection coefficient calculated in the previous section with $Z_c/2$ instead of Z_c.

Therefore, the expression of S_{21} is simply derived from Equation A.7 as

$$S_{21} \approx 1 - \frac{Q/Q_c}{1 + 2jQ(\omega - \omega_0')/\omega_0'}, \tag{A.10}$$

where

$$\begin{aligned} \omega_0' &= \frac{1}{\sqrt{L(C + C_c)}}, \\ Q_{\text{int}} &\approx \frac{R}{Z_R} \approx R\sqrt{\frac{C + C_c}{L}}, \\ Q_c &\approx \frac{Z_{cpl}^2}{(Z_c/2)Z_R} \approx \frac{2Z_c}{(Z_c C_c \omega_0')^2}\sqrt{\frac{C + C_c}{L}}, \\ Q^{-1} &= Q_{\text{int}}^{-1} + Q_c^{-1}. \end{aligned} \tag{A.11}$$

Appendix B

Spectral diffusion formulas for two and three pulse echoes

This appendix aims at giving a simple derivation of the echo decay due to spectral diffusion in two and three pulse echo sequences, as introduced in Section 4.2 with the sudden-jump model,

$$V(2\tau + T_w) = V_0 \exp\left\{-\frac{T_w}{T_1}\right\} \exp\left\{-\tau \left[\Gamma_0 + \frac{\Gamma_{\mathrm{SD}}}{2}\left(R\tau + 1 - e^{-RT_w}\right)\right]\right\} \tag{B.1}$$

2.1 Magnetic dipole-dipole interaction

Spectral diffusion is a consequence of the magnetic dipole-dipole interaction between two spins i and j, which is given by Equation 2.28,

$$\mathcal{H}_{dd} = \frac{\mu_0}{4\pi} r^{-3} [\boldsymbol{\mu_i}.\boldsymbol{\mu_j} - 3r^{-2}(\boldsymbol{\mu_i}.\mathbf{r})(\boldsymbol{\mu_j}.\mathbf{r})] \tag{B.2}$$

In the following derivation, we assume that the magnetic field is oriented along a principal axis of the **g**-tensor, such that the electron spin magnetic moments are aligned with the magnetic field. Moreover, we will be dealing with electron spins only. In the secular approximation (see Equation 2.32),

$$\mathcal{H}_{dd} = \mu_B^2 \frac{\mu_0}{4\pi} r^{-3} \mathrm{g}_{\mathrm{eff},i} \mathrm{g}_{\mathrm{eff},j} (1 - 3\cos^2\theta_r) S'_{zi} S'_{zj}. \tag{B.3}$$

Here, we drop the flip-flop term because it does not affect the spin frequency.

For two spins $S = 1/2$, we get

$$\mathcal{H}_{dd} = \mu_B^2 \frac{\mu_0}{4\pi} \mathrm{g}_{\mathrm{eff},i} \mathrm{g}_{\mathrm{eff},j} \frac{1 - 3\cos^2\theta_r}{r^3} s'_{z,i} s'_{z,j}, \tag{B.4}$$

where $s'_{z,i}, s'_{z,j} = \pm 1/2$, $\boldsymbol{r}$ is the vector separating the two spins and θ_r is the angle between $\boldsymbol{r}$ and the polarisation axis z'.

2.2 Dipolar linewidth

We start by deriving the dipolar linewidth of Equation 2.46. To do so, we follow the statistical theory of Abragam [Abr61], also found in Maryasov *et al.* [MDS82], and we calculate the free induction decay (FID) signal in the static limit, where the dephasing of the spins is dominated by the magnetic dipole interaction. After a $\pi/2$ pulse, in the rotating frame at the spin frequency ω_s, each spin rotates in the transverse plane of the

Bloch sphere and acquires a phase corresponding to its detuning from the central spin frequency ω_s. Therefore, the FID signal is given by

$$V_{\mathrm{FID}}(t) = \langle e^{\sum_j i\phi_j} \rangle_{\text{distribution of spins } j}. \tag{B.5}$$

Each perturbing spin j shifts the spin i frequency by the amount $\Delta\omega_j$ which translates into a phase shift $\phi_j = \Delta\omega_j t$,

$$\begin{aligned} \Delta\omega_j &= \frac{\mathcal{H}_{dd}\left|S_i = \frac{1}{2}\right\rangle - \mathcal{H}_{dd}\left|S_i = -\frac{1}{2}\right\rangle}{\hbar} \\ &= \mu_B^2 \frac{\mu_0}{4\pi} \frac{\mathrm{g}_{\mathrm{eff},i}\mathrm{g}_{\mathrm{eff},j}}{\hbar} \frac{1 - 3\cos\theta_r{}^2}{r^3} s'_{z,j} \\ &= \mu_B^2 \frac{\mu_0}{4\pi} \frac{\mathrm{g}_{\mathrm{eff},i}\mathrm{g}_{\mathrm{eff},j}}{\hbar} \frac{1 - 3\cos\theta_r{}^2}{r^3} \frac{\mathrm{sign}(s'_{z,j})}{2}. \end{aligned} \tag{B.6}$$

Assuming that all the spins j are weakly interacting with each other, they are treated as independent perturbers and the sum can be taken out of the average,

$$V_{\mathrm{FID}}(t) = \prod_j \langle e^{i\phi_j} \rangle. \tag{B.7}$$

Now the average is performed over a small volume $d\Omega$ around lattice site j: $\phi_j = 0$ if there is no spin at site j, with probability $1 - cd\Omega$, and $\phi_j = \Delta\omega_j t$ if there is a spin at site j, with probability $cd\Omega$. Therefore, the average over a small volume $d\Omega$ is

$$\langle e^{i\phi_j} \rangle = 1 - cd\Omega(1 - e^{i\Delta\omega_j t}). \tag{B.8}$$

Now we use a trick by taking the logarithm of V_{FID},

$$\ln V_{\mathrm{FID}} = \sum \ln\Big(1 - cd\Omega(1 - e^{i\Delta\omega_j t})\Big), \tag{B.9}$$

which can be linearized because the concentration is small,

$$\ln V_{\mathrm{FID}} \sim \sum -cd\Omega(1 - e^{i\Delta\omega_j t}). \tag{B.10}$$

Finally, the sum is replaced by an integral, as the concentration of spins is very dilute,

$$\begin{aligned} \ln V_{\mathrm{FID}} &\sim \int -cd\Omega(1 - e^{i\Delta\omega_j t}) \\ V_{\mathrm{FID}} &\sim \exp\left\{\int -cd\Omega(1 - e^{i\Delta\omega_j t})\right\} \end{aligned} \tag{B.11}$$

We observe that the integral has a real part, $A = \int -cd\Omega(1 - \cos\Delta\omega_j t)$ which describes the decay of the FID signal, and an imaginary part, $B = \int -cd\Omega \sin\Delta\omega_j t$, which adds a phase. We focus on the calculation of the decay amplitude, i.e. on the real part of the integral.

$$A = \int -cd\Omega(1 - \cos\Delta\omega_j t) = \int -2cd\Omega \sin^2\frac{\Delta\omega_j t}{2}. \tag{B.12}$$

Writing $\Delta\omega_j$ as $\eta(\theta_r)/r^3$ leads to

$$A = -4\pi c \int_0^\pi \sin\theta_r d\theta_r \int_0^\infty r^2 dr \sin^2\frac{\eta(\theta_r)t}{2r^3}. \tag{B.13}$$

At this point, it is worth noticing that this integral is independent of the sign of $\Delta\omega_j$ which means that it is the same if the spin j is up or down. Hence this calculation is independent of the spin polarization and of the spin temperature.

To integrate on r, we use the change of variable $x = |\eta(\theta_r)|t/(2r^3)$ to get

$$\int_0^\infty r^2 dr \sin^2 \frac{\eta(\theta_r)t}{2r^3} = \frac{|\eta(\theta_r)|t}{6} \int_0^\infty \frac{\sin^2 x}{x^2} dx = \frac{|\eta(\theta_r)|t}{6} \frac{\pi}{2}. \tag{B.14}$$

The integral over θ_r gives

$$\begin{aligned} \int_0^\pi \sin\theta_r |\eta(\theta_r)| d\theta_r &= \mu_B^2 \frac{\mu_0}{4\pi} \frac{g_{\text{eff,i}} g_{\text{eff,j}}}{2\hbar} \int_0^\pi \sin\theta_r \left|1 - 3\cos^2\theta_r\right| d\theta_r \\ &= \mu_B^2 \frac{\mu_0}{4\pi} \frac{g_{\text{eff,i}} g_{\text{eff,j}}}{2\hbar} \frac{8}{3\sqrt{3}}. \end{aligned} \tag{B.15}$$

Wrapping up,

$$A = -\frac{\pi \mu_0 \mu_B^2 g_{\text{eff,i}} g_{\text{eff,j}} c}{9\sqrt{3}\hbar} t, \tag{B.16}$$

and the FID signal is decaying with amplitude

$$|V_{\text{FID}}(t)| = \exp\left\{ -\frac{\pi \mu_0 \mu_B^2 g_{\text{eff,i}} g_{\text{eff,j}} c}{9\sqrt{3}\hbar} t \right\} \tag{B.17}$$

To obtain the shape of the spin line broadened by dipolar coupling, we take the Fourier transform of the FID decay. This operation gives a Lorentzian lineshape, of distribution

$$g(\Delta\omega) = \frac{1}{\pi} \frac{\Delta\omega_{dd}}{\Delta\omega^2 + \Delta\omega_{dd}^2}, \tag{B.18}$$

with HWHM $\Delta\omega_{dd} = \pi \mu_0 \mu_B^2 g_{\text{eff,i}} g_{\text{eff,j}} c/(9\sqrt{3}\hbar)$.

We call its FWHM Γ_{dd} (in angular frequency unit), which is given by

$$\boxed{\Gamma_{dd} = \frac{2\pi \mu_0 \mu_B^2 g_{\text{eff,i}} g_{\text{eff,j}} c}{9\sqrt{3}\hbar}.} \tag{B.19}$$

2.3 Spin dynamics and spin flip probability

This dipolar linewidth is a static property, where the frequency of each spin is shifted due to its dipolar coupling with neighboring electron spins. This dipolar coupling makes also the central spin sensitive to all spin dynamics in its environment, which will therefore affect any echo decay, depending on the number of spin flips during the pulse sequence time. Here, we thus move to spin dynamics and calculate the signal amplitude due to spin flips in the bath.

Beforehand, the probability of a spin flip during a time interval T needs to be calculated. This is done by Bai and Fayer ([BF89], Appendix A). We consider only electron spins $S = 1/2$. Each spin has two energy levels, the ground state $|g\rangle$ and the excited state $|e\rangle$. The population of each level will go back to equilibrium following the equations

$$\begin{aligned} \frac{dn_{|g\rangle}}{dt} &= -R_\uparrow n_{|g\rangle} + R_\downarrow n_{|e\rangle} \\ \frac{dn_{|e\rangle}}{dt} &= -R_\downarrow n_{|e\rangle} + R_\uparrow n_{|g\rangle}, \end{aligned} \tag{B.20}$$

where $R_\uparrow$ is the spin flip rate from $|g\rangle$ to $|e\rangle$ and $R_\downarrow$ is the spin flip rate from $|e\rangle$ to $|g\rangle$.

The difference in population evolves as

$$\begin{aligned} \frac{dn_{|g\rangle} - n_{|e\rangle}}{dt} &= -2R_\uparrow n_{|g\rangle} + 2R_\downarrow n_{|e\rangle} \\ &= -(R_\uparrow + R_\downarrow)(n_{|g\rangle} - n_{|e\rangle}) - (R_\uparrow - R_\downarrow)(n_{|g\rangle} + n_{|e\rangle}). \end{aligned} \tag{B.21}$$

We call $R = R_\uparrow + R_\downarrow$. The total population is fixed with $N = n_{|g\rangle} + n_{|e\rangle}$. Moreover, solving the equation at equilibrium gives $R_\uparrow N_{|g\rangle,eq} = R_\downarrow N_{|e\rangle,eq}$ so $(N_{|g\rangle,eq} - N_{|e\rangle,eq})/(N_{|g\rangle,eq} + N_{|e\rangle,eq}) = (R_\downarrow - R_\uparrow)/(R_\uparrow + R_\downarrow)$.

Using all this information leads to

$$\frac{dn_{|g\rangle} - n_b}{dt} = -R[(n_{|g\rangle} - n_b) - (N_{|g\rangle,eq} - N_{b,eq})], \tag{B.22}$$

which solution is

$$n_{|g\rangle}(t) - n_{|e\rangle}(t) = N_{|g\rangle,eq} - N_{|e\rangle,eq} + e^{-Rt}[(n_{|g\rangle,0} - n_{|e\rangle,0}) - (N_{|g\rangle,eq} - N_{|e\rangle,eq})]. \tag{B.23}$$

Now the question is the following: what is the probability that a spin flips during the interval T? The spin can flip multiple times, what matters is its initial and final states.

We consider the density of probability to be in state $|g\rangle$ or $|e\rangle$, $\rho_{|g\rangle} = n_{|g\rangle}/N$ and $\rho_{|e\rangle} = n_{|e\rangle}/N$.

The probably that a spin flips from the ground state to the excited state is

$$P_{flip,\uparrow} = P(\rho_{|g\rangle}(0) = 1 \cap \rho_{|e\rangle}(T) = 1) = P(\rho_{|g\rangle}(0) = 1)P(\rho_{|e\rangle}(T) = 1|\rho_{|g\rangle}(0) = 1). \tag{B.24}$$

The first term is simply given by the probability of being in the groud state at equilibrium, $P(\rho_{|g\rangle}(0) = 1) = \rho_{|g\rangle,eq}$.

The second term requires to calculate $\rho_{|e\rangle}(T)$ knowing that $\rho_{|g\rangle}(0) = 1$,

$$\rho_{|g\rangle} - \rho_{|e\rangle} = 1 - 2\rho_{|e\rangle} = (\rho_{|g\rangle,eq} - \rho_{b,eq}) + e^{-RT}[1 - (\rho_{|g\rangle,eq} - \rho_{|e\rangle,eq})], \tag{B.25}$$

which simplifies into

$$\rho_{|e\rangle}(T) = \rho_{|e\rangle,eq}(1 - e^{-RT}). \tag{B.26}$$

Therefore, $P(\rho_{|e\rangle}(T) = 1|\rho_{|g\rangle}(0) = 1) = \rho_{|e\rangle,eq}(1 - e^{-RT})$.

In the end,

$$P_{flip,\uparrow} = \rho_{|g\rangle,eq}\rho_{|e\rangle,eq}(1 - e^{-RT}), \tag{B.27}$$

and the symmetry of in $|g\rangle$ and $|e\rangle$ in this equation implies that $P_{flip,\uparrow} = P_{flip,\downarrow}$.

This probability can be simplified further with the expression of the equilibrium populations,

$$\begin{aligned}
\rho_{|g\rangle,eq} &= \frac{e^{\frac{\Delta E}{2k_BT}}}{e^{\frac{\Delta E}{2k_BT}} + e^{-\frac{\Delta E}{2k_BT}}} \\
\rho_{|e\rangle,eq} &= \frac{e^{-\frac{\Delta E}{2k_BT}}}{e^{\frac{\Delta E}{2k_BT}} + e^{-\frac{\Delta E}{2k_BT}}} \\
\rho_{|g\rangle,eq}\rho_{|e\rangle,eq} &= \frac{1}{\left(e^{\frac{\Delta E}{2k_BT}} + e^{-\frac{\Delta E}{2k_BT}}\right)^2} = \frac{1}{4}\operatorname{sech}^2\frac{\Delta E}{2k_BT}.
\end{aligned} \tag{B.28}$$

Finally, the spin flip probability is

$$\boxed{P_{flip}(T) = P_{flip,\uparrow}(T) = P_{flip,\downarrow}(T) = \frac{1}{4}\operatorname{sech}^2\frac{\Delta E}{2k_BT}\left(1 - e^{-RT}\right).} \tag{B.29}$$

2.4 Spectral diffusion in three-pulse echo experiments

The three pulse echo (3PE) sequence is a succession of three $\pi/2$ pulses. The first pulse lets the spins acquire a phase during time τ. Then the second pulse stores the spin state on the quantization axis for a time T_w, which can be as long as the spin-lattice relaxation time T_1. Finally the last pulse produces an echo after a time τ. The interest of the three pulse echo sequence is that it is sensitive to fluctuations on the time scale T_w which is typically $\gg \tau$. Hence it can probe much slower fluctuations than the usual two pulse echo sequence.

The amplitude of the echo, occurring at time $t = 2\tau + T_w$ after the initial pulse, is given by

$$\begin{aligned} V(2\tau + T_w) &= \langle e^{\sum i\phi_j} \rangle_{\text{distribution of spins j, history of perturbation}} \\ \phi_j &= \int_0^{\tau} \Delta\omega_j(t)dt - \int_{\tau+T_w}^{2\tau+T_w} \Delta\omega_j(t)dt \end{aligned} \tag{B.30}$$

Spin flips are modelled by "sudden jumps": the spin j flips suddenly from $+1/2$ to $-1/2$, such that

$$\phi_j = \Delta\omega_j \left[\int_0^{\tau} h(t)dt - \int_{\tau+T_w}^{2\tau+T_w} h(t)dt \right], \tag{B.31}$$

where h takes two values, ± 1.

If the perturbers j can be taken as statistically independent, the sum can be taken again out of the average,

$$V(2\tau + T_w) = \prod \langle e^{i\phi_j} \rangle_{\text{distribution of spins j, history of perturbation}} \tag{B.32}$$

Note that the hypothesis of independent spins is true if the spin flip originates from spin-lattice relaxation but it is false if neighboring spins exchange their spin (flip-flop). So far we did not find any theory paper discussing the particular flip-flop problem.

We start by averaging over the history of the perturbation. If the spin flip rate R is small, $R\tau \ll 1$, and $T_w \gg \tau$, the spin flips mainly during the time interval T_w. All the spin flips during time interval τ are neglected.

Three scenarios are possible:

- the spin flips from up to down: $\phi_j = 2\Delta\omega_j\tau$ with probability $P_{flip}(T_w)$,
- the spin flips from down to up: $\phi_j = -2\Delta\omega_j\tau$ with probability $P_{flip}(T_w)$,
- no spin flip during T_w: ϕ_j=0 with probability $1 - 2P_{flip}(T_w)$.

Therefore, the average of the history of the perturbation is

$$\langle e^{i\phi_j} \rangle_{\text{history of perturbation}} = 1 - 2P_{flip}(1 - \cos 2\Delta\omega_j\tau) = 1 - 4P_{flip} \sin^2 \Delta\omega_j\tau. \tag{B.33}$$

Then we average over the distribution of perturbing spins j in a small volume $d\Omega$,

$$\langle e^{i\phi_j} \rangle = (1 - cd\Omega) + cd\Omega(1 - 4P_{flip} \sin^2 \Delta\omega_j\tau) = 1 - cd\Omega 4P_{flip} \sin^2 \Delta\omega_j\tau. \tag{B.34}$$

We use the same trick as previously with the logarithm,

$$\begin{aligned} \ln V(\tau, T_w) &= \sum \ln \langle e^{i\phi_j} \rangle \\ \ln V(\tau, T_w) &\sim \sum -4cd\Omega P_{flip} \sin^2 \Delta\omega_j\tau \\ V(\tau, T_w) &\sim \exp\left\{ \int -4cd\Omega P_{flip} \sin^2 \Delta\omega_j\tau \right\}. \end{aligned} \tag{B.35}$$

This integral can be calculated as

$$A = \int -4cd\Omega P_{flip} \sin^2 \Delta\omega_j \tau = -4cP_{flip} 2\pi \int_0^\pi \sin\theta_r d\theta_r \int_0^\infty r^2 dr \sin^2 \frac{\eta(\theta_r)\tau}{r^3}. \quad \text{(B.36)}$$

For the integral over r, we use the change of variable $x = |\eta(\theta_r)|\tau/r^3$,

$$\int_0^\infty r^2 dr \sin^2 \frac{\eta(\theta_r)\tau}{r^3} = \frac{|\eta(\theta_r)|\tau}{3} \int_0^\infty \frac{\sin^2 x}{x^2} dx = \frac{|\eta(\theta_r)|\tau}{3} \frac{\pi}{2}. \quad \text{(B.37)}$$

The integral over θ_r gives

$$\int_0^\pi \sin\theta_r |\eta(\theta_r)| d\theta_r = \frac{\mu_B^2 g_{\text{eff},i} g_{\text{eff},j}}{2\hbar} \int_0^\pi \sin\theta \left|1 - 3\cos^2\theta\right| d\theta = \frac{\mu_0}{4\pi} \frac{\mu_B^2 g_{\text{eff},i} g_{\text{eff},j}}{2\hbar} \frac{8}{3\sqrt{3}} \quad \text{(B.38)}$$

Summing up,

$$A = -P_{flip} c \frac{4\pi\mu_0 \mu_B^2 g_{\text{eff},i} g_{\text{eff},j}}{9\sqrt{3}\hbar} \tau. \quad \text{(B.39)}$$

Replacing P_{flip} with Equation B.29 gives

$$\begin{aligned} A &= -c \frac{\pi\mu_0 \mu_B^2 g_{\text{eff},i} g_{\text{eff},j} \tau}{9\sqrt{3}\hbar} \operatorname{sech}^2 \frac{\Delta E}{2k_B T} (1 - e^{-RT_w}) \\ &= -\frac{\Gamma_{\text{SD}}}{2} \tau (1 - e^{-RT_w}), \end{aligned} \quad \text{(B.40)}$$

where Γ_{SD} is the spectral diffusion linewidth defined by

$$\Gamma_{\text{SD}} = \Gamma_{dd} \operatorname{sech}^2 \frac{\Delta E}{2k_B T}. \quad \text{(B.41)}$$

Finally,

$$\boxed{V(2\tau + T_w) = \exp\left\{-\frac{\Gamma_{\text{SD}}}{2}\tau \left(1 - e^{-RT_w}\right)\right\}.} \quad \text{(B.42)}$$

2.5 Spectral diffusion in two pulse echo experiments

The two pulse echo (2PE) sequence is a succession of a $\pi/2$ pulse and a π pulse, separated by time τ. At time 2τ, the spins refocus and produce an echo. The decay of this echo with 2τ gives directly the coherence time T_2.

The 2PE experiment is actually a particular case of the 3PE, when $T_w = 0$. In this case, the term which was derived in the previous section vanishes. However, there is still a signature of spectral diffusion in the 2PE decay. To see it, we need to consider spin flips during the τ intervals, always in the limit of less than a spin flip during time τ ($R\tau \ll 1$).

Again we have to calculate

$$\begin{aligned} V(2\tau) &= \langle e^{\sum i\phi_j} \rangle_{\text{distribution of spins j, history of perturbation}} \\ \phi_j &= \Delta\omega_j [\int_0^\tau h(t)dt - \int_\tau^{2\tau} h(t)dt], \end{aligned} \quad \text{(B.43)}$$

where h takes two values: ± 1 and a perturbing spin jumps at maximum once during its history.

Five scenarios are possible:

- the spin flips downwards between t_1 and $t_1 + dt$, where $0 < t_1 < \tau$: $\phi_j = 2\Delta\omega_j t_1$ with probability $P_{flip}(dt)$,
- the spin flips upwards between t_1 and $t_1 + dt$, where $0 < t_1 < \tau$: $\phi_j = -2\Delta\omega_j t_1$ with probability $P_{flip}(dt)$,
- the spin flips downwards between t_2 and $t_2 + dt$, where $\tau < t_2 < 2\tau$: $\phi_j = 2\Delta\omega_j(\tau - t_2)$ with probability $P_{flip}(dt)$,
- the spin flips upwards between t_2 and $t_2 + dt$, where $\tau < t_2 < 2\tau$: $\phi_j = -2\Delta\omega_j(\tau - t_2)$ with probability $P_{flip}(dt)$,
- no spin flip: $\phi_j = 0$ with probability $1 - \sum_{0<t<2\tau} 2P_{flip}(dt)$.

Moreover, the spin flip probability during the small time interval dt is

$$P_{flip}(dt) = \frac{1}{4}\operatorname{sech}^2\frac{\Delta E}{2k_BT}\left(1 - e^{-Rdt}\right) \sim \frac{1}{4}\operatorname{sech}^2\frac{\Delta E}{2k_BT}Rdt. \tag{B.44}$$

First, we average over the spin history,

$$\begin{aligned}
\langle e^{i\phi_j}\rangle_{\text{spin history}} &= \left(1 - \int_0^{2\tau} 2P_{flip}(dt)\right) + \int_0^{\tau} P_{flip}(dt)\left[e^{2i\Delta\omega_j t} + e^{-2i\Delta\omega_j t}\right] + \\
&\quad \int_{\tau}^{2\tau} P_{flip}(dt)\left[e^{2i\Delta\omega_j(\tau-t)} + e^{-2i\Delta\omega_j(\tau-t)}\right] \\
&= \left(1 - \int_0^{2\tau} 2P_{flip}(dt)\right) + 2\int_0^{\tau} P_{flip}(dt) 2\cos 2\Delta\omega_j t \\
&= \left(1 - R\tau\operatorname{sech}^2\frac{\Delta E}{2k_BT}\right) + \operatorname{sech}^2\frac{\Delta E}{2k_BT}R\int_0^{\tau}\cos 2\Delta\omega_j t \\
&= \left(1 - R\tau\operatorname{sech}^2\frac{\Delta E}{2k_BT}\right) + \operatorname{sech}^2\frac{\Delta E}{2k_BT}R\tau\frac{\sin 2\Delta\omega_j\tau}{2\Delta\omega_j\tau} \\
&= 1 - R\tau\operatorname{sech}^2\frac{\Delta E}{2k_BT}\left(1 - \frac{\sin 2\Delta\omega_j\tau}{2\Delta\omega_j\tau}\right).
\end{aligned} \tag{B.45}$$

Now we average over the spin distribution in a small volume $d\Omega$,

$$\begin{aligned}
\langle e^{i\phi_j}\rangle_{\text{spin history, distribution of perturbers}} &= (1 - cd\Omega) + cd\Omega\left[1 - R\tau\operatorname{sech}^2\frac{\Delta E}{2k_BT}\left(1 - \frac{\sin 2\Delta\omega_j\tau}{2\Delta\omega_j\tau}\right)\right] \\
&= 1 - cd\Omega R\tau\operatorname{sech}^2\frac{\Delta E}{2k_BT}\left(1 - \frac{\sin 2\Delta\omega_j\tau}{2\Delta\omega_j\tau}\right).
\end{aligned} \tag{B.46}$$

We linearize due to the low concentration,

$$\begin{aligned}
\ln V(2\tau) &= \sum \ln\langle e^{i\phi_j}\rangle \sim \sum -cd\Omega R\tau\operatorname{sech}^2\frac{\Delta E}{2k_BT}\left(1 - \frac{\sin 2\Delta\omega_j\tau}{2\Delta\omega_j\tau}\right) \\
V(2\tau) &\sim \exp\left\{-\int cd\Omega R\tau\operatorname{sech}^2\frac{\Delta E}{2k_BT}\left(1 - \frac{\sin 2\Delta\omega_j\tau}{2\Delta\omega_j\tau}\right)\right\}.
\end{aligned} \tag{B.47}$$

Let's focus on the integral

$$\begin{aligned}
A &= \int cd\Omega R\tau\operatorname{sech}^2\frac{\Delta E}{2k_BT}\left(1 - \frac{\sin 2\Delta\omega_j\tau}{2\Delta\omega_j\tau}\right) \\
&= cR\tau\operatorname{sech}^2\frac{\Delta E}{2k_BT}2\pi\int_0^{\pi}\sin\theta_r d\theta_r\int_0^{\infty} r^2 dr\left(1 - \frac{\sin\frac{2\eta(\theta_r)\tau}{r^3}}{\frac{2\eta(\theta_r)\tau}{r^3}}\right)
\end{aligned} \tag{B.48}$$

To integrate over r, we use the change of variable $x = 2|\eta|\tau/r^3$,

$$\int_0^\infty r^2 dr \left(1 - \frac{\sin\frac{2\eta(\theta_r)\tau}{r^3}}{\frac{2\eta(\theta_r)\tau}{r^3}}\right) = \frac{2|\eta|\tau}{3}\int_0^\infty \left(1 - \frac{\sin x}{x}\right)\frac{1}{x^2}dx = \frac{2|\eta|\tau}{3}\frac{\pi}{4}. \tag{B.49}$$

Again, the integral over θ_r gives

$$\int_0^\pi \sin\theta_r |\eta(\theta_r)| d\theta_r = \frac{\mu_B^2 g_{\text{eff,i}} g_{\text{eff,j}}}{2\hbar}\int_0^\pi \sin\theta \left|1 - 3\cos^2\theta\right| d\theta = \frac{\mu_0}{4\pi}\frac{\mu_B^2 g_{\text{eff,i}} g_{\text{eff,j}}}{2\hbar}\frac{8}{3\sqrt{3}}. \tag{B.50}$$

Wrapping up:

$$A = cR\tau^2 \frac{\pi\mu_0\mu_B^2 g_{\text{eff,i}} g_{\text{eff,j}}}{9\sqrt{3}\hbar}\operatorname{sech}^2\frac{\Delta E}{2k_B T} = \frac{\Gamma_{SD} R}{2}\tau^2. \tag{B.51}$$

Finally,

$$\boxed{V(2\tau) = \exp\left\{-\frac{\Gamma_{\text{SD}} R}{2}\tau^2\right\}.} \tag{B.52}$$

2.6 Summary and open questions

The two previous results of Equation B.52 and Equation B.42 can be combined to get a more general expression of the echo decay, valid for both two and three pulse echoes, in the limit of $R\tau \ll 1$,

$$\boxed{V(2\tau + T_w) = V_0 \exp\left\{-\frac{T_w}{T_1}\right\}\exp\left\{-\tau\left[\Gamma_0 + \frac{\Gamma_{\text{SD}}}{2}\left(R\tau + 1 - e^{-RT_w}\right)\right]\right\},} \tag{B.53}$$

where Γ_0 is the linewidth which includes all dephasing effects except for spectral diffusion, like instantaneous diffusion or relaxation. All linewidths and rates are expressed in rad.s^{-1} and s^{-1} respectively. The T_1 term describes the spin-lattice relaxation which happens during the interval T_w as it can be of the order of T_1. This formula can be found in the literature, for instance in [Böt+06].

Remarks and open questions:

- This derivation assumes that the perturbing spins are statistically independent. Spins flip for two main reasons: spin-lattice relaxation with rate $1/T_1$ or flip-flops where two resonant neighboring ions exchange their spins. In case of spin-flips due to spin-lattice relaxation, the perturbing spins can indeed be considered as independent. However, for flip-flops, pairs of spins need to be considered. Indeed, if two spins, quite far away from the probed spin, exchange their spin, the probed spin will not see any change in its local magnetic field. In the work of Böttger *et. al.*, the formula above is nevertheless applied also for flip-flops [Böt+06] and this is what we do in our analysis of spectral diffusion in Chapter 11.
- Another open question is related to the treatment of the inhomogeneous spin line. We know from Section 2.5 that the inhomogeneous linewidth is caused by charge defects in the crystal. Here, we make the assumption that there is no correlation between the spin frequency and its distance from a crystal defect. However, correlations could affect the flip-flop dynamics because two nearby spins would be more likely to be resonant.

Bibliography

[AB12] A. Abragam and B. Bleaney. *Electron Paramagnetic Resonance of Transition Ions*. OUP Oxford, June 2012 (cit. on pp. 23, 29, 30, 32, 33, 35, 36, 38, 39).

[Abe+11] Eisuke Abe et al. "Electron spin ensemble strongly coupled to a three-dimensional microwave cavity". In: *Applied Physics Letters* 98.25 (June 2011), p. 251108 (cit. on p. 58).

[Abr61] A. Abragam. *The Principles of Nuclear Magnetism*. Clarendon Press, 1961 (cit. on pp. 37, 54, 179).

[Afz+13] M. Afzelius et al. "Proposal for a coherent quantum memory for propagating microwave photons". In: 15.6 (June 2013), p. 065008 (cit. on pp. 2, 12, 175).

[Alb+20] B. Albanese et al. "Radiative cooling of a spin ensemble". In: *Nature Physics* 16.7 (July 2020), pp. 751–755 (cit. on pp. 133, 158).

[Alb+21] Emanuele Albertinale et al. "Detecting spins by their fluorescence with a microwave photon counter". In: *Nature* 600.7889 (2021), pp. 434–438 (cit. on p. 176).

[Ant+68] AA Antipin et al. "Paramagnetic resonance and spin-lattice relaxation of Er^{3+} and Tb^{3+} ions in crystal lattice of $CaWO_4$". In: *Soviet physics solid state, USSR* 10.2 (1968), pp. 468–+ (cit. on pp. 40, 41, 131).

[Ant+81] A.A. Antipin et al. "Anisotropy of Er^{3+} spin-lattice relaxation in $LiYF_4$ crystals". In: *Fizika Tverdogo Tela* 23.9 (1981), pp. 2700–2707 (cit. on pp. 131, 132).

[Aru+19] Frank Arute et al. "Quantum supremacy using a programmable superconducting processor". In: *Nature* 574.7779 (Oct. 2019), pp. 505–510 (cit. on pp. 1, 11).

[Bar+13] N. Bar-Gill et al. "Solid-state electronic spin coherence time approaching one second". In: *Nature Communications* 4.1 (Apr. 2013), p. 1743 (cit. on pp. 2, 12).

[Ber+07] S. Bertaina et al. "Rare-earth solid-state qubits". In: *Nature Nanotechnology* 2.1 (Jan. 2007), pp. 39–42 (cit. on pp. 2, 3, 12, 13, 31, 32, 34, 78, 117).

[Ber+09] S. Bertaina et al. "Spin-Orbit Qubits of Rare-Earth-Metal Ions in Axially Symmetric Crystal Fields". In: *Physical Review Letters* 103.22 (Nov. 2009), p. 226402 (cit. on pp. 30, 32).

[BF67] W. S. Brower and P. H. Fang. "Dielectric Constants of $PbWO_4$ and $CaWO_4$". In: *Journal of Applied Physics* 38.5 (Apr. 1967), pp. 2391–2392 (cit. on p. 90).

[BF89] Y. S. Bai and M. D. Fayer. "Time scales and optical dephasing measurements: Investigation of dynamics in complex systems". In: *Physical Review B* 39.15 (May 1989), pp. 11066–11084 (cit. on pp. 71, 181).

[Bie+16a] A. Bienfait et al. "Controlling spin relaxation with a cavity". In: *Nature* 531.7592 (Mar. 2016), pp. 74–77 (cit. on pp. 8, 17, 53, 54).

[Bie+16b] A. Bienfait et al. “Reaching the quantum limit of sensitivity in electron spin resonance”. In: *Nature Nanotechnology* 11.3 (Mar. 2016), pp. 253–257 (cit. on pp. 3, 13, 45, 97).

[Bie16] Audrey Bienfait. “Magnetic resonance with quantum microwaves”. PhD thesis. Université Paris-Saclay, Oct. 2016 (cit. on p. 97).

[Böt+06] Thomas Böttger et al. “Optical decoherence and spectral diffusion at 1.5 μm in Er^{3+}:Y_2SiO_5 versus magnetic field, temperature, and Er^{3+} concentration”. In: *Physical Review B* 73.7 (Feb. 2006), p. 075101 (cit. on pp. 71–73, 170, 186).

[Böt+09] Thomas Böttger et al. “Effects of magnetic field orientation on optical decoherence in Er^{3+}:Y_2SiO_5”. In: *Physical Review B* 79.11 (Mar. 2009), p. 115104 (cit. on pp. 72, 80, 126).

[Car+18] B. Car et al. “Selective Optical Addressing of Nuclear Spins through Superhyperfine Interaction in Rare-Earth Doped Solids”. In: *Physical Review Letters* 120.19 (May 2018), p. 197401 (cit. on p. 77).

[Car+19] B. Car et al. “Optical study of the anisotropic erbium spin flip-flop dynamics”. In: *Physical Review B* 100.16 (Oct. 2019), p. 165107 (cit. on p. 72).

[Car+89] W. T. Carnall et al. “A systematic analysis of the spectra of the lanthanides doped into single crystal LaF_3”. In: *The Journal of Chemical Physics* 90.7 (Apr. 1989), pp. 3443–3457 (cit. on p. 28).

[CG84] M. J. Collett and C. W. Gardiner. “Squeezing of intracavity and traveling-wave light fields produced in parametric amplification”. In: *Physical Review A* 30.3 (Sept. 1984), pp. 1386–1391 (cit. on p. 49).

[Che+20] Songtao Chen et al. “Parallel single-shot measurement and coherent control of solid-state spins below the diffraction limit”. In: *Science* 370.6516 (Oct. 2020), pp. 592–595 (cit. on pp. 2, 12, 176).

[Che+21a] Qi-Ming Chen et al. “The scattering coefficients of superconducting microwave resonators: I. Transfer-matrix approach”. In: *arXiv:2109.07762 [cond-mat, physics:quant-ph]* (Sept. 2021) (cit. on p. 47).

[Che+21b] Qi-Ming Chen et al. “The scattering coefficients of superconducting microwave resonators: II. System-bath approach”. In: *arXiv:2109.07766 [cond-mat, physics:quant-ph]* (Sept. 2021) (cit. on pp. 49, 50).

[CTM97] R. F. C. Claridge, W. C. Tennant, and D. G. McGavin. “X-band EPR of $Fe^{3+}/CaWO_4$ at 10K: Evidence for large magnitude high spin Zeeman interactions”. In: *Journal of Physics and Chemistry of Solids* 58.5 (May 1997), pp. 813–820 (cit. on p. 31).

[Dev+95] Michel H Devoret et al. “Quantum fluctuations in electrical circuits”. In: *Les Houches, Session LXIII* 7.8 (1995), pp. 133–135 (cit. on p. 48).

[Din+11] I. Diniz et al. “Strongly coupling a cavity to inhomogeneous ensembles of emitters: Potential for long-lived solid-state quantum memories”. In: *Physical Review A* 84.6 (Dec. 2011), p. 063810 (cit. on pp. 57, 58).

[Dol20] Gavin Patrick Dold. “milliKelvin ESR of rare-earth doped crystals using superconducting resonators”. PhD thesis. UCL (University College London), 2020 (cit. on p. 79).

[EL13] Andreas Erb and Jean-Côme Lanfranchi. "Growth of high-purity scintillating $CaWO_4$ single crystals for the low-temperature direct dark matter search experiments CRESST-II and EURECA". In: *CrystEngComm* 15.12 (2013), pp. 2301–2304 (cit. on p. 83).

[Enr71] Bernal G. Enrique. "Optical Spectrum and Magnetic Properties of Er3+ in CaWO4". In: *The Journal of Chemical Physics* 55.5 (Sept. 1971), pp. 2538–2549 (cit. on p. 27).

[Fer+15] Xavier Fernandez-Gonzalvo et al. "Coherent frequency up-conversion of microwaves to the optical telecommunications band in an Er:YSO crystal". In: *Physical Review A* 92.6 (Dec. 2015), p. 062313 (cit. on pp. 2, 3, 12, 13).

[FH62] P. A. Forrester and C. F. Hempstead. "Paramagnetic Resonance of Tb^{3+} Ions in $CaWO_4$ and CaF_2". In: *Physical Review* 126.3 (May 1962), pp. 923–930 (cit. on pp. 84, 85, 105).

[FW62] A. J. Freeman and R. E. Watson. "Theoretical Investigation of Some Magnetic and Spectroscopic Properties of Rare-Earth Ions". In: *Physical Review* 127.6 (Sept. 1962), pp. 2058–2075 (cit. on pp. 24, 26).

[GC85] C. W. Gardiner and M. J. Collett. "Input and output in damped quantum systems: Quantum stochastic differential equations and the master equation". In: *Physical Review A* 31.6 (June 1985), pp. 3761–3774 (cit. on p. 49).

[GKT78] R. M. Golding, M. Kestigian, and C. W. Tennant. "EPR of high-spin Fe^{3+} in calcium tungstate, $CaWO_4$". In: *Journal of Physics C: Solid State Physics* 11.24 (Dec. 1978), pp. 5041–5049 (cit. on pp. 31, 84, 85).

[GM64] C. G. B. Garrett and F. R. Merritt. "PMR spectra of Nd^{3+} in compensated and uncompensated $CaWO_4$". In: *Applied Physics Letters* 4.2 (Jan. 1964), pp. 31–32 (cit. on pp. 31, 84).

[Gri99] David J. Griffiths. *Introduction to electrodynamics*. Prentice-Hall, Upper Saddle River, New Jersey, 1999 (cit. on p. 52).

[HB60] C. F. Hempstead and K. D. Bowers. "Paramagnetic Resonance of Impurities in $CaWO_4$. I. Two S-State Ions". In: *Physical Review* 118.1 (Apr. 1960), pp. 131–134 (cit. on pp. 87, 151).

[Hea+08] J. E. Healey et al. "Magnetic field tuning of coplanar waveguide resonators". In: *Applied Physics Letters* 93.4 (July 2008), p. 043513 (cit. on pp. 109, 155).

[HH74] P. Hu and S. R. Hartmann. "Theory of spectral diffusion decay using an uncorrelated-sudden-jump model". In: *Physical Review B* 9.1 (Jan. 1974), pp. 1–13 (cit. on p. 71).

[HR06] Serge Haroche and J.-M. Raimond. *Exploring the Quantum: Atoms, Cavities, and Photons*. OUP Oxford, Aug. 2006 (cit. on pp. 52, 53).

[JM12a] B. Julsgaard and K. Mølmer. "Reflectivity and transmissivity of a cavity coupled to two-level systems: Coherence properties and the influence of phase decay". In: *Physical Review A* 85.1 (Jan. 2012), p. 013844 (cit. on p. 58).

[JM12b] Brian Julsgaard and Klaus Mølmer. "Measurement-induced two-qubit entanglement in a bad cavity: Fundamental and practical considerations". In: *Physical Review A* 85.3 (Mar. 2012), p. 032327 (cit. on p. 54).

[KA62] J. R. Klauder and P. W. Anderson. "Spectral Diffusion Decay in Spin Resonance Experiments". In: *Physical Review* 125.3 (Feb. 1962), pp. 912–932 (cit. on p. 69).

[Kan+21] Shun Kanai et al. “Generalized scaling of spin qubit coherence in over 12,000 host materials”. In: *arXiv:2102.02986 [quant-ph]* (Feb. 2021) (cit. on pp. 74, 75).

[KI92] Vadim V Kurshev and Tsuneki Ichikawa. “Effect of spin flip-flop on electron-spin-echo decay due to instantaneous diffusion”. In: *Journal of Magnetic Resonance (1969)* 96.3 (Feb. 1992), pp. 563–573 (cit. on p. 76).

[Kie66] A. Kiel. “Theory of Electric Shifts of the Optical and Magnetic Resonance Properties of Paramagnetic Ions in Crystals”. In: *Physical Review* 148.1 (Aug. 1966), pp. 247–256 (cit. on p. 43).

[Kin+20] Jonathan M. Kindem et al. “Control and single-shot readout of an ion embedded in a nanophotonic cavity”. In: *Nature* 580.7802 (Apr. 2020), pp. 201–204 (cit. on p. 176).

[Kol+12] R. Kolesov et al. “Optical detection of a single rare-earth ion in a crystal”. In: *Nature Communications* 3.1 (Aug. 2012), p. 1029 (cit. on p. 176).

[Kra30] HA Kramers. “General theory of paramagnetic rotation in crystals”. In: *Proc. Acad. Sci. Amsterdam.* Vol. 33. 1930, p. 959 (cit. on p. 27).

[Kub+10] Y. Kubo et al. “Strong Coupling of a Spin Ensemble to a Superconducting Resonator”. In: *Physical Review Letters* 105.14 (Sept. 2010), p. 140502 (cit. on pp. 60, 114).

[Kub+11] Y. Kubo et al. “Hybrid Quantum Circuit with a Superconducting Qubit Coupled to a Spin Ensemble”. In: *Physical Review Letters* 107.22 (Nov. 2011), p. 220501 (cit. on pp. 2, 12).

[KWM11] Z. Kurucz, J. H. Wesenberg, and K. Mølmer. “Spectroscopic properties of inhomogeneously broadened spin ensembles in a cavity”. In: *Physical Review A* 83.5 (May 2011), p. 053852 (cit. on p. 57).

[Li+20] Pei-Yun Li et al. “Hyperfine Structure and Coherent Dynamics of Rare-Earth Spins Explored with Electron-Nuclear Double Resonance at Subkelvin Temperatures”. In: *Physical Review Applied* 13.2 (Feb. 2020), p. 024080 (cit. on pp. 3, 13, 79, 117).

[LJ06] Guokui Liu and Bernard Jacquier. *Spectroscopic Properties of Rare Earths in Optical Materials*. Springer Science & Business Media, Jan. 2006 (cit. on pp. 23, 24, 27).

[LJ66a] G. H. Larson and C. D. Jeffries. “Spin-Lattice Relaxation in Some Rare-Earth Salts. I. Temperature Dependence”. In: *Physical Review* 141.1 (Jan. 1966), pp. 461–478 (cit. on p. 39).

[LJ66b] G. H. Larson and C. D. Jeffries. “Spin-Lattice Relaxation in Some Rare-Earth Salts. II. Angular Dependence, Hyperfine Effects, and Cross Relaxation”. In: *Physical Review* 145.1 (May 1966), pp. 311–324 (cit. on p. 39).

[Ma+14] Wen-Long Ma et al. “Uncovering many-body correlations in nanoscale nuclear spin baths by central spin decoherence”. In: *Nature Communications* 5.1 (Sept. 2014), p. 4822 (cit. on pp. 74, 126, 134).

[Mac+15] C. Macklin et al. “A near–quantum-limited Josephson traveling-wave parametric amplifier”. In: *Science* 350.6258 (Oct. 2015), pp. 307–310 (cit. on p. 98).

[MDS82] A. G Maryasov, S. A Dzuba, and K. M Salikhov. "Spin-polarization effects on the phase relaxation induced by dipole-dipole interactions". In: *Journal of Magnetic Resonance (1969)* 50.3 (Dec. 1982), pp. 432–450 (cit. on pp. 42, 179).

[MG66] W. B. Mims and R. Gillen. "Broadening of Paramagnetic-Resonance Lines by Internal Electric Fields". In: *Physical Review* 148.1 (Aug. 1966), pp. 438–443 (cit. on pp. 43, 44, 111).

[MG67] W. B. Mims and R. Gillen. "Local Electric Fields and the Paramagnetic Resonance of Charge-Compensated Sites in (Ca, Ce)WO_4". In: *The Journal of Chemical Physics* 47.9 (Nov. 1967), pp. 3518–3532 (cit. on pp. 30, 31).

[Mim65] W. B. Mims. "Electric Field Shift in Paramagnetic Resonance for Four Ions in a Calcium Tungstate Lattice". In: *Physical Review* 140.2A (Oct. 1965), A531–A535 (cit. on pp. 32, 43, 111).

[Mim68] W. B. Mims. "Phase Memory in Electron Spin Echoes, Lattice Relaxation Effects in $CaWO_4$: Er, Ce, Mn". In: *Physical Review* 168.2 (Apr. 1968), pp. 370–389 (cit. on p. 69).

[MNM61] W. B. Mims, K. Nassau, and J. D. McGee. "Spectral Diffusion in Electron Resonance Lines". In: *Physical Review* 123.6 (Sept. 1961), pp. 2059–2069 (cit. on p. 69).

[Moo06] Gordon E. Moore. "Cramming more components onto integrated circuits, Reprinted from Electronics, volume 38, number 8, April 19, 1965, pp.114 ff." In: *IEEE Solid-State Circuits Society Newsletter* 11.3 (Sept. 2006), pp. 33–35 (cit. on pp. 1, 11).

[MT85] D. G McGavin and W. C Tennant. "EPR study of high-spin ferric ion in a completely rhombic environment. Fe^{3+} in $CaWO_4$". In: *Journal of Magnetic Resonance (1969)* 61.2 (Feb. 1985), pp. 321–332 (cit. on p. 31).

[Ort+18] Antonio Ortu et al. "Simultaneous coherence enhancement of optical and microwave transitions in solid-state electronic spins". In: *Nature Materials* 17.8 (Aug. 2018), pp. 671–675 (cit. on p. 80).

[OSu+21] James O'Sullivan et al. "Random-access quantum memory using chirped pulse phase encoding". In: *arXiv:2103.11697 [quant-ph]* (Aug. 2021) (cit. on p. 61).

[Pla+12] Jarryd J. Pla et al. "A single-atom electron spin qubit in silicon". In: *Nature* 489.7417 (Sept. 2012), pp. 541–545 (cit. on pp. 2, 12).

[Por56] A. M. Portis. "Spectral Diffusion in Magnetic Resonance". In: *Physical Review* 104.3 (Nov. 1956), pp. 584–588 (cit. on p. 69).

[Poz11] David M. Pozar. *Microwave Engineering*. John Wiley & Sons, Nov. 2011 (cit. on pp. 47, 177, 178).

[Pro+13] S. Probst et al. "Anisotropic Rare-Earth Spin Ensemble Strongly Coupled to a Superconducting Resonator". In: *Physical Review Letters* 110.15 (Apr. 2013), p. 157001 (cit. on p. 60).

[Pro+15] S. Probst et al. "Microwave multimode memory with an erbium spin ensemble". In: *Physical Review B* 92.1 (July 2015), p. 014421 (cit. on pp. 2, 12, 79).

[Pro+17] S. Probst et al. "Inductive-detection electron-spin resonance spectroscopy with 65 spins/Hz sensitivity". In: *Applied Physics Letters* 111.20 (Nov. 2017), p. 202604 (cit. on pp. 45, 97).

[Pro+20] Sebastian Probst et al. “Hyperfine spectroscopy in a quantum-limited spectrometer”. In: *Magnetic Resonance* 1.2 (Dec. 2020), pp. 315–330 (cit. on p. 77).

[Pro16] Sebastian Probst. *Hybrid quantum system based on rare earth doped crystals*. Vol. 16. KIT Scientific Publishing, 2016 (cit. on p. 158).

[Rak+20] Jelena V. Rakonjac et al. “Long spin coherence times in the ground state and in an optically excited state of $^{167}Er^{3+}$:Y_2SiO_5 at zero magnetic field”. In: *Physical Review B* 101.18 (May 2020), p. 184430 (cit. on pp. 2, 12, 80).

[Ran+13] V. Ranjan et al. “Probing Dynamics of an Electron-Spin Ensemble via a Superconducting Resonator”. In: *Physical Review Letters* 110.6 (Feb. 2013), p. 067004 (cit. on p. 60).

[Ran+18] Miloš Rančić et al. “Coherence time of over a second in a telecom-compatible quantum memory storage material”. In: *Nature Physics* 14.1 (Jan. 2018), pp. 50–54 (cit. on pp. 2, 12, 80).

[Ran+20a] V. Ranjan et al. “Electron spin resonance spectroscopy with femtoliter detection volume”. In: *Applied Physics Letters* 116.18 (May 2020), p. 184002 (cit. on pp. 3, 13, 97).

[Ran+20b] V. Ranjan et al. “Multimode Storage of Quantum Microwave Fields in Electron Spins over 100 ms”. In: *Physical Review Letters* 125.21 (Nov. 2020), p. 210505 (cit. on pp. 2, 12).

[Ran+20c] V. Ranjan et al. “Pulsed electron spin resonance spectroscopy in the Purcell regime”. In: *Journal of Magnetic Resonance* 310 (Jan. 2020), p. 106662 (cit. on pp. 5, 14, 61, 62, 64, 137).

[RHM65] L. G. Rowan, E. L. Hahn, and W. B. Mims. “Electron-Spin-Echo Envelope Modulation”. In: *Physical Review* 137.1A (Jan. 1965), A61–A71 (cit. on p. 78).

[Rus+21] Andrei Ruskuc et al. “Nuclear spin-wave quantum register for a solid state qubit”. In: *arXiv:2108.12723 [quant-ph]* (Aug. 2021) (cit. on p. 176).

[RV64] U. Ranon and V. Volterra. “Paramagnetic Resonance of Yb^{3+} in $CaWO_4$”. In: *Physical Review* 134.6A (June 1964), A1483–A1485 (cit. on pp. 30, 31, 84).

[Sag+15] Erhan Saglamyurek et al. “Quantum storage of entangled telecom-wavelength photons in an erbium-doped optical fibre”. In: *Nature Photonics* 9.2 (Feb. 2015), pp. 83–87 (cit. on pp. 2, 12).

[Sch+10] D. I. Schuster et al. “High-Cooperativity Coupling of Electron-Spin Ensembles to Superconducting Cavities”. In: *Physical Review Letters* 105.14 (Sept. 2010), p. 140501 (cit. on p. 60).

[Sho94] P.W. Shor. “Algorithms for quantum computation: discrete logarithms and factoring”. In: *Proceedings 35th Annual Symposium on Foundations of Computer Science*. Nov. 1994, pp. 124–134 (cit. on pp. 1, 11).

[SJ01] Arthur Schweiger and Gunnar Jeschke. *Principles of Pulse Electron Paramagnetic Resonance*. Oxford University Press, 2001 (cit. on pp. 36, 42, 61, 63, 69, 70, 76–78, 168).

[SN70] J. P. Sattler and J. Nemarich. “Electron Paramagnetic Resonance of Yb^{3+} in Scheelite Single Crystals”. In: *Physical Review B* 1.11 (June 1970), pp. 4249–4256 (cit. on p. 34).

[Som+21] Aaron Somoroff et al. “Millisecond coherence in a superconducting qubit”. In: *arXiv:2103.08578 [cond-mat, physics:quant-ph]* (Mar. 2021) (cit. on pp. 2, 12).

[Ste52] K. W. H. Stevens. "Matrix Elements and Operator Equivalents Connected with the Magnetic Properties of Rare Earth Ions". In: *Proceedings of the Physical Society. Section A* 65.3 (Mar. 1952), pp. 209–215 (cit. on p. 27).

[TA75] J. S. Thorp and E. A. E. Ammar. "The dielectric constants of $CaWO_4$, $Nd/CaWO_4$ and $Gd/CaWO_4$". In: *Journal of Materials Science* 10.6 (June 1975), pp. 918–922 (cit. on p. 90).

[Tak+08] Susumu Takahashi et al. "Quenching Spin Decoherence in Diamond through Spin Bath Polarization". In: *Physical Review Letters* 101.4 (July 2008), p. 047601 (cit. on p. 69).

[Tam+14] T. H. Taminiau et al. "Universal control and error correction in multi-qubit spin registers in diamond". In: *Nature Nanotechnology* 9.3 (Mar. 2014), pp. 171–176 (cit. on p. 176).

[Tos+17] Guilherme Tosi et al. "Silicon quantum processor with robust long-distance qubit couplings". In: *Nature Communications* 8.1 (Sept. 2017), p. 450 (cit. on pp. 2, 12).

[Tyr+03] A. M. Tyryshkin et al. "Electron spin relaxation times of phosphorus donors in silicon". In: *Physical Review B* 68.19 (Nov. 2003), p. 193207 (cit. on pp. 79, 125).

[Tyr+12] Alexei M. Tyryshkin et al. "Electron spin coherence exceeding seconds in high-purity silicon". In: *Nature Materials* 11.2 (Feb. 2012), pp. 143–147 (cit. on pp. 2, 12, 76, 79).

[Wan+09] H. Wang et al. "Improving the coherence time of superconducting coplanar resonators". In: *Applied Physics Letters* 95.23 (Dec. 2009), p. 233508 (cit. on pp. 93, 143).

[WCL14] Lewis A. Williamson, Yu-Hui Chen, and Jevon J. Longdell. "Magneto-Optic Modulator with Unit Quantum Efficiency". In: *Physical Review Letters* 113.20 (Nov. 2014), p. 203601 (cit. on pp. 2, 7, 12, 16, 111, 175).

[Wei12] Mitchel Weissbluth. *Atoms and Molecules*. Elsevier, Dec. 2012 (cit. on pp. 23, 26).

[Wol+13] Gary Wolfowicz et al. "Atomic clock transitions in silicon-based spin qubits". In: *Nature Nanotechnology* 8.8 (Aug. 2013), pp. 561–564 (cit. on pp. 68, 80).

[WSD05] W. M. Witzel, Rogerio de Sousa, and S. Das Sarma. "Quantum theory of spectral-diffusion-induced electron spin decoherence". In: *Physical Review B* 72.16 (Oct. 2005), p. 161306 (cit. on p. 74).

[WWM05] Jin Wang, H. M. Wiseman, and G. J. Milburn. "Dynamical creation of entanglement by homodyne-mediated feedback". In: *Physical Review A* 71.4 (Apr. 2005), p. 042309 (cit. on p. 54).

[Wyb65] Brian G. Wybourne. *Spectroscopic properties of rare earths*. Tech. rep. Interscience Publishers, 1965 (cit. on pp. 23, 27).

[Xia+13] Ze-Liang Xiang et al. "Hybrid quantum circuits: Superconducting circuits interacting with other quantum systems". In: *Reviews of Modern Physics* 85.2 (Apr. 2013), pp. 623–653 (cit. on pp. 2, 12).

[Yin+13] Chunming Yin et al. "Optical addressing of an individual erbium ion in silicon". In: *Nature* 497.7447 (May 2013), pp. 91–94 (cit. on p. 176).

[YL08] Wen Yang and Ren-Bao Liu. "Quantum many-body theory of qubit decoherence in a finite-size spin bath". In: *Physical Review B* 78.8 (Aug. 2008), p. 085315 (cit. on p. 74).

[Zhe+04] Wen-Chen Zheng et al. "Investigations of the optical spectra and EPR parameters in $CaWO_4$:Yb^{3+}". In: *Spectrochimica Acta Part A: Molecular and Biomolecular Spectroscopy* 60.13 (Nov. 2004), pp. 3169–3171 (cit. on p. 34).

[ZHL12] Nan Zhao, Sai-Wah Ho, and Ren-Bao Liu. "Decoherence and dynamical decoupling control of nitrogen vacancy center electron spins in nuclear spin baths". In: *Physical Review B* 85.11 (Mar. 2012), p. 115303 (cit. on p. 79).

[ZT64] Allan Zalkin and David H. Templeton. "X-Ray Diffraction Refinement of the Calcium Tungstate Structure". In: *The Journal of Chemical Physics* 40.2 (Jan. 1964), pp. 501–504 (cit. on p. 30).

université PARIS-SACLAY | ÉCOLE DOCTORALE Physique en Île-de-France (PIF)

Titre : Dynamique des spins électroniques d'ions erbium dans des cristaux de scheelite, sondés avec des résonateurs supraconducteurs à des températures de l'ordre du millikelvin

Mots clés : ions de terres rares, résonance paramagnétique électronique, dispositifs quantiques hybrides

Résumé : L'un des nombreux défis des technologies quantiques est d'interfacer de l'information quantique stationnaire et durable avec des photons se propageant dans les réseaux de communication. Les cristaux dopés à l'erbium sont particulièrement adaptés à cette tâche. En effet, les ions erbium ont une transition optique à 1.5 μm qui se situe dans la fenêtre spectrale où les fibres optiques ont le minimum de pertes. De plus, les ions erbium ont un degré de liberté de spin car leur état fondamental est un doublet qui se comporte comme un spin effectif $1/2$. Le fort moment magnétique de ce spin électronique est un avantage pour se coupler efficacement à d'autres systèmes quantiques, comme des spins nucléaires voisins ou des processeurs supraconducteurs. Jusqu'à maintenant, le temps de cohérence du spin électronique de l'erbium, sur une transition sensible au champ magnétique, était cependant limité à 50 μs, ce qui est insuffisant pour ces applications de réseaux quantiques. Dans cette thèse, nous améliorons ce temps de cohérence de presque trois ordres de grandeur. D'abord, nous choisissons la scheelite ($CaWO_4$) comme cristal pour sa faible densité de moments magnétiques et nous travaillons avec des cristaux nominalement non dopés, de sorte que la concentration résiduelle d'impuretés comme l'erbium est de l'ordre de la partie par milliard. Ensuite, nous refroidissons l'échantillon jusqu'à 10 mK, afin de supprimer le processus de décohérence venant du couplage magnétique entre les ions erbium et d'autres impuretés. A cette température, des temps de cohérence jusqu'à 30 ms sont mesurés et nous montrons qu'ils sont limités par l'interaction de l'erbium avec les spins nucléaires du cristal. Nous étudions également un cristal de scheelite avec une concentration d'erbium 10^4 fois plus grande, ce qui est plus adapté pour des applications de mémoires quantiques, et nous mesurons des temps de cohérence jusqu'à 1 ms. Ces deux expériences confirment que les ions erbium dans la scheelite sont intéressants pour réaliser des nœuds de réseaux quantiques et des systèmes quantiques hybrides, grâce à leur forte sensibilité au champ magnétique et leurs longs temps de cohérence.

université PARIS-SACLAY

ÉCOLE DOCTORALE
Physique en Île-de-France (PIF)

Title : Electron spin dynamics of erbium ions in scheelite crystals, probed with superconducting resonators at millikelvin temperatures

Keywords : rare-earth ions, electron spin resonance, hybrid quantum devices

Abstract : One of the many challenges of quantum technologies is to interface long-lived stationary quantum information with propagating photons in communication networks. Erbium doped crystals are particularly suited for this task. Indeed, erbium ions have an optical transition at 1.5 μm which falls in the spectral window where optical fibers have minimal losses. Moreover, erbium ions have a spin degree of freedom because their ground state is a doublet which behaves as an effective electron spin half. The large magnetic moment of this electron spin is an advantage to couple efficiently to other quantum systems, such as neighboring nuclear spins or superconducting processors. Up to now, the coherence time of the erbium electron spin, on a magnetically-sensitive transition, was however limited to 50 μs, which is insufficient for these quantum network applications. In this thesis, we improve this coherence time by nearly three orders of magnitude. We first choose scheelite ($CaWO_4$) as a host crystal for its low magnetic moment density and we work with a nominally undoped crystal, such that the residual concentration of impurities like erbium is of the order of part per billion. We then cool the sample down to 10 mK, in order to quench the decoherence process arising from the magnetic coupling of the erbium ions to other impurities. At this temperature, coherence times up to 30 ms are reported and are shown to be limited by the interaction of erbium with the nuclear spins of the host crystal. We also study a scheelite crystal with a 10^4 times larger erbium concentration, which is more suited for quantum memory applications, and measure coherence times up to 1 ms. Both experiments confirm that erbium ions in scheelite are interesting for realizing quantum network nodes and hybrid quantum systems, due to their large magnetic field sensitivity and their long coherence times.